

Transition metal complexes and photoswitchable self assembled monolayers on Au(111): Surface spectroscopic characterization



Christian-Albrechts-Universität zu Kiel

Institut für Anorganische Chemie

Dissertation zur Erlangung des Doktorgrades der Naturwissenschaften

Dr. rer. nat.

der Mathematisch-Naturwissenschaftlichen-Fakultät der

Christian-Albrechts-Universität zu Kiel

vorgelegt von

Hanne Jacob

Kiel 2015

Erster Gutachter: Prof. Dr. Felix Tuzek

Zweiter Gutachter: Prof. Dr. Wolfgang Bensch

Tag der mündlichen Prüfung: Kiel, den 08.05.2015

Zum Druck genehmigt: Kiel, den 08.05.2015

Prof. Dr. Wolfgang Duschl, Dekan

Die vorliegende Dissertation wurde unter Anleitung von
Prof. Dr. Felix Tuczek
in der Zeit von
April 2011 bis März 2015
am Institut für Anorganische Chemie
im Rahmen des Sonderforschungsbereiches
SFB 677 "Funktion durch Schalten"
an der Christian-Albrechts-Universität zu Kiel
angefertigt.



Für meine geliebte Familie

Danksagung

Mein aufrichtiger Dank gilt Prof. Dr. Felix Tuczek für die anregenden Arbeitsbedingungen, die gewährten Freiheiten, die vielen spektroskopischen Möglichkeiten und das weitgefächerte Thema meiner Dissertation. Ich hatte bis zum Schluss viel Freude an der Bearbeitung dieses Themas.

Für die Übernahme des Zweitgutachtens bedanke ich mich recht herzlich bei Prof. Dr. Wolfgang Bensch.

Beim technischen Personal der Universität möchte ich mich für die Anfertigung von Glasgeräten, die Bereitstellung aller Chemikalien und den netten Umgang bedanken. Frau Pehlke, Frau Pick und vor allem Frau Cornelissen danke ich für die Aufnahme zahlreicher Spektren und auch für die Hilfe mit dem Vertex Spektrometer.

Ich möchte mich herzlich bei meinen Kooperationspartnern Dr. Thomas Strunskus, Sandra Ulrich, Sujoy Karan, Dr. Thiruvancheril Gopakumar und Torben Jasper-Tönnies bedanken. Ohne euch wären nicht so tolle Veröffentlichungen entstanden. Besonderen Dank richte ich an Thomas Strunskus für die Hilfe bei den Auswertungen und Aufnahmen von XPS und NEXAFS Daten und die tollen, aber auch sehr anstrengenden Zeiten in Berlin am BESSY II.

Meiner besten Freundin Dagmar Preugschat und meinen Freunden Finn Petersen, Bettina Schwager, Friederike Schulz, Matthias Baack, Michael Hinz und Franziska Wendt danke ich für die vielen schönen Stunden außerhalb der Uni und ihre Freundschaft.

Bei meinem liebsten Kommilitonen und auch besten Freund Finn Petersen möchte ich mich unendlich doll bedanken. Ohne dich wäre das Studium nur halb so lustig gewesen. Ich danke dir für deine viele Hilfe, Geduld, tolle Gespräche, ein immer offenes Ohr und auch Interesse

an meinem Privatleben.

Bedanken möchte ich mich bei meinen verstorbenen Großeltern, die mich immer finanziell und mental unterstützt haben, weil sie immer stolz auf mich waren.

Ich möchte auch meinen lieben Kollegen Sven Olaf Schmidt und Bettina Schwager für die unvergesslich tolle und lustige Zeit in unserem Labor danken.

Danke an meine Bachelor-Studenten Benjamin Herzigkeit und Alexander Schlimm für die viele Synthesearbeit.

Ich bedanke mich bei Dagmar Preugschat, Elena Willson, Finn Petersen und Jan Schürmann für das Korrekturlesen dieser Arbeit.

Bei meinem lieben Freund Jan Schürmann bedanke ich mich für die schöne Zeit zusammen, ohne die mir ein gutes Arbeiten deutlich schwerer gefallen wäre. Du hast mich immer wieder aufgefangen und warst der beste Beistand, den ein jeder sich nur wünschen kann.

Ich bedanke mich bei meiner ganzen Familie für das Interesse am Fortgang dieser Arbeit und die Unterstützung.

Der größte Dank gilt meinen lieben Eltern, Peter und Elke Jacob, die mich immer finanziell unterstützt haben und mir durch ihren stets gezeigten Stolz immer wieder Motivation gegeben haben, um diese Arbeit fertig zu stellen.

Vielen Dank an alle!

*”So eine Arbeit wird eigentlich nie fertig, man muß sie für fertig erklären,
wenn man nach Zeit und Umständen das möglichste getan hat.”*

(J.W.v. Goethe: ”Italienische Reise, 16.3.1787”)

Abstract

The main scope of this thesis was the synthesis and fixation of spin crossover transition metal complexes, particularly iron(III), to Au(111) surfaces. The synthesized systems were characterized in bulk and the adsorbed systems were characterized with surface spectroscopic methods like IRRAS (infrared reflection absorption spectroscopy), XPS (X-ray photoelectron spectroscopy) and NEXAFS (near edge X-ray absorption fine structure). In cooperation with the AG of Prof. Dr. Richard Berndt (Institute for Experimental and Applied Physics, Christian-Albrechts-University of Kiel) STM (scanning tunneling microscopy) measurements of a dinuclear iron(III) complex were performed. Furthermore, in cooperation with Prof. Dr. R. Herges (Otto Diels-Institute of Organic Chemistry, Christian-Albrechts-University of Kiel) and Prof. Dr. Thisbe K. Lindhorst (Otto Diels-Institute of Organic Chemistry, Christian-Albrechts-University of Kiel), self-assembled organic monolayers on Au(111) surfaces were characterized by IRRAS, SERS and XPS and their photoswitching behavior was tested with the help of IRRAS. This work is arranged in an introduction and four chapters:

The first chapter deals with the synthesis of dinuclear iron(III) complexes with disulfide-bridging ligands for the fixation on Au(111) surfaces, their characterization in bulk material and the surface-spectroscopic characterization of the adsorbed mononuclear complexes on Au(111) with IRRAS, XPS and NEXAFS.

The second chapter shows the utilization of one of these dinuclear iron(III) complexes as a chemical wire on an Au(111) surface. In this dinuclear complex, a reversible switching process in form of a conformational change of the salen-ligand (bis(3-salicylidene-amino-propyl)amine) was monitored by STM and can be identified as a Bailar-Twist.

The third chapter presents the characterization of a methoxyazobenzene functionalized molecular TATA ("triazatriangulene") platform on Au(111) by XPS, SERS, STM, IRRAS

and PM-IRRAS. The thermal back relaxation from *cis* to *trans* of these systems was determined by PM-IRRAS and a half-life of 42 seconds was determined.

The fourth chapter deals with the preparation and surface spectroscopic characterization of glycoside containing self assembled monolayers on Au(111) surfaces. These azobenzene functionalized azomannose-derivatives were adsorbed on Au(111) surfaces and the photochemical switching process, a *trans* to *cis* isomerization of the containing azobenzene unit, was followed by IRRAS.

Kurzzusammenfassung

Das Hauptziel der hier vorliegenden Arbeit war die Synthese und Fixierung von Spin-Crossover Übergangsmetallkomplexen, hauptsächlich Eisen(III)-Systemen, auf Gold(111)-Oberflächen. Die synthetisierten Systeme wurden im Feststoff charakterisiert und die oberflächenfixierten Systeme daraufhin oberflächenspektroskopisch mittels IRRAS (Infrarot Reflections Absorptionsspektroskopie), XPS (X-ray photoelectron spectroscopy) und NEXAFS (Near edge X-ray absorption fine structure) untersucht. Im Rahmen einer Kooperation mit der AG von Prof. Dr. Richard Berndt wurden STM Messungen an einem zweikernigen Eisen(III) System vorgenommen. Des Weiteren wurden in Kooperation mit der AG von Prof. Dr. Rainer Herges (Otto Diels-Institut für Organische Chemie, Christian-Albrechts-Universität zu Kiel) und der AG von Prof. Dr. Thisbe K. Lindhorst (Otto Diels-Institut für Organische Chemie, Christian-Albrechts-Universität zu Kiel) organische self assembled monolayers auf Au(111) mittels IRRAS, SERS und XPS umfassend charakterisiert und auf ihr photoschaltbares Verhalten mittels IRRAS auf der Oberfläche getestet. Die vorliegende Arbeit teilt sich in Einleitung sowie die folgenden Kapitel auf:

Das erste Kapitel befasst sich mit der Synthese zweikerniger Eisen(III)-Komplexe mit Disulfidbrücken-Liganden zur Fixierung auf Au(111)-Oberflächen. Ebenso stand deren spektroskopische Charakterisierung im Feststoff und der adsorbierten monomeren Komplexe auf Au(111) mittels IRRAS, XPS und NEXAFS im Vordergrund.

Im zweiten Kapitel findet ein solches zweikerniges Eisen(III)-System Anwendung als "chemischer Draht" auf einer Au(111)-Oberfläche. An diesem System konnte ein reversibler Schaltprozess in Form einer Konformationsänderung des salten-Liganden (*Bis*(3-salicylidenamino-propyl)-amin) mittels STM gezeigt werden und als ein Bailar-Twist identifiziert werden.

Das dritte Kapitel zeigt die Charakterisierung einer Methoxyazobenzol funktionalisierten

molekularen TATA ("triazatriangulen") Plattform auf Au(111) mittels XPS, SERS, STM, IRRAS sowie PM-IRRAS. An diesem System konnte eine thermische Rückrelaxation mit Hilfe von IRRAS detektiert und eine Halbwertszeit von 42 Sekunden auf der Oberfläche für die *cis* zu *trans* Rückisomerisierung bestimmt werden.

Im vierten Kapitel ist die Präparation und oberflächenspektroskopische Charakterisierung von mannosehaltigen self assembled monolayers auf Au(111)-Oberflächen gezeigt. Diese Azobenzol funktionalisierten Mannose-Derivate wurden auf Au(111) fixiert, und die photochemische *trans* zu *cis* Isomerisierung einer enthaltenen Azobenzoleinheit konnte mittels IRRAS detektiert werden.

Publikationen

Diese Dissertation basiert auf folgenden Publikationen, die in verschiedenen Fachzeitschriften erschienen sind:

- H. JACOB, K. Kathirvel, F. Petersen, T. Strunskus, A. Bannwarth, S. Meyer, F. Tuczek*

”Grafting of functionalized [Fe(III)(salten)] complexes to Au(111) surfaces via thiolate groups: Surface spectroscopic characterization and comparison of different linker designs”

Langmuir, **2013**, 29 (27), 8534-8543.

Eigenanteil: maßgeblich an der Konzeption beteiligt; Synthese der verwendeten Moleküle, Vorbereitung und Durchführung der Messungen; Datenanalyse; federführend in der Erstellung des Manuskriptes, federführend in der Diskussion der Ergebnisse; Korrespondenz mit dem Verlag.

- S. Karan, T. Gopakumar, H. JACOB, S. Meyer, F. Tuczek* and R. Berndt*

”Remotely triggered geometrical isomerization of a binuclear complex”

J. Am. Chem. Soc., **2014**, 136 (17), 6163-6166.

Eigenanteil: Synthese und Charakterisierung der zwei untersuchten Komplexe im Bulk-Material; maßgeblich beteiligt an der Diskussion und Interpretation der Ergebnisse; beteiligt an der Konzeption des Manuskriptes;

- H. JACOB, S. Ulrich, U. Jung, S. Lemke, T. Rusch, C. Schütt, F. Petersen, S. Strunskus, O. Magnussen, R. Herges* and F. Tucek*

”Monitoring the reversible photoisomerization of an azobenzene- functionalized molecular triazatriangulene platform on Au(111) by IRRAS”

Phys. Chem. Chem. Phys., **2014**, 16, 22643-22650.

Eigenanteil: maßgeblich an der Konzeption beteiligt; federführend in der Erstellung des Manuskriptes; Umbau des Spektrometers; Vorbereitung und Durchführung der Messungen; Datenanalyse; maßgeblich an der Diskussion und Interpretation der Ergebnisse beteiligt; Koordination der Kooperation;

- V. Chandrasekaran, H. JACOB, F. Petersen, K. Kathirvel, F. Tucek* and T. K. Lindhorst*

”Synthesis and surface-spectroscopic characterization of photoisomerizable glyco-SAMs on Au(111)”

Chem. Eur. J., **2014**, 20, 8744-8752.

Eigenanteil: Präparationen der Proben; Vorbereitung und Durchführung der Messungen; beteiligt an der Datenanalyse; maßgeblich beteiligt und federführend in der Diskussion der Ergebnisse; wesentlicher Anteil an der Erstellung des Manuskriptes;

- BeilsteinTV, 2015. ”Fixation of metal complexes on surfaces” [Video-Podcast] Februar 2015. Verfügbar unter: www.beilstein.tv

- T. Jasper-Tönnies, H. JACOB, F. Tucek* and R. Berndt*

”Reversible Switching of Fe(pap)₂”

Manuscript *in preparation*.

- A. Schlimm, H. JACOB, F. Petersen, T. Strunskus and F. Tucek*

”Grafting of [Fe(ethinyltolyl)salten] complexes to an azide-terminated prefunctionalized surface using a click reaction”

Manuscript *in preparation*.

Vorträge

- 13. Norddeutsches Doktorandenkolloquium der Anorganischen Chemie, September 2011, Walsrode
"Iron salten complexes and functionalized ligands for self-assembly on the gold surface"
- Summer school vom Sonderforschungsbereich 677, August 2012, Ratzeburg
"Iron salten complexes for self assembly on gold surfaces: surface spectroscopic characterization"
- Euro Intelligent Materials, September 2013, Kiel
"Grafting of functionalized [Fe(III)(salten)] complexes to Au(111) surfaces via thiolate groups: surface spectroscopic characterization"
- Kolloquium im Institut für Anorganische Chemie, Dezember 2013, Kiel

Poster

- Internationale Konferenz des Sonderforschungsbereiches 677, Oktober 2011, Schleswig
- Internationale Konferenz des Sonderforschungsbereiches 677, August 2012, Plön
- Wissenschaftsforum der Chemie der GDCh, September 2013, Darmstadt
- 5th EuCheMS Chemistry Congress, August 2014, Istanbul

Contents

1	Introduction	1
1.1	Natural phenomena - the source of inspiration	1
1.2	Molecular electronics	3
1.2.1	Molecular switches	5
1.2.2	Azobenzene as a photo-switchable unit	5
1.3	Self-assembled monolayers (SAMs)	9
1.4	Surface analytical techniques - Overview	14
1.4.1	Infrared spectroscopy	16
1.4.2	Infrared reflection absorption spectroscopy	18
2	Functionalization of Au(111) surfaces with spin crossover complexes	25
2.1	Spin Crossover Phenomenon	25
2.2	Motivation	29
2.3	Grafting of Functionalized [Fe(III)(salten)] Complexes to Au(111) Surfaces via Thiolate Groups: Surface Spectroscopic Characterization and Comparison of Different Linker Designs	35
2.4	Conclusion	47
2.5	Outlook	50
3	Functionalization of Au(111) surfaces with dinuclear complexes	57
3.1	Chemical wires	57
3.2	Motivation	59
3.3	Remotely triggered geometrical isomerization of a binuclear complex	61
3.4	Conclusion	67
3.5	Outlook	70
4	Characterization of switchable azobenzene functionalized Triazatriangulene platforms (TATA)	75

4.1	Switchable Surfaces	75
4.2	Motivation	76
4.3	Monitoring the reversible photoisomerization of an azobenzene- functionalized molecular triazatriangulene platform on Au(111) by IRRAS	81
4.4	Conclusion	90
4.5	Outlook	93
5	Characterization of switchable glyco-SAMs on Au(111)	97
5.1	Glycosides and cell adhesion	97
5.2	Motivation	99
5.3	Synthesis and surface-spectroscopic characterization of photoisomerizable glyco- SAMs on Au(111)	101
5.4	Conclusion	111
5.5	Outlook	113
6	Summary and Outlook	115
7	General procedures and analytical techniques	117
8	Appendix	121
8.1	Supporting information on the <i>Langmuir</i> publication	121
8.2	Supporting information on the <i>Journal of the American Chemical Society</i> publication	165
8.3	Supporting information on the <i>Physical Chemistry Chemical Physics</i> publication	171
8.4	Supporting information on the <i>Chemistry-A European Journal</i> publication .	187
9	References	213
10	Eidesstattliche Erklärung	233
11	Curriculum vitae	235

1 Introduction

1.1 Natural phenomena - the source of inspiration

Years ago, the swiss engineer Georges de Mestral went outside for a walk with his dogs. He noticed small fruits of a plant sticking to his dog's fur and was astonished.

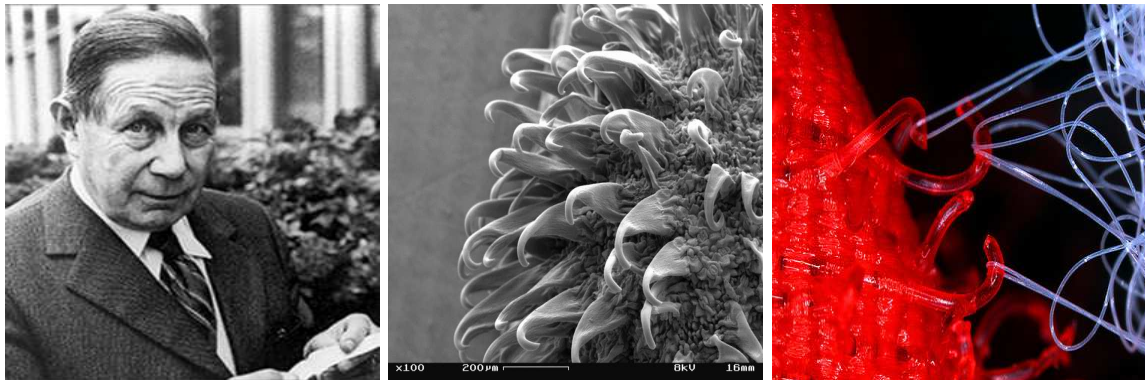


Figure 1: On the left hand side a picture of Georges de Mestral, in the middle an electron microscope image of a burdock fruit and the function principle of a hook-and-loop fastener on the right hand side is shown.^[1-3]

After putting these small fruits under a microscope, he recognized that the burdock (*Arctium lappa*), a plant species of the Carduoideae, has elastic, coarse and hook-shaped fibres which stick to smaller fibres and can be removed without breaking. The hook-and-loop fastener was born and in 1951 de Mastral obtained the patent for this invention which brought industry and nature closer together.

Another interesting phenomenon in nature are geckos and their ability to walk on vertical surfaces. A gecko can weigh up to 300 g and is the heaviest animal that has the possibility to use this sort of dry adhesion, which is based on a very weak *van-der-Waals* attraction. The feet of a gecko have small fine structures with densely fine hair (Setae). With this dense packed hair, the gecko has a lot of small points which lead to small adhesion forces. The sum of all these small adhesion points amounts to a huge adhesion force.

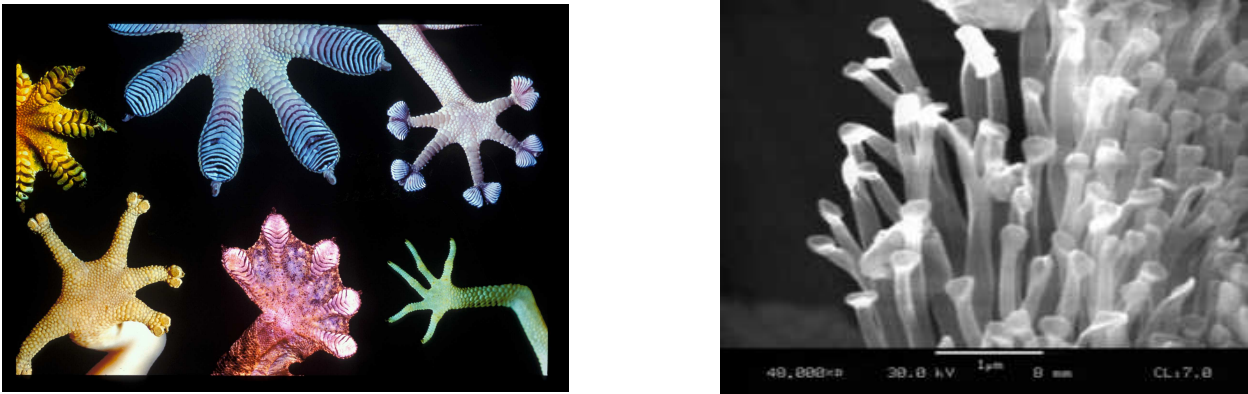


Figure 2: On the left hand side different gecko feet are shown and an electron microscopic image of Setae is shown on the right hand side.^[4,5]

In addition, the lotus effect enables water and dirt particles to run off the surface of a leaf in drops. The trick of the lotus leaf is a very thin and fine cuticle which causes a hydrophobic behavior. Furthermore, the surface possesses small nubs which are able to adhere dirt particles and the water droplets can run off the leaf. The roughness of the surface minimizes the contact area between leaf and droplet which allows a frictionless rolling. This effect is a useful prototype for the global industry to realize self-cleaning surfaces for aircraft carriers or house fronts.

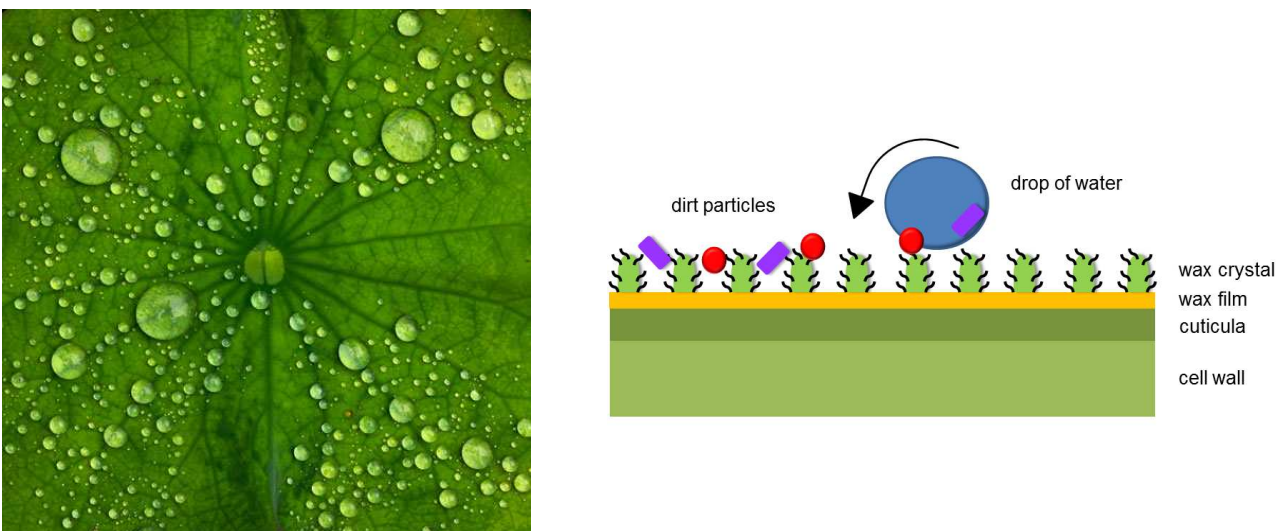


Figure 3: Water droplets on a lotus leaf and the self cleaning principle of the lotus leaf.^[6]

In flora and fauna we can find a lot of interesting phenomena which are worthy of study and can be helpfully applied to our every day life. The transfer of these phenomena to abiotic systems occupy the work of many scientists all over the world. The branch of research which has the effort to mimic bio phenomena to all day life is called bionic (biology and technics).

In industry, surfaces and the adjustment of their properties play a big role. Surfaces are getting more and more 'intelligent'. Giving a surface different behavior and composition can lead to model systems for the study of organic and biological interfaces. Furthermore, applications in the field of adhesion, lubrication, corrosion, protection, wetting, photochemical and electrochemical processes can be reached.

The SFB 677 in Kiel aims to learn from nature by combining the fields of chemistry, physics and material science in the synthesis, characterization and behavior of nanomolecular machines. This requires cooperation with biological, zoological and medical work-groups. These nanosystems will applied to the fields of medicine, sensor materials and storage devices. The main subject is a molecular switching process, which can be effected through external stimuli like pressure, electromagnetic fields e.g. light or voltage. Different projects in the SFB 677 try to bring molecular switches in different environments like homogeneous solutions, functional materials and on surfaces.^[7]

1.2 Molecular electronics

Molecular electronics is the attempt to widen the conventional electronics to electronics which work with molecules or molecular function units in a nanoscale dimension. It is the further development of microelectronics. In molecular electronics the inter- and intramolecular interactions shall be exploited for potential applications. These molecules will be the active part to store, forward and process information. In molecular electronics, one can distinguish between monomolecular electronics and supramolecular electronics. In supramolecular electronics, associations of molecules have the effect of the functional elements and in

monomolecular electronics, every single molecule acts as an individual functional element.^[8,9] For example, magnetic materials like storage devices can be found in hard discs. The research on magnetic materials on molecular level is very interesting and promises high storage capacities.

The endeavor to build smaller storage devices is a big challenge for industry and research. We wish to have smaller and lighter devices like MP3 players or smart phones with a big storage capacity for music files or photographs. The trend that smaller and faster electronic devices would become available was clearly predicted by Gordon Moore in 1965. This empiric law means that the number of transistors in an integrated circuit per square centimeter doubles every 24 months.^[10,11]

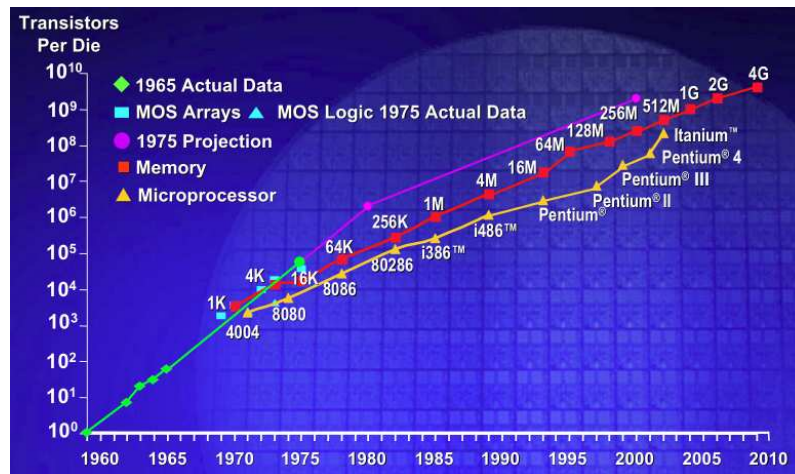


Figure 4: The figure shows Moore's empiric predicted law.^[12]

Molecular electronics open up the possibility to reach storage capacities up to 10^{11} Bit/cm².^[13] A bistability of the system serves as a basis to build up molecular storage devices and sensors. This binary code has two different states: ON and OFF or 0 and 1. It is important that these different states can be achieved reversibly. Switching between these states requires a geometry change or a change of the magnetic moment. Furthermore, it is necessary to read out these two different states of the molecules by either their magnetism or optical properties. The most studied molecular systems for realizing molecular electronics are molecular wires, diodes and self assembled monolayers between electrodes.^[14-20]

1.2.1 Molecular switches

Nature offers a lot of molecular switching processes. For example, the retinal molecule, linked to an opsin protein, can undergo an isomerization in the presence of light, from a *cis* to a *trans* conformation. This process is the basis for the vision of human beings and animals. The isomerization of one C=C double bond in the molecule of 11-*cis*-retinal to the all-*trans*-retinal starts a signal transduction. *Trans*-retinal can be transferred back to 11-*cis*-retinal by an enzymatic process.^[21]

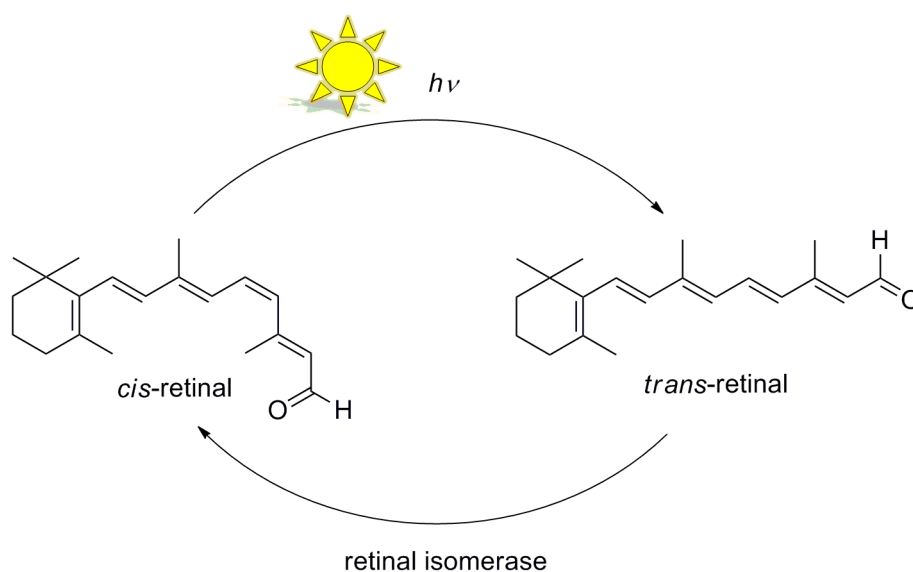


Figure 5: Reversible conversion from *cis*-retinal to *trans*-retinal by light and back isomerization by retinal-isomerase.

Molecular switches can be defined as molecules which can exist in two different states. Important is that these molecules have a spatially fixed position. They also need to satisfy special requirements like chemical stability, reversibility and a control of the macro level with the micro level. Examples are acid-base reactions (pH-switches), redox reactions (redox-switches), photochemical reactions like conformational switches, thermal reactions and quantum effects.

1.2.2 Azobenzene as a photo-switchable unit

An established and well known photo-switchable system is azobenzene, which was discovered by Hartley in 1937. These molecules can be switched by irradiation with UV light from the

thermodynamical stable (54 kJ/mol stabilization) *trans* to a metastable *cis* conformation.^[22] The transfer back to the *trans* isomer can be effected by irradiation with blue light or through thermal back-relaxation.

Azobenzene containing molecules are one of the most studied photo-switchable systems in literature. The photo-isomerization has been studied in detail on molecules in solution, gas phase and embedded in polymer films.^[23-25]

The *trans* isomer has a planar structure and a vanishing dipole moment. In the *cis* isomer the phenyl rings are twisted at 60° to each other. It possesses a dipole moment of 3.2 Debye. Regarding the molecule in general the switching process leads to a significant change of the molecular length.^[26,27]

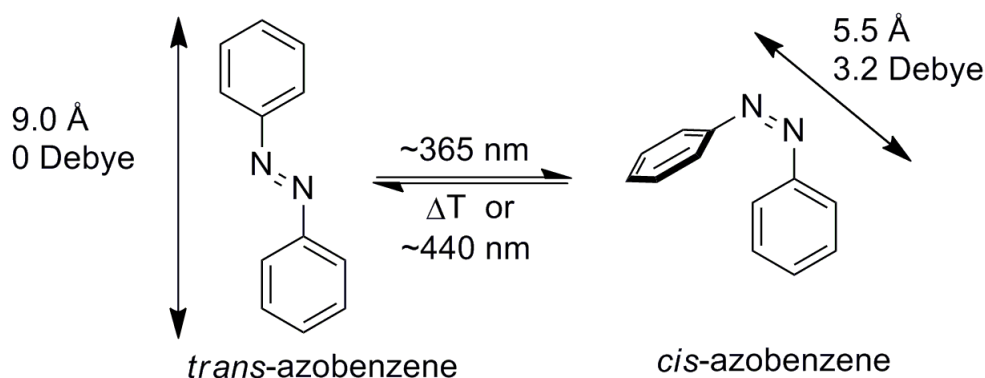


Figure 6: The structure of an azobenzene molecule in the *trans* and *cis* isomer.

The exact mechanism of the *trans* to *cis* isomerization is not fully understood yet, but a topic of current research. Different isomerization pathways are proposed in literature. The 'inversion mechanism' involves an inversion of the phenyl groups bound to the azo-nitrogen atoms. The 'concerted inversion mechanism' follows a synchronous inversion of both nitrogen atoms with a linear transition state and the 'rotation mechanism' includes a breaking of the double bond of the azo-unit followed by a rotation of the phenyl rings.^[28-31]

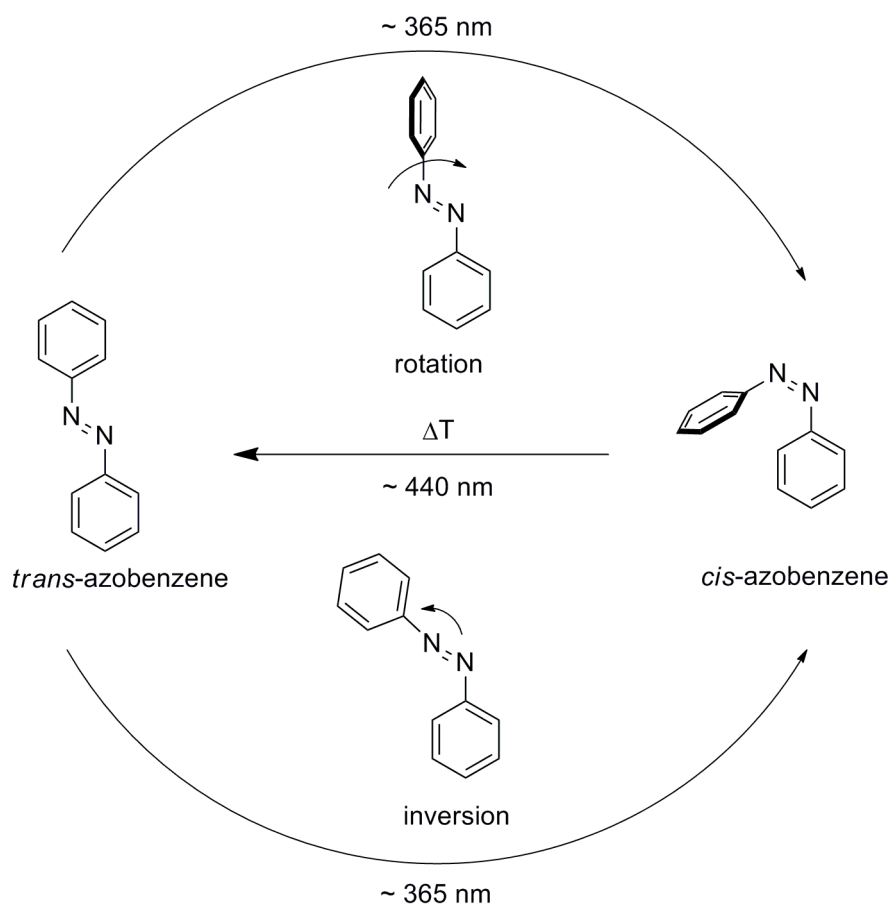


Figure 7: Schematic view of the mechanism for the isomerization process of azobenzene.

The conversion from the *trans* to *cis* isomer can be easily followed by UV/Vis spectroscopy through the change of the absorption maximum. Other techniques like IR, Raman or NMR can also be used to identify the two different isomers.^[32] The *trans* isomer exhibits a strong absorption band at around 360 nm. By irradiation with UV light of this wavelength, this absorption band decreases drastically in intensity and a new, weaker absorption band at around 440 nm appears.^[32,33] Irradiation with visible light of 440 nm transfers the system back to the starting state.

Molecules containing azobenzene can have promising properties for optical data storage.^[34,35] Examples of other photochromic organic molecules are spiropyrans^[36-40], fulgides^[41-44] and diarylethenes.^[45-48]

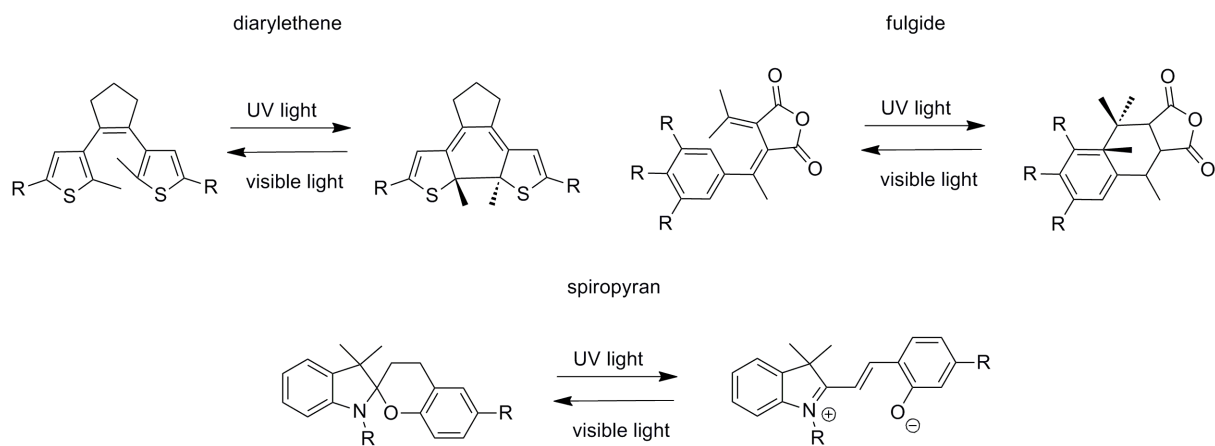


Figure 8: Diarylethene, fulgide and spiropyran as photochromic molecules.

1.3 Self-assembled monolayers (SAMs)

Self-assembled monolayers (SAMs) are ordered molecular assemblies formed on a solid substrate or interface by spontaneous self-organization of the molecules.^[49-51]

Novel properties and applications of these monolayers on substrates include corrosion protection, molecular recognition, photolithography, biocompatibility, surface-wetting control, photoresponsive structures and electron transfer control.

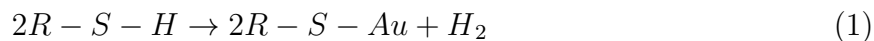
Surfaces can be planar like Au(111), silicon, HOPG (highly ordered pyrolytic graphite), Ag(111), SiO₂ or curved like in nanoparticles.^{[49][52]} Gold is the most commonly used surface, because it is chemically inert, easy to acquire and biocompatible.^[53,54] The production of highly ordered assemblies of molecules on surfaces depends on factors like surface roughness and cleanness as well as substance purity, solvent, concentration, temperature and immersion time.

Either through immersion of a substrate in a solution of a surface-active molecule, or from vapor gas phase deposition in UHV, molecules can arrange themselves and bind to the surfaces through different forces.^[55,56]

Two different binding processes can be distinguished:

1. Chemisorption

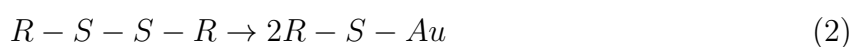
The molecules bind covalently to the substrate by a surface-affine head group and form chemical bonds. Thiol derivatives (-SH) are the best studied surface binding molecules which result in stable films with a high binding energy of around 190 kJ/mol (45 kcal/mol) due to the thermodynamically favourable formation of the Au-S bond^[57]:



The thiolate bond is formed after the dissociation of hydrogen from the sulfur. Alkanethiols form densely packed monolayers with a high degree of order and less defects. Selenol (-SeH), alkyne and isonitrile head groups are also known in literature.^[58-62]

The self-assembly of alkanethiols from the respective disulfides on Au(111) surfaces was reported for the first time in 1983 by Nuzzo and Allara.^[63]

In the case of disulfides, the S-S bond cleavage results through the reduction of the disulfide from the electron rich metal surface:



The spacer group of the molecules has the function to stabilize the film itself and acts as the backbone. Through the spacer group, the thermodynamical stability and thickness of the resulting film on the surface is defined. These films can have different thicknesses between 0.1 nm to several nm.

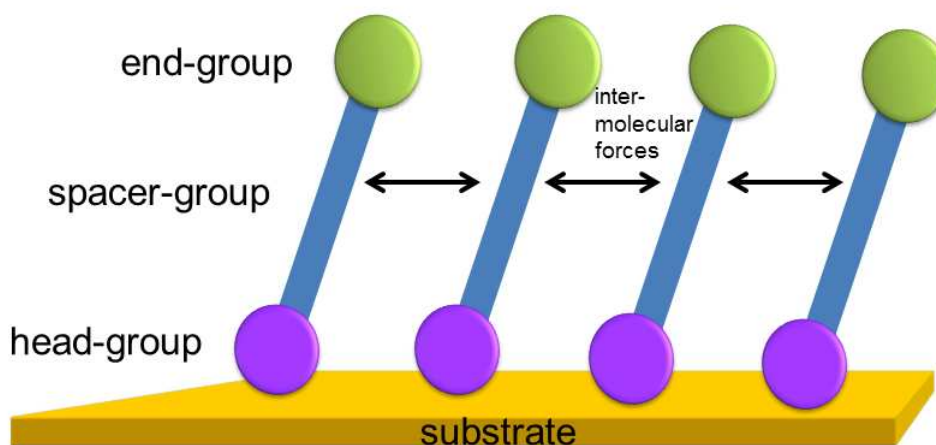


Figure 9: General structure of self-assembled monolayers on a substrate.

The *van-der-Waals* interactions of the alkyl chains of the molecules lead to a stabilization and straightening of the alkyl chains on the surface. In aromatic systems, the result is electrostatic interactions like π - π interactions.

The tail- or end group of the molecule can adjust the electronic, physical and chemical surface properties of the film. While -OH terminated SAMs provide a hydrophilic surface, -CH₃ terminated SAMs result in hydrophobic surface properties.

In general, the formation of SAMs follows the Langmuir adsorption isotherm where lateral interactions can be neglected.^[64-69] This kinetic model describes the proportionality of the rate of deposition on the surface in respect to the free space of the surface, expressed by the following equation:

$$k(1 - \Theta) = \frac{d\Theta}{dt} \quad (3)$$

where Θ is the amount of area, k the rate constant and t is the time.

If lateral interactions play an important role, the adsorption process can be described by the Frumkin isotherm^[57], that represents an extension of the Langmuir isotherm:

$$K_{\text{Fr}}(A) = \frac{\Theta}{1 - \Theta} \cdot (e)^{2a\Theta} \quad (4)$$

where Θ is the amount of area and a the interaction coefficient.

The SAM formation on a surface involves two major steps.^[49] In the first initial step, the free molecules physisorb on the surface and lead to a saturation-coverage (Fig. 10, Fig. 11 (2)). In this step a local energy minimum is reached while the molecules are disordered on the surface and lying flat. The initial driving force for the assembly is the chemical affinity between the adsorbate and the substrate. The velocity of this process is very fast. The formation of an Au-S bond conforms the highness of the energy barrier. In this step, the molecule is chemisorbed and dissociated hydrogen dimerizes and desorbes (Fig. 11 (3)).

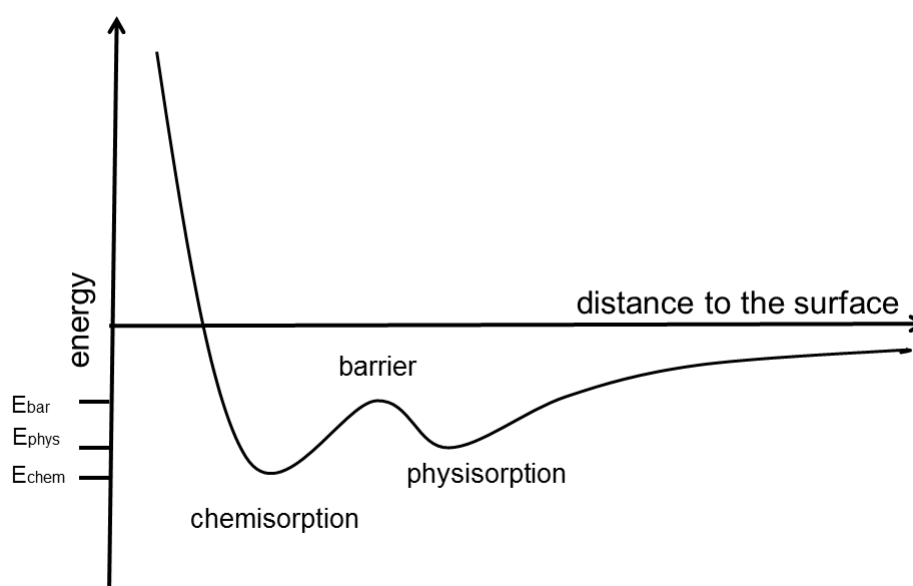


Figure 10: Energetic potential of the process of the SAM formation on the surface.

The second, slower step is the self-assembly of the molecules to each other. The molecules will arrange themselves in a standing-up phase because of the intermolecular interactions like *van-der Waals*, π - π or hydrogen bondings. (Fig. 11 (4)) The arrangement will minimize the free energy of the layer and ends in a potential minimum.^[65-70]

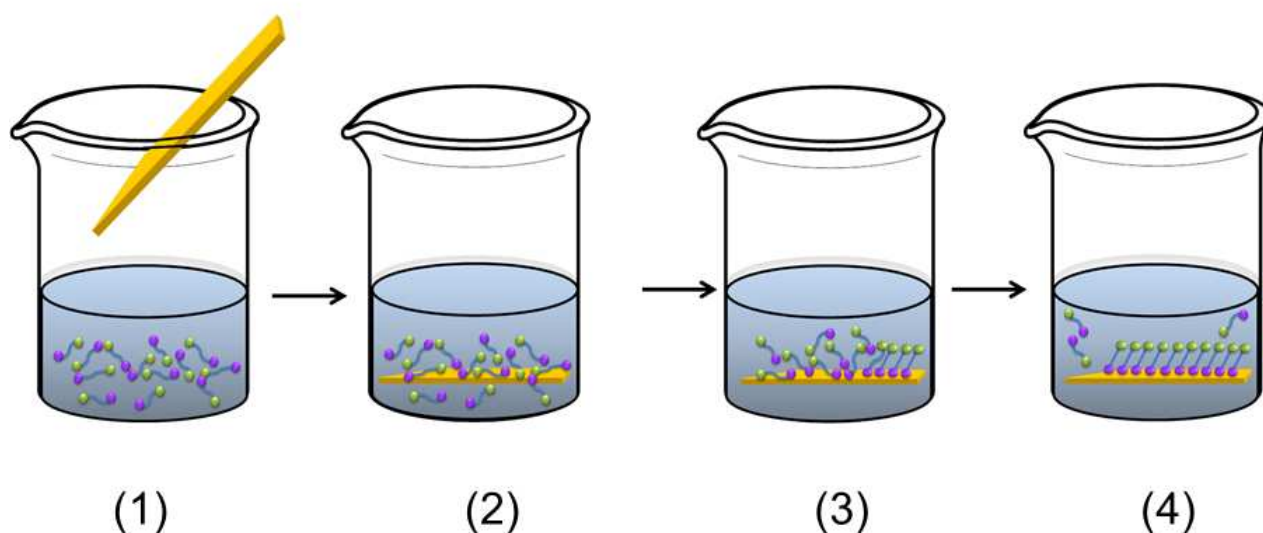


Figure 11: Kinetic process in different steps of the self-assembly of molecules in solution to a substrate.

The kinetics also depends on several factors like temperature, preparation conditions, immersion time, solvent, the molecules used as well as the substrate. Preparation at room temperature and using low concentrations reduce defects and highly ordered films can be obtained. Normally, the preparation ends with a rinsing process of the substrate, using the same clean solvent to remove bi- and multilayers on the SAM.

2. Physisorption

In this process molecules do not form covalent bonds with the substrate but rather adsorb by physical forces like *van-der Waals* forces. In general, these forces are weaker than chemical bonds and have binding energies of around 4 to 40 kJ/mol.^[71]

The organization of monomolecular assemblies at solid interfaces provides a rational approach for fabricating films with a well-defined composition, structure and thickness.

1.4 Surface analytical techniques - Overview

Surface sensitive analytical techniques are essential to characterize surfaces and adsorbed molecules. Plenty of analytical techniques are known and several Nobel prizes regarding these have been awarded in the last decades.^[72]

The characterization of surfaces and their properties is anything but trivial. Every special method divulges different information, but not every surface method delivers all required information. Established surface sensitive techniques and the obtainable analytical information are summarized below:

Scanning tunneling microscopy (STM) gives information about the electronic density of electrons on the surface.

Atomic force microscopy (AFM) can give information about the topography of the investigated surface.

Transmission electron microscopy (TEM) gives information about surface structures.

X-ray absorption spectroscopy (XPS) gives quantitative and qualitative information about elemental composition, oxidation states and chemical environment.

Auger electron spectroscopy (AES) gives quantitative and qualitative information about elemental composition, oxidation states and chemical environments.

Ultraviolet photoelectron spectroscopy (UPS) gives information about electronic structure.

Near edge X-ray absorption fine structure (NEXAFS) gives information about electronic structure, geometrics and angles of the adsorbed molecules.

Surface extended X-ray absorption fine structure (SEXAFS) gives information about coordination numbers and bond lengths.

Low energy electron diffraction (LEED) gives information about surface structures.

Thermal desorption spectroscopy (TDS) gives information about binding energies of the molecules on the surface and the number of molecules on the surface.

Surface enhanced Raman spectroscopy (SERS) gives vibrational information of the adsorbed molecules.

Sum frequency generation (SFG) gives vibrational information of the adsorbed molecules.

A more special and less common technique is **infrared reflection absorption spectroscopy** (IRRAS). This technique has become more and more popular for surface chemistry in recent years.^[73-78]

In the publications presented in this dissertation, IRRAS was used to characterize the surface adsorbed molecules in detail, in comparison with the help of other surface sensitive methods like XPS, SERS, NEXAFS and STM. In the next chapter, IRRAS will be explained in more detail.

1.4.1 Infrared spectroscopy

Infrared spectroscopy determines the selective absorption of infrared light (IR) from chemical compounds. This type of spectroscopy is based on the excitation of vibrations of molecules and molecular functional groups. Different functional groups absorb the IR light with specific energies and allow their assignments from the resulting spectra. The plot of the absorbed intensity over the energy of radiation in frequency units leads to the obtained spectrum. IR spectroscopy refers to the spectral range from 10 cm^{-1} to 14000 cm^{-1} . The most interesting and utilized region is the middle IR (MIR region) of 400 cm^{-1} to 4000 cm^{-1} .

Molecules are not rigid; on the contrary they also vibrate in the ground state.^[79-84] A molecule with N atoms has $3N$ degrees of freedom. For linear molecules $3N-5$ modes and for non-linear molecules $3N-6$ modes of vibrations can be found. The vibrations of a diatomic molecule can be explained by the harmonic oscillator model with Hooke's law:

$$\nu = \frac{1}{2\pi} \cdot \sqrt{\frac{k}{\mu}} \quad (5)$$

where ν is the vibration frequency, k the force constant and μ the reduced mass defined as $\mu = \frac{m_1 \cdot m_2}{m_1 + m_2}$. Through absorption of IR light, these vibrations can be excited to discrete higher energetic vibrational levels. From quantum chemical considerations, these energy levels are given by $E_\nu = (\nu + \frac{1}{2})h\nu$ with $\nu=0, 1, 2, 3\dots$ with ν as quantum vibration number. For the harmonic oscillator, the selection rule of a vibrational transition is given by $\nu=\pm 1$. The approximation of the harmonic oscillator only acts as a model.

In reality, under consideration of anharmonicity, the Morse potential describes a better model. Here, transitions of $\Delta\nu=\pm 2, \pm 3, \pm 4\dots$ are also permitted and can be observed in the IR spectra. These transitions are called 'overtones'. This intensity of these vibrations is reduced in comparison to the first transition. The Morse potential contains correction

terms^{[83][85]} and is expressed by the following equation:

$$V(R) = D_e \cdot (1 - e^{-a(r-r_e)})^2 \quad (6)$$

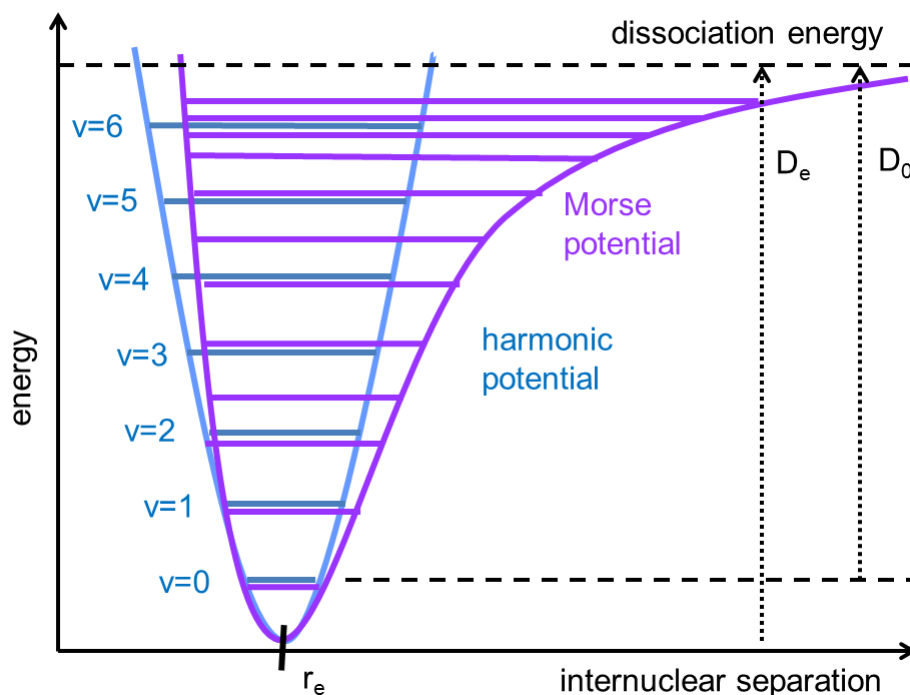


Figure 12: The harmonic (blue) and Morse potential (violet) are shown .

where D_e is the dissociation energy, r the distance between the atoms, r_e the equilibrium bond distance and a is a constant, that controls the 'width' of the potential.

The most important requirement of the IR-spectroscopy is the interaction between the electromagnetic radiation of the light with the electrons of the molecule. This is only the case, when the dynamic dipole moment of the excited vibration transition changes during the vibration. Vibrations in which the transition dipole moment does not change are IR inactive and can not be observed in the spectrum. For example, homonuclear molecules can not be excited by absorption of IR radiation.

1.4.2 Infrared reflection absorption spectroscopy

IR spectroscopy on surfaces was discovered by G. Greenler in 1966.^[86] Different names for this technique, like reflection absorption infrared spectroscopy (RAIRS) or grazing-angle infrared spectroscopy (GAIRS), are used. The most common name is infrared reflection-absorption spectroscopy (IRRAS) as suggested by the International Union of Pure and Applied Chemistry (IUPAC).

This surface sensitive technique provides vibrational information as well as information about the orientation of absorbed molecules on metal reflecting surfaces. This technique is predestined for the investigation of self assembled monolayers on surfaces and enables to get a full vibrational analysis of very thin films with a thickness of several Ångström, is non-destructive and does not require UHV techniques. For the investigation of adsorbed molecules on surfaces by IRRAS some requirements have to be fulfilled:

This technique requires a clean substrate, often a metallic surface, where the infrared beam can be reflected. The adsorbed molecules on the surface will be passed two times by the IR radiation, which leads to an increasing intensity. In general IRRAS intensities are very weak and in the range between 10^{-3} to 10^{-4} absorbance units.^[73-78] Due to the relatively thin film, very sensitive semiconducting detectors are required. The most commonly used detectors are MCT (mercury cadmium telluride). A p-polarized radiation of the incident light is needed and grazing angle of incidence is used. Theoretical considerations show that the electromagnetic radiation reaches a maximum at 82° , because at this angle the largest percentage of the p-polarized E-field are perpendicular to the surface. This angle is also called grazing angle or magic angle.

The sensitivity of IRRAS is a strong function of the angle of incidence (the angle between the surface plane and the incoming beam). Small errors in sample flatness yield in large errors in pseudo-absorbance values. IRRAS measurements need a reference measurement

as background. Due to the extremely weak signals in IRRAS and in order to minimize the disturbance from the atmosphere, an absolutely clean reference sample is necessary.

Surface selection rule: Due to the special surface selection rule, only vibrations with a transition dipole moment or a component of the transition dipole moment perpendicular to the surface can be observed in the IRRA spectrum.

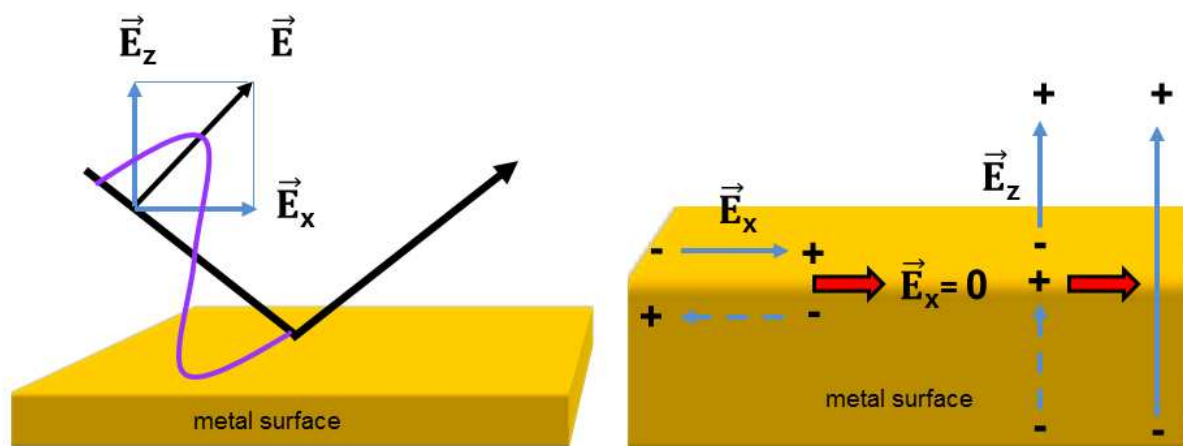


Figure 13: The image charge effect on the surface.

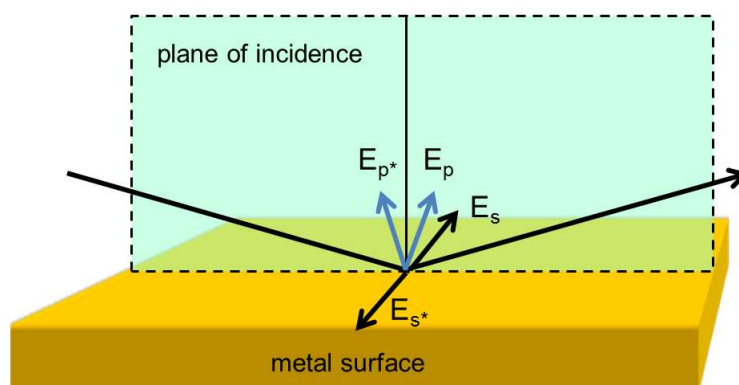


Figure 14: Electric vectors of the s- and p- component of the incident light.

The electric fraction (E-field) of the used IR-light, considered as electromagnetic wave, can interact with the containing charge of the surface. These are electrons and positive charges of the atomic cores. The oscillating electric field vector of the s-polarized radiation is per-

pendicular to the plane of incidence and parallel to the surface normal. The interaction of the light with the containing electrons leads to a displacement through the electric force of the E-field and a polarization of the surface results. This polarization is opposing to the cause. The electric field parallel to the surface results in 0. The oscillating electric field vector of the p-polarized radiation is parallel to the plane of incidence and perpendicular to the surface normal. This fraction of light generates a polarization field which is aligned to the surface and will be summed up. The normal component of the incident field increases. Only vibrations of a molecule with a transition dipole moment or a component of the transition dipole moment, which are oriented perpendicular to the surface, can interact with the p-polarized light and contribute to the spectrum.

The sensitivity of IRRAS can be increased by the polarization modulation technique, which is named as polarization-modulation infrared reflection absorption spectroscopy (PM-IRRAS).^[87-90] This extended technique is able to eliminate atmospheric disturbances like CO₂ and H₂O. PM-IRRAS utilizes a high frequency modulation between s- and p-polarized light whereby two simultaneous measurements of these two signals are possible; the spectrum without adsorbat as a reference spectrum (s-polarized) and the spectrum with adsorbat (p-polarized). Due to the simultaneous measurement, CO₂ and H₂O can be avoided and the necessity of a reference background sample like in IRRAS is not required in PM-IRRAS. Shorter scan times in PM-IRRAS help to avoid experimental drifts and instabilities.

Spectrometer

During this thesis a Bruker Vertex 70 FT-IR spectrometer was used for conventional IR-RAS measurements. This spectrometer is equipped with a liquid nitrogen cooled MCT semiconductor detector to gain adequate sensitivity.

For the duration of the measurement and one hour before, the sample chamber was purged



Figure 15: The used Bruker Vertex 70 and PMA-50 unit are shown.

with dry nitrogen to reduce atmospheric disturbances in the chamber. For all shown spectra in this thesis, the resolution was set at 4 cm^{-1} . For conventional IRRAS measurements a deuterated hexadecylthiol SAM on Au(111) was used as the reference background.

A p-polarized infrared beam is focused through an IR-transparent window onto the sample surface at grazing incidence. The sample, acting as a mirror, reflects the beam out of a second vacuum-sealed window, where it is focussed on the photoconductive semiconductor MCT detector. The spectrometer comprises a detection range from 5000 to 800 cm^{-1} . As sample holder, a horizontal reflection unit for grazing incidence (Bruker A518) at an angle of 82° was used.

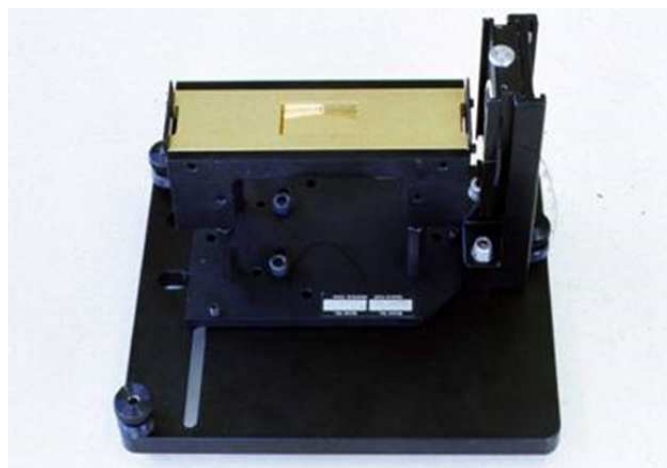


Figure 16: Bruker A518 sample holder with a grazing incidence of 82° .

For IRRAS measurements Au(111) samples of 2 cm x 3 cm dimension were used. This size of sample is necessary due to the cross section of the beam.

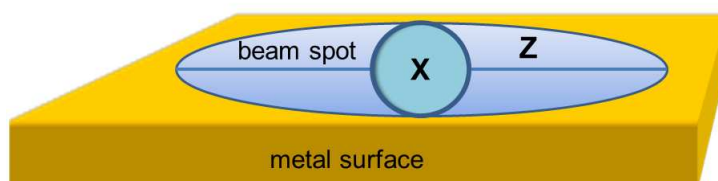


Figure 17: Ellipsoidal beam spot on the sample.

As aperture setting 1.5 mm was used, resulting in a circular spot on the surface (X in Fig. 17). By multiplying the aperture setting with the so called Bruker factor of 1.8 mm and the factor A of $1/\cos(\alpha) = 1 / \cos(82^\circ)$, an ellipsoidal spot of around 2.7 mm x 19.4 mm results on the surface sample (Z in Fig. 17). Therefore, large samples with dimensions of 20 mm x 30 mm are suitable for IRRAS measurements. The obtained IRRAS data were processed using an OPUS 6.0 program from Bruker, Germany.

For PM-IRRAS measurements a Bruker Vertex 70 FT-IR spectrometer with a polarization modulation accessory Bruker PMA 50 was used. The photoelastic modulator (PEM) modulates the infrared beam by rotating the polarization of the light sinusoidally at the frequency of the birefringence modulation, introduced mechanically to the ZnSe crystal.

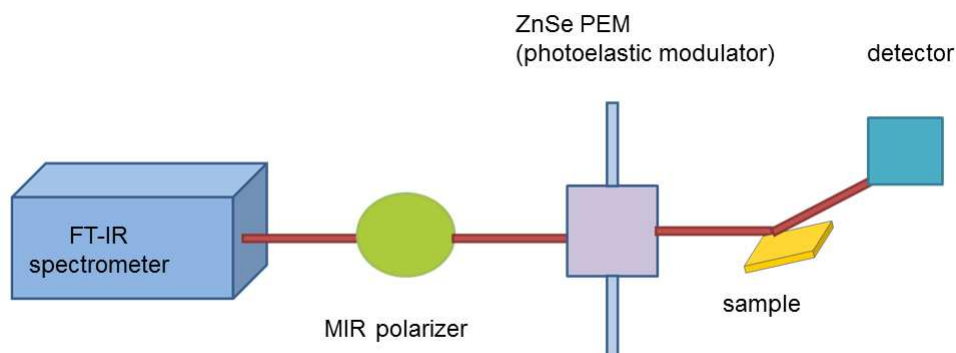


Figure 18: Schematic optical setup for PM-IRRAS.

The resolution for PM-IRRA spectra was set as 4 cm^{-1} at an angle of incidence of 82° . The PEM maximum efficiency was set for the half-wave retardation at 1800 cm^{-1} to analyze the C-O stretching region, at 2900 cm^{-1} to analyze of the C-H stretching vibration bands and at 1500 cm^{-1} to analyze of the finger print region. The instrumental and optical setup of the spectrometer are shown in Figure 19.



Figure 19: PM-IRRAS instrumental setup. On the left hand side the spectrometer, in the middle the sample holder and on the right hand side the look-in amplifier and PEM.

The low frequency signal is the average interferogram $I_A = \frac{(I_p + I_s)}{2}$, the high frequency signal is the differential interferogram $I_D = \frac{(I_p - I_s)}{2}$ and the differential reflectance spectrum is defined as $\frac{\Delta R}{R} = \frac{I_D}{I_A}$.

Due to the different reflectivity of s- and p-polarized infrared radiation at a metal surface,

the differential spectrum is multiplied by the Bessel function, i.e. a background is obtained: $\frac{\Delta R}{R} = J_2(\phi_0) \cdot \frac{I_D}{I_A}$ where $J_2(\phi_0)$ is the second-order Bessel function. The electronic block diagram of the used PMA 50 accessory is shown in Figure 20.

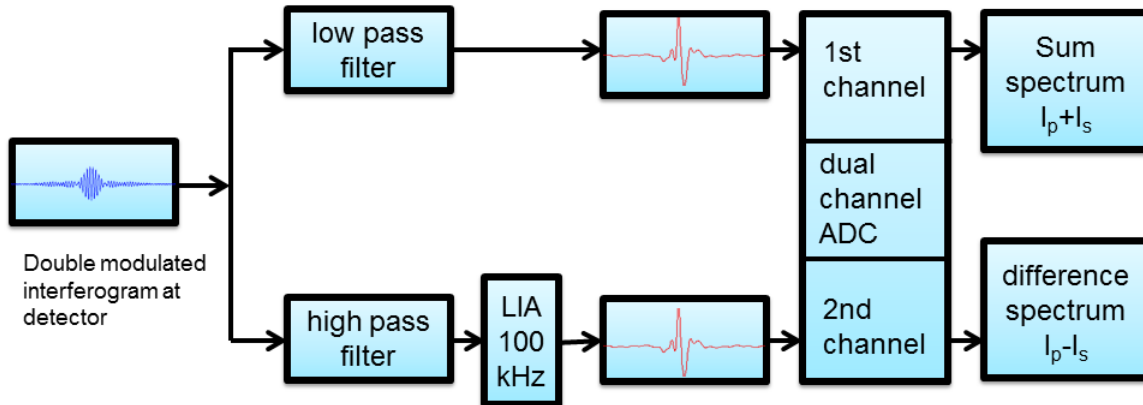


Figure 20: Block diagram of the PMA 50 setup.

2 Functionalization of Au(111) surfaces with spin crossover complexes

2.1 Spin Crossover Phenomenon

In 1931, Cambi *et al.* reported the "Spin crossover" phenomenon for the first time. An iron(III)-thiocarbamate complex shows an interesting property: by changing the temperature, the spin state changed to another spin state.^[91,92] Spin crossover can occur in transition metal compounds with electron configurations of d^4 to d^7 . The most known examples in literature are iron(II)/iron(III), cobalt(II)/cobalt(III), chromium(III) and manganese(II)/manganese(III) compounds. This effect can be observed in liquid phase as well as in solid state compounds. Spin crossover in general describes the phenomenon that a compound can exist in two different spin states: a high spin state (with the maximal number of unpaired electrons) and a low spin state (with the maximal number of paired electrons). In the case of iron(III) the spin multiplicity is $S=5/2$ in high spin state and $S=1/2$ in low spin state. As considered in an octahedral coordination sphere, the present five d-orbitals split into two sets of orbitals with different energy: the three t_{2g} (d_{xy} , d_{yz} and d_{xz}) orbitals with bonding nature with lower energy and the two e_g orbitals (d_{z^2} and $d_{x^2-y^2}$) with anti-bonding nature of higher energy. The thermodynamical stable spin state depends on the size of the ligand field splitting Δ ($10Dq$) between t_{2g} and e_g and the spin-pairing energy P :

- if Δ is bigger than P , the compound has a low spin state. The degenerated orbitals with same energy will be filled up by double before orbitals with higher energy will be filled up.
- If Δ is smaller than P , orbitals will be filled up as stated in Hund's rule. All d-orbitals will be populated and will result in a high spin state.
- If Δ is in the range of P , a transition from one state to another can occur. For spin crossover components, Δ and P are in the same range of thermal energy ($k_b \cdot T$).

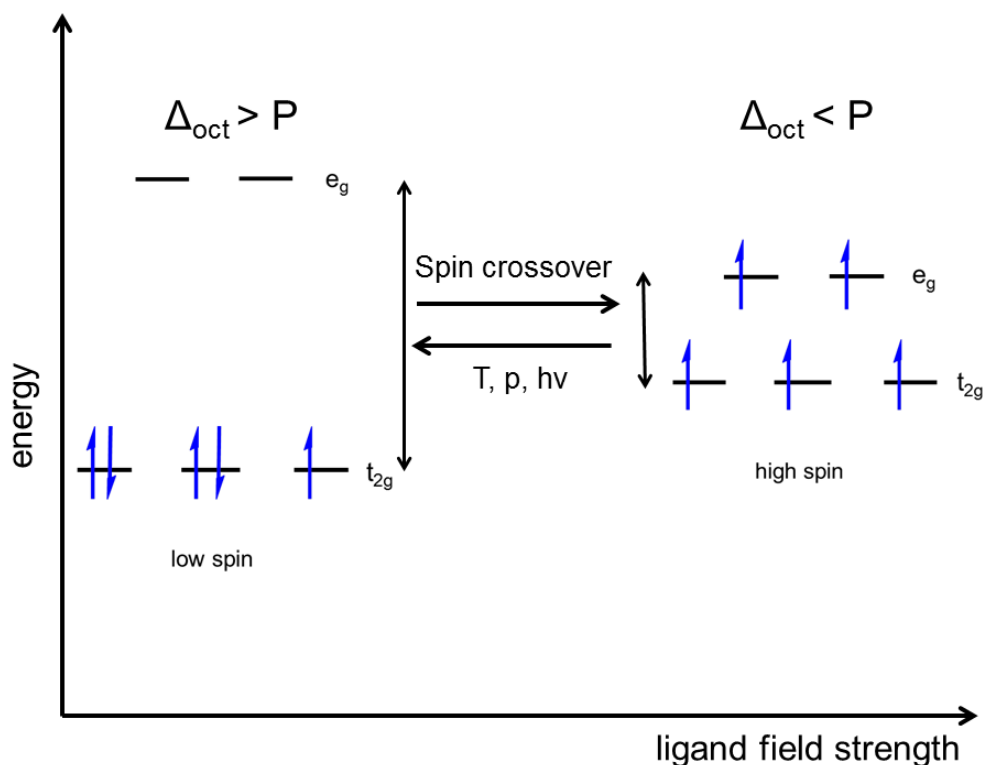


Figure 21: High spin state and low spin state for a d^5 system, for example iron(III).

This requirement is fulfilled in most cases in the presence of nitrogen-donating ligand systems.^[93] A reversible spin transition between these two states can be induced by different external stimuli like pressure, electrochemical stimuli, light and changing the temperature.^[94-108] In most examples discussed in literature, this bistability is given at low temperatures (below 100 K). Only several examples show this desired bistability at or around room temperature.^[109] For data storage materials, a spin transition temperature of 300 K and a broad hysteresis are preferred.^[110]

A prominent example for the spin crossover phenomenon can be found in our human body and vertebrates. Haemoglobin which is contained in our red corpuscles, is an iron-containing protein-complex and provides the red colour to our blood. The central atom of the haemoglobin is a Fe^{2+} (deoxy-haemoglobin) in a high spin state that changes to a Fe^{3+} by binding molecular oxygen (oxy-haemoglobin) in a low spin state. EPR studies prove this fact.^[111]

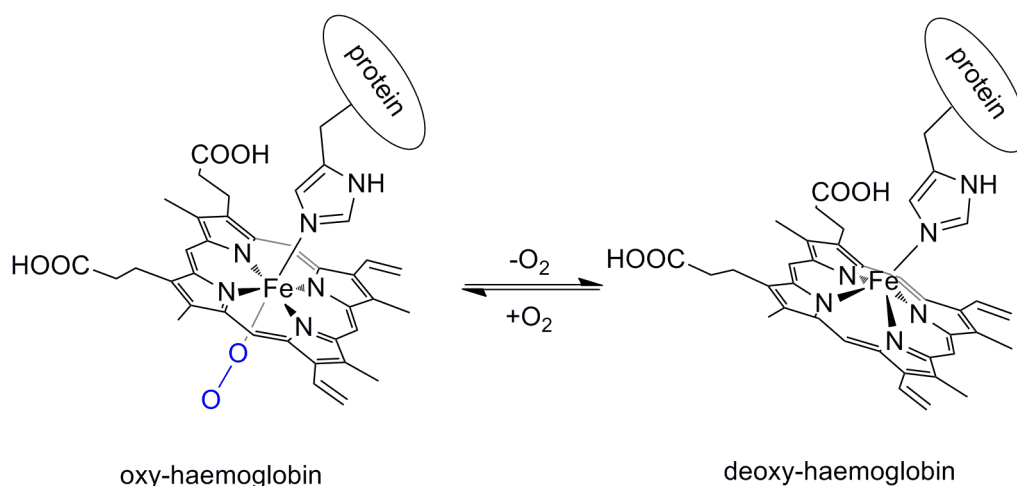


Figure 22: Oxy-haemoglobin and deoxy-haemoglobin.

In 1985, the so called "Light-induced-excited spin state trapping" effect was discovered. Using green light of the visible spectrum, a transition from 1A_1 state to 1T_1 or 1A_2 , is followed by an intersystem crossing into the respective triplet and a further intersystem crossing to the long-lived quintet 5T_2 state.^[112,113] The relaxation back in the ground state is both spin and parity forbidden and tunnels non-adiabatic through the potential barrier. The 'reverse-LIESST' effect is termed for the excitation of the 5T_2 state with red light whereby the 1A_1 state repopulates.^[112]

Another possible way to realize a light induced spin transition, published by Boillot and Roux, is to shift the excitation energy from the metal center to the coordinated ligands. Photoisomerizable ligands like styrylpyridines were coordinated to an iron centre. The isomerization of these ligands leads to a change in the geometry and is followed by a change of the ligand field strength and ligand field splitting.^[114-116] Several systems in literature are known which undergo LD-LISC effect at room temperature.^{[115][117]} Applications of the LIESST and LD-LISC effect in optical storage and devices are possible.

Spin crossover can be observed by Mößbauer spectroscopy, optical spectroscopy, magnetic susceptibility, X-ray-absorption spectroscopy methods and vibrational spectroscopy as well

as by crystal structure analysis.

The spin crossover phenomenon occurs widely for iron(III) complexes and several of the complexes which exhibit this behavior contain a salen ligand system.^[118,119]

2.2 Motivation

Spin crossover complexes are potential systems for data storage materials, catalysis, chemical modified electrodes and sensors.^{[110][120,121]} Spin crossover materials on surfaces have gained a wide interest in the field of science and industry.^[122] Fixing these complexes to metal surfaces or to adsorb these molecules on surfaces can be very interesting in the application for memory devices, storage materials and sensors. The fixation of transition metal complexes to surfaces can be reached by three different techniques which is schematically shown in Figure 23.

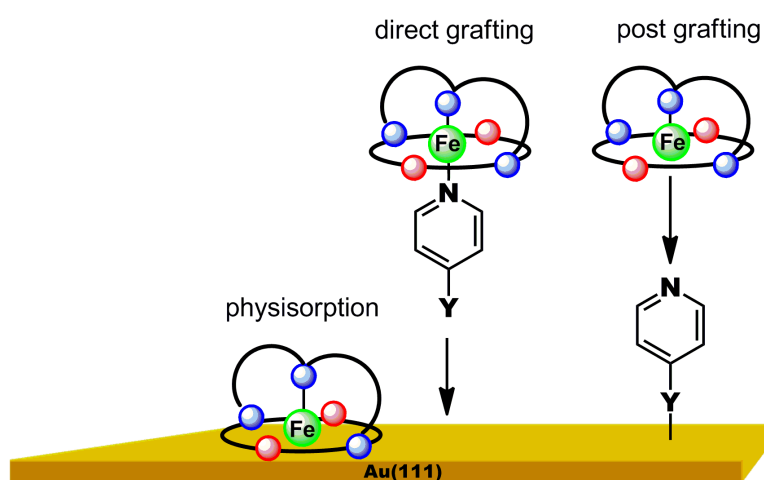


Figure 23: Different methods to bring transition metal complexes to a surface.

The first technique is the direct deposition of a metal complex either by chemical vapor deposition or by physisorption from solution. Therefore, some conditions have to be fulfilled. It is important that the complex can evaporate from the bulk material or can be deposited from the solution without destroying the structure. For surface preparation, these molecules need a high quality of cleanness. By evaporating a substance, very clean functionalized surfaces can be obtained. Deposition from the solution mostly results in lower quality films. Here the conditions of preparation are very important. High quality solvents, clean glassware and clean substances are required.

The second method to get metal functionalized surfaces is the direct grafting method. Here a functionalized metal complex with an anchor group for the surface fixation is needed. This

method is more demanding. In this case, the metal complex has to be built up from the ligand system. A surface affine anchor group like a sulfur containing group is required. The functionalization of a metal complex with a thiol containing group will lead to different problems during the synthesis. In the case of iron as central metal ion, a thiol containing group will directly coordinate to the iron center and can also build up coordination polymers. Thiols are very affine to different metals as we know from the high affinity to gold, where the result is a very strong covalent bond.^[57] This covalent bond of around 180 kJ/mol will lead to a stability of the metal containing complexes on surface in the case when the ligand system and oxidation state is also stable.

The utilization of sulfur protecting groups can avoid the problems of building coordination polymers and direct coordination of the sulfur to the metal center. Different sulfur protecting groups are known in literature. A very elegant way to protect the sulfur group is the oxidation from a thiol to a disulfide group. The thiol group protected as disulfide becomes to a relative stable disulfide and can also be used for the grafting of metal complexes. If the disulfide ligand contains another functional group like a nitrile or pyridine, this group can be coordinated to the metal center of a complex.

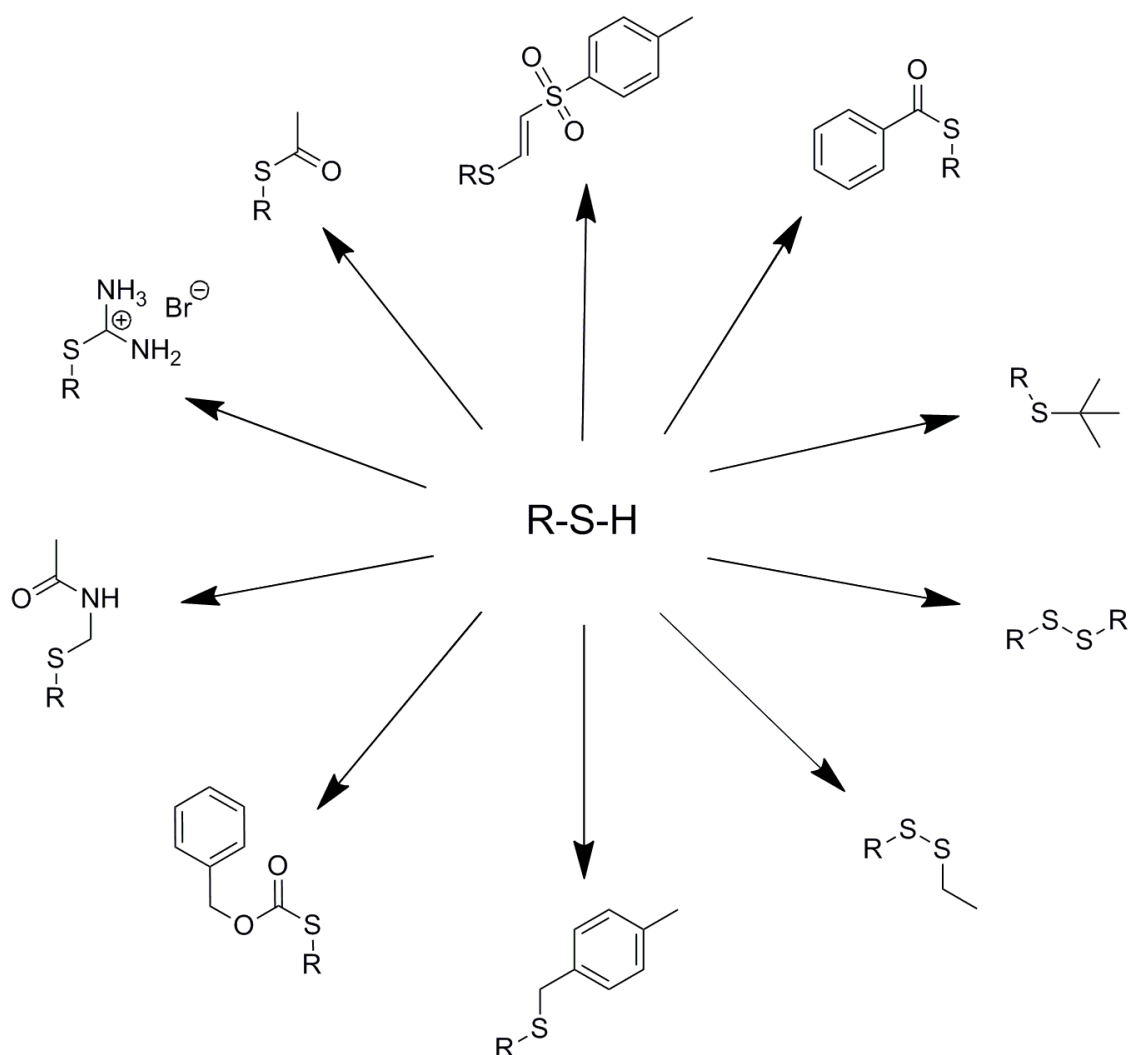


Figure 24: Possible protecting groups for thiol containing derivatives.

The third method to fix metal complexes to surfaces is the post-grafting of metal containing systems to a prefunctionalized surface or to click metal containing ligands *via* click reactions, for example, a Huisgen click reaction to self assembled monolayers.^[123,124]

Gopakumar *et al.* published in 2012 in *Angewandte Chemie* the vacuum deposited $[\text{Fe}(\text{II})(\text{bpz})_2(\text{phen})]$ complex.^[125,126] Previous work of Naggert *et al.* showed the preservation of the LIESST effect of these molecules after vacuum deposition on a surface.^[127] This complex can be switched in the second layer of molecules on a surface at 5 K between two different electronic states, a high spin to a low spin state.

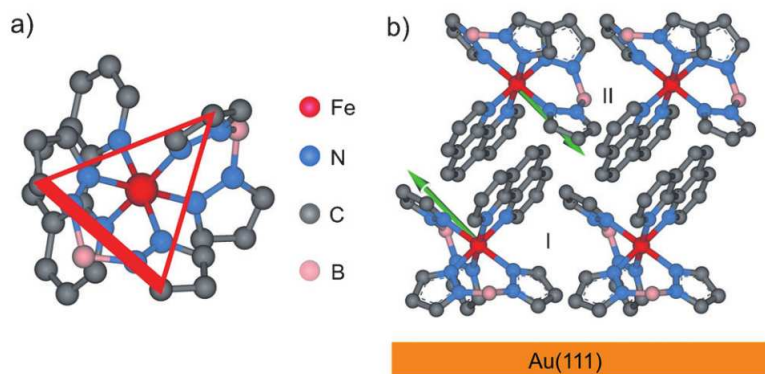


Figure 25: The picture on the left hand side shows the structure of $[\text{Fe}(\text{bpz})_2(\text{phen})]$ and the picture on the right hand side shows a model of these molecules on a surface.^[125]

Switching behavior of these molecules in the first layer was not observed. The switching process in the second layer is, however, selective and reversible by inducing electrons to the molecules on the surface. This process was named as ELIESST (Electron Induced Excited Spin State Trapping) and can be compared to previous work of Meded *et al.*^[128]

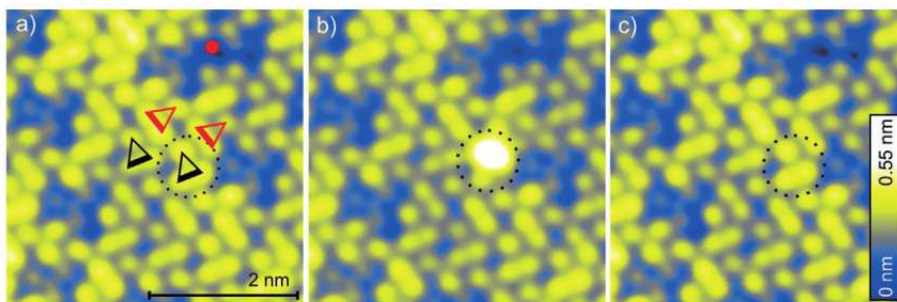


Figure 26: STM pictures of $[\text{Fe}(\text{bpz})_2(\text{phen})]$ on Au(111) surface.^[125]

Further work from Ludwig *et al.* on $[\text{Fe}(\text{II})(\text{bpz})_2(\text{phen})]$ complexes showed that the electronic structure of this molecule in the two different spin-states can also be detected via UPS (UV-photoelectron-spectroscopy).^[129]

In the following publication, two Fe(III) complexes supported by the pentadentate ligand salten (bis(3-salicylidene-aminopropyl)amine), were synthesized and functionalized with a disulfide linker for surface fixation (Fig. 27). The two different ligand systems were analyzed in bulk with elemental analysis, NMR, Raman and IR spectroscopy. Furthermore, the Fe(III)

complexes of these two different ligand systems were synthesized and also analyzed in bulk with elemental analysis, Raman and IR spectroscopy. DFT calculations were carried out to obtain the complete vibrational information of these molecules and to understand these systems in detail. Furthermore, the dinuclear complexes were grafted to Au(111) surfaces from an ethanolic solution, and monomer adsorbed molecules were obtained after disulfide bridge cleavage. Thiolate fixed monomers and still disulfide bridged dimers were detected and were analyzed in detail using XPS, NEXAFS and IRRAS. The expected intact geometry of the complex was only found for one of the complexes. The [Fe(III)salten(pyS)] complex showed an interesting anomaly after grafting to a surface. This complex changed the geometry of the ligand system on surface.

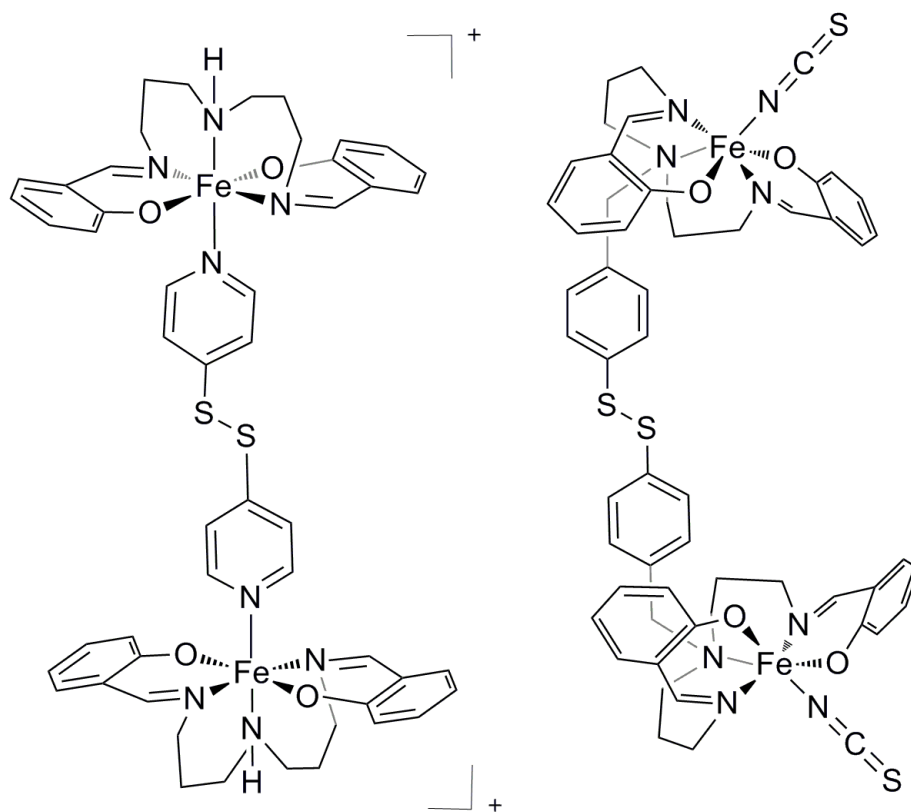


Figure 27: Structure of the two different investigated dinuclear complexes. On the left hand side $[\text{Fe}(\text{III})\text{salten}(\text{pyS})]_2(\text{BPh}_4)_2$ and on the right hand side $[\text{Fe}(\text{III})\text{thiotolylsalten}(\text{NCS})]$.

Publication in

Langmuir

2.3 Grafting of Functionalized [Fe(III)(salten)] Complexes to Au(111) Surfaces via Thiolate Groups: Surface Spectroscopic Characterization and Comparison of Different Linker Designs

H. Jacob, K. Kathirvel, F. Petersen, T. Strunskus, A. Bannwarth, S. Meyer, F. Tucek

Langmuir **2013**, 29(27), 8534-8543.

DOI: 10.1021/la400663y.

Grafting of Functionalized [Fe(III)(salten)] Complexes to Au(111) Surfaces via Thiolate Groups: Surface Spectroscopic Characterization and Comparison of Different Linker Designs

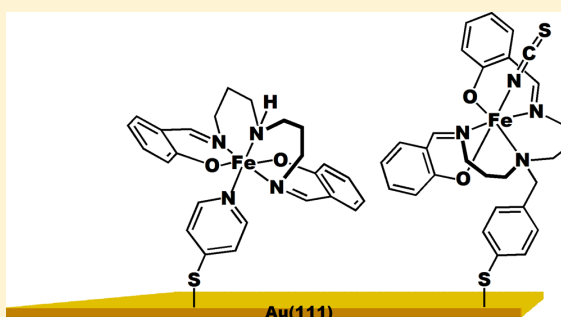
Hanne Jacob,[†] Ketheeswari Kathirvel,[†] Finn Petersen,[†] Thomas Strunskus,[‡] Alexander Bannwarth,[†] Sven Meyer,[†] and Felix Tuczek^{*,†}

[†]Institut für Anorganische Chemie, Christian-Albrechts-Universität Kiel, Max-Eyth-Straße 2, 24118 Kiel, Germany

[‡]Technische Fakultät, Christian-Albrechts-Universität Kiel, Kaiserstraße 2, 24143 Kiel, Germany

Supporting Information

ABSTRACT: Functionalization of surfaces with spin cross-over complexes is an intensively studied topic. Starting from dinuclear iron(III)-salten complexes $[\text{Fe}(\text{salten})(\text{pyS})]_2(\text{BPh}_4)_2$ and $[\text{Fe}(\text{thiotolylsalten})(\text{NCS})]_2$ with disulfide-containing bridging ligands, corresponding mononuclear complexes $[\text{Fe}(\text{salten})(\text{pyS})]^+$ and $[\text{Fe}(\text{thiotolylsalten})(\text{NCS})]$ are covalently attached to Au(111) surfaces (pySH, pyridinethiol; salten, bis(3-salicylidene-aminopropyl)amine). The adsorbed monolayers are investigated by infrared reflection absorption spectroscopy (IRRAS) in combination with X-ray photoelectron spectroscopy (XPS) and near-edge X-ray absorption fine structure (NEXAFS). Comparison of the surface vibrational spectra with bulk data allows us to draw conclusions with respect to the geometry of the adsorbed complexes. An anomaly is observed in the spectra of the surface-adsorbed monolayer of $[\text{Fe}(\text{salten})(\text{pyS})]^+$, which suggests that the salten ligand is partially decoordinates from the Fe(III) center and one of its phenolate arms binds to the Au(111) surface. For complex $[\text{Fe}(\text{thiotolylsalten})(\text{NCS})]$ that is bound to the Au(111) surface via a thiolate-functionalized salten ligand, this anomaly is not observed, which indicates that the coordination sphere of the complex in the bulk is retained on the surface. The implications of these results with respect to the preparation of surface-adsorbed monolayers of functional transition-metal complexes are discussed.



INTRODUCTION

Surfaces functionalized with transition-metal complexes have broad applications in catalysis, as sensors, and as chemically modified electrodes. Moreover, by the attachment of functional metal complexes, surfaces with novel physicochemical (e.g., spin-switchable) properties can be obtained.¹ One class of compounds that can successfully be employed for such applications is transition-metal salen complexes (salen = N,N' -ethylenebis(salicylimine)). These complexes have been fixed to surfaces by physisorption, either from the gas phase or from homogeneous solution, or by chemical grafting methods.² Of particular interest are recent experiments on the deposition of Co(III) and Mn(III) salen complexes on prefunctionalized (i.e., alkanethiol-coated) surfaces by Laskin et al.³ These systems have attracted significant attention in research areas ranging from catalysis to single-molecule magnets.^{4–6}

Because of their planar geometry exhibiting two unoccupied sites in positions that are trans to each other, transition-metal salen complexes can in principle serve as platforms for the coordination of other molecules, binding with one side to the surface and with the other side to an external ligand.⁷ However, if deposited directly onto Au(111) surfaces (Figure 1a), planar

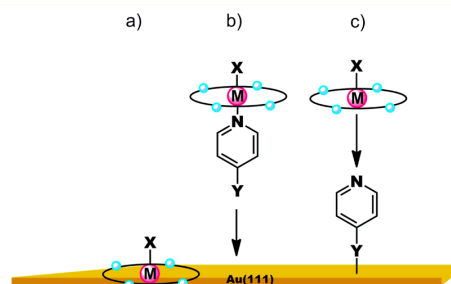


Figure 1. Different deposition methods of transition-metal salen complexes on surfaces: (a) physisorption (direct deposition) of a complex, (b) direct grafting, and (c) postgrafting.

metal complexes often lose their capacity to coordinate additional molecules axially.^{8,9} These complexes thus may be attached to the surface by bifunctional linkers that have one

Received: February 21, 2013

Revised: June 4, 2013

Published: June 10, 2013

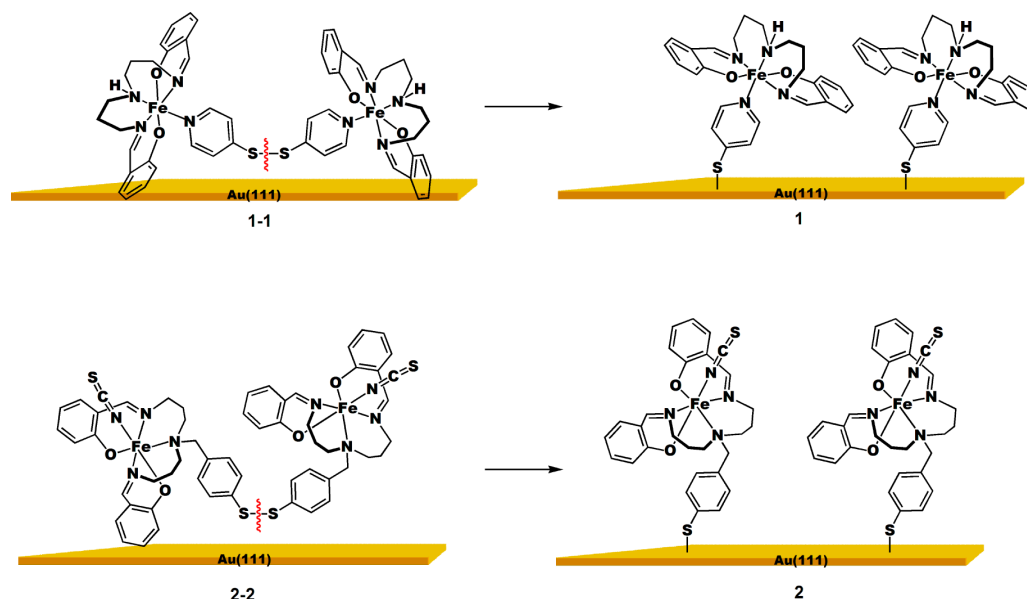


Figure 2. Two investigated precursors, $[\text{Fe}(\text{salten})(\text{pyS})_2](\text{BPh}_4)_2$ (1-1) and $[\text{Fe}(\text{thiotolyl-salten})(\text{NCS})_2]_2$ (2-2), and the covalent attachment of corresponding monomeric complexes **1** and **2**, respectively, via thiolate groups generated by S–S cleavage of the disulfide groups on Au(111).

function (e.g., a thiol) binding to the surface and another (e.g., nitrile or *N*-heterocycle) function coordinating to the complex (Figure 1b,c).¹⁰ In this approach, the metal complex can be bound along with the linker to the surface, which might be termed direct grafting (Figure 1b), or the metal center can be coordinated to a surface that has been prefunctionalized with the linker molecule (*vide supra*), which might be termed post-grafting (Figure 1c).^{11,12}

Applying the latter approach, Poppenberg et al. have coordinated Pd(II) ions and terphenyl ligands to a pyridyl-terminated SAM and demonstrated a reaction on top of a prefunctionalized surface by using XPS for characterization.¹³ Complementary information to XPS can be obtained from NEXAFS. By a comparison of mono- and multilayer spectra, these techniques in particular allow us to determine whether the surface-adsorbed complexes are chemically intact.

Another powerful tool for obtaining information on monolayers adsorbed to metal surfaces is infrared reflection absorption spectroscopy (IRRAS). A characteristic feature of this method is the surface selection rule that states that only the vibrations with a component of the transition dipole moment perpendicular to the surface plane can interact with the incident light and contribute to the infrared spectrum.^{14–18} In this way, IRRAS also provides information on the orientation and geometry of surface-adsorbed molecules, which has been used for the characterization of purely organic SAMs as well as for assemblies of transition-metal complexes linked to monolayers of organic molecules.^{19–21}

Herein we employ the mentioned spectroscopic methods to study surface-adsorbed layers of $[\text{Fe}(\text{salten})\text{L}]$ molecules (salten = bis(3-salicylideneaminopropyl)amine). Two methods of covalent attachment are compared: first, complex $[\text{Fe}(\text{salten})(\text{pyS})]^+$ (**1**) is bound to an Au(111) surface by a bifunctional linker, 4-pyridine-thiol, that is generated *in situ* by S–S cleavage of dinuclear complex $[\text{Fe}(\text{salten})(\text{pyS})_2](\text{BPh}_4)_2$ (1-1) bridged by 4,4'-di(thiopyridine) (Figure 2, top). Second, dinuclear

complex $[\text{Fe}(\text{thiotolylsalten})(\text{NCS})_2]$ (2-2) bridged by a 4,4'-di(thiotolyl) unit is investigated, which also binds in monomeric form (i.e., as $[\text{Fe}(\text{thiotolylsalten})(\text{NCS})]$ (**2**)) to a gold surface after S–S cleavage of the linker (Figure 2, bottom). The $[\text{Fe}(\text{thiotolylsalten})(\text{NCS})_2]$ complex has been employed before for Au nanoparticle functionalization.²²

The salten ligand is related to tetradentate ligand salen but in addition contains a central secondary amine function that renders it pentadentate. Salten complexes attached to a surface by a bifunctional linker (such as complex **1**) thus cannot bind external ligands in the fashion depicted in Figure 1. Complex **2**, which is attached to the surface by a thiolate function appended to the salten ligand, does, however, have this capability.

Depending on coligand L that occupies the sixth position, two different coordination geometries exist for pseudo-octahedral $[\text{Fe}(\text{salten})\text{L}]$ complexes. These isomeric forms can be distinguished by the relative disposition of the two phenolate groups (Figure 3): if L is a strong or a bulky ligand (e.g.,

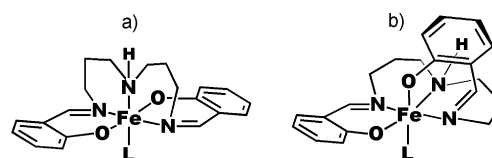


Figure 3. Different geometries of $[\text{Fe}(\text{salten})\text{L}]$: (a) trans geometry and (b) cis geometry.

pyridine), then the trans geometry is formed (Figure 3a).²³ For weaker ligands such as chlorine and thiocyanate, the complexes exhibit cis geometry (Figure 3b).²⁴

In the present study, surface-vibrational spectroscopy (IRRAS) is employed to obtain information on the geometry and orientation of $[\text{Fe}(\text{salten})(\text{pyS})]^+$ (**1**) attached to Au(111) by a pyridine thiol. To determine the coordination geometry of surface-adsorbed **1**, we studied the infrared and Raman spectra of

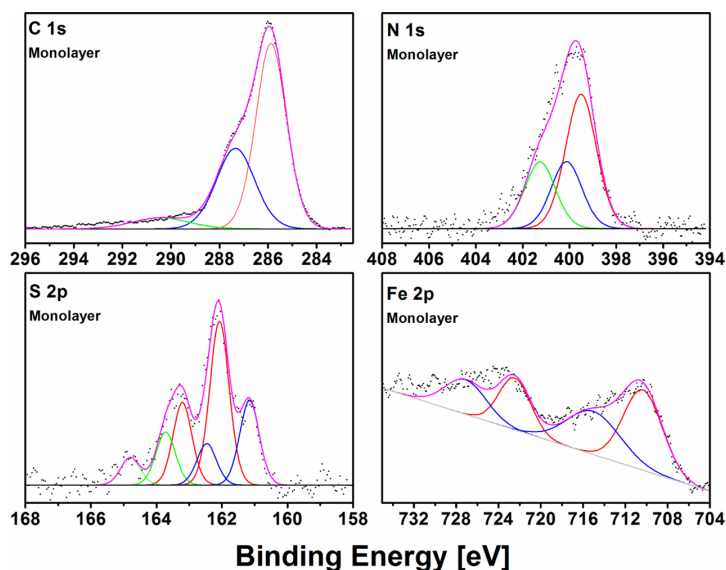


Figure 4. C 1s, N 1s, S 2p, and Fe 2p XP spectra of $[\text{Fe}(\text{salten})(\text{pyS})]^+(1)$ in monolayers.

$[\text{Fe}(\text{salten})(\text{pyS})]_2(\text{BPh}_4)_2$ (1-1) and $[\text{Fe}(\text{salten})(\text{py})](\text{BPh}_4)$ (which have the trans geometry) as well as $[\text{Fe}(\text{salten})\text{Cl}]$ (cis geometry) in the bulk. All vibrational spectra are evaluated with the help of theoretical spectra obtained from DFT calculations. XPS and NEXAFS data of the monolayers of **1** are also compared to those obtained from thick layers of **1-1**.

For comparison, dinuclear complex $[\text{Fe}(\text{thiotolysalten})(\text{NCS})]_2$ (**2-2**) is also investigated in the bulk and in its mononuclear form **2** adsorbed on Au(111), employing the same methods. In this case, precursor **2-2** has cis geometry,²² and it is of interest to determine whether this geometry is retained on the surface (cf. Figure 2, bottom). The implications of the results for the covalent attachment of functional transition-metal complexes to surfaces are discussed.

EXPERIMENTAL SECTION

DFT Calculations. All input geometries were derived from single-crystal structures of appropriate salten-type complexes.^{23,24} Preoptimization was carried out using Avogadro²⁵ program (molecular mechanics with the UFF force field).²⁶ Full geometric optimizations and frequency calculations were carried out using the unrestricted BP86 functional with the TZVP basis set.^{27,28} All operations were performed as implemented in the Gaussian09 software package.²⁹ Calculated IR spectra were exported with Gaussview 5.0.

Vibrational Spectroscopy. Bulk IR spectra were recorded with a Bruker ATR FT-IR spectrometer in the range of 400 to 4000 cm^{-1} with a resolution of 4 cm^{-1} . Raman spectra were measured using an ISF66/FRA106 Fourier transform Raman spectrometer (Bruker AXS GmbH, Germany) with an Nd/YAG laser at a wavelength of $\lambda_{\text{ex}} = 1064$ nm.

IRRAS. IRRAS was performed using a Bruker Vertex 70 FT-IR spectrometer equipped with a liquid-nitrogen-cooled MCT detector and a horizontal reflection unit for grazing incidence (Bruker A518). A p-polarized beam at an incident angle of 80° to the surface normal was used for measurements. The resolution was set to 4 cm^{-1} . The sample chamber was purged with dry nitrogen before and during measurements. A deuterated hexadecane-thiol SAM on Au(111) was used to record the background spectrum. The IRRAS data were processed using the OPUS program (Bruker, Germany).

XPS/NEXAFS. The XPS and NEXAFS data were recorded in electron storage ring BESSY II, Berlin. XP and NEXAFS spectra for C, N, O, B, and S were acquired at the HE-SGM beamline, and the XPS and

NEXAFS data for Fe were acquired at the PM4 beamline with the SurICat endstation. XP high-resolution spectra were recorded in normal emission with a Scienta SES 100 analyzer at a 50 eV pass energy. Carbon 1s spectra were acquired with an excitation energy of 400 eV; nitrogen 1s spectra, with 500 eV; sulfur 2p spectra, with 350 eV; and iron 2p spectra, with 950 eV. XP spectra were fitted with the program CASA-XPS.³⁰ S 2p XP spectra were fitted with two lines of equal width with a fixed splitting of 1.2 eV and a fixed intensity ratio of 1:2 for the doublet.³¹ The Fe 2p spectra were fitted with a fixed split between the 2p_{3/2} and 2p_{1/2} lines and the corresponding satellites of 12 eV, keeping the intensity ratio of 2p_{3/2} to 2p_{1/2} between 2 and 3.^{32,33} NEXAFS spectra were recorded by measurement of the partial electron yield using a self-built channel-plate detector (HE-SGM) or by measurement of the sample current (PM-4).

Gold Substrates. Glass substrates with a 50 Å titanium base layer and a 1000 Å evaporated gold film were purchased from EMF Corporation (Ithaca, NY) for IRRAS measurements. XPS and NEXAFS measurements were made on sputtered Au/Cr/Si wafers (Au 206 nm/Cr 8 nm).

Preparation of Thick Films. Thick films (several nanometers in thickness) of $[\text{Fe}(\text{salten})(\text{pyS})]_2(\text{BPh}_4)_2$ (**1-1**) and $[\text{Fe}(\text{thiotolysalten})(\text{NCS})]_2$ (**2-2**) were prepared by depositing a drop of an ethanolic solution of the respective complex on an Au(111) surface, followed by drying.

Preparation of Monolayers. Monolayers of $[\text{Fe}(\text{salten})(\text{pyS})]^+$ (**1**) and $[\text{Fe}(\text{thiotolysalten})(\text{NCS})]$ (**2**) were prepared by immersing Au(111) substrates in 0.5 mM solutions of the respective dinuclear complexes, $[\text{Fe}(\text{salten})(\text{pyS})]_2(\text{BPh}_4)_2$ (**1-1**) and $[\text{Fe}(\text{thiotolysalten})(\text{NCS})]_2$ (**2-2**) in ethanol p.a. (Carl Roth) at room temperature. After 48 h of immersion, the sample was removed from the solution, thoroughly rinsed with ethanol p.a., and finally dried in a stream of nitrogen gas.

Chemicals. All starting materials were supplied by Sigma–Aldrich or abcr. Solvents were dried and distilled before using. Ethanol p.a. (Carl Roth) was used for all monolayer preparations.

RESULTS AND DISCUSSION

The two iron(III) complexes $[\text{Fe}(\text{salten})(\text{pyS})]^+$ (**1**) and $[\text{Fe}(\text{thiotolysalten})(\text{NCS})]$ (**2**) were adsorbed to Au(111) surfaces by cleavage of the disulfide groups of the dinuclear precursor complexes $[\text{Fe}(\text{salten})(\text{pyS})]_2(\text{BPh}_4)_2$ (**1-1**) and $[\text{Fe}(\text{thiotolysalten})(\text{NCS})]_2$ (**2-2**), respectively. The syntheses

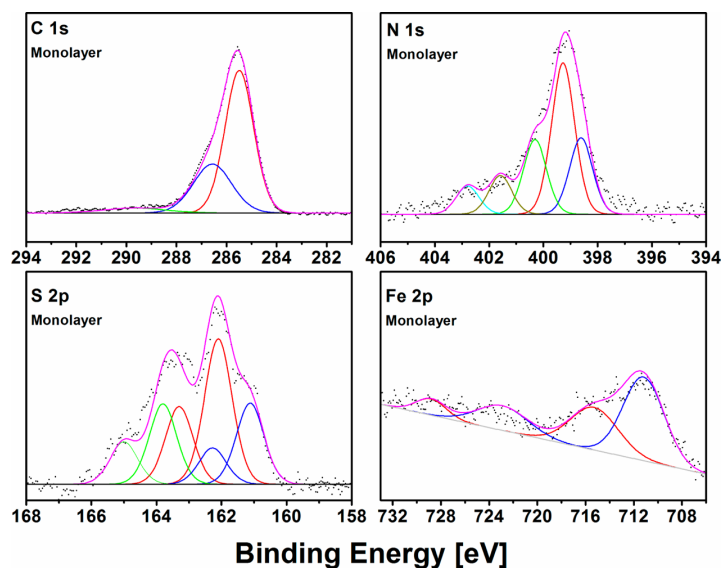


Figure 5. C 1s, Fe 2p, and N 1s XP spectra of $[\text{Fe}(\text{thiotolylsalten})(\text{NCS})]$ (**2**) in monolayers.

of **1-1** and **2-2** were performed according to the literature and are described in the Supporting Information.^{34–37} To ensure the integrity of the surface-adsorbed monolayers, both systems were first characterized by XPS and NEXAFS.

XPS Data of 1 and 2. $[\text{Fe}(\text{salten})(\text{pyS})]^+$ (**1**). C 1s, N 1s, S 2p, and Fe 2p XP spectra of a monolayer of $[\text{Fe}(\text{salten})(\text{pyS})]^+$ (**1**) on Au(111) are shown in Figure 4. Corresponding XP spectra of thick films of $[\text{Fe}(\text{salten})(\text{pyS})]_2(\text{BPh}_4)_2$ (**1-1**) and C 1s, N 1s, and Fe 2p NEXAFS data of **1** and **1-1** are presented and analyzed in the Supporting Information, Figures S1 and S2, respectively. The C 1s XP spectrum of **1** (Figure 4, top left) shows three different species. The major peak at 285.8 eV (red) corresponds to the aromatic and aliphatic carbon atoms whereas the minor peak at 287.4 eV (blue) can be assigned to the carbon atoms bound to heteroatoms (C–N, C–O). The areas of the two peaks (cf. Table S1) match quite well with the stoichiometry of the complex. In addition, there is a $\pi-\pi^*$ shakeup satellite at 290.5 eV (green) that is due to the carbon atoms of salten phenyl groups.

The N 1s XP spectrum of **1** (Figure 4 top right) shows the contributions of three different species. The major peak at 399.5 eV (red) corresponds to the imine nitrogen atoms, the minor peak at 400.1 eV (blue) corresponds to the secondary amine of the salten ligand, and the other minor peak at 401.3 (green) corresponds to the pyridine nitrogen.

The S 2p spectrum of **1** (Figure 4 bottom left) exhibits three components as well. The highest contribution (54% of the total intensity) is derived from a species with a doublet at 162.0/163.2 eV (red) that corresponds to thiolate bound to Au(111).^{38–40} At lower energies (i.e., at 161.2/162.4 eV), a second species (28%, blue) is observed, which in agreement with the literature is assigned to sulfur atoms adsorbed to Au or to a thiolate species in a different bonding configuration.^{41,42} The latter assignment is also supported by Mazzarello et al.⁴³ The alternative explanation (i.e., the generation of sulfur atoms) is associated with the decomposition of sulfur-containing molecules on the Au(111) surface.³¹ On the high-energy side of the thiolate feature (i.e., at 163.7/164.8 eV), a third species (18%, green) appears that by

comparison with the XP spectrum of **2-2** (see below) is assigned to disulfide.

The S 2p XP spectrum of a thick film of **1-1** is very broad (cf. Figure S1). However, this has previously been observed in XPS studies of such systems.³⁸ In the B 1s spectrum of **1-1** (Figure S1), a clear signal is detected at 187.5 eV that originates from the counterion being present in the thick layer. On going to the monolayer, the counterion is obviously removed. Charge compensation might be provided by the formation of a negatively charged thiolate group by which the complex is attached to the surface. The presence of iron in the monolayer of **1** is finally indicated by the Fe 2p XP spectrum that exhibits two maxima at ~ 725 eV (cf. Figure 4 bottom right). Fitting these features with the spin-orbit split Fe 2p signals and the corresponding shakeup satellites gives an Fe 2p_{3/2} signal at 710.4 eV and an Fe 2p_{1/2} signal at 722.5 eV (cf. Table S1). Although the peak at 722.5 eV is less well defined because of the low signal-to-noise ratio of this spectrum, the peak at 710.4 eV clearly indicates the presence of Fe(III) in the surface-adsorbed layer of **1**.^{32,44}

$[\text{Fe}(\text{thiotolylsalten})(\text{NCS})]$ (2**).** The C 1s, N 1s, S 2p and Fe 2p XP spectra of $[\text{Fe}(\text{thiotolylsalten})(\text{NCS})]$ (**2**) are shown in Figure 5. Corresponding XP spectra of thick films of $[\text{Fe}(\text{thiotolylsalten})(\text{NCS})]_2$ (**2-2**) and C 1s and N 1s and Fe 2p NEXAFS spectra of **2** and **2-2** are provided and analyzed in Supporting Information Figures S3 and S4, respectively. By analogy to **1**, the C 1s XP spectrum of **2** (Figure 5 top left) shows three components whereby the major peak at 285.5 eV (red) can be assigned to the aromatic and aliphatic C atoms and the minor peak at 286.6 eV (blue) can be assigned to the C atoms bound to heteroatoms (C–N, C–O). Again, peak areas (cf. Table S2) match well with the stoichiometry of the complex. A $\pi-\pi^*$ shakeup satellite is found at 290.5 eV (green), which is due to the carbon atoms of phenyl groups of the thiotolylsalten ligand. The N 1s XP spectrum of **2** (Figure 5 top right) shows five components. The peak at 398.6 eV (blue) can be assigned to thiocyanate nitrogen atoms; the major peak at 399.3 eV (red), to the imine nitrogens; and the peak at 400.3 eV, to the tertiary

amine. The tail of the N 1s signal to higher energies can be fitted with two peaks at 401.6 (brown) and 402.8 eV (cyan), which in the literature have been attributed to ammonium and amine oxide groups, respectively.⁴⁵ These features are obviously derived from the decomposition of the complex on the Au surface, leading to the generation of free amines that can be protonated and oxidized.

By analogy to compound 1, the S 2p spectrum of the monolayer of 2 (Figure 5 bottom left) exhibits three components. The highest contribution (48% of the total intensity) is derived from a species with peaks at 162.1/163.3 eV (red), which again corresponds to thiolate bound to Au(111).^{38–40} The species at lower energy (161.1/162.3 eV, 26%, blue) is again assigned to adsorbed sulfur atoms.⁴¹ Note, however, that this peak should also account for the sulfur of the thiocyanate group that is present in 2-2 and 2.⁴⁶ The third species in the S 2p spectrum on the high-energy side of the thiolate feature (i.e., at 163.8/165.0 eV, 26%) is assigned to disulfide. Signals at comparable positions are also observed for the S 2p XP spectrum of a thick film of 2-2 (cf. Figure S3). As for 1, the presence of iron in the monolayer of 2 is indicated by the Fe 2p XPS signal that exhibits two maxima at ~ 710 and at ~ 725 eV (very weak, Figure 5 bottom right). Fitting this spectrum with a correlated spin-orbit split pair of Fe 2p signals including the corresponding shakeup satellites (cf. Experimental Section) gives an Fe 2p_{3/2} signal at 711.18 eV, again indicating the presence of Fe(III) centers in the surface-adsorbed layer.^{32,44}

To conclude, the XPS data presented in this section are compatible with the formation of monolayers of 1 and 2 on Au(111) by cleavage of the disulfide bonds present in precursor molecules 1-1 and 2-2, respectively, and allow the identification of a (limited) degree of decomposition taking place upon surface deposition of the complexes. These findings are supported by comparison with XP spectra of thick films as well as NEXAFS data collected for monolayers and multilayers of 1 and 2 (cf. Figures S1–S4). The S 2p XP spectra of systems 1 and 2, in contrast, exhibit major changes upon going from the multilayers to the monolayer. This indicates that a large fraction of dimeric molecules have been cleaved at the S–S linkage, leading to thiolate-bound monomeric complexes 1 and 2, respectively, on the surface. Whereas S–S cleavage is almost complete for 1-1, 36% of the 2-2 molecules appear to have retained the disulfide bond on the Au(111) surface. This point is further considered in the vibrational analysis presented in the following sections and in the Results and Discussion.

Vibrational Analysis. To analyze the IRRA spectra of complexes 1 and 2 adsorbed on Au(111), precursor complexes 1-1 and 2-2 have been investigated in the bulk by IR and Raman spectroscopy, employing DFT frequency calculations for the assignment of the vibrational modes. For a basic understanding of these spectra, vibrational data of [Fe(salten)Cl] and [Fe(salten)(py)]⁺ are presented and analyzed first. These compounds represent the two possible coordination geometries (cis and trans) of [Fe(salten)] complexes (cf. Figure 3).

[Fe(salten)Cl]. This complex exhibits a *cis* configuration (Figure 3 b). Experimental IR and Raman spectra extending over a broad wavenumber range are given along with theoretical simulations by DFT in Figures S5 and S6. In the high-energy region, C–H vibrations of the aliphatic and the aromatic parts of the salten ligand are found. The N–H stretching vibration is located at 3239 cm⁻¹ (calculated 3354 cm⁻¹). Infrared and Raman spectra of [Fe(salten)Cl] in the fingerprint region are shown in Figure 6. For a more detailed analysis, the prominent

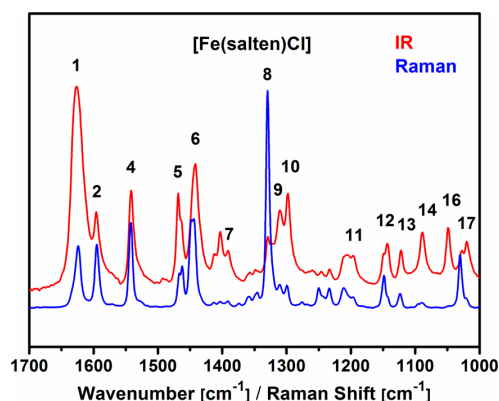


Figure 6. Experimental IR and Raman spectra of [Fe(salten)Cl].

features in this region have been numbered. The most intense vibrations are the imine stretching vibrations of the coordinated ligand (bands 1 and 2), which are found at 1626 and 1595 cm⁻¹, respectively (Tables 1 and S3). As evident from the calculation, these vibrations mix with the C–C ring deformation and C–H bending modes of the salten ligand. The eigenvectors of the two modes with the highest imine stretching character (calculated at 1594 and 1606 cm⁻¹, cf. Table S3) are shown in Figure S7. It is clearly seen that the mode at lower energy is correlated with the imine stretching vibration to the phenolate coordinated trans to the chlorine ligand whereas the mode at higher energy is correlated with the imine stretching vibration of the phenolate coordinated cis to the chlorine ligand. A similar splitting between trans and cis stretching modes is observed for the phenolate C–O stretches that are calculated at 1314 and 1322 cm⁻¹ (for the eigenvectors cf. Figure S8). Again, the mode at lower energy is correlated with the vibration of the trans-axial phenolate whereas the mode at higher energy is correlated with the vibration of the phenolate cis to the chlorine ligand. Bands 9 and 10 in the spectrum of [Fe(salten)Cl] observed at 1310 and 1298 cm⁻¹, respectively, are assigned to these vibrations.

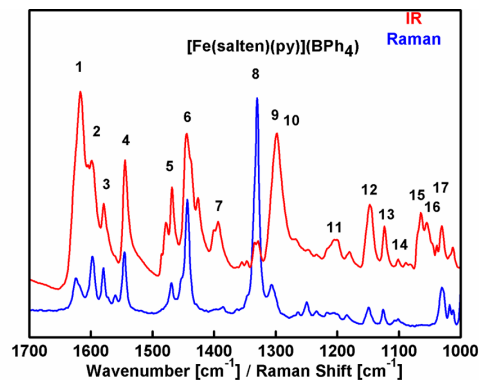
Between the imine stretching vibrations at ~ 1600 cm⁻¹ and the phenolate C–O stretching vibrations at ~ 1300 cm⁻¹, several characteristic C–C ring deformations and C–H bending vibrations of the aliphatic and aromatic parts of the salten ligand are found (Table 1). These vibrations are associated with bands 4 to 7 in Figure 8. Below 1300 cm⁻¹, further C–H bending and C–C ring deformation vibrations are found (bands 10–17 in Figure 8). Assignments of all bands and correlations with calculated vibrational modes are given in Tables 1 and S3.

trans-[Fe(salten)(py)](BPh₄). In contrast to the [Fe(salten)-Cl] complex considered above, [Fe(salten)(py)]BPh₄ has the trans configuration (cf. Figure 3a). Experimental spectra in a broad wavenumber range are given along with theoretical simulations in Figures S9 and S10. Experimental IR and Raman spectra of [Fe(salten)(py)](BPh₄) in the fingerprint region are shown in Figure 7. The analysis of the experimental spectrum of this compound is complicated by the presence of the BPh₄⁻ counterion. A comparison between the experimental and calculated spectra of this anion is given in Figure S11.

The imine stretching vibrations of [Fe(salten)(py)]⁺ are found at about the same frequencies as in [Fe(salten)Cl]. However, a C–C stretching vibration of the pyridine ring is found in the same frequency region such that three bands (bands 1–3) are now observed (Figure 7). In the trans configuration of the

Table 1. Frequency Calculations and Vibrational Assignments for $[\text{Fe}(\text{salten})(\text{pyS})]^+$ (1) on Au(111) and Analogous Systems Studied for Comparison

peak no.	bulk $[\text{Fe}(\text{salten})\text{-Cl}]$	calculated $[\text{Fe}(\text{salten})\text{-(py)}]^+$	bulk $[(\text{Fe}(\text{salten})\text{-(py)})(\text{BPh}_4)]$	bulk $[\text{Fe}(\text{salten})\text{-(pyS)}]_2(\text{BPh}_4)_2$	calculated $[\text{Fe}(\text{salten})\text{-(py)}]^+$ (cis)	IRRAS $[\text{Fe}(\text{salten})\text{-(pyS)}]^+$ on Au(111)	assignments
1	1626	1589	1627		1588	1623	(CC) pyridine ring, (C=N) and (CC) phenyl stretching
		1587	1617	1613	1586	1616	
2	1595	1586	1599	1597	1583		
		1580			1576		
		1578			1574		
3	1542	1563	1579	1579	1563	1598	(CC) pyridine ring deformation
		1520	1545	1543	1523	1543	(CC) phenyl ring deformation
		1517			1514		
5	1469	1449	1469	1468	1449	1472	(CH ₂) and (CH _{arom}) bending
6	1442	1420	1444	1443	1425	1448	(CH ₂) and (CH _{arom}) bending
7	1390	1372	1393	1395	1412	1399	(CH ₂) bending
8	1329	1338	1329	1335	1341	1338	(CH _{pyridine}), (CH _{arom}), and (CH ₂) bending
		1331			1340		
		1320					
9	1310	1297	1297	1292	1303	1313	(CH _{arom}) and (CH ₂) bending;
10	1298	1294			1294	1268	(C–O) stretching
11	1205	1209	1203	1202	1204	1215	(CH _{arom}) and (CH ₂) bending
12	1144	1153	1146	1149	1152	1149	(CH) phenyl deformation; (CH ₂) wagging
13	1121	1123	1124	1123	1117	1121	(CH _{arom}) and (CH ₂) bending
14	1089	1082	1101	1099	1077	1097	(CH ₂) bending
15		1063	1064	1060	1064	1064	(CH _{pyridine}) bending
16	1049	1044	1052	1049	1047	1047	(CH _{pyridine}), (CH _{arom}), and (CH ₂) bending
17	1028	1027	1029	1031	1021	1021	(CH _{pyridine}), (CH _{arom}), and (CH ₂) bending

**Figure 7.** Experimental IR and Raman spectra of $[\text{Fe}(\text{salten})(\text{py})]\text{-(BPh}_4\text{)}$.

$[\text{Fe}(\text{salten})(\text{py})]^+$ fragment, the imine stretching vibrations split into a symmetric (in-phase) and an antisymmetric (out-of-phase) combination, both of which are oriented within the equatorial plane. The symmetric combination is calculated at 1587 cm^{-1} whereas two antisymmetric combinations mixed with C–H bending vibrations are calculated at 1586 and 1578 cm^{-1} (for the eigenvectors cf. Figure S12). Observed positions of bands 1–3 are between 1627 and 1579 cm^{-1} (cf. Tables 1 and S5). For the phenolate C–O stretches, however, no such symmetric–antisymmetric splitting is found, and stretching modes are localized on either of the phenolate moieties (bands 9/10, for the eigenvectors see Figure S13; calculated frequencies 1297 and 1294 cm^{-1}).

Between the imine stretching vibration at $\sim 1600\text{ cm}^{-1}$ and the phenolate C–O stretching vibrations at $\sim 1300\text{ cm}^{-1}$, several characteristic modes of C–C stretching and C–H bending character are found (bands 4–7). Furthermore, characteristic vibrations appear at frequencies $< 1300\text{ cm}^{-1}$ (bands 11–17). Assignments of all bands and correlations to calculated vibrations are given in Tables 1 and S5.

$[\text{Fe}(\text{salten})(\text{pyS})]_2(\text{BPh}_4)_2$ (1-1). As expected, the IR and Raman spectra of $[\text{Fe}(\text{salten})(\text{pyS})]_2(\text{BPh}_4)_2$ (1-1) (Figures S14 and S15) are very similar to those of $[\text{Fe}(\text{salten})(\text{py})](\text{BPh}_4)$ considered in the previous section. The IR spectrum of 1-1 in the fingerprint region is given in Figure 8; the positions and assignments of the numbered bands are given in Table 1. Significant bands in the region of 1570 cm^{-1} can be assigned to the C–C phenyl ring stretching vibrations that mix with stretching vibrations of the salten unit. C–C phenyl ring stretching vibrations are also derived from the counterion (vide supra). Another significant band of the counterion at around 1400 cm^{-1} can be assigned to C–H bending modes of the phenyl ring, which are also present in the salten unit.

IRRAS of $[\text{Fe}(\text{salten})(\text{pyS})]^+$ (1). On the basis of the experimental and theoretical information collected in the previous sections, the vibrational features observed in the IRRA spectrum of $[\text{Fe}(\text{salten})(\text{pyS})]^+$ (1) on Au(111) can be assigned (Table 1). In Figure 8, this spectrum is shown along with those of $[\text{Fe}(\text{salten})\text{Cl}]$, *trans*- $[\text{Fe}(\text{salten})(\text{py})](\text{BPh}_4)$ (calculated and observed), and $[\text{Fe}(\text{salten})(\text{pyS})]_2(\text{BPh}_4)_2$ (1-1). To consider the possibility that the surface-attached $[\text{Fe}(\text{salten})(\text{pyS})]^+$ (1) complex attains the cis configuration on the surface, hypothetical complex *cis*- $[\text{Fe}(\text{salten})(\text{py})]^+$ has also been treated by DFT. The theoretical IR spectrum of this complex (cf. Figure S16) is given in Figure 8 as well;

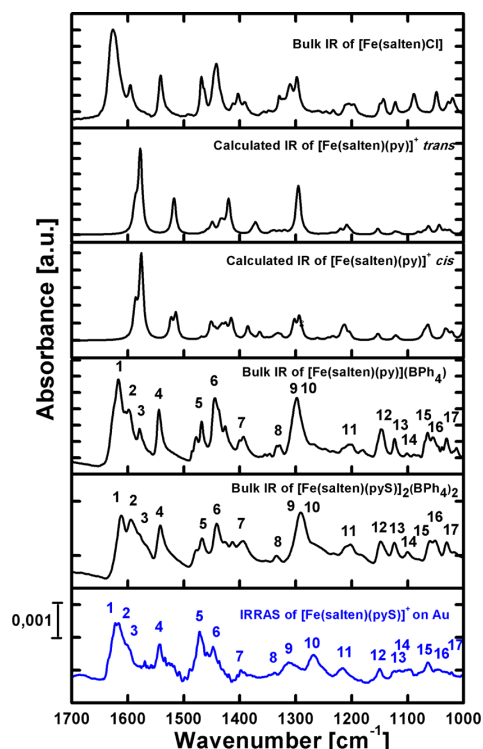


Figure 8. Comparison of the bulk IR of $[\text{Fe}(\text{salten})\text{Cl}]$, the DFT-calculated spectrum of $\text{trans-}[\text{Fe}(\text{salten})(\text{pyS})]^+$ and $\text{cis-}[\text{Fe}(\text{salten})(\text{pyS})]^+$, bulk IR of $\text{trans-}[\text{Fe}(\text{salten})(\text{py})]^+(\text{BPh}_4)$, bulk IR of $[\text{Fe}(\text{salten})(\text{pyS})]_2(\text{BPh}_4)_2$ (1-1), and the IRRS spectrum of $[\text{Fe}(\text{salten})(\text{pyS})]^+$ (1) on Au(111).

corresponding vibrational frequencies are collected in Table S7. Vibrational bands of **1** adsorbed on Au(111) are numbered by analogy to those of the complexes studied for comparison.

Band 1 of complex **1** observed at 1623 cm^{-1} is assigned to a pyridine ring deformation. Bands 2 and 3 observed at 1616 and 1598 cm^{-1} are associated with the imine stretching vibrations. Band 4 observed at 1543 cm^{-1} corresponds to one of two $\text{C}-\text{C}_{(\text{arom})}$ deformation vibrations. Bands 5 and 6 observed at 1472 and 1448 cm^{-1} , respectively, are assigned to $\text{CH}_{(\text{arom})}/\text{CH}_2$ bending vibrations. Band 7 observed at 1399 cm^{-1} is a CH_2 bending vibration. Band 8 observed at 1338 cm^{-1} , finally, corresponds to a vibration of mixed $\text{CH}_{(\text{pyridine})}/\text{CH}_{(\text{arom})}/\text{CH}_2$ bending character.

Notably, bands 9 and 10 exhibit a very large splitting for complex **1** adsorbed on Au(111). On the basis of a comparison with the bulk spectra, both of these bands have to be attributed to phenolate–CO stretches. With respect to these vibrations, the axial mode of $\text{cis-}[\text{Fe}(\text{salten})(\text{py})]^+$ is calculated at 1294 cm^{-1} and the equatorial mode is calculated at 1303 cm^{-1} (eigenvectors are given in Figure S18). Note that the calculated splitting (9 cm^{-1}) is larger than in the trans complex where “the” C–O stretch is relatively sharp and, because of the small splitting between the two components (calcd $\sim 3\text{ cm}^{-1}$), intense. The calculation of the cis complex, however, cannot account for the much larger splitting ($\sim 45\text{ cm}^{-1}$) between bands 9 and 10 observed in the IRRS spectrum of **1**. Moreover, such a large splitting does not appear in any of the other spectra (cf. Figure 8). From this observation, we conclude that one axial phenolate arm

decoordinates from the complex and rebinds to the Au(111) surface (Figure 9). This reaction might be induced by a trans effect of the pyridine thiol ligand that electronically couples the metal center with the surface.

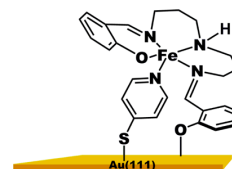


Figure 9. Hypothetical geometry of complex $[\text{Fe}(\text{salten})(\text{pyS})]^+$ on Au(111).

To test this hypothesis, we deposited salicylaldehyde on Au(111) and measured the IRRS spectrum. A peak observed at 1250 cm^{-1} (cf. Figure S19) is attributed to the C–O stretch of the phenolate–Au bond. We thus conclude that peak 10 at 1268 cm^{-1} in the IRRS spectrum of $[\text{Fe}(\text{salten})(\text{pyS})]^+$ (1) corresponds to the Au-coordinated phenolate unit and peak 9 at 1313 cm^{-1} corresponds to the Fe-coordinated phenolate. Importantly, no evidence for the surface selection rule is found for the monolayer of **1** on Au(111) (i.e., the intensities in the IRRS spectrum of **1** more or less match those of the corresponding bulk spectra (Figure 8)).

Bulk and Surface Spectra of $[\text{Fe}(\text{thiotolylsalten})(\text{NCS})]_2$ (2-2). For comparison, complex $[\text{Fe}(\text{thiotolylsalten})(\text{NCS})]_2$ (2-2) has been synthesized and deposited on Au(111) as well. In this system, the metal should be more decoupled from the surface than in complex **1**, which was bound to Au(111) by a pyridine thiol linker. Experimental spectra of 2-2 recorded over a broad wavenumber range are given along with theoretical simulations in Figures S20 and S21. IR and Raman spectra of 2-2 in the fingerprint region are given in Figure S22. As expected, these spectra are very similar to those of $[\text{Fe}(\text{salten})\text{Cl}]$ and $[\text{Fe}(\text{salten})(\text{pyS})]_2(\text{BPh}_4)_2$ (1-1). Of course, vibrations 3 and 15 are missing because no pyridine unit is present. Band positions and assignments based on DFT calculations are collected in Table 2.

In Figure 10, the IRRS spectrum of $[\text{Fe}(\text{thiotolylsalten})(\text{NCS})]_2$ (2) is shown (red) along with the bulk spectrum of $[\text{Fe}(\text{thiotolylsalten})(\text{NCS})]_2$ (2-2, calculated and observed) and the IRRS spectrum of $[\text{Fe}(\text{salten})(\text{pyS})]^+$ (1, blue).

The intense bands at 1617 and 1600 cm^{-1} (bands 1 and 2) in the IRRS spectrum of $[\text{Fe}(\text{thiotolylsalten})(\text{NCS})]_2$ (2) can be assigned to the imine stretching vibrations. Band 4 at 1542 cm^{-1} corresponds to the C–C phenyl ring deformation. At 1471 and 1448 cm^{-1} , CH_2 and CH_{arom} bending vibrations, at 1396 cm^{-1} CH_2 bending vibrations, and at 1337 cm^{-1} , CH_{arom} and CH_2 bending vibrations are observed (bands 5–8, cf. Table 2). The C–O stretching region (bands 9 and 10) is the most interesting region compared to $[\text{Fe}(\text{salten})(\text{pyS})]^+$ (1). In contrast to the IRRS spectrum of **1** where a large splitting of the C–O bands has been observed (vide supra), no such splitting is observed in the spectrum of $[\text{Fe}(\text{thiotolylsalten})(\text{NCS})]_2$ (2) on Au(111). This indicates that the phenolate coordination of surface-adsorbed complex **2** corresponds to that present in compound 2-2 in the bulk, which has the cis configuration.

The NCS stretching vibration of compound **2** is observed at 2040 cm^{-1} in the IRRS spectrum; however, it has a smaller intensity as compared to that in the bulk spectrum. This indicates that the NCS stretching vibration of the adsorbed complex is

Table 2. Frequency Calculations and Vibrational Assignments for [Fe(thiotolysalten)(NCS)]₂ (2-2) in the Bulk and for [Fe(thiotolysalten)(NCS)] (2) on Au(111)

peak no.	bulk [Fe(thiotolysalten)NCS]	calculated [Fe(thiotolysalten)NCS]	IRRAS [Fe(thiotolysalten)NCS] on Au(111)	assignments
NCS	2080	2108	2040	NCS stretching vibration
1	1611	1660	1617	(C=N) and (CC) phenyl stretching
2	1597	1572	1600	(CC) pyridine ring,
(3)				(CC) phenyl ring deformation
4	1543	1524	1542	(CH ₂) and (CH _{arom}) bending
5	1469	1483	1470	(CH ₂) and (CH _{arom}) bending
6	1445	1459	1447	(CH ₂) and (CH _{arom}) bending
7	1401	1445	1396	(CH ₂) bending
8	1339	1419	1338	(CH _{arom}) and (CH ₂) bending
9	1312	1340	1315	(CH _{arom}) and (CH ₂) bending;
10	1290	1324	1290	(C–O) stretching
11	1248	1203	1248	(CH _{arom}) and (CH ₂) bending
12	1204	1144	1199	(CH) phenyl deformation;
				(CH ₂) wagging
13	1152	1119	1149	(CH _{arom}) and (CH ₂) bending
14	1122	1075	1123	(CH ₂) bending
(15)				(CH _{pyridine}) bending
16	1047	1051		(CH _{arom}) and (CH ₂) bending
17	1029	1027		(CH _{arom}) and (CH ₂) bending

oriented at a small angle with respect to the surface and thus appears with reduced intensity. Interestingly, the C–N stretching frequency of **2** adsorbed to the Au(111) surface (2040 cm⁻¹) is lowered by 40 cm⁻¹ with respect to the bulk value of **2-2** (2080 cm⁻¹), indicating that the Fe(III) centers of surface-adsorbed **2** are more electron-rich as compared to those of bulk **2-2**.

As shown by the analysis of the S 2p XP spectra of **2**, about one-third of the **2-2** molecules appear to have retained the disulfide bond in the monolayer. From the existing data, we cannot decide whether these molecules are weakly attached to the gold surface by the S–S moieties or physisorbed to the thiolate-bound monolayer of **2**. In the IRRA spectrum of **2**, however, the presence of disulfide-bridged (i.e., non-Au-bound) complexes in the monolayer does not lead to a splitting or a broadening of the vibrational peaks associated with the thiotolysalten ligand. We therefore conclude that the splitting of the disulfide bridge has only minor consequences with respect to the electronic and geometric structures of the iron center in this system. This is supported by the similarity of the NEXAFS spectra (in particular, that for Fe 2p) for the monolayer and the thick film (cf. Figure S4).

SUMMARY AND CONCLUSIONS

In the preceding sections, XP and vibrational spectra of [Fe(salten)(pyS)]⁺ (**1**) and [Fe(thiotolysalten)(NCS)] (**2**) complexes adsorbed to Au(111) have been recorded and interpreted. These molecules are generated from corresponding dinuclear Fe(III) precursors [Fe(salten)pyS](BPh₄) (**1-1**) and

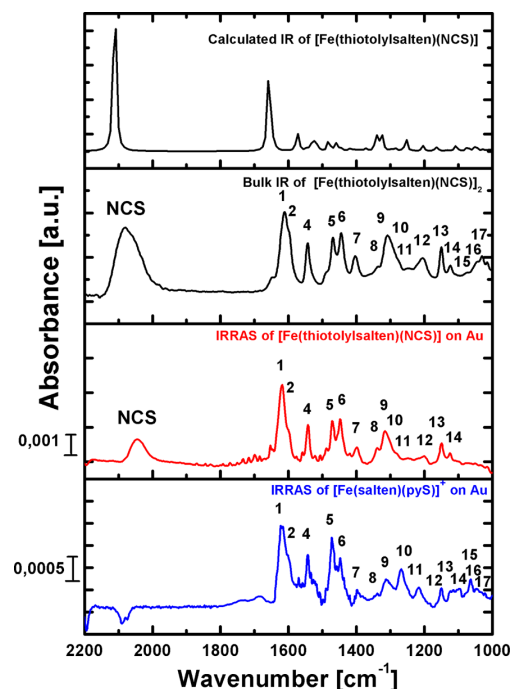


Figure 10. Comparison of the DFT-calculated *cis*-[Fe(thiotolysalten)(NCS)], bulk IR of [Fe(thiotolysalten)(NCS)]₂ (**2-2**), IRRA spectrum of [Fe(thiotolysalten)(NCS)] (**2**) on Au(111), and IRRA spectrum of [Fe(salten)(pyS)]⁺ (**1**) on Au(111).

[Fe(thiotolysalten)(NCS)] (**2-2**) upon adsorption to an Au(111) surface. Monomeric fragments [Fe(salten)(pyS)]⁺ (**1**) and [Fe(thiotolysalten)(NCS)] (**2**) are bound to the surface via pyridine thiol and thiotolyl groups, respectively. These findings are supported by NEXAFS data. For compound **2**, however, XPS indicates that 36% of the molecules retain their S–S bond in the monolayer. The higher efficiency of **1** with respect to S–S cleavage may be due to an electron-withdrawing effect of the pyridine groups bound to the center S–S moiety, possibly activating the S–S bond toward cleavage. For compound **2** having tolyl groups bound to the S–S moiety instead, this effect would be absent, leading to less-complete S–S bond cleavage on the surface. Although both thiols and disulfides lead to thiolate-bound monolayers on Au, it is known that disulfides less effectively displace thiolate-bound molecules from surfaces than thiols.⁴⁷ Correspondingly, molecules of **2-2** might be less effective than molecules of **1-1** in forming thiolate-bound complexes on a surface that is already partially covered with thiolate-bound molecules. From this perspective, an activation of the disulfide bond may in fact be relevant to achieving complete coverage of the surface by one monolayer of thiolate-bound molecules.

Peak positions and intensities in the IRRA spectra along with the information from XPS and NEXAFS indicate that monolayers of **1** and **2** are present on the Au(111) surfaces. For complex **1**, however, the phenolate C–O stretches exhibit an anomalously large splitting. As a matter of fact, this splitting cannot be accounted for by DFT calculations on intact *trans*- and (hypothetical) *cis*-[Fe(salten)(py)]⁺ complexes and hence is attributed to a decoordination of one phenolate arm from the iron center and a possible rebinding to the Au(111) surface. The

deposition of $[\text{Fe}(\text{thiotolylsalten})(\text{NCS})]_2$ (2-2) on a gold surface, in contrast, does not lead to such a splitting of the phenolate C–O stretches in the adsorbed monolayer of $[\text{Fe}(\text{thiotolylsalten})(\text{NCS})]$ (2). On the basis of X-ray structural data, this complex has cis geometry in the bulk.²² From the spectroscopic data, it is concluded that this geometry is retained on the surface. The relative intensity of the C–N stretch is lower in the monolayer than in the bulk; this observation indicates that the thiocyanate group is significantly tilted with respect to the surface normal. The fact that the C–N stretching frequency of 2 adsorbed to the Au(111) surface (2040 cm^{-1}) is lowered by 40 cm^{-1} with respect to the bulk value of 2-2 (2080 cm^{-1}) reflects some transfer of electron density from the surface to the Fe(III) center of surface-adsorbed 2.

What are the reasons for the decoordination of one phenolate arm of the salten ligand from the metal center of surface-adsorbed $[\text{Fe}(\text{salten})(\text{pyS})]^+$ (1) as opposed to the retention of the phenolate coordination observed for complex 2? From other surface-spectroscopic studies, it is known that the gold surface acts as both a strong and an electron-donating ligand for transition-metal complexes.⁸ For complexes directly deposited on gold, this has the consequence that these complexes in general do not add axial ligands any more (vide supra). In coordination chemistry, this influence is described as the trans effect, which means that a strong ligand weakens the ligand trans to it. A similar phenomenon observed for surface-adsorbed complexes has been termed the surface trans effect.⁸ We tried to avoid or minimize this interaction by attaching complex 1 via a bifunctional organic linker molecule to the surface. Nevertheless, the results obtained in this study indicate that the trans effect is still present if the complex is bound to the surface by a relatively short linker exhibiting a delocalized π system such as pyridine thiol. In particular for phenolate acting as a strong π donor, the metal–ligand bond trans to the surface-bound ligand is weakened to such a degree that this ligand is decoordinated.

For complex 2, which is attached to the surface via a thiotolyl group, the interaction of the metal center with the gold surface is much weaker, and the mixed salten–NCS coordination of dimeric precursor complex 2-2 is retained. This may be due to the CH_2 group of the thiotolyl moiety that electronically decouples the iron center from the surface. Nevertheless, the lowering of the thiocyanate CN stretching frequency by 40 cm^{-1} with respect to the bulk indicates that there is still a nonvanishing electronic influence of the Au(111) surface on the metal center of the adsorbed complex. Understanding and controlling these phenomena is of paramount importance when applications of surface-attached transition-metal complexes in the fields of spin-switching^{1,48} and catalysis are addressed.⁴

■ ASSOCIATED CONTENT

Supporting Information

¹H NMR, ¹³C{¹H} NMR, elemental analysis data of synthesized compounds, details of experimental methods, and calculations. This material is available free of charge via the Internet at <http://pubs.acs.org>.

■ AUTHOR INFORMATION

Corresponding Author

*E-mail: ftuczek@ac.uni-kiel.de. Fax: +49 431 880-1523.

Notes

The authors declare no competing financial interest.

■ ACKNOWLEDGMENTS

We thank the Deutsche Forschungsgemeinschaft (DFG) for funding this research (SFB 677). We also thank Dr. Antje Vollmer, Dr. Ruslan Ovsyannikov, and Maximilian Bauer for support at the SurICat beamline of BESSY II, Berlin, and A. Terfort (Frankfurt) for the gift of deuterated hexadecanethiol. H.J. also thanks Benjamin Herzigkeit for synthesis work performed during his bachelor's thesis and Uschi Cornelissen for Raman measurements.

■ REFERENCES

- (1) Alam, M. S.; Stocker, M.; Gieb, K.; Mueller, P.; Haryono, M.; Student, K.; Grohmann, A. Spin-State Patterns in Surface-Grafted Beads of Iron(II) Complexes. *Angew. Chem., Int. Ed.* **2010**, *49*, 1159–1163.
- (2) Kuck, S.; Chang, S.-H.; Klöckner, J.-P.; Prosenč, M. H.; Hoffmann, G.; Wiesendanger, R. Steering Two-Dimensional Molecular Growth via Dipolar Interaction. *ChemPhysChem* **2009**, *10*, 2008–2011.
- (3) Laskin, J.; Wang, P.; Hadjar, O. Soft-Landing of Co(III)(salen)⁺ and Mn(III)(salen)⁺ on Self-Assembled Monolayer Surfaces. *J. Phys. Chem. C* **2010**, *114*, 5305–5311.
- (4) Venkataraman, N. S.; Kuppuraj, G.; Rajagopal, S. Metal–Salen Complexes as Efficient Catalysts for the Oxygenation of Heteroatom Containing Organic Compounds—Synthetic and Mechanistic Aspects. *Coord. Chem. Rev.* **2005**, *249*, 1249–1268.
- (5) Chiang, W.; Vanengen, D.; Thompson, M. E. Second-Order Non-Linear Optical Properties of Fe(Salen) Complexes. *Polyhedron* **1996**, *15*, 2369–2376.
- (6) Koley, M. K.; Manoharan, P. T.; Koley, A. P. Synthesis and Characterization of a Stable Paramagnetic Hexacoordinated Oxochromium(IV) Complex with Dianionic Tetradentate Schiff Base Ligand Salen. *Inorg. Chim. Acta* **2010**, *363*, 3798–3802.
- (7) Sarasukutty, S.; Prabhakaran, C. P. Studies on Iron(III) Thiocyanate Complexes of N,N' Ethylene Bis (Salicylideneimine), N,N' Bis *o*-Hydroxybenzylidene *o*-Phenylenediamine and N,N' Propylene Bis (Salicylideneimine). *J. Inorg. Nucl. Chem.* **1977**, *39*, 374–376.
- (8) Hieringer, W.; Flechtner, K.; Kretschmann, A.; Seufert, K.; Auwärter, W.; Barth, J. V.; Görling, A.; Steinrück, H.-P.; Gottfried, J. M. The Surface Trans Effect: Influence of Axial Ligands on the Surface Chemical Bonds of Adsorbed Metalloporphyrins. *J. Am. Chem. Soc.* **2011**, *133*, 6206–6222.
- (9) Wäckerlin, Ch.; Tarafder, K.; Siewert, D.; Girovsky, J.; Hählen, T.; Iacovita, Ch.; Kleibert, A.; Nolting, F.; Jung, T. A.; Oppeneer, P. M.; Ballav, N. On-Surface Coordination Chemistry of Planar Molecular Spin Systems: Novel Magnetochemical Effects Induced by Axial Ligands. *Chem. Sci.* **2012**, *3*, 3154–3160.
- (10) Silien, Ch.; Buck, M.; Goretzki, G.; Lahaye, D.; Champness, N. R.; Weidner, T.; Zharnikov, M. Self-Assembly of a Pyridine-Terminated Thiol Monolayer on Au(111). *Langmuir* **2009**, *25*, 959–967.
- (11) Silien, Ch.; Lahaye, D.; Caffio, M.; Schaub, R.; Champness, N. R.; Buck, M. Electrodeposition of Palladium onto a Pyridine-Terminated Self-Assembled Monolayer. *Langmuir* **2011**, *27*, 2567–2574.
- (12) Darlatt, E.; Traulsen, Ch. H.-H.; Poppenberg, J.; Richter, S.; Kühn, J.; Schalley, Ch. A.; Unger, W. E. S. Evidence of Click and Coordination Reactions on a Self-Assembled Monolayer by Synchrotron Radiation Based XPS and NEXAFS. *J. Electron Spectrosc. Relat. Phenom.* **2012**, *185*, 85–89.
- (13) Poppenberg, J.; Richter, S.; Darlatt, E.; Traulsen, Ch. H.-H.; Min, H.; Unger, W. E. S.; Schalley, Ch. A. Successive Coordination of Palladium(II)-Ions and Terpyridine-Ligands to a Pyridyl-Terminated Self-Assembled Monolayer on Gold. *Surf. Sci.* **2012**, *606*, 367–377.
- (14) Kind, M.; Wöll, C. Organic Surfaces Exposed by Self-Assembled Organothiol Monolayers: Preparation, Characterization and Application. *Prog. Surf. Sci.* **2009**, *84*, 230–278.
- (15) Arnold, R.; Terfort, A.; Wöll, C. Determination of Molecular Orientation in Self-Assembled Monolayers Using IR Absorption

- Intensities: The Importance of Grinding Effects. *Langmuir* **2001**, *17*, 4980–4989.
- (16) Gregoriou, V. G.; Rodman, S. E. *Vibrational Spectroscopy of Thin Organic Films*; *Handbook of Vibrational Spectroscopy*; J. Wiley: New York, 2006
- (17) Hollins, P. Surface Infrared Spectroscopy. *Vacuum* **1994**, *45*, 705–714.
- (18) Greenler, R. G. Infrared Study of Adsorbed Molecules on Metal Surfaces by Reflection Techniques. *J. Chem. Phys.* **1966**, *44*, 310.
- (19) Rajalingam, K.; Strunskus, T.; Terfort, A.; Fischer, R. A.; Wöll, C. Metallization of a Thiol-Terminated Organic Surface Using Chemical Vapor Deposition. *Langmuir* **2008**, *24*, 7886–7994.
- (20) Shekhah, O.; Wang, H.; Strunskus, T.; Cyganik, P.; Zacher, D.; Fischer, R.; Wöll, C. Layer-by-Layer Growth of Oriented Metal Organic Polymers on a Functionalized Organic Surface. *Langmuir* **2007**, *23*, 7440–7442.
- (21) Zawisza, I.; Wittstock, G.; Boukherroub, R.; Szunerits, S. PM IRRAS Investigation of Thin Silica Films Deposited on Gold. Part 1. Theory and Proof of Concept. *Langmuir* **2007**, *23*, 9303–9309.
- (22) Mayer, C. R.; Cucchiari, G.; Jullien, J.; Dumur, F.; Marrot, J.; Dumas, E.; Sécheresse, F. Functionalization of Gold Nanoparticles by Iron(III) Complexes Derived from Schiff Base Ligands. *Eur. J. Inorg. Chem.* **2008**, 3614–3623.
- (23) Hirose, S.; Hayami, S.; Maeda, Y. Magnetic Properties of Iron(III) Complexes with Photoisomerizable Ligands. *Bull. Chem. Soc. Jpn.* **2000**, *73*, 2059–2066.
- (24) Nemeč, I.; Boča, R.; Gembický, M.; Dlháň, L.; Herchel, R.; Renz, F. High-Spin Schiff Base Dinuclear Iron(III) Complexes Bridged by N-Oxide Ligands. *Inorg. Chim. Acta* **2009**, *362*, 4754–4759.
- (25) <http://avogadro.openmolecules.net>.
- (26) Becke, A. D. Density-Functional Exchange-Energy Approximation with Correct Asymptotic Behavior. *Phys. Rev. A: Gen. Phys.* **1988**, *38*, 3098–3100. Perdew, J. P. *Phys. Rev. B: Condens. Matter* **1986**, *157*, 200–206.
- (27) Schaefer, A.; Horn, H.; Ahlrichs, R. Fully Optimized Contracted Gaussian-Basis Sets for Atoms Li to Kr. *J. Chem. Phys.* **1992**, *97*, 2571–2577.
- (28) Schaefer, A.; Huber, C.; Ahlrichs, R. Fully Optimized Contracted Gaussian-Basis Sets of Triple Zeta Valence Quality for Atoms Li to Kr. *J. Chem. Phys.* **1994**, *100*, 5829–5835.
- (29) Frisch, M. J.; Trucks, G. W.; Schlegel, H. B.; Scuseria, G. E.; Robb, M. A.; Cheeseman, J. R.; Scalmani, G.; Barone, V.; Mennucci, B.; Petersson, G. A.; Nakatsuji, H.; Caricato, M.; Li, X.; Hratchian, H. P.; Izmaylov, A. F.; Bloino, J.; Zheng, G.; Sonnenberg, J. L.; Hada, M.; Ehara, M.; Toyota, K.; Fukuda, R.; Hasegawa, J.; Ishida, M.; Nakajima, T.; Honda, Y.; Kitao, O.; Nakai, H.; Vreven, T.; Montgomery, J. A., Jr.; Peralta, J. E.; Ogliaro, F.; Bearpark, M.; Heyd, J. J.; Brothers, E.; Kudin, K. N.; Staroverov, V. N.; Kobayashi, R.; Normand, J.; Raghavachari, K.; Rendell, A.; Burant, J. C.; Iyengar, S. S.; Tomasi, J.; Cossi, M.; Rega, N.; Millam, J. M.; Klene, M.; Knox, J. E.; Cross, J. B.; Bakken, V.; Adamo, C.; Jaramillo, J.; Gomperts, R.; Stratmann, R. E.; Yazyev, O.; Austin, A. J.; Cammi, R.; Pomelli, C.; Ochterski, J. W.; Martin, R. L.; Morokuma, K.; Zakrzewski, V. G.; Voth, G. A.; Salvador, P.; Dannenberg, J. J.; Dapprich, S.; Daniels, A. D.; Farkas, Ö.; Foresman, J. B.; Ortiz, J. V.; Cioslowski, J.; Fox, D. J. *Gaussian 09*, revision A.1; Gaussian, Inc.: Wallingford, CT, 2009.
- (30) Casa XPS, casaxps.com; Casa Software Ltd., 2009.
- (31) Heister, K.; Zharnikov, M.; Grunze, M. Characterization of X-ray Induced Damage in Alkanethiolate Monolayers by High-Resolution Photoelectron Spectroscopy. *Langmuir* **2001**, *17*, 8–11.
- (32) Yamashita, T.; Hayes, P. Analysis of XPS Spectra of Fe²⁺ and Fe³⁺ Ions in Oxide Materials. *Appl. Surf. Sci.* **2008**, *254*, 2441–2449.
- (33) Stoch, J.; Capecki, A. Decomposition of 2p_{3/2} Bands in XPS Spectra of Fe, Co and Ni Compounds. *Surf. Interface Anal.* **1990**, *15*, 206–210.
- (34) Bannwarth, A.; Schmidt, S.-O.; Peters, G.; Sönnichsen, F. D.; Thimm, W.; Herges, R.; Tuzcek, F. Fe(III) Spin Crossover Complexes with Photoisomerizable Ligands: Experimental and Theoretical Investigations on the LD-LISC Effect. *Eur. J. Inorg. Chem.* **2012**, 2776–2783.
- (35) Boča, R.; Fukuda, Y.; Gembický, M.; Herchel, R.; Jaroščík, R.; Linert, W.; Renz, F.; Yuzurihara, J. Spin Crossover in Mononuclear and Binuclear Iron(III) Complexes with Pentadentate Schiff Base Ligands. *Chem. Phys. Lett.* **2000**, *325*, 411–419.
- (36) Ohta, S.; Yoshimura, C.; Matsumoto, N.; Okawa, H.; Ohyoshi, A. The Synthesis, Magnetic, and Spectroscopic Properties of Binuclear Iron(III) Complexes bridged by Pyrazine, 1,1'-Tetramethylenebis(imidazol), or Bis(pyridine) Compounds Exhibiting a Spin-Equilibrium Behavior. *Bull. Chem. Soc. Jpn.* **1986**, *59*, 155–159.
- (37) Soomro, S. A.; Benmouna, R.; Berger, R.; Meier, H. Preparation and Photochemistry of Dendrimers with Isolated Stilbene Chromophores. *Eur. J. Org. Chem.* **2005**, 3586–3593.
- (38) Wackerbarth, H.; Marie, R.; Grubb, M.; Zhang, J.; Hansen, A. G.; Chorkendorff, I.; Christensen, C. B. V.; Boisen, A.; Ulstrup, J. Thiol- and Disulfide-Modified Oligonucleotide Monolayer Structures on Polycrystalline and Single-Crystal Au(111) Surfaces. *J. Solid State Electrochem.* **2004**, *8*, 474–481.
- (39) Hallmann, L.; Bashir, A.; Strunskus, T.; Adelung, R.; Staemmler, V.; Wöll, Ch.; Tuzcek, F. Self-Assembled Monolayers of Benzylmercaptan and *p*-Cyanobenzylmercaptan on Au(111) Surfaces: Structural and Spectroscopic Characterization. *Langmuir* **2008**, *24*, 5726–5733.
- (40) Castner, D. G. X-ray Photoelectron Spectroscopy Sulfur 2p Study of Organic Thiol and Disulfide Binding Interactions with Gold Surfaces. *Langmuir* **1996**, *12*, 5083–5086.
- (41) Vericat, C.; Vela, M. E.; Benitez, G.; Carro, P.; Salvarezza, R. C. Self-Assembled Monolayers of Thiols and Dithiols on Gold: New Challenges for a Well-Known System. *Chem. Soc. Rev.* **2010**, *39*, 1805–1834.
- (42) Cyganik, P.; Buck, M.; Strunskus, T.; Shaporenko, A.; Wilton-Ely, J. D. E. T.; Zharnikov, M.; Wöll, C. Competition as a Design Concept: Polymorphism in Self-Assembled Monolayers of Biphenyl-Based Thiols. *J. Am. Chem. Soc.* **2006**, *128*, 13868–13878.
- (43) Mazzarello, R.; Cossaro, A.; Verdini, A.; Rousseau, R.; Casalis, L.; Danisman, M. F.; Floreano, L.; Scandolo, S.; Morgante, A.; Scoles, G. Structure of a CH₃S Monolayer on Au(111) Solved by the Interplay between Molecular Dynamics Calculations and Diffraction Measurements. *Phys. Rev. Lett.* **2007**, *98*, 016102–1–016102–4.
- (44) Grosvenor, A. P.; Kobe, B. A.; Biesinger, M. C.; McIntyre, N. S. Investigation of Multiplet Splitting of Fe 2p XPS Spectra and Bonding in Iron Compounds. *Surf. Interface Anal.* **2004**, *36*, 1564–1574.
- (45) Pippig, F.; Sarghini, S.; Hollaender, A.; Paulussen, S.; Terryn, H. TFAA Chemical Derivatization and XPS. Analysis of OH and NHX Polymers. *Surf. Interface Anal.* **2009**, *41*, 421–429.
- (46) Burger, K.; Furlani, C.; Mattogno, G. XPS Structural Characterization of Spin-State Crossover in Fe^{II}(NCS)₂(phen)₂. *J. Electron Spectrosc. Relat. Phenom.* **1980**, *21*, 249–256.
- (47) Biebuyck, H. A.; Bain, C. D.; Whitesides, G. M. Comparison of Organic Monolayers on Polychrystalline Gold Spontaneously Assembled from Solutions Containing Dialkyl Disulfides or Alkanethiols. *Langmuir* **1994**, *10*, 1825–1831.
- (48) Gopakumar, T. G.; Matino, F.; Naggert, H.; Bannwarth, A.; Tuzcek, F.; Berndt, R. Electron-Induced Spin Crossover of Single Molecules in a Bilayer on Gold. *Angew. Chem., Int. Ed.* **2012**, *51*, 6262–6266.

2.4 Conclusion

In this publication we successfully reported the synthesis of two different dinuclear [Fe(III) (salten)] complexes bridged by disulfide bridged ligands. The [Fe(salten)(pyS)]₂(BPh₄)₂ presents a new unknown dinuclear system and forms mononuclear monolayers after the disulfide bridge bond cleaves on the gold surface. The second system [Fe(thiotolylsalten)(NCS)]₂ was investigated by different TEM/SEM techniques on gold nanoparticles before by Mayer *et al.*^[130] This system also forms mononuclear monolayers on gold after disulfide bond cleavage through the reduction of the electron rich gold surface.

We presented the spectroscopic characterization of the ligand systems in bulk material by elemental analysis, NMR, Raman and IR and the characterization of the formed Fe(III) complexes with elemental analysis, Raman and IR. After a detailed vibrational analysis of these two [Fe(salten)] complexes, in comparison with performed DFT calculations, the adsorbed monomers on Au(111) surfaces were analyzed in detail using XPS, NEXAFS and IRRAS. The two systems were analyzed in detail in their chemical compositions and vibrational information on Au(111).

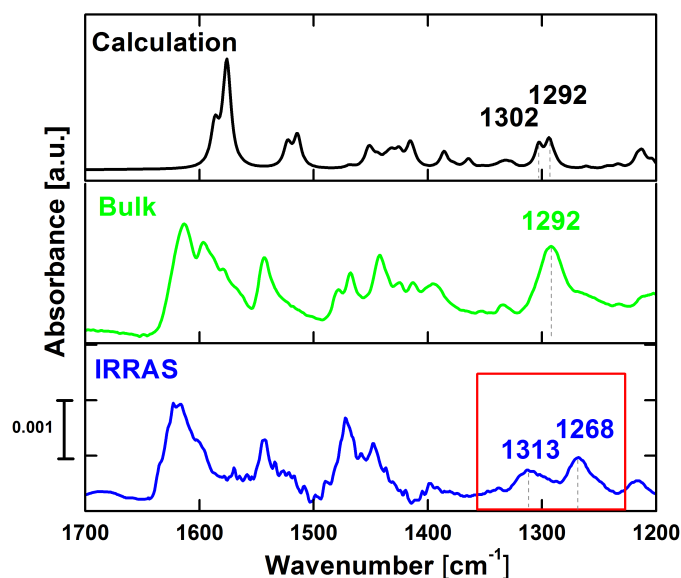


Figure 28: Comparison of the calculated IR spectrum of [Fe(salten)(pySH)], bulk IR spectrum of [Fe(salten)(pyS)]₂(BPh₄)₂ and IRRAS spectrum of [Fe(salten)(pyS)]⁺ monolayers on Au(111).

Due to a reproducible finding in all recorded IRRAS data of the $[\text{Fe}(\text{salten})(\text{pyS})]^+$ complex on Au(111) (Fig. 28), we achieved a possible model system to understand the resulting anomaly. We proposed a structural geometry change of the ligand system by decooordination of a phenolate arm from the Fe(III) central atom to the Au(111) surface (Fig. 29, left). We were able to find a suitable reason for the big shift of one of the C-O stretching vibrations of the ligand system on the surface.

By decooordination of one phenolate arm of the salten ligand, the phenolate can bind to the gold surface. One possible reason could be that the pyridine thiolate is a conjugated system and transfers electrons from the surface to the iron center of the complex. Due to this, one phenolate arm can decoordinate and bind to the surface and the resulting geometry of the adsorbed molecules changes in comparison to the bulk material.

We supported this assumption by adsorbing salicylaldehyde to a Au(111) surface. In this spectrum we clearly observe a band at 1250 cm^{-1} (Fig. 29, right). Due to the result of this experiment, we assigned the band in the IRRAS spectrum of $[\text{Fe}(\text{salten})(\text{pyS})]^+$ to a decoordinated phenolate-arm to the surface.

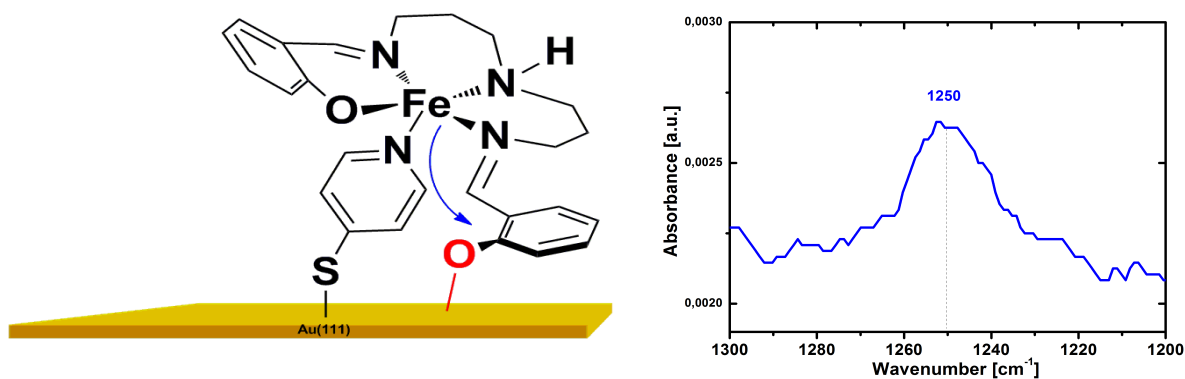


Figure 29: Decoordination of the phenolate arm of the salten ligand to the gold surface and IRRAS of salicylaldehyde on Au(111).

We achieved a new way for the fixation of spin crossover systems to Au(111) surfaces by using disulfide containing linkers and showed that these complexes can bind to the surface in

spite of their bulky ligand systems. Some percent of dinuclear complexes are still remained on surface. The dinuclear molecules of $[\text{Fe}(\text{salten})(\text{pyS})]_2^{2+}$ with intact disulfide bridge were analyzed using STM and the results are presented in the next chapter.

In summary, we demonstrated a new and gainful method to fix transition metal complexes by covalent attachment to Au(111) surfaces. Surface vibrational information about the adsorbed complexes, the geometry of the complexes on the surface as well as quantitative and qualitative information about the chemical composition of the molecules were obtained.

2.5 Outlook

Further projects on the fixation of spin crossover materials on surfaces are in progress in our working group. The deposition of spin crossover complexes from chemical vapor deposition in cooperation with the working group of Prof. Dr. Richard Berndt are also the focus of current research.

Moreover, reactions on prefunctionalized SAMs like azides can offer new possibilities to obtain metal containing functionalized surfaces. SAMs of azide terminated alkanethiols are well known in literature and their behavior on surface has been well researched.^[124]

Azide terminated SAMs show time dependent radiation damage under synchrotron and X-ray radiation. After a click reaction of an alkyne terminated molecule, 1,2,3 triazole groups result from a 1,3 dipolar cycloaddition.^[131,132]

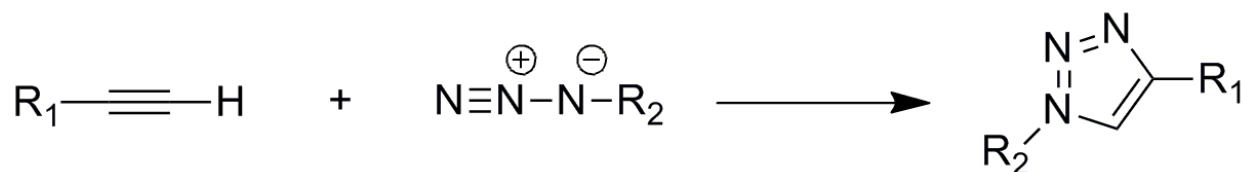


Figure 30: 1-4-Click product of the Huisgen click reaction.

Our first experiments on Huisgen click reaction (Fig. 31) on Au(111) with a spin crossover ligand system, Bis(2,6-pyrazol-1-yl)4-pyridin (bpp), were successful according to Darlatt *et al.*, who successfully clicked a terpyridine ligand system to an azide terminated SAM.^[124]

In most cases, click reactions are carried out in the presence of water or water containing solutions and copper(I)salts act as catalyst. Copper(II) salts in the presence of a reducing agent like sodium ascorbate or hydrazine can also be used.^[133,134]

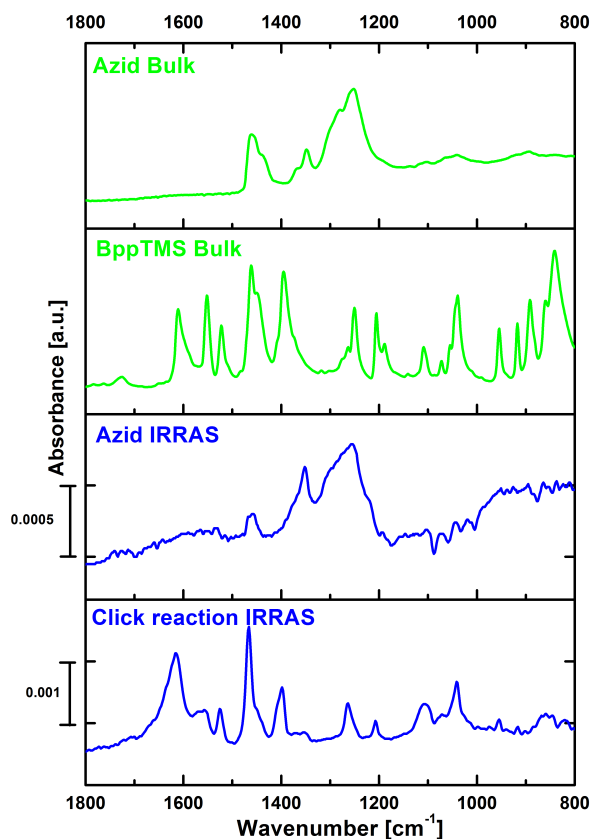


Figure 31: Bulk IR spectra of 11-azido-undecanethiol and bpp ligand in comparison with the IRRA spectra of 11-azido-undecanethiolate and the click product of 11-azido-undecane-thiolate with the bpp ligand on Au(111).

The functionalization of the salen ligand with a benzyl group and an alkyne for click reaction can be successfully reached in a functionalization reaction of the secondary amine unit (Fig. 32). In different experiments we tried to click this functionalized ligand to an azide terminated SAM with common click reaction conditions. The salen ligand, however, is not stable in the presence of water containing solutions because of the labile imine groups. Different click reaction conditions were carried out. A click reaction in toluene with a Ru(Cl₂)COD catalyst seems to be a potential way to click this labile ligand system to a prefunctionalized SAM. First experiments on this system showed the reduction of the azide stretching vibration band in the IRRA spectrum and new appearing bands in the fingerprint region. If this system can be successfully clicked to an azide terminated SAM, there will be the possibility to change an anionic ligand through an azobenzene as a light switchable unit to realize the

LD-LISC effect in these monolayers (Fig. 34). One option would be the abstraction of an anionic chlorine ligand through silver triflate and coordinating thiocyanate or a neutral ligand like azobenzene with an IR active headgroup to follow the *trans* to *cis* isomerization under irradiation via IRRAS. To detect the LD-LISC effect special surface sensitive techniques like NEXAFS or XMCD can be used. The grafting of dinuclear complexes with azobenzene containing ligands, like the system shown in Figure 33, has been also tried out.

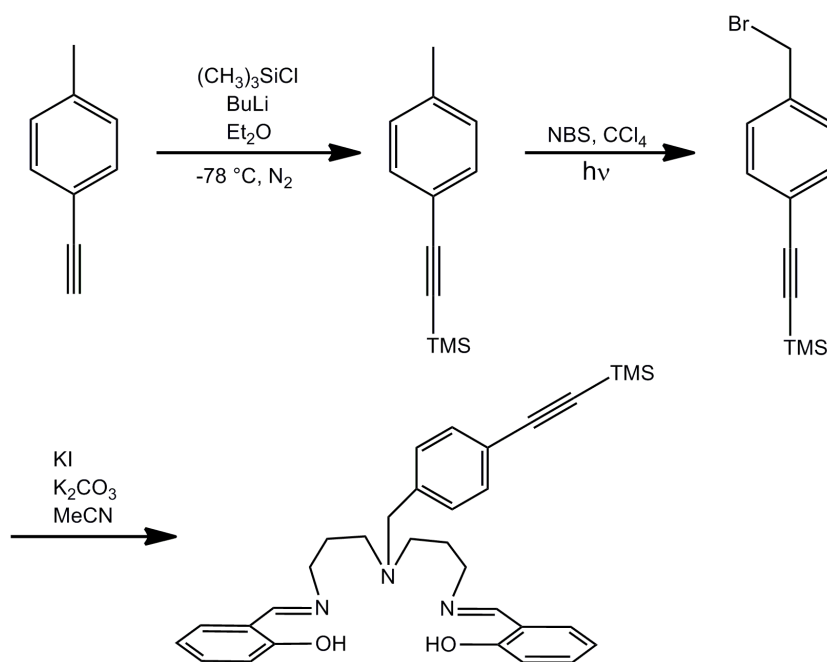


Figure 32: Synthetic route for salten-ligand functionalization with an alkyne for click reactions.

These systems were successfully synthesized and the adsorption of these complexes from solution to Au(111) surfaces were tried out in all available solvents. These huge complexes are completely insoluble in organic solvents and all surface preparations were impossible. A click reaction would be more efficient because of the smaller salten-systems, which lead to a better solubility. The post coordination of metal containing ligands to ligand functionalized SAMs is also well known in literature. Layer by layer can be coordinated to SAMs.^[135,136]

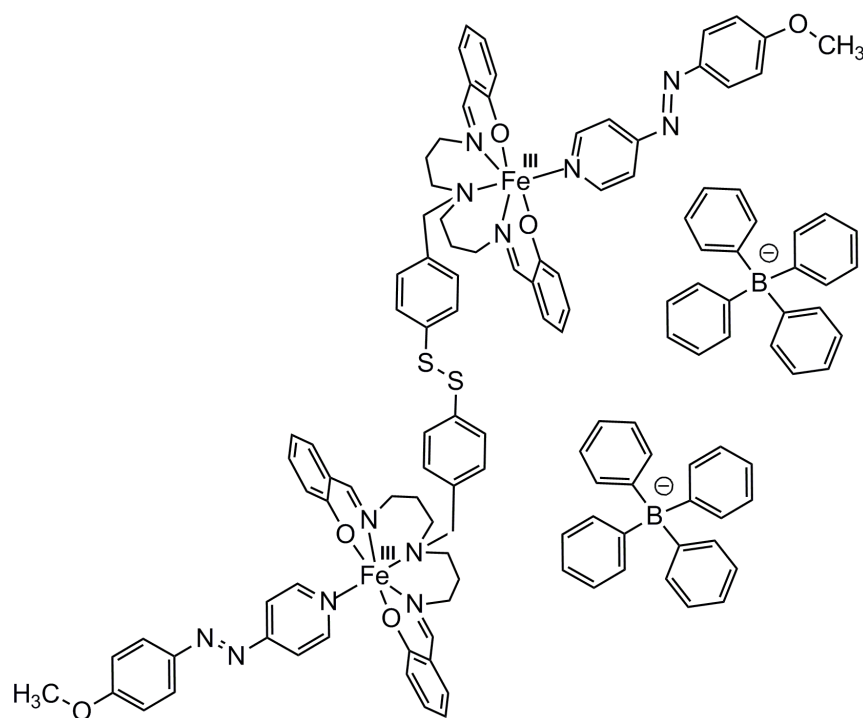


Figure 33: Dinuclear $[\text{Fe}(\text{thiotolylsalten})]_2$ complex with an coordinated azobenzene unit.

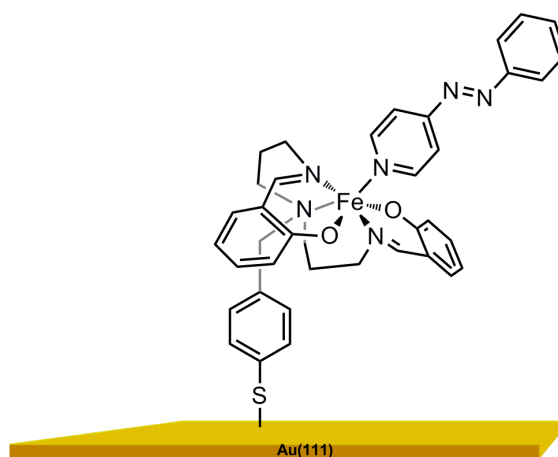


Figure 34: Resulting monomer of $[\text{Fe}(\text{thiotolylsalten})\text{azopyridine}]$ on the surface.

Moreover, the functionalization of triazatriangulenium (TATA) derivatives with an alkyne-functionalized salten ligand could lead to a new system for surface functionalization (Fig. 35). In these systems the molecules are more separated from each other and offer the possibility to coordinate switchable units. In this systems the switchable units obtain more sterical freedom for the isomerization process.

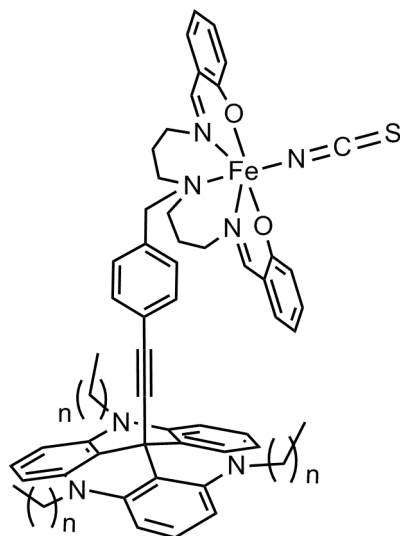


Figure 35: [Fe(III)(ethynyltolylsalten)(NCS)] functionalized TATA platform.

Furthermore, Fe(III)TMTAA (tetramethyltetraazaannulene) complexes with azobenzene functionalized molecules were synthesized and characterized regarding their switching behavior in solution (Fig. 36). These systems did not show adequate switching efficiency. The best result was obtained with the [Fe(III)(TMTAA)Cl(1-methyl-5-(4'-methoxyphenylazo)-imidazole)].^[137]

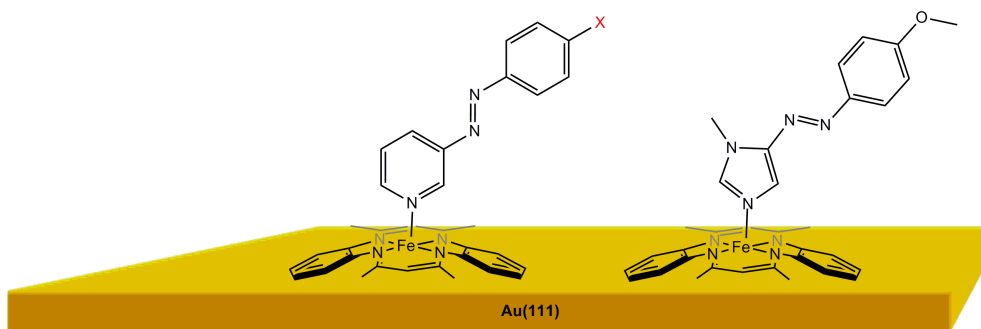


Figure 36: TMTAA molecules with different switchable units for IRRAS investigations.

These molecules were deposited from solution to Au(111) surfaces and vibrational information were obtained using IRRAS. DFT calculations were performed and compared with observed frequency bands. These molecules are potential light switchable monolayers. Switching experiments have been performed but did not lead to visible changes in the spectra yet.

3 Functionalization of Au(111) surfaces with dinuclear complexes

3.1 Chemical wires

Chemical wires have an analog functionality compared to a convention wire. The function of a wire is to conduct electric charge from one place connected to another. A fundamental question is the understanding of the transport of charge through a single molecule.^[138-140]

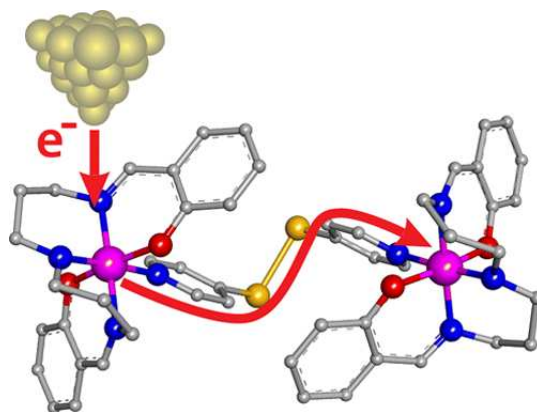


Figure 37: Schematic view of a chemical wire.

To understand this transport phenomenon, different chemical wires with different lengths were connected to an electrode and measured.^[141] Different chemical wires are known in literature. Well known systems are polyenes, polypyrroles, dendrimers, polythiophenes and nanotubes. These systems can offer interesting applications in optoelectronic components like displays, sensors or semiconducting materials.^[142]

Conjugated organic polymers have found applications today; in light emitting diodes, thin film field-effect transistors and photovoltaic cells.^[143-149] An example of this are huge molecules with conjugated double bonds and delocalized π -electron systems which make the charge transport possible. The embedding of these chemical wires in mesoporous materials can be achieved through direct embedding of the synthesized polymer and also through direct

polymerization in the cavities.^[150,151]

Different mechanisms for this charge transport can be responsible for tunnel mechanisms between the highest occupied molecular orbital (HOMO) and the lowest unoccupied molecular orbital (LUMO) or hopping-mechanism. The discovery of the metallic conductivity of polysulfurnitride (SN)_n in the 1960s also raised the interest of scientists to find applications for chemical wires.^[152]

3.2 Motivation

Transition metal complexes can show interesting behavior on surfaces. Spin state switching of molecules on surface can lead to interesting applications such as data storage devices or sensors.

In our first step to find a suitable way to adsorb and bind transition metal complexes to metal surfaces, we investigated the physisorbed mononuclear complex $[\text{Fe}(\text{salten})\text{Cl}]$ with the help of IRRAS, XPS and STM on Au(111).

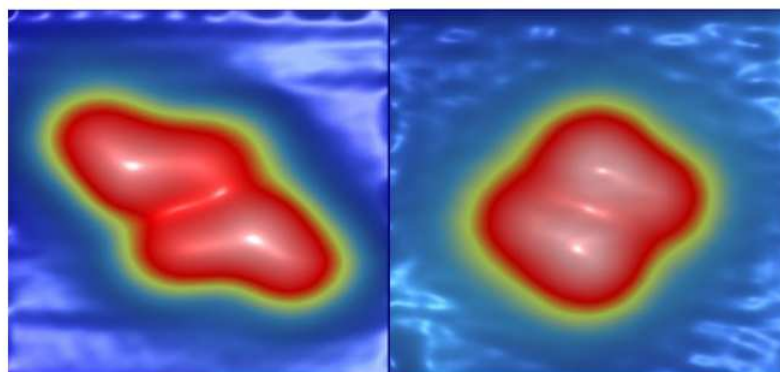


Figure 38: STM pictures of different types of $[\text{Fe}(\text{salten})\text{Cl}]$ dimers on Au(111).

The formation of dimers leads to the motivation to investigate a possible coupling between the two iron metal centers. For this reason, we investigated the dinuclear complex $[\text{Fe}(\text{salten})(\text{pyS})]_2^{2+}$ on a Au(111) surface (Fig. 39). Dinuclear complexes can have special interesting behavior on surface. The magnetic intramolecular coupling between the two iron(III) centers has been investigated using low temperature STM on a Au(111) surface.

The main goal of this project was to synthesize a dinuclear iron complex which can be used as a chemical wire on surface. Electrospray deposition can be used to deposit huge molecules with high molecular weights and counter-ions. These can be removed and complexes with charge can be deposited.

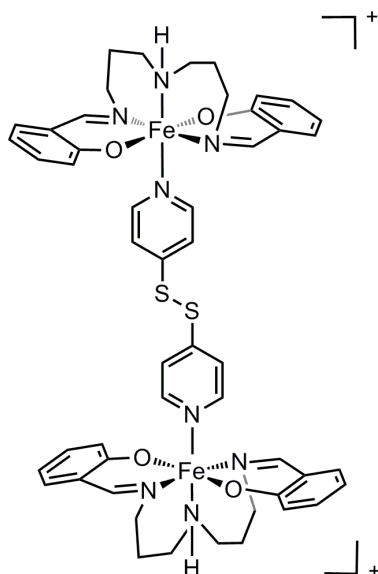


Figure 39: Dinuclear $[\text{Fe}(\text{salten})(\text{pyS})]_2^{2+}$ complex with two iron(III) central atoms for STM investigations.

Expecting no charge conductance, the reference system $[\text{Fe}(\text{salten})(\text{dimethylpy})]_2^{2+}$ complex with an isolating ethyl bridge, was synthesized.

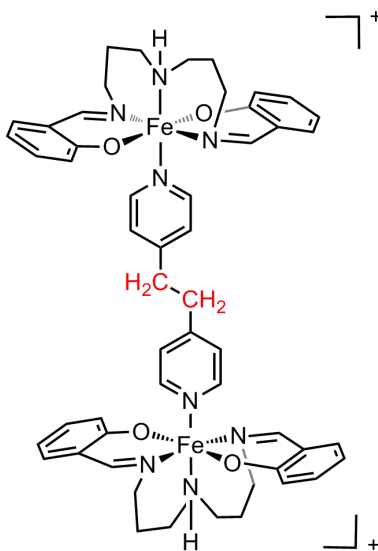


Figure 40: Dinuclear $[\text{Fe}(\text{salten})(\text{dimethylepy})]_2^{2+}$ complex with two iron(III) central atoms for STM investigations as isolating reference molecule.

Publication in
Journal of the American Chemical Society

3.3 Remotely triggered geometrical isomerization of a binuclear complex

S.Karan, T. Gopakumar, H. Jacob, S. Meyer, F. Tucek* and R. Berndt*

J. Am. Chem. Soc. **2014**, 136, 6163-6166.

DOI: 10.1021/ja500154g.

Remotely Triggered Geometrical Isomerization of a Binuclear Complex

Sujoy Karan,[†] Thiruvancheril G. Gopakumar,[‡] Hanne Jacob,[¶] Sven Meyer,[¶] Felix Tuczek,^{*,¶} and Richard Berndt^{*,†}

[†]Institut für Experimentelle und Angewandte Physik, Christian-Albrechts-Universität zu Kiel, 24098 Kiel, Germany

[‡]Department of Chemistry, Indian Institute of Technology Kanpur, Kanpur 208016, India

[¶]Institut für Anorganische Chemie, Christian-Albrechts-Universität zu Kiel, 24098 Kiel, Germany

Supporting Information

ABSTRACT: Binuclear organometallic molecules are model systems for investigating intramolecular spin-coupling and charge-transfer processes. Using electrospray ionization, Fe(salten) dimers linked by dipyridyl disulfide are deposited on gold for probing with a low-temperature scanning tunneling microscope. Each monomer constitutes a multistable switch owing to its geometric isomerism. Controlled and reversible remote switching within a single dimer is demonstrated. The process is attributed to intramolecular electron transfer.

One approach to molecule-based functional devices relies on switches on surfaces. Switching in molecular layers has been achieved using stimuli like light, temperature, and electric fields.^{1–8} Upon injecting current with a scanning tunneling microscope (STM), changes of molecular conformation, spin, and adsorption state have been observed.^{9–15}

Usually the current-induced changes occur directly under the STM tip.¹⁶ For molecule-based logic, however, a lateral energy transfer appears to be necessary. Few examples—controlled molecular hopping¹⁷ and tautomerization propagating over an intervening molecule¹⁸—have been reported from custom-made molecular arrays. Implementing a pathway for energy transfer within a single molecule by chemical synthesis is a desirable alternative to on-surface preparation with a STM.

Here we demonstrate controlled and reversible remote switching within a single binuclear organometallic molecule. By injecting current to one subunit, a reversible isomerization of the other via a Bailar twist¹⁹ is induced. The choice of the linker between the subunits is seen to be crucial for electron transfer comparing results from electron-rich disulfides and less conducting ethyl chains.

As a switch we synthesized the binuclear compound [Fe(salten)pyS]₂ (Figure 1a).²⁰ It is composed of two iron(III) bis(3-salicylideneaminopropyl)amine (Fe-salten) subunits that are coupled via a dipyridyl disulfide (pySSpy) linker. To enable single-molecule experiments in ultrahigh vacuum and at low temperature (~5 K), we used electrospray ionization for deposition of molecules onto Au(111).²¹

The geometry of pseudo-octahedral [Fe(salten)L] complexes depends on the coligand L. Strong or bulky ligands, e.g., pyridine or pyridine derivatives, lead to a *trans* geometry

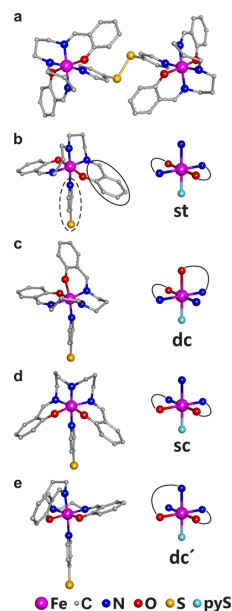


Figure 1. Structures of [Fe(salten)pyS]₂ dimer and monomers. H atoms are not shown. (a) Calculated structure of [Fe(salten)pyS]₂. (b–e) Geometrical isomers of the (thiopyridine)-Fe(salten) subunit: (b) symmetric *trans* (st), (c) dissymmetric *cis* (dc), (d) symmetric *cis* (sc), and (e) second dissymmetric *cis* (dc'). Solid and dotted ellipses indicate phenolate and the coligand L = pyridine thiolate, respectively. The molecular structures in the left panel are represented by simplified symbols of the quasi-octahedral cores on the right. Arches indicate the positions of phenolate rings.

(Figure 1b).²² Weaker ligands favor a *cis* configuration (Figure 1c).²³ While the *cis* configuration is dissymmetric, the *trans* configuration exhibits a C₂ axis. Besides these geometries, which have been observed in crystals before,^{22,23} two additional configurations are conceivable, namely a symmetric *cis* configuration with a mirror plane (Figure 1d), and a second dissymmetric configuration with both phenolate groups *cis* to

Received: January 10, 2014

Published: April 14, 2014

the axial ligand (Figure 1e). Below we use the naming scheme st, dc, sc, and dc' introduced in Figure 1. The dimer of Figure 1a with two st subunits is accordingly denoted st-st. Our calculations (see Computational Methods in the Supporting Information for details) show that with L = pyridine thiolate, the st and dc isomers are most stable (see Table S1). The energies of dc' and sc are higher by ~ 0.5 and 0.9 eV, respectively, in agreement with the fact that dc and st are experimentally observed²² whereas dc' and sc are hypothetical.

After deposition of sub-monolayer amounts of [Fe(salten)-pyS]₂ onto Au(111), STM images reveal three closely related dimeric patterns (Figure 2). They may be divided in halves

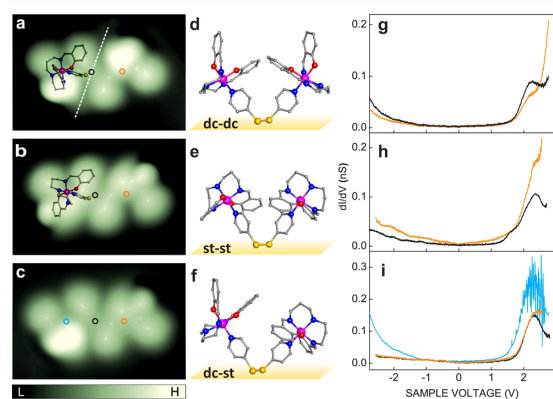


Figure 2. (a–c) STM images (3.5×2.4 nm²) of three distinct structures of [Fe(salten)pyS]₂ on Au(111). The data are displayed in a pseudo-three-dimensional fashion with the color scale covering a range of 0.21 nm. Images (in all the figures) were acquired with sample voltages $V = 0.20$ – 0.25 V at constant currents $I = 10$ – 50 pA. A dotted line in (a) separates the two subunits of the binuclear molecule. Colored circles indicate the positions where dI/dV spectroscopy was performed. In (a) and (b), top views of models of dc and st monomers are overlaid on one half. (d–f) Side views of [Fe(salten)pyS]₂ comprising different isomers. (g–i) dI/dV spectra recorded at the positions indicated in a–c. Before opening the current feedback, the STM was operated at $V = 2.7$ V and $I = 100$ pA.

(dotted line in Figure 2a) that exhibit either three (Figure 2a) or three major and one minor (Figure 2b) lobes. Two patterns are composed of identical halves (Figure 2a,b), and the third one (Figure 2c) is a combination thereof. The submolecular contrasts may be understood on the basis of the structures of dimers (Figure 2d–f) comprising combinations of the isomers shown in Figure 1. The molecules are assumed to adsorb with the disulfide linker attached to the substrate. The molecule of Figure 2a is a symmetric dc-dc dimer. Its highest lobes appear to originate from the phenolate ligand. The pattern of Figure 2b is consistent with a st-st dimer (Figure 2e) where the phenolate ligands are located at heights similar to that Fe, with a propyl chain (C3 linkage) above one of them. The propyl chain is likely causing the extra lobe in the image. Finally, the asymmetric species of Figure 2c combines the dc and st subunits and is denoted dc-st. The abundances of st-st, dc-st, and dc-dc dimers determined from large-scale images ($\sim 40\%$, 35% , and 25% , respectively) are consistent with the calculated sequence of energies (Table S1). A dc configuration of a subunit of the adsorbed [Fe(salten)pyS]₂ seems to be at conflict with the st configuration reported for bulk materials. However, infrared reflection absorption spectra indicate that on

Au(111) a dc configuration is also possible,²⁰ which is consistent with our STM observations.

Spectra of the differential conductance dI/dV of the three species (Figure 2g–i) were acquired at the positions marked in the STM images. With the tip above the disulfide moiety, all species show a prominent unoccupied electronic state at ~ 2.35 V (black lines). Indication of this resonance is also discernible closer to the centers of the individual subunits (orange lines). The similarity of the spectra of all species lends support to the geometric interpretation of the STM images in Figure 2a–c.

dc-st molecules display a striking anomaly when the tip is placed over the center of the dc subunit (blue circle and line in Figure 2c,i). Fluctuations occur at sample voltages exceeding ~ 1.5 V, which signal rapid changes of the tunneling junction. Figure 3b presents the result of current injection to the dc

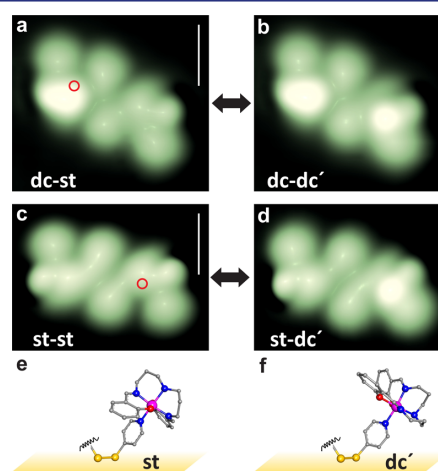


Figure 3. Reversible isomerization of dc-st and st-st molecules. STM images recorded (a,c) before and (b,d) after injecting current at 1.6 V at the positions marked by red circles in a and c. Scale bars correspond to 1 nm. (e,f) Side views of st and dc' subunits, respectively.

subunit of the dc-st dimer shown in Figure 3a. The st subunit has switched to a new state with a bright protrusion at its center. We attribute it to the dc' isomer of Figure 1e, where the phenolate ligand with its conjugated π system is located above the Fe center (Figure 3f).

The manipulated monomer is located ~ 1 nm away from the point of current injection; i.e., the switching occurs remotely. The process is fully reversible. By injecting another current pulse on the dc side, the original dc-st state is restored. Remarkably, the dc unit itself does not switch to any other configuration so long as nondestructive currents and voltages are used.

On st-st dimers (Figure 3c) a transformation to st-dc' was occasionally found (Figure 3d). However, the switching took place locally, i.e., at the st subunit to which the current was injected. st-dc dimers behaved similarly (reversible, local switching to dc'-dc).

We suggest that the isomerization between st and dc' is effected by a Bailar twist,¹⁹ whereby two opposite triangular faces of the octahedral coordination shell rotate by 120° with respect to each other. Figure 4 shows the transformation of a dc' isomer to st via a twist of the upper triangle, while the lower one is fixed to the substrate. It involves only one flexible C3

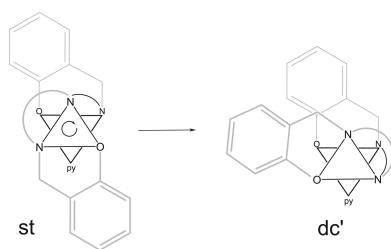


Figure 4. Isomerization of st to dc' via a Bailar twist. Two opposite triangular faces of the octahedral coordination shell of [Fe(salten)pyS] are displayed with black lines. C3 linkages are indicated by arches, and C–N double bonds are omitted. In the Bailar twist transforming the st isomer to dc', the upper triangle rotates clockwise by 120° with respect to the lower one, which is fixed to the substrate by the pyridine disulfide linker. Further rotation is sterically inhibited.

linkage, while all other metal–ligand bonds remain fixed. It may be reversed, but the ligands do not allow for further rotation. Consequently, the st subunit represents a two-state configurational switch. The absence of any switching from dc subunits can also be understood on the basis of this mechanism (see Figure S1). A twist from dc to dc' would involve a propylene and an iminophenol bridge. The conjugated π system of the latter is more rigid and thus suppresses this twist. Another conceivable twist involving only a flexible C3 linkage leads to the unfavorable (*vide supra*) sc configuration. This explains why remote switching is found only when injecting electrons into the dc part of dc-st dimers (or the resulting dc-dc' dimers) and not on st-st dimers. dc cannot be switched and thus serves as a relay to transfer the excitation energy to the other subunit, while st uses the energy itself to convert to dc'.

The mechanism of the remote switching is of particular interest. Remote switching on dc-st and only local switching on st-st are difficult to reconcile with a force-related mechanism. Moreover, the threshold voltage of ~ 1.5 V, which is close to the onset of the unoccupied molecular resonance, and the absence of switching at reversed polarity favor an electron-induced process.

The different total energies of the dimers (Table S1) are essentially due to the different energies of their subunits rather than their mutual interaction. This means that a sufficient fraction of the excitation energy has to be transferred from the dc to the st subunit to achieve isomerization to dc'.

The injection of an electron to the dc subunit locally creates an electronically and possibly vibrationally excited state. To discriminate between vibrational and electronic energy-transfer mechanisms, a dimer linked by a less electron-rich dipyriddyethane moiety was synthesized. Using deposition conditions similar to those used before, $\sim 60\%$ st-st and $\sim 40\%$ dc-st dimers were observed (see Figure S2a), which appear very similar to the disulfide-linked molecules. Switching experiments on dipyriddyethane-linked dimers, however, led to strikingly different results. On the dc-st species, remote switching was never observed. Occasionally, we found local interconversion between st and dc' when tunneling directly into these subunits (Figure S2b,c).

The results from the dipyriddyethane-linked dimers allow for the following conclusions. First, through-space tunneling from the excited dc subunit to the st part is not relevant for switching. The absence of remote switching of sulfide-linked st-st molecules is also in line with this interpretation. Next,

vibrational energy transfer may tentatively be excluded. The energies of the S–S stretching and bending modes are lower than the energies of the modes of the Fe(salten) monomers. This, along with the bonding of the S atoms to Au, is expected to make vibrational energy transfer over the S–S linker rather inefficient. The fact that the dipyriddyethane bridge does not enable remote switching despite its different vibrational modes does not favor vibrational energy transfer. This leaves electron transfer through the disulfide bridge, possibly involving the S–Au bonds, as the most likely scenario. Our calculations for sulfide-linked dimers indeed show that the lowest unoccupied molecular orbital exhibits a high electron density at the disulfide bridge and overlaps with the Fe(salten) subunits (see Figure S3). With a dipyriddyethane bridge, this orbital is localized to the separate subunits and hardly overlaps via the ethyl chain (Figure S3).

In conclusion, a custom-made binuclear Fe(salten) complex on Au exhibits geometrical isomerism of the individual subunits. Reversible switching between two isomers has been achieved within single molecules. A disulfide bridge connecting the molecular subunits enables remote switching, whereas an ethyl link is inactive. It is conceivable that our approach may be extended to implement basic logic functions within a single molecule.

■ ASSOCIATED CONTENT

📄 Supporting Information

Experimental details; computational methods; calculated total energy differences for [Fe(salten)pyS] and [Fe(salten)pyS]₂; Bailar twists not observed in the experiments; STM data from dipyriddyethane-linked dimers; calculated orbital energies of [Fe(salten)pyS]₂ and [Fe(salten)pyCH₂]₂; oxidation state of Fe centers. This material is available free of charge via the Internet at <http://pubs.acs.org>.

■ AUTHOR INFORMATION

Corresponding Authors

ftuczek@ac.uni-kiel.de

rbe@email.uni-kiel.de

Notes

The authors declare no competing financial interest.

■ ACKNOWLEDGMENTS

We thank the Deutsche Forschungsgemeinschaft for support via SFB 677.

■ REFERENCES

- (1) Weigelt, S.; Busse, C.; Petersen, L.; Rauls, E.; Hammer, B.; Gothelf, K. V.; Besenbacher, F.; Linderoth, T. R. *Nat. Mater.* **2006**, *5*, 112.
- (2) Alemani, M.; Peters, M. V.; Hecht, S.; Rieder, K.-H.; Moresco, F.; Grill, L. *J. Am. Chem. Soc.* **2006**, *128*, 14446.
- (3) Gopakumar, T. G.; Müller, F.; Hietschold, M. *J. Phys. Chem. B* **2006**, *110*, 6051.
- (4) Pace, G.; Ferri, V.; Grave, C.; Elbing, M.; von Hänisch, C.; Zhamikov, M.; Mayor, M.; Rampi, M. A.; Samori, P. *Proc. Natl. Acad. Sci. U.S.A.* **2007**, *104*, 9937.
- (5) Kumar, A. S.; Ye, T.; Takami, T.; Yu, B.-C.; Flatt, A. K.; Tour, J. M.; Weiss, P. S. *Nano Lett.* **2008**, *8*, 1644.
- (6) van der Molen, S. J.; Liao, J.; Kudernac, T.; Agustsson, J. S.; Bernard, L.; Calame, M.; van Wees, B. J.; Feringa, B. L.; Schönenberger, C. *Nano Lett.* **2009**, *9*, 76.
- (7) Saedi, A.; van Houselt, A.; van Gastel, R.; Poelsema, B.; Zandvliet, H. J. W. *Nano Lett.* **2009**, *9*, 1733.

(8) Comstock, M. J.; Strubbe, D. A.; Berbil-Bautista, L.; Levy, N.; Cho, J.; Poulsen, D.; Fréchet, J. M. J.; Louie, S. G.; Crommie, M. F. *Phys. Rev. Lett.* **2010**, *104*, 178301.

(9) Morgenstern, K. *Prog. Surf. Sci.* **2011**, *86*, 115.

(10) Lastapis, M.; Martin, M.; Riedel, D.; Hellner, L.; Comtet, G.; Dujardin, G. *Science* **2005**, *308*, 1000.

(11) Choi, B.-Y.; Kahng, S.-J.; Kim, S.; Kim, H.; Kim, H. W.; Song, Y. J.; Ihm, J.; Kuk, Y. *Phys. Rev. Lett.* **2006**, *96*, 156106.

(12) Wintjes, N.; Bonifazi, D.; Cheng, F.; Kiebele, A.; Stöhr, M.; Jung, Th.; Spillmann, H.; Diederich, F. *Angew. Chem.* **2007**, *119*, 4167.

(13) Wang, Y. F.; Kröger, J.; Berndt, R.; Hofer, W. A. *J. Am. Chem. Soc.* **2009**, *131*, 3639.

(14) Gopakumar, T. G.; Matino, F.; Naggert, H.; Bannwarth, A.; Tuzcek, F.; Berndt, R. *Angew. Chem., Int. Ed.* **2012**, *51*, 6262.

(15) Miyamachi, T.; Gruber, M.; Davesne, V.; Bowen, M.; Boukari, S.; Joly, L.; Scheurer, F.; Rogez, G.; Yamada, T. K.; Ohresser, P.; Beaurepaire, E.; Wulfhekel, W. *Nat. Commun.* **2012**, *3*, 938.

(16) Electron-induced remote switching via electronic surface states has been reported: Maksymovych, P.; Dougherty, D. B.; Zhu, X.-Y.; Yates, J. T., Jr. *Phys. Rev. Lett.* **2007**, *99*, 016101. Also see ref 14. Electric-field-induced changes over nanometer distances have been reported in, e.g., ref 2. However, single molecules were not addressed.

(17) Heinrich, A. J.; Lutz, C. P.; Gupta, J. A.; Eigler, D. M. *Science* **2002**, *298*, 1381.

(18) Liljeroth, P.; Repp, J.; Meyer, G. *Science* **2007**, *317*, 1203.

(19) Kepert, D. L. *Prog. Inorg. Chem.* **1977**, *23*, 1.

(20) Jacob, H.; Kathirvel, K.; Petersen, F.; Strunskus, T.; Bannwarth, A.; Meyer, S.; Tuzcek, F. *Langmuir* **2013**, *29*, 8534.

(21) Hamann, C.; Woltmann, R.; Hong, I.-P.; Hauptmann, N.; Karan, S.; Berndt, R. *Rev. Sci. Instrum.* **2011**, *82*, 033903.

(22) Matsumoto, N.; Ohta, S.; Yoshimura, C.; Ohyoshi, A.; Kohata, S.; Okawa, H.; Maeda, Y. *J. Chem. Soc., Dalton Trans.* **1985**, 2575.

(23) Mayer, C. R.; Cucchiaro, G.; Jullien, J.; Dumur, F.; Marrot, J.; Dumas, E.; Sécheresse, F. *Eur. J. Inorg. Chem.* **2008**, 3614.

3.4 Conclusion

Controlled and reversible switching of a single dinuclear $[\text{Fe}(\text{salten})(\text{pyS})]_2^{2+}$ molecule was presented using STM. The switching process is attributed to an electron transfer through the dipyridinedisulfide linker between the two iron(III) centers. By injecting electrons with the STM tip into one subunit of the molecule, a geometric isomerization of the other subunit can be observed. The linkage pyridinedisulfide bridge is a conjugated electron rich system and can conduct the injected electrons through the molecule.

An electron poor system, a dipyridine with an ethyl chain, was also investigated. This system does not show the reversible switching. The synthesized complexes were deposited by electrospray ionization in UHV at around 5 K onto an Au(111) single crystal. From bulk characterization it is known that the geometry of this pseudo-octahedral $[\text{Fe}(\text{salten})\text{X}]$ complex depends on the coligand X. If a strong or sterically demanding ligand is coordinated to the iron center, the complex will tend to adopt a *trans* geometry regarding the imine groups while weaker and smaller ligands favor a *cis* geometry. These two configurations were observed in bulk crystal material.

Moreover, two different additional configurations are possible; a symmetric *cis* which exhibits a mirror plane and a dissymmetric configuration where the two phenolate groups are oriented *cis* to the axial ligand. Three different configurations of dimers were found on the surface in different percentages which are consistent with the calculated sequences of energies. A dc-dc, st-st and dc-st dimer. A dc configuration was not observed from bulk material, but as published in *Langmuir*, we showed that a dc configuration on surface is possible for this complex. This behavior in the STM images supports our explanation of the anomaly in the obtained IRRA spectra. Only the dc-st and st-st dimer can be reversibly switched by injecting a current of 1.6 eV. This remote switching process is effected by the Bailar twist.

Coordination compounds can exist in different enantiomers when they belong to a chiral

point group. Different mechanisms for ligand exchange are known. This process can be dissociative and non-dissociative. For example, in trigonal pyramidal coordinated compounds (coordination number 5), a Berry Pseudorotation can take place. For octahedrally coordinated compounds, a Ray-Dutt twist and a Bailar twist are known racemization mechanisms. These mechanisms are very similar and have been studied in detail in theoretical and experimental studies. [153,154]

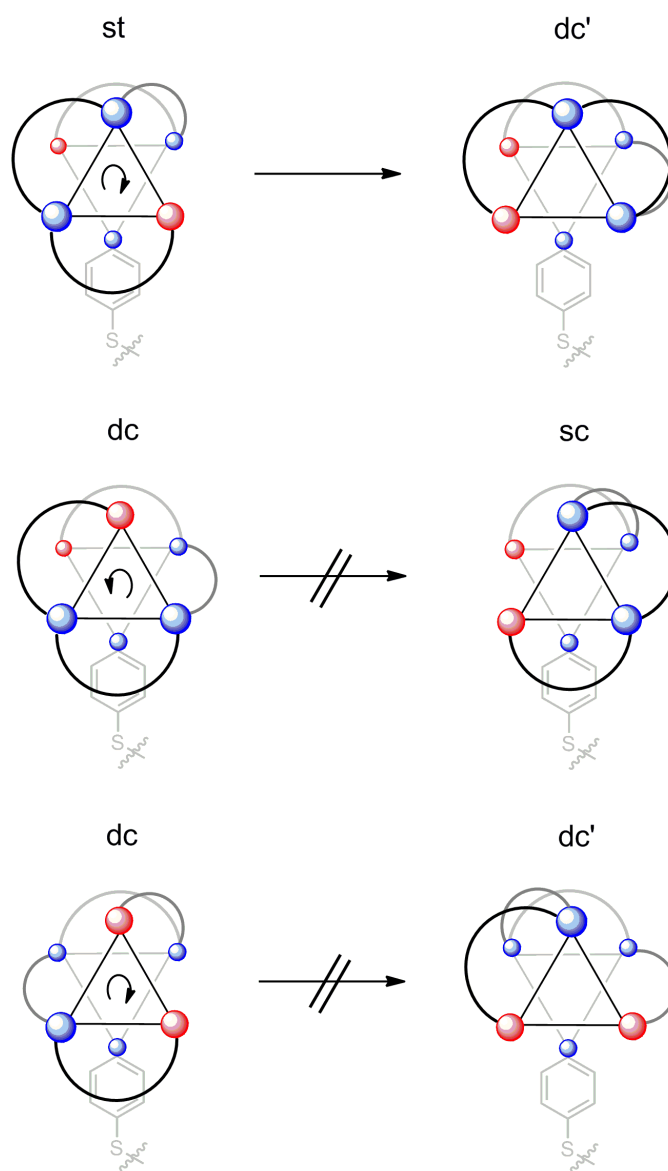


Figure 41: Schematic figure of the observed Bailar-twist in the salten ligand system. Nitrogen atoms are shown as blue balls and oxygen atoms as red balls.

The Bailar twist can be explained as a trigonal geometrical isomerization of the coordinated ligands to a metal center. This process is non-dissociative. The Bailar twist involves a 120° rotation of a trigonal face of the octahedron to the opposite trigonal face. Compared to the Ray Dutt twist, that involves a rotation of an imaginary C_3 axis, the Bailar twist contains a rotation of a C_3 axis. This twist can be observed by injecting electrons with the STM tip into a st conformation of the salen system. The st conformation changes to a dc' conformation. The twist from a dc conformation to a sc or dc' conformation is not observed in the experiments. A change from the dc to a dc' conformation would involve a twist around the rigid imine bridge. Furthermore the change from the dc to a sc' conformation is too high in energy and was determined by DFT calculations.

In summary, this publication shows a new controlled and reversible switching concept of a dinuclear iron(III) complex.

3.5 Outlook

In further projects with the Department of Applied Physics, Christian-Albrechts-University of Kiel, new chemical wires shall be synthesized and tested with STM for the switching and electron transport behaviors. These new molecules were designed as shown in Fig. 42.

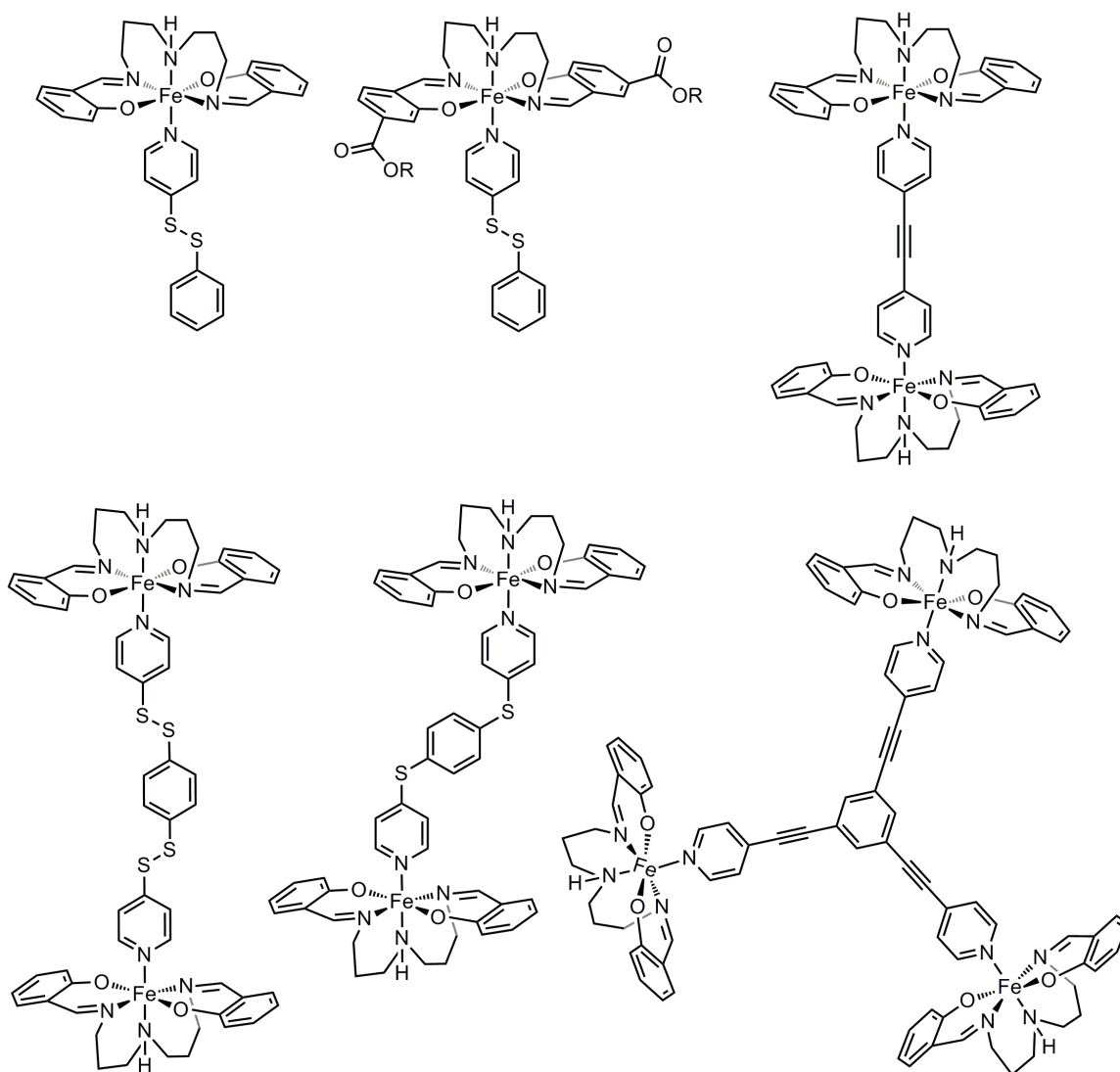


Figure 42: Iron(III)-salten complexes with different pyridine containing linkers for STM investigations.

These new molecules have a similar salten-ligand system and iron(III) as a metal center. The linkage molecule will be modified through different conjugated linker. In order to understand these geometrical tip-induced isomerization processes, dinuclear (dyads) and trinuclear (tri-

ads) iron (III) complexes with different elemental compositions shall be measured. Disulfide, sulphur as well as azobenzene containing linkers are possible. The linker molecules can vary in length and composition to increase and decrease the distance between the "input" and "output".

Furthermore, other substrates like Au(110) and Cu₂N on Cu(100) shall be tested because they have no surface state near the Fermi level. Regarding the transport of the excitation energy, the role of the metal surface and the Au-S bond is still not fully understood.

Moreover, another spin crossover compound [Fe(pap)₂]ClO₄ (pap=N-2-pyridyl-methyldene-2 hydroxyphenylamino) was synthesized for STM measurements in cooperation with Sujoy Karan and Torben Jasper-Tönnies (working group of Prof. Berndt, Institute of Applied Physics, Christian-Albrechts-University of Kiel).

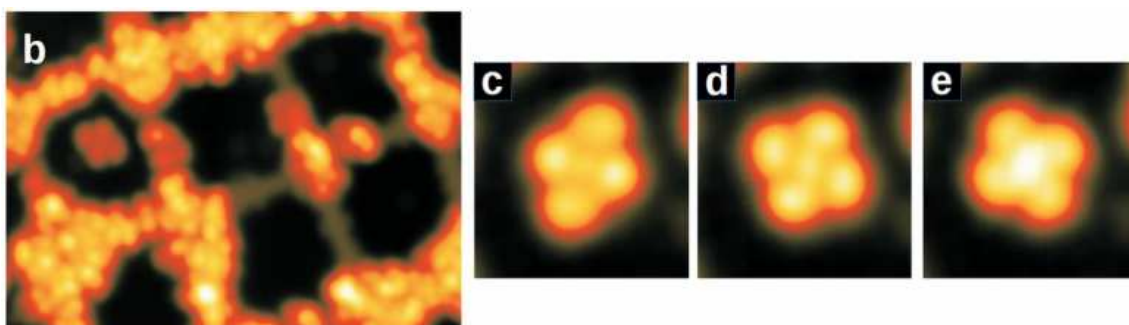


Figure 43: [Fe(pap)₂]⁺ on Cu₂N.

These molecules were successfully deposited on Au(111) and Cu₂N surfaces and investigated at cryogenic temperatures in UHV. The [Fe(pap)₂]ClO₄ was successfully deposited with ESI and can be also evaporated without destroying by chemical vapor deposition. On Au(111), the molecules are still intact on the surface but release their ClO₄⁻ counter ions. Unfortunately, these counter ions are mobile on the surface and lead to disturbing noise of the tunneling current. Furthermore, measurements on Cu(100) were performed. On this substrate, the mobility of the counter ions was suppressed. On Cu(100), no switching behavior of [Fe(pap)₂]⁺ molecules could be observed. To decouple the molecules electronically from the surface, Cu₂N monolayers were used as the surface. In this case, single molecules of

$[\text{Fe}(\text{pap})_2]^+$ were resolved. Current injection with the STM tip leads to 3 different separated states with different shapes in the images. These states can be interpreted as a conformational changes of the ligand system and perhaps as a spin change. To understand these systems in more detail, the paramagnetic $[\text{Ni}(\text{pap})_2]$ and the diamagnetic $[\text{Co}(\text{pap})_2]\text{ClO}_4$ were synthesized and are a subject of current research (Fig. 44).

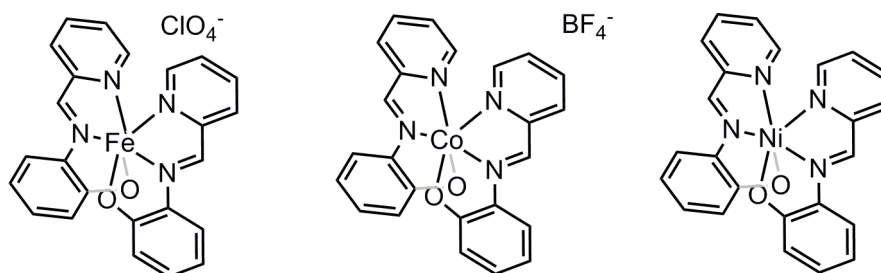


Figure 44: Pap-containing molecules for STM measurements.

The explanation of these results and a manuscript for publication is currently in progress.

4 Characterization of switchable azobenzene functionalized Triazatriangulene platforms (TATA)

4.1 Switchable Surfaces

Surfaces with tailored properties are helpful for a lot of applications like self-cleaning surfaces, corrosion protection and optical devices. In literature, several examples of switchable surfaces and materials are known. For example, the Ikeda polymer which acts as a small molecular motor through the isomerization process of the embedded switchable molecules in a polymer.^[35] The big challenge in building switchable surfaces is the arrangement of the molecules on the surface. By using azobenzene containing self assembled monolayers with alkyl chains, the sterical freedom of the molecules has to be big enough for the geometric conformation change. In densely packed monolayers the azobenzene moieties are sterically hindered in the isomerization process.^[155-157] In only several cases, photoswitching of azobenzene containing thiolate bounded self-assembled monolayers can show switching behavior. The formation of mixed SAMs with diluter molecules leads to more space and freedom for the azobenzene molecules. The construction of molecules with huge spacer groups also can help to realize more freedom for the molecules. Tegeder *et al.* published a thiol functionalized tripodal adamantane derivative with an azobenzene switchable unit, perpendicular to the surface. This system can be reversibly switched in the monomer as well as in SAMs formed on a substrate.^[157-159]

To obtain well ordered and arranged SAMs on surfaces, new concepts for the deposition are needed. The construction of tripodale and functionalized surface binding ligand system can lead to more efficient switchable surfaces.

4.2 Motivation

In the last years, the "bottom-up" approach has become more and more famous and promises a lot of practical innovations. To be based on atoms and molecules, molecular machines, molecular motors and molecular storage devices can be built up gradually. In literature, a lot of synthetic molecular shuttles, rotors and machines which are partly imitations of natural phenomena are known.^[160-172]

The attempt to miniaturize data storage devices is relevant to many fields of industry.



Figure 45: SEM picture of a ciliated epithelium in a human lung.^[173]

A ciliated epithelium is a layer of epithelial cells which can be found in the respiratory passages and has a cleaning function. Cilia are versatile and make up the main component of the ciliated epithelium (Fig. 45). They are able to transport mucus and unwanted substances from our lungs.

The so called 'platform-approach' was published from Kubitschke *et al.* in 2009. This 'platform approach' can be used to realize a synthetic molecular cilia adsorbed on a surface to mimic a fascinating natural phenomenon and to reach a directional transport of particles on a surface.^[174]

Moreover, these systems are reversible molecular switches for potential storage devices.

This concept achieves a completely new concept to realize monomolecular adlayers on metal surfaces.

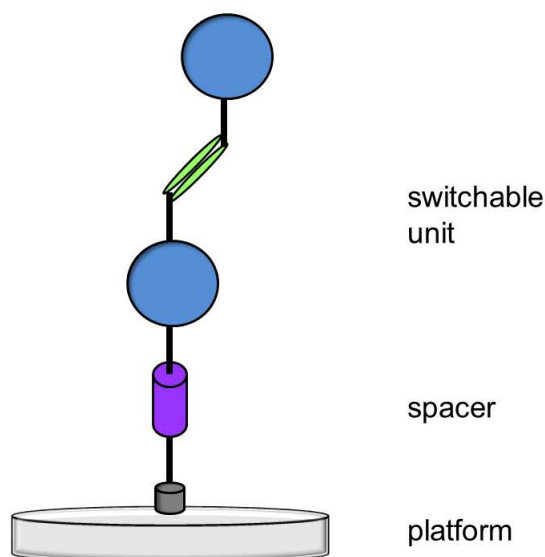


Figure 46: Schematic view of the platform approach.

For this approach, flat platform molecules will be used and a molecular switch can be connected to a reactive center on this platform. In contrast to alkanethiol SAMs, this approach offers more sterical freedom for the switching process. Side chains of the platform are variable in length in order to adjust the space of the molecules on surface to each other. The molecular platform is connected to a rotatable spacer, an alkyne group, which is linked to an isomerizable functionalized molecule.

Laursen and Krebs published a synthesis of triazatriangulenum salts in 2000 and Kubitschke *et al.* the functionalization of these molecules with azobenzene containing switching units perpendicular to the "platform".^[175,176] STM measurements show the formation of well ordered monolayers of these molecules on gold surfaces with different lattice constants by varying the alkyl chains connected to the platform.^[177]

These molecules were characterized in detail in their switching behavior in solution as well as adsorbed on surfaces. A lot of spectroscopic techniques were used to understand these molecules on surfaces in detail.^[178-184]

The main goal of this project is the detection of the azobenzene unit on the platform with IRRAS. Due to the surface selection rule, the vibrations of the azobenzene unit perpendicular to the surface can be observed in the IRRA spectrum. A lot of different functionalized TATA platforms were measured with IRRAS but did not lead to a clear significant observation of the azobenzene unit (Fig. 47).

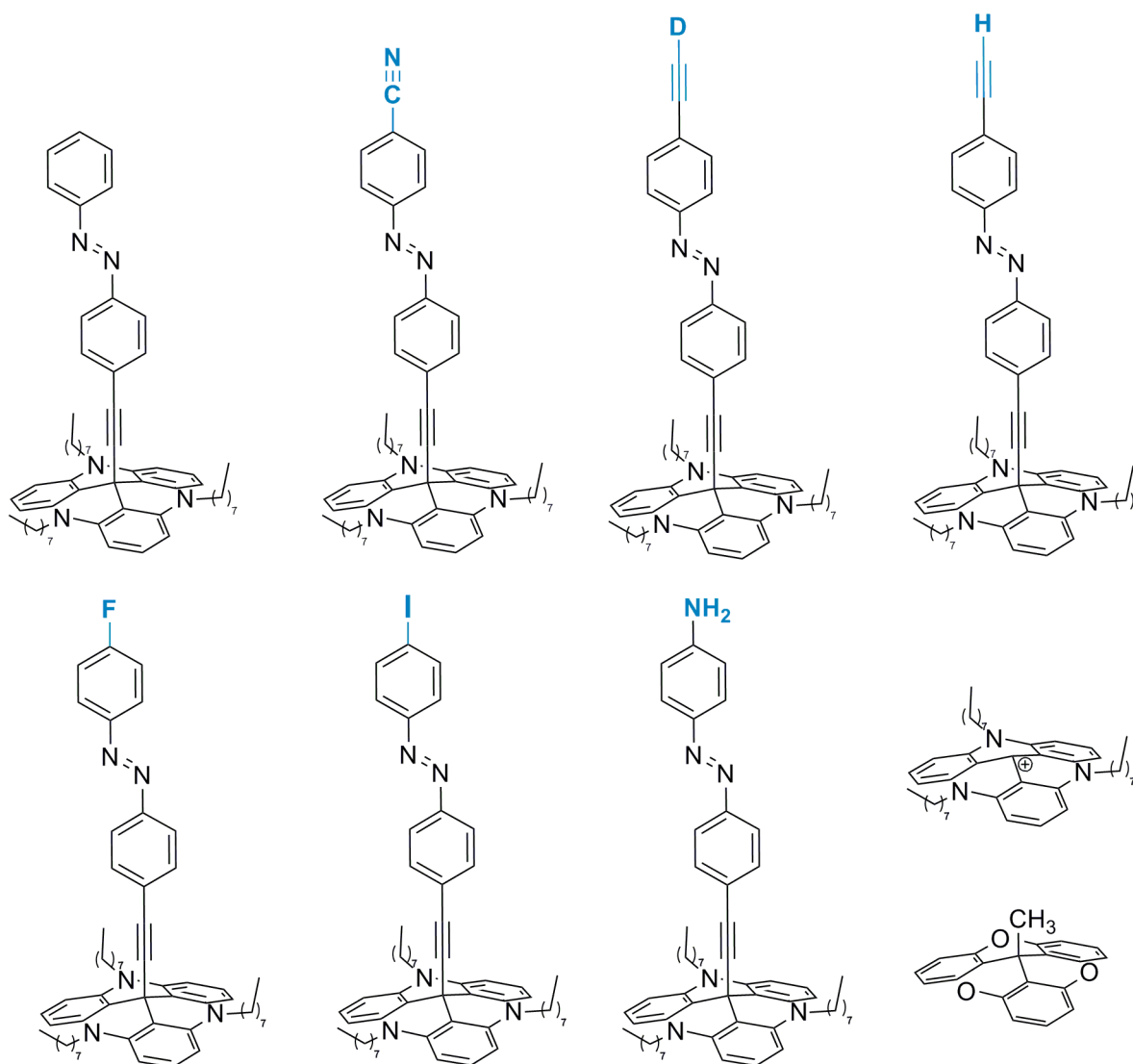


Figure 47: Several functionalized TATA molecules with different head-groups.

The methoxyazo-functionalized TATA however, gave a significant IRRA spectrum and showed

the C-O stretching vibration of methoxy-groups of the azobenzene unit on the TATA platform (Fig. 48).

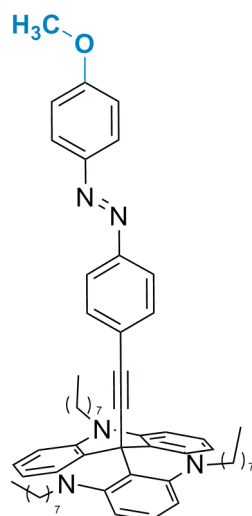


Figure 48: A methoxyazo-functionalized TATA platform.

As already reported in our *Langmuir* and *Chemistry - A European Journal* publication, the C-O stretching vibration leads to a strong absorbance band in the IR bulk spectra as well as in the IRRA spectra. This marker group seems to be the best candidate to investigate these molecules in their switching behavior from *trans* to *cis* isomer by irradiation with UV light with a wavelength of 365 nm.

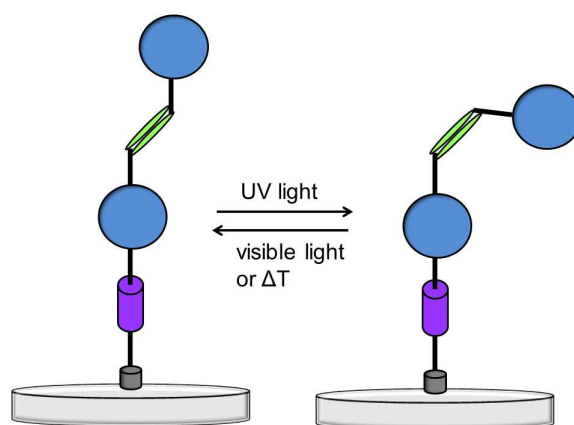


Figure 49: Schematic view of the *trans* to *cis* isomerization.

The following publication shows the results of the methoxy-azo-TATA regarding its switching

behavior in solution, DFT frequency vibrational analysis and the investigation of the adsorbed molecules on Au(111) surfaces using STM, XPS, SERS and IRRAS. The vibrational information of these molecules were analyzed in detail and assigned fully in bulk as well as on surface. Furthermore, PM-IRRAS data were recorded and the main prominent stretching vibration of the C-O-methoxy marker group was analyzed regarding time dependent irradiation experiments.

Publication in
Physical Chemistry Chemical Physics

**4.3 Monitoring the reversible photoisomerization of an azobenzene-
functionalized molecular triazatriangulene platform on Au(111) by
IRRAS**

H. Jacob, S. Ulrich, U. Jung, S. Lemke, T. Rusch, C. Schütt, F. Petersen, T. Strunskus, O.
Magnussen, R. Herges* and F. Tuczek*

Phys. Chem. Chem. Phys. **2014**, 16, 22643-22650.

DOI: 10.1039/C4CP03438D.



Cite this: *Phys. Chem. Chem. Phys.*, 2014, 16, 22643

Monitoring the reversible photoisomerization of an azobenzene-functionalized molecular triazatriangulene platform on Au(111) by IRRAS†

Hanne Jacob,^a Sandra Ulrich,^b Ulrich Jung,^c Sonja Lemke,^c Talina Rusch,^c Christian Schütt,^b Finn Petersen,^a Thomas Strunskus,^d Olaf Magnussen,^c Rainer Herges*^b and Felix Tuczek*^a

Spectroscopic evidence of a reversible, photoinduced *trans* ↔ *cis* photoisomerization is provided for an azobenzene-functionalized triazatriangulene (TATA) platform on Au(111). As shown by scanning tunneling microscopy (STM) and X-ray photoelectron spectroscopy (XPS), these molecules form a well-ordered self-assembled monolayer (SAM) on Au(111). The surface-adsorbed azo-TATA platforms are also investigated by infrared reflection absorption spectroscopy (IRRAS); a methoxy marker group at the upper phenyl ring of the azo moiety is employed to monitor the switching state. The IRRAS data are analyzed by comparison with theoretical and transmission IR spectra as well as bulk and surface-enhanced Raman spectroscopic (SERS) data. IRRAS shows that the methoxy group is oriented perpendicular to the surface in *trans*- and tilted with respect to the surface normal in *cis*-configuration. This indicates that the photoswitching capability of the azobenzene moieties is retained on the gold surface. The lifetime of the *cis*-configuration is, however, reduced by a factor of $\sim 10^3$ with respect to the homogeneous solution.

Received 4th August 2014,
Accepted 17th September 2014

DOI: 10.1039/c4cp03438d

www.rsc.org/pccp

Introduction

The functionalization of surfaces with monolayers of switchable molecules is both of fundamental importance and of significant interest with respect to applications as in data storage, sensors, and molecular electronics.^{1,2} While azobenzenes are a class of well investigated molecular switches exhibiting reversible *cis*-*trans* photoisomerization in homogeneous solution,^{3,4} switching of these molecules in monolayers on metal surfaces is more intricate. The main problems that arise are as follows: (i) azobenzene-modified alkylthiols form highly-packed monolayers, therefore the switching process may be sterically hindered;⁵ (ii) electronic coupling to the metal surface can efficiently quench the excited state;^{6–9} the lifetime of the photo-switched isomer thus may be short and the quantum yield of isomerization may be small. Triazatriangulene (TATA) platforms, in contrast, both reduce the

electronic coupling with the surface and control the distance of the switchable units from each other as a function of the size of the side chains at the platforms.¹⁰ Moreover, the bare TATA cation as well as the azobenzene-functionalized TATA molecules form well-ordered and stable hexagonal monolayers on Au(111) surfaces with commensurate lattice constants.¹¹ The “platform approach” is thus a suitable method to prepare self-assembled monolayers of functional molecules on, *e.g.*, gold with control of intermolecular distances (Fig. 1).

Here we present spectroscopic proof that our approach allows the deposition of well-defined SAMs of azobenzenes on Au(111) that retain their photoswitching capability. In previous publications we investigated the switching behaviour of functionalized

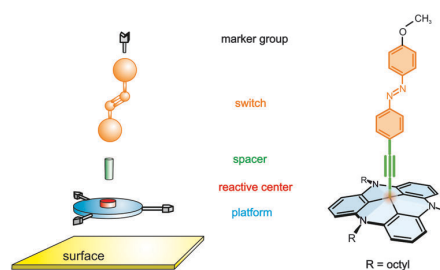


Fig. 1 The platform approach: general scheme (left), methoxy-azo-TATA (right).

^a Institut für Anorganische Chemie, Christian-Albrechts-Universität Kiel, Max-Eyth-Str. 2, 24118 Kiel, Germany. E-mail: ftuczek@ac.uni-kiel.de

^b Institut für Organische Chemie, Christian-Albrechts-Universität Kiel, Otto-Hahn-Platz 4, 24098 Kiel, Germany. E-mail: rherges@oc.uni-kiel.de

^c Institut für Experimentelle und Angewandte Physik der Christian-Albrechts-Universität Kiel, Leibnizstraße 11-19, 24118 Kiel, Germany

^d Technische Fakultät der Christian-Albrechts-Universität Kiel, Kaiserstraße 2, 24143 Kiel, Germany

† Electronic supplementary information (ESI) available. See DOI: 10.1039/c4cp03438d

TATA molecules on gold surfaces by means of electrochemistry and surface plasmon spectroscopy.^{12,13} Whereas the half-life of the thermal back-isomerization of the azobenzene unit from *cis* to *trans* is about 20 hours in solution, cyclic voltammetric measurements on the surface indicated half-lives that are shorter by 4–5 orders of magnitude. As a possible explanation for this finding an influence of the surface on the switching process was invoked.¹² To further address this issue, we synthesized (*E*)-12*c*-[4-(4-methoxyphenyldiazenyl)-phenyl]ethynyl-4,8,12-tri-*n*-octyl-4,8,12-triazatriangulene (“methoxy-azo-TATA”), an azobenzene-TATA with a methoxy group in the *para* position to the azobenzene unit.¹⁴ Herein this molecule is investigated in solution by NMR and UV/Vis spectroscopy as well as adsorbed on a gold surface by STM, XPS and (PM-) IRRAS. The methoxy group is used as a spectroscopic marker to monitor the switching process on the Au surface. Based on an upright position of the azo group and the surface selection rule, the C_(phenyl)–O stretching vibration in the IRRAS experiment exhibits a higher intensity in the *trans* as compared to the *cis* configuration of the azo group. The implications of our findings on the preparation of switchable monolayers on surfaces based on the platform concept are discussed.

Results and analysis

The switching behaviour of (*E*)-12*c*-[4-(4-methoxyphenyldiazenyl)-phenyl]ethynyl-4,8,12-tri-*n*-octyl-4,8,12-triazatriangulene (“methoxy-azo-TATA”) was first investigated by UV/Vis- and NMR spectroscopy in solution. Upon irradiation with UV light (365 nm) the *trans* isomer switches to the *cis* isomer.

This can be monitored in the UV/Vis spectra by a decreasing intensity of the $\pi \rightarrow \pi^*$ band at 333 nm and 368 nm and an increasing intensity of the $n \rightarrow \pi^*$ band at 451 nm (Fig. 2). Furthermore, new sets of signals appear in the NMR spectra, which can be assigned to the *cis* isomer (Fig. 3).

Reisomerization from *cis* to *trans* either occurs thermally or can be initiated by irradiation with blue light (440 nm); this process has also been followed by UV/Vis and NMR spectroscopy. The maximum *cis* concentration was determined by comparing the integrals of specific ¹H-NMR signals, and the

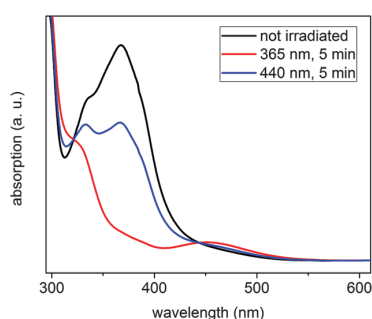


Fig. 2 UV spectra of methoxy-azo-TATA in toluene under ambient conditions. Upon irradiation with UV light (365 nm) the $\pi \rightarrow \pi^*$ transition band decreases and the $n \rightarrow \pi^*$ transition band increases in intensity.

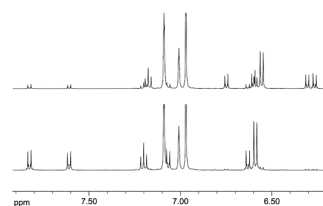


Fig. 3 Aromatic region of the ¹H-NMR spectra of methoxy-azo-TATA in *trans* (bottom) and after irradiation with UV light (365 nm) in *cis* (top) configuration in toluene under ambient conditions.

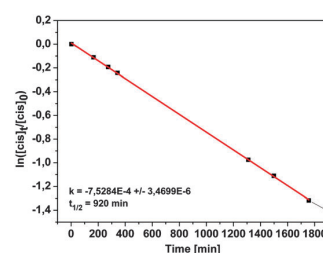


Fig. 4 Plot of the natural logarithm of the *cis* concentration as a function of time to determine the half-life of methoxy-azo-TATA in toluene.

half-life of the *cis* configuration under ambient conditions was obtained by following the decrease of the *cis* signals after irradiation for several days. The maximum *cis* concentration (74%) after irradiation with UV light (365 nm) of methoxy-azo-TATA is in good agreement with other azobenzene-functionalized TATA platforms,¹⁴ and thermal back-isomerization follows a first-order rate law with a half-life of 920 min (*cf.* Fig. 4).

Having demonstrated the reversible photoisomerization of the title compound in solution, its switching properties on a gold surface were investigated. STM measurements of methoxy-azo-TATA adlayers on Au(111) reveal a hexagonally ordered superstructure with intermolecular distances of 12.7 ± 0.5 Å (see Fig. 5a). Specifically, the lattice constants and the angles between different rotational domains are in agreement with a $(\sqrt{19} \times \sqrt{19})R23.4^\circ$ superstructure (Fig. 5b), which was also found in previous STM studies of self-assembled adlayers based

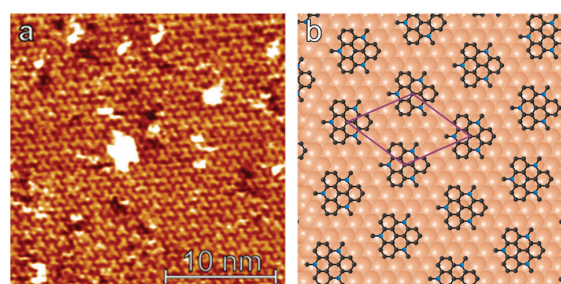


Fig. 5 (a) STM image (25×25 nm²) of a methoxy-azo-TATA adlayer on Au(111), (b) schematic model of a $(\sqrt{19} \times \sqrt{19})R23.4^\circ$ superstructure, where the C (black) and N (blue) atoms of the platform are shown (hydrogen atoms omitted, only first C atoms of octyl side-chains are shown).

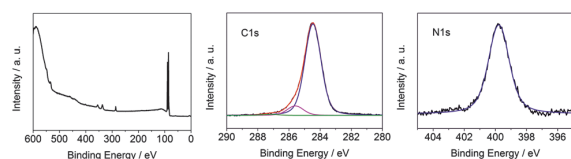


Fig. 6 XP spectra of the methoxy-azo-TATA monolayer. Left: survey-spectrum; middle: C 1s-spectrum along with fit (blue: aliphatic and aromatic C, magenta: C connected to N, green: C connected to O); right: N 1s spectrum with fit (blue).

on octyl-TATA platforms, including those with vertically attached azobenzene units.^{10,11} The triangular shape of the observed molecules, clearly visible in the STM images, indicates a planar adsorption of the octyl-TATA platform unit and suggests an orientation of the methoxy-azo moiety perpendicular to the surface.

Chemical and structural information on a monolayer of methoxy-azo-TATA deposited on Au(111) was also obtained by X-ray photoelectron spectroscopy. The survey XP spectrum is dominated by the Au 4d and 4f core levels and furthermore exhibits, as expected, O 1s, N 1s and C 1s features (Fig. 6, left). The thickness of the adlayer was estimated from the ratios of the C 1s/Au 4f_{7/2} signals and a known reference substance (here dodecylthiol with a known thickness of 1.7 ± 0.1 nm)¹⁵ giving a value of 1.15 nm for methoxy-azo-TATA. Taking into account the lower packing density of this molecule on gold as compared to dodecylthiol SAMs this result indicates the presence of a complete monolayer of methoxy-azo-TATA on the Au(111) surface.

The C 1s spectrum (Fig. 6 middle) consists of three signals. The main peak centered at 284.5 eV is due to the aliphatic and aromatic C atoms of the platform and the azo group, the peak at 285.6 eV can be assigned to the C atoms directly connected to nitrogen atoms, and the C atoms directly connected to the oxygen atom correspond to the signal at 287.2 eV. The relative intensities of these three contributions ($0.9 \pm 0.03/0.09 \pm 0.03/0.01 \pm 0.01$) deviate somewhat from the expected values (0.78/0.19/0.03). Whereas the discrepancy of the relative C(O) signal intensity can be attributed to the uncertainty of the fit procedure associated with the low oxygen content of methoxy-azo-TATA, the deviation of the relative C(N) signal intensity from the expected value (found 0.09/calc. 0.19) is outside the experimental error. A similar discrepancy is found when comparing the intensity of the N 1s signal at 400 eV (Fig. 6 right) to the total C 1s signal intensity (found: $0.05 \pm 0.02/1$; calc. 0.09/1). It should be mentioned, however, that these C/N ratios have been determined on the basis of a homogeneous surface layer.¹⁶ For the monolayer of methoxy-azo TATA on gold this condition is not met. The molecular monolayer rather consists of close-packed, horizontal TATA platforms directly on top of the metal surface (*vide supra*) carrying vertically oriented, laterally separated azo moieties. The assumption of a uniform photoelectron inelastic mean free path (IMFP)¹⁶ for such a strongly inhomogeneous arrangement is certainly problematic. Specifically, the octyl side chains of one platform may partly cover adjacent platforms such that the XPS signals of the platforms are attenuated with respect to the azo

moieties and the octyl sidearms. As the platforms have a higher nitrogen content than the other constituents of the methoxy-azo-TATA molecule, the N/C values are systematically underestimated in the presented analysis of the XPS data. The actual attenuation of the XPS signals associated with the C- and N-atoms of the platform is, however, difficult to assess.

Having characterized the structure and the composition of the monolayer of methoxy-azo-TATA on gold by STM and XPS, this system was then investigated by vibrational spectroscopy. First, gap-mode surface-enhanced Raman spectroscopy (SERS) was employed.^{17–20} As shown in Fig. 7, the SERS data closely correspond to the bulk Raman spectrum of methoxy-azo-TATA on the one hand and the calculated Raman spectrum of methoxy-azo-benzene on the other. Furthermore, the SERS spectra of methoxy-azo-TATA are in good agreement with those of our previous study performed on a series of azobenzene-functionalized TATA adlayers on Au(111).^{21a}

To interpret the experimental SERS data density functional theory calculations on methoxy-azo-TATA were performed. Octyl side chains were replaced by propyl to save computational costs (see Experimental section). The theoretical Raman spectrum derived from this calculation together with a previous study^{21a} allows a complete assignment of the spectral peaks, as presented in the ESI† (Table S2).

In the range between 1100 and 1650 cm^{-1} the spectra mainly consist of valence vibrations of the aromatic rings constituting the azobenzene moiety. The two intense peaks below 1200 cm^{-1} have contributions from C–N stretching motions whereas those in the range between 1400 and 1500 cm^{-1} have contributions from the N=N unit as well as aromatic in plane C–H bending and CH₃O bending vibrations. The C–C stretch of the ethynyl group is observed at 2220 cm^{-1} . Contributions from other molecular constituents are much less pronounced; in particular, the TATA platform exhibits a much smaller Raman scattering cross section than azobenzene.^{21a} Nevertheless, as found by DFT

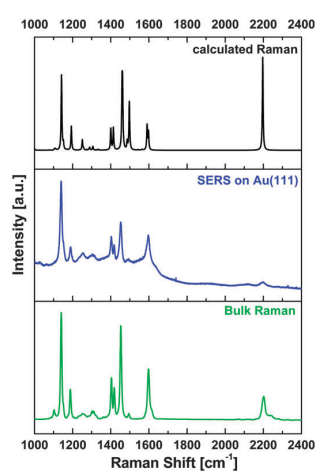


Fig. 7 Calculated Raman spectrum (B3LYP/6-31++G** level of DFT) of methoxy-azo-TATA (black), SERS spectrum of methoxy-azo-TATA on Au(111) (blue) and the bulk Raman spectrum of methoxy-azo-TATA (green).

most of the peaks between 450 and 1650 cm^{-1} have small contributions from this group.

Complementing the vibrational information from SERS, the surface-adsorbed methoxy-azo-TATA platform was also investigated by infrared absorption-reflection spectroscopy (IRRAS). Through the surface selection rule this technique also provides specific information about the orientation of the adsorbed molecules with respect to the surface. In order to assign the vibrational bands bulk IR data were recorded as well, and theoretical spectra were generated from DFT based on the same optimized structure of methoxy-azo-TATA as that employed for SERS (*vide supra*). Theoretical, bulk and surface vibrational spectra are given in Fig. 8 for the high-frequency vibrations (left) and for the fingerprint region (right). Scaling of the calculated frequencies has been performed in analogy to the theoretical Raman spectrum (*cf.* Experimental). Comparison of the surface and bulk data on one hand with predictions from DFT on the other hand allows a detailed assignment of the observed vibrations; the numbering of the bands refers to the DFT calculation comprising all normal modes of the molecule (*cf.* Table S3, ESI[†]).

At around 3000 cm^{-1} the calculated bulk spectrum (Fig. 8 left top) exhibits a number of bands, which mostly derive from C–H stretching vibrations of the phenyl units constituting the TATA platform, the phenyl rings of the azo unit and C–H stretching vibrations of the alkyl side chains (*cf.* Table S3, ESI[†]). In the region of aliphatic C–H stretching vibrations, the experimental bulk spectrum of methoxy-azo-TATA exhibits four broad features at $\sim 2950 \text{ cm}^{-1}$, $\sim 2920 \text{ cm}^{-1}$, $\sim 2870 \text{ cm}^{-1}$ and $\sim 2850 \text{ cm}^{-1}$ (Fig. 8 left bottom). The shoulder at 2950 cm^{-1} can be assigned to asymmetric CH_3 stretching vibrations of the aliphatic side chains and the CH_3 group on top of the azo unit. The most intense feature at 2920 cm^{-1} corresponds to asymmetric CH_2 stretching vibrations from the alkyl side chains of

the TATA platform, the shoulder at 2870 cm^{-1} probably corresponds to the symmetric CH_3 stretching vibrations of the alkyl side chains, and the more intense feature at 2850 cm^{-1} is associated with symmetric CH_2 stretching vibrations. All of these features are also observed with slightly different intensities in the IRRAS spectrum (Fig. 8 left middle).

Above 3000 cm^{-1} the bulk spectrum shows four additional bands which, in contrast to the theoretical prediction, are much weaker than the bands below 3000 cm^{-1} (Fig. 8 left bottom). The bands at 3094 cm^{-1} (band 1) and 3071 cm^{-1} (band 2) can be assigned to aromatic C–H stretching vibrations from the TATA-platform whereas two bands at 3044 cm^{-1} (band 3) and 3019 cm^{-1} (band 4) can be attributed to a C–H stretch of the phenyl ring connected to the platform and another aromatic C–H stretch from the TATA platform, respectively. In IRRAS most of these bands are absent except one small peak at 3017 cm^{-1} . Assignment to an aromatic C–H stretch of the platform (peak 4) would at first appear incompatible with the surface selection rule; however, closer inspection shows that the transition dipole moment (TDM) of this vibration makes an angle of 45° with respect to the surface.

The “fingerprint” region ranging from ~ 1700 to 1000 cm^{-1} is shown in the right panel of Fig. 8. At around 1600 cm^{-1} three vibrations of C=C character appear which also include C=C vibrations of the azo phenyl groups and correspondingly are visible in the IRRAS spectrum (see also Fig. S1, ESI[†]). Between 1500 and 1300 cm^{-1} C–H bending vibrations of the methoxy group, the N=N stretching vibration and C–C ring deformations from the azo group are located. At 1260 cm^{-1} the $\text{C}_{(\text{phenyl})}\text{O}(\text{Me})$ stretch of the methoxy group is observed. Importantly, this is by far the most intense peak in the IRRAS spectrum (Fig. 8 right middle), thus proving that the methoxy-azo unit in azo-functionalized TATA platforms is in fact oriented perpendicular to the surface. The remaining bands, in particular below 1200 cm^{-1} , can mostly be attributed to C–H bending vibrations (*cf.* Table S3 and Fig. S1, ESI[†]).

Having determined the vibrational properties of the methoxy-azo functionalized TATA platforms on gold, these systems were finally subjected to switching experiments. To investigate the *cis-trans* isomerization of the azobenzene unit by IRRAS, the intensity change of the most intense $\text{C}_{(\text{phenyl})}\text{O}(\text{Me})$ stretching vibration occurring upon photoirradiation was monitored. Based on the surface selection rule the intensity of this vibrational band should be correlated with the *trans* or *cis* configuration of the azo group, as shown in Fig. 9. Due to the upright orientation of the methoxy group (*vide supra*), the $\text{C}_{(\text{phenyl})}\text{O}(\text{Me})$ transition dipole moment (TDM) is nearly perpendicular to the surface plane in the *trans* configuration. In the *cis* configuration, on the other hand, the TDM makes an angle of 30° with respect to the surface. By switching the molecule to the *cis* isomer, the intensity of the C–O stretching band thus should decrease by 75% in the IRRAS spectrum.

In order to rapidly detect a switching process after optical excitation, PM-IRRAS was employed.^{22,23} A special illumination unit was constructed and inserted into the PM-IRRAS sample chamber to directly irradiate the samples on the sample holder and immediately start the IRRAS measurement after irradiation.

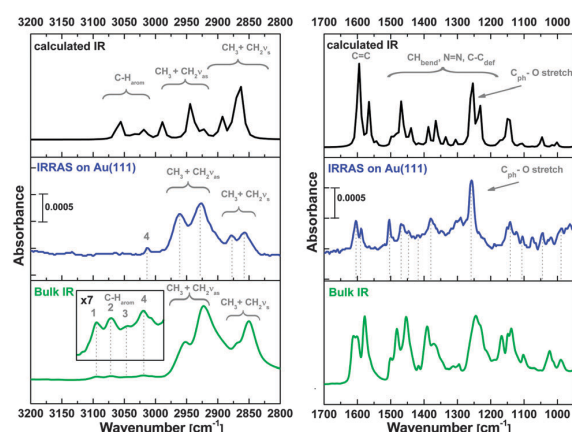


Fig. 8 IR data of methoxy-azo-TATA. Left: CH-stretching vibration region, right: fingerprint region. The spectra in the top panels show the calculated, the spectra in the middle in blue the IRRAS of the surface-adsorbed monolayer and the green spectra at the bottom the bulk data. Band numbers correspond to Table S3 (ESI[†]).

PCCP

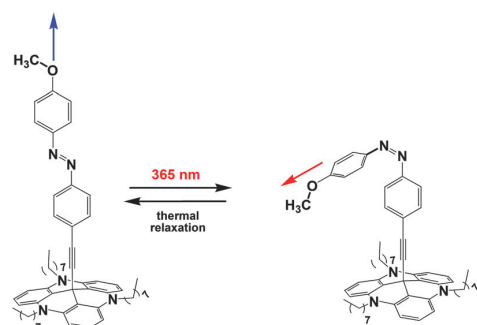


Fig. 9 Different orientations of the transition dipole moment of the C–O stretching vibration in *trans* and *cis* conformation.

Additional advantages of the PM-IRRAS technique over conventional IRRAS are that no background measurements are necessary, atmospheric disturbances are absent and scan times are much shorter. However, treatment of the experimental data is more complicated as a Bessel-type background has to be subtracted.²⁴ All irradiation spectra were recorded with a resolution of 4 cm^{-1} . For an analysis of the $\text{C}_{(\text{phenyl})}\text{O}(\text{Me})$ stretching vibration the PM maximum efficiency was set for the half-wave retardation at 1800 cm^{-1} with a sensitivity of 100 mV (gain factor 10).

The results of the switching experiments are shown in Fig. 10. Upon continuous irradiation with 365 nm the intensity of the $\text{C}_{(\text{phenyl})}\text{O}(\text{Me})$ peak drops from a value of 0.0013 to 0.006, corresponding to a reduction of 54% and a transition to the *cis* configuration. Subsequent measurements in time intervals of 15 s (20 scans) after switching the LED off revealed an exponential increase of the peak corresponding to a thermal backrelaxation of *cis* to *trans* (cf. Fig. S2, ESI[†]).

The spectra obtained over 20 scans shown in Fig. 10 result from summing up of 10 individual runs. A logarithmic intensity vs. scan time plot (cf. Fig. 11) gives a monoexponential decay with a half-life of 42 ± 10 seconds for the photoinduced *cis* state of the TATA platform on Au(111), about 3 orders of magnitude smaller than in solution.

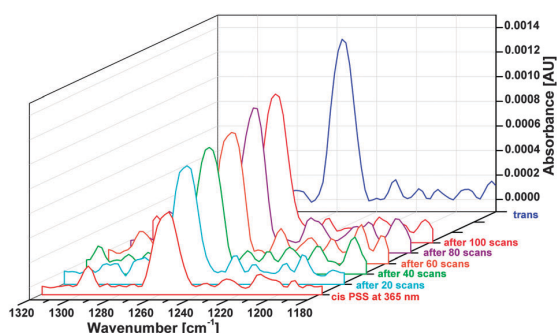


Fig. 10 $\text{C}_{(\text{phenyl})}\text{O}(\text{Me})$ stretching band data of methoxy-azo-TATA monolayer on Au(111) obtained with PM-IRRAS under continuous irradiation with 365 nm (red) and after 20, 40, 60, 80 and 100 scans (cyan, green, brown, violet and orange, respectively) with the LED switched off. The spectrum of *trans* is shown for comparison (blue).

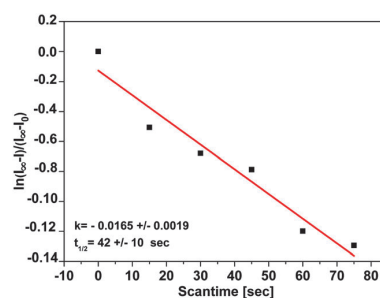


Fig. 11 Plot of $\ln[(I_{\infty} - I)/(I_{\infty} - I_0)]$ vs. time, showing a monoexponential decay of *cis* to *trans* with a half-life of 42 ± 10 s.

Discussion and conclusions

In the preceding sections surface-analytical and -spectroscopic investigations on an azobenzene functionalized TATA platform have been presented. The switching behavior of methoxy-azo-TATA was analyzed in solution by using UV spectroscopy and NMR. Moreover, the molecules were adsorbed on Au(111) surfaces. XPS and STM measurements indicate that the adsorbed molecules are intact and form well-ordered monolayers. Vibrational-spectroscopic data of the adlayers on Au(111) were obtained using SERS and IRRAS and interpreted with the help of DFT. The dominant intensity of the $\text{C}_{(\text{phenyl})}\text{O}(\text{Me})$ stretch in the IRRA spectrum shows that the azobenzene moieties attached to the TATA platform are in the *trans* configuration. The absolute intensity of this peak in the IRRA spectrum conforms to the surface coverage determined for the TATA platforms.¹¹ IRRA spectra of a SAM of an alkoxy-azobenzene-terminated alkanethiol give an intensity of the $\text{C}_{(\text{phenyl})}\text{O}(\text{Me})$ stretch of about 0.01.²⁵ From STM data it is known that the area per molecule is 137 \AA^2 for 8-TATA derivatives.^{21a} On the other hand, the area per molecule was determined to be 25.2 \AA^2 for pure SAMs of azobenzene-containing molecules with amide-thiol functions and 30.4 \AA^2 for pure SAMs of azobenzene-containing molecules with ether-thiol functions.^{21b} This indicates that the surface coverage of methoxy-azo-TATAs is about 1/5 compared to a SAM of corresponding linear azobenzene-containing thiols and would correspond to an absolute IRRAS intensity of 0.020 for the $\text{C}_{(\text{phenyl})}\text{O}(\text{Me})$ stretch of a monolayer of methoxy-azo-TATA molecules. Our experimentally obtained value is 0.010–0.020, depending upon the sample, in good agreement with this estimate.

By PM-IRRAS it was demonstrated that the azobenzene unit attached to the TATA platforms can reversibly be switched from the *trans* to the *cis* configuration. For these experiments the $\text{C}_{(\text{phenyl})}\text{O}(\text{Me})$ stretching vibration from the headgroup of the azo functionalized platform molecule has been employed. The transition dipole moment (TDM) in the *trans* configuration is nearly perpendicular to the surface whereas in the *cis* configuration it makes an angle of 30° with respect to the surface. The corresponding intensity reduction (theoretically 75%) is experimentally found to be somewhat smaller (55%). The origin of this discrepancy is not entirely clear; however, in a

spectroscopic investigation of another azobenzene-functionalized self-assembled monolayer (SAM) a comparable intensity change upon *trans*-to-*cis* isomerization has been found.²⁶

Importantly, the present study contributes another case to the – so far – very limited number of studies where spectroscopic evidence for a reversible photoisomerization in a monolayer on a metal surface has been obtained. Apart from the mentioned *trans* ↔ *cis* isomerization of an azobenzene-functionalized self-assembled monolayer (SAM) on Au(111) the photoisomerization of a spiroopyran on gold has been monitored by sum-frequency generation (SFG) vibrational spectroscopy.^{26,27} HREELS has been employed to detect the photoswitching of *tert*-butyl azobenzene on Au.²⁸ Furthermore, reversible photoswitchability was observed for azo-functionalized SAMs by ellipsometry and dynamic contact angle measurements.²⁹ In one case IRRAS has been used to detect a *trans*-*cis* isomerization in a molecular adlayer.²⁵

An interesting result of the present investigation is the rapid thermal relaxation of the *cis*-azobenzene moieties back to the *trans* configuration, which is found to proceed with a half-life of 42 ± 10 s. Notably, within the experimental error, this agrees with the thermal half-life of the photoexcited *cis*-state determined for an azobenzene-functionalized TATA platform on gold by surface-plasmon spectroscopy (time constant $\tau = 54.0 \pm 9.9$ s;¹² *i.e.*, $t_{1/2} = 37.4 \pm 6.8$ s) and corresponds to a decrease of the half-life by a factor of $\sim 10^3$ with respect to the homogeneous solution ($t_{1/2} = 920$ min).

Possible origins of the enhanced *cis* → *trans* relaxation rate for surface-adsorbed, azobenzene-functionalized platforms have been considered in ref. 12. For molecules adsorbed on a metal surface, spin exchange with the electrons of the conduction band is possible. As found by DFT, highly delocalized molecular orbitals of the platform are located close to the Fermi energy of the gold substrate, mediating strong electronic coupling between the metal surface and the adsorbed molecule. This opens a new pathway for *cis* → *trans* backisomerization with a distinctively lowered energy barrier than in solution. To the best of our knowledge, the present study is the first example where such a thermal backrelaxation process after photoisomerization of a surface-adsorbed molecule has been evidenced by IRRAS.

Experimental

The synthesis of the triazatriangulenium (TATA) cation was performed by the procedure of Laursen and Krebs,³⁰ and the azobenzene-functionalized TATA platforms methoxy-azo-TATA were synthesized as published by Kubitschke *et al.*¹⁴ NMR spectra were recorded using a Bruker DRX 500 (¹H-NMR: 500 MHz, ¹³C-NMR: 125.8 MHz) spectrometer with toluene-*d*₈ as solvent. UV spectra were measured in toluene with the UV/Vis spectrometer Perkin-Elmer Lambda 14. STM and XPS measurements were performed on Au(111) single crystals (MaTeck GmbH, Jülich, Germany). For gap-mode SERS^{17–20} (111)-oriented Au films (250 nm) with a Cr adhesion promoter (5 nm) on glass (“Arrandees” supplied by Dr D. Schroer, D-33824 Werther, Germany) were used. Glass substrates with a 50 Å titanium base layer and a 1000 Å

evaporated gold film were purchased from EMF Corporation (Ithaca, NY) for IRRAS and PM-IRRAS measurements.

All gold substrates were annealed in a butane gas flame, single crystals for five minutes and glass substrates with gold film for one minute. The monolayers were prepared by immersing the substrate into a solution of bare TATA molecules in ethanol (Merck, p.a.) at room temperature or functionalized derivatives in toluene (Merck, p.a.) at 80 °C for one hour. Afterwards, excess molecules were removed by immersing the substrates for 15 minutes at the same temperature as before in pure solvent. Finally, samples were removed from the solution and dried in the air.

In order to assign the peaks in the Raman and IRRA spectra to molecular vibrations, quantum chemical calculations were performed at the B3LYP/6-31++G(d,p)^{31,32} level of density functional theory (DFT) using Gaussian09.³³ We corrected the calculated frequencies in such a way that they optimally match the experimental values. Consequently, after scaling with the equation $0.927 \cdot \text{calc. wavenumber} + 63.318 \text{ cm}^{-1}$ we found very good agreement between theory and experiment. The octyl side chains were replaced by propyl side chains due to the fact that the corresponding vibrational modes are not important for the comparison between the experimental and the theoretical results as well as to save computational costs. The optimized geometry of methoxy-azo-TATA is given in Table S1 (ESI†).

XPS measurements were performed at the beamline HE-SGM of the synchrotron facility BESSY II using the PREVAC endstation. The experimental station is equipped with a hemispherical VG Scienta R3000 photoelectron analyzer. The energy resolution $E/\Delta E$ of the beamline with 150 μm slits is 800. XP survey spectra were acquired at 700 eV photon energy using an analyzer pass energy of 100 eV. For the C 1s and N 1s spectra the photon energy was 400 eV and 500 eV with pass energies of 20 eV and 50 eV, respectively. All spectra were acquired at normal electron emission. For quantitative comparison the spectra were corrected by the number of individual scans, the effective X-ray beam current, and the photoionization cross sections.^{34,35} Background correction was performed using a Shirley background for the Au 4f signals, a combination of a Shirley and a linear background for the C 1s signal and a linear background for all other signals. Peak fitting was performed using the program Fityk³⁶ employing Voigt profiles.

Scanning Tunneling Microscopy (STM) measurements were performed in a PicoPlus SPM (Agilent, Inc., Santa Clara, USA) under ambient conditions, using mechanically cut Pt/Ir tips. Samples for gap-mode SERS measurements^{18–20,21a} were prepared by immersion of the adlayer-modified substrates into aqueous gold colloid solutions (particle size of about 20 nm)³⁷ for ~48 h. Afterwards, the samples were dried in air. The gold colloid was prepared by reduction of HAuCl₄ by sodium citrate. For Raman spectroscopic measurements two spectrometers were used: (i) a Dilor XY-Raman spectrometer (Horiba) with an Ar/Kr mixed gas laser (RM 2018, Spectra Physics) emitting at a wavelength of $\lambda_{\text{ex}} = 647.1$ nm ($P_{\text{ex}} = 10$ to 30 mW, size of laser spot on the sample: 0.5 mm × 1 mm); and (ii) an ISF66/FRA106 Fourier transform Raman spectrometer (Bruker AXS GmbH) with a

Nd:YAG laser at a wavelength of $\lambda_{\text{ex}} = 1064$ nm. All Raman spectroscopic measurements were carried out under ambient conditions.

Bulk IR spectra were recorded using a Bruker ATR FT-IR spectrometer in the range of 400 to 4000 cm^{-1} with a resolution of 4 cm^{-1} . The surface adsorbed molecules were investigated by using a Bruker VERTEX 70 FT-IR spectrometer equipped with a Polarization Modulation Accessory (PMA) 50 unit (Bruker Optik GmbH, Ettlingen, Germany). This instrument allows recording of IRRAS and PM-IRRAS data with a spectral range from 4000 down to 800 cm^{-1} . IRRAS data were collected with a liquid nitrogen cooled MCT detector in a horizontal reflection unit for grazing incidence (Bruker A518). The sample chamber was purged with dry nitrogen before and during measurements. A deuterated hexadecane-thiol SAM on Au(111) was used as a reference for the background spectrum for conventional IRRAS spectra. Each spectrum contains 2048 averaged spectra. A *p*-polarized beam at an incident angle of 80° to the surface normal was used for measurements. All spectra were recorded with 4 cm^{-1} resolution. PM-IRRAS data were collected with the PMA 50 accessory using a liquid nitrogen-cooled MCT detector. The PEM maximum efficiency was set for the half-wave at 1800 cm^{-1} for analysis of the C–O stretching mode. All spectra were recorded at 4 cm^{-1} resolution.

Processing of IRRAS and PM-IRRAS data was carried out using the OPUS software Version 6.5 (Bruker, Germany). Baseline correction of the resulting IRRAS data was performed by the rubber band method in an interactive mode. PM-IRRAS data were processed by the implicit removal of the Bessel function through manual baseline correction.²⁴

For the *trans*-to-*cis* isomerization of methoxy-azo-TATA the samples were irradiated using a LED (Nichia NC4U133(T)), peak wavelength: 365 (± 9) nm, 1 LEDs, power dissipation: 12 W, luminous flux: 10 lm, distance ~ 5 cm).

Acknowledgements

The authors thank Deutsche Forschungsgemeinschaft (DFG) for funding of this research (SFB 677). We also want to thank Andreas Terfort (Frankfurt) for a gift of deuterated hexadecanethiol, Uschi Cornelissen for Raman measurements and Benjamin Sahlmann for providing the LED illumination unit used in the PM-IRRAS experiments. We further thank Christof Wöll (Karlsruhe) for providing the Prevac endstation and the HE-SGM CRG as well as the BESSY staff for technical support of the XPS measurements.

Notes and references

- W. R. Browne and B. L. Feringa, *Annu. Rev. Phys. Chem.*, 2009, **60**, 407–428.
- Y.-S. Fu, J. Schwaböel, S.-W. Hla, A. Dilullo, G. Hoffmann, S. Klyatskaya, M. Ruben and R. Wiesendanger, *Nano Lett.*, 2012, **12**, 3931–3935.
- S. Venkataramani, U. Jana, M. Dommaschk, F. D. Sönnichsen, F. Tuzcek and R. Herges, *Science*, 2011, **331**, 445–448.
- S. Thies, H. Sell, C. Schuett, C. Bornholdt, C. Naether, F. Tuzcek and R. Herges, *J. Am. Chem. Soc.*, 2011, **133**, 16243–16250.
- R. Klajn, *Pure Appl. Chem.*, 2010, **82**, 2247–2279.
- R. J. Maurer and K. Reuter, *Angew. Chem.*, 2012, **124**, 12175–12177.
- M. J. Comstock, N. Levy, A. Kirakosian, J. Cho, F. Lauterwasser, J. H. Harvey, D. A. Strubbe, J. M. J. Fréchet, D. Trauner and S. G. Louie, *et al.*, *Phys. Rev. Lett.*, 2007, **99**, 038301.
- C. Bronner, G. Schulze, K. J. Franke, J. I. Pascual and P. Tegeder, *J. Phys.: Condens. Matter*, 2011, **23**, 484005.
- P. Tegeder, *J. Phys.: Condens. Matter*, 2012, **24**, 394001.
- B. Baisch, D. Raffa, U. Jung, O. Magnussen, C. Nicolas, J. Lacour, J. Kubitschke and R. Herges, *J. Am. Chem. Soc.*, 2009, **131**, 442–443.
- S. Kuhn, B. Baisch, U. Jung, T. Johannsen, J. Kubitschke, R. Herges and M. Magnussen, *Phys. Chem. Chem. Phys.*, 2010, **12**, 4481–4487.
- U. Jung, C. Schütt, O. Filinova, J. Kubitschke, R. Herges and O. Magnussen, *J. Phys. Chem. C*, 2012, **116**, 25943–25948.
- U. Jung, J. Kubitschke, R. Herges and O. Magnussen, *Electrochim. Acta*, 2013, **112**, 869–880.
- J. Kubitschke, C. Näther and R. Herges, *Eur. J. Org. Chem.*, 2010, 5041–5055.
- T. Kondo, M. Yanagida, K. Shimazu and K. Uosaki, *Langmuir*, 1998, **14**, 5656–5658.
- Surface Analysis by Auger and X-Ray Photoelectron Spectroscopy*, ed. D. Briggs and J. T. Grant, IM Publications and Surface Spectra Limited, Chichester and Manchester, 2003, ISBN: 1-901019-04-7.
- M. Fleischmann, P. J. Hendra and A. J. McQuillan, *Chem. Phys. Lett.*, 1974, **26**, 163–166.
- D. L. Jeanmaire and R. P. Van Duyne, *J. Electroanal. Chem.*, 1977, **84**, 1–20.
- M. G. Albrecht and H. Creighton, *J. Am. Chem. Soc.*, 1977, **99**, 5215–5217.
- U. Jung, M. Müller, N. Fujimoto, K. Ikeda, K. Uosaki, U. Cornelissen, F. Tuzcek, C. Bornholdt, D. Zargarani, R. Herges and O. Magnussen, *J. Colloid Interface Sci.*, 2010, **341**, 366–375.
- (a) U. Jung, S. Kuhn, U. Cornelissen, F. Tuzcek, T. Strunskus, V. Zaporotchenko, J. Kubitschke, R. Herges and O. Magnussen, *Langmuir*, 2011, **27**, 5899–5908; (b) U. Jung, O. Filinova, S. Kuhn, D. Zargarani, C. Bornholdt, R. Herges and O. Magnussen, *Langmuir*, 2010, **26**, 13913–13923.
- M. A. Ramin, G. Le Bourdon, N. Daugey, B. Bennetau, L. Vellutini and T. Buffeteau, *Langmuir*, 2011, **27**, 6076–6084.
- A. H. Kycia, K. Koczur, J. J. Leitch, J. Lipkowski, V. Zamlynyy and M. W. P. Petryk, *Anal. Bioanal. Chem.*, 2013, **405**, 1537–1546.
- T. Buffeteau, B. Desbat, D. Blaudez and J. M. Turlet, *Appl. Spectrosc.*, 2000, **54**, 1646–1650.
- S. Y. Wang, D. C. Huang and Y. T. Tao, *Chin. Chem. Soc.*, 2012, **59**, 9–17.

- 26 S. Wagner, F. Leyssner, C. Kördel, S. Zarwell, R. Schmidt, M. Weinelt, K. Rück-Braun, M. Wolf and P. Tegeder, *Phys. Chem. Chem. Phys.*, 2009, **11**, 6242–6248.
- 27 T. A. Darwish, Y. Tong, M. James, T. L. Hanley, Q. Peng and S. Ye, *Langmuir*, 2012, **28**, 13852–13860.
- 28 C. Gahl, D. Brete, F. Leyssner, M. Koch, E. R. McNellis, J. Mielke, R. Carley, L. Grill, K. Reuter, P. Tegeder and M. Weinelt, *J. Am. Chem. Soc.*, 2013, **135**, 4273–4281.
- 29 U. Siemeling, C. Bruhn, F. Bretthauer, M. Borg, F. Träger, F. Vogel, V. Azzam, M. Badin, T. Strunskus and C. Wöll, *Dalton Trans.*, 2009, 8593–8604.
- 30 B. W. Laursen and F. C. Krebs, *Angew. Chem.*, 2000, **112**, 3574–3576 (*Angew. Chem., Int. Ed.*, 2000, **39**, 3432–3434).
- 31 A. D. Becke, *J. Chem. Phys.*, 1993, **98**, 5648–5652.
- 32 C. Lee, W. Yang and R. G. Parr, *Phys. Rev. B: Condens. Matter Mater. Phys.*, 1988, **37**, 785–789.
- 33 M. J. Frisch, G. W. Trucks, H. B. Schlegel, G. E. Scuseria, M. A. Robb, J. R. Cheeseman, G. Scalmani, V. Barone, B. Mennucci, G. A. Petersson and H. Nakatsuji, *et al.*, *Gaussian 09, Revision D.01*, Gaussian, Inc., Wallingford, CT, 2009.
- 34 J. J. Yeh, *Atomic Calculation of Photoionization Cross-Sections and Asymmetry Parameters*, Gordon and Breach Science Publishers, Langhorne, PE, USA, 1993.
- 35 J. J. Yeh and I. Lindau, *At. Data Nucl. Data Tables*, 1985, **32**, 1–155.
- 36 M. Wojdyr, *J. Appl. Crystallogr.*, 2010, **43**, 1126–1128.
- 37 P. C. Lee and D. Meisel, *J. Phys. Chem.*, 1982, **86**, 3391–3395.

4.4 Conclusion

In this publication we successfully reported the characterization of an azobenzene functionalized TATA platform. This TATA platform contains a methoxyazobenzene switching unit perpendicular to the triazatriangulenium platform. The *trans* to *cis* isomerization with UV light of a wavelength at 365 nm in a toluene solution was followed with the help of UV/Vis and NMR spectroscopy whereas the maximum *cis* concentration was determined to 74 % and the half-life follows a first-order rate law to 920 minutes. The adsorption of these molecules on a Au(111) single crystal surface led to hexagonally ordered monolayers with intermolecular distances of $12.7 \pm 0.5 \text{ \AA}$ and clearly visible triangular shapes. XPS data of methoxy-azo-TATA contain carbon, oxygen and nitrogen and allow a determination of the thickness of this layer to 1.15 nm. The SERS data of methoxy-azo-TATA show a clear similarity to the bulk Raman data and observed bands were assigned and compared with the DFT calculated Raman spectrum.

The focus in this publication lays on the IRRAS data analysis. The surface selection rule of this technique provides important information regarding the orientation of the adsorbed monolayer on a metal surface. Methoxy-azo-TATA adsorbed on Au(111) result in a clear IRRA spectra with intensities of around 10^{-3} absorbance units. This indicates the presence of a very thin film of a monomolecular layer. Close packed alkoxy-azobenzene terminated alkanethiols show an intensity of 0.01 absorbance units.^[185] The absolute intensity of the C-O stretching vibration fits well with the determined surface coverage for the methoxy-azo-TATA by STM. The surface coverage of the methoxy-azo-TATA is around 1/5 of a linear azobenzene thiol. Theoretical DFT calculated infrared spectrum, the bulk IR spectrum and IRRA spectrum of methoxy-azo-TATA were compared and showed obvious similarities. A complete vibrational analysis of the molecule has been performed and the assignments of all calculated frequencies have been compared to the observed bands in bulk and IRRAS. The high frequency region clearly shows the phenyl C-H stretching vibration of the azobenzene unit and the presence of the alkyl chains connected to the platform as well as the CH_3

head-group on top of the methoxyazobenzene unit. The fingerprint region clearly shows significant vibrational features of the azo-phenyl groups like C=C ring stretching vibrations, C-H bending vibrations, C-C ring deformation vibrations and the N=N stretching vibration of the azobenzene unit. The most prominent band in the IRRAS, the C-O stretching vibration at 1260 cm^{-1} , clearly shows the perpendicularly located azobenzene unit on the TATA platform. Due to the strong intensity of the C-O stretching vibration, this band was used as a marker group for performing switching experiments. This vibration has a perpendicular to the surface oriented transition dipole moment in the case of the *trans* isomer and changes to a transition dipole moment with an angle of 30° with respect to the surface in the *cis* configuration (Fig. 50).

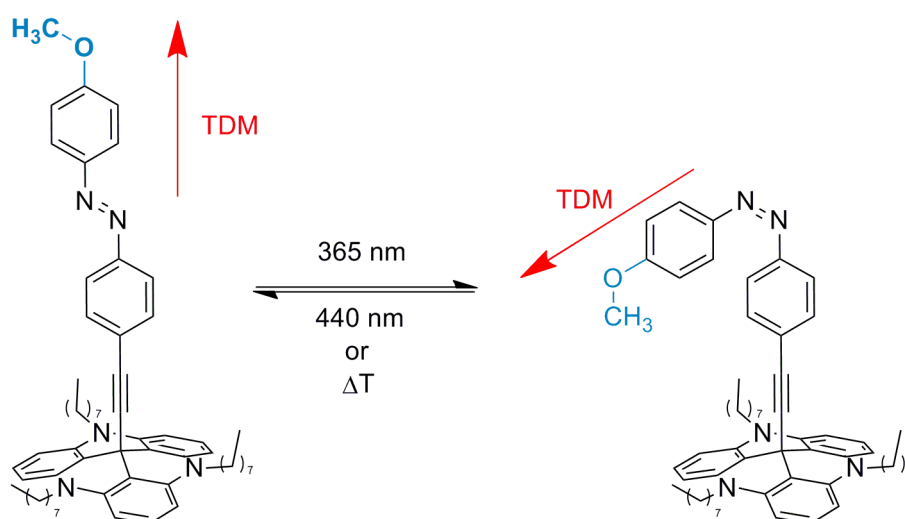


Figure 50: Change of the transition dipole moment through isomerization.

By irradiation the *trans* isomer with 365 nm UV light, we expected a decrease of 75 % of the C-O stretching vibration intensity in the IRRA spectrum by $\cos(60)^\circ$ in the case that all azobenzene units switch to the *cis* configuration. Upon continuous irradiation of the sample directly in the spectrometer chamber and recording a spectrum in the photostationary state, the result was a 54 % decrease of the C-O stretching vibration. The intensities of the absorbance units change from 0.0013 for the *trans* isomer to 0.0006 for the *cis* isomer. The reason for this can be that the maximum *cis* concentration in solution, however, not add up

to 100%. Furthermore, time dependent measurements without continuous irradiation were performed by recording PM-IRRA spectra in intervals of 15 seconds after switching off the 365 nm LED. The C-O stretching vibration clearly increases from spectra to spectra due to the thermal back-relaxation of the methoxyazo-unit from *cis* to *trans* isomer. An exponential slope can be observed during 15 to 75 seconds of relaxation time. The logarithmic intensity versus the scan time results in a monoexponential decay and provides a half-life of 42 ± 10 seconds. Compared to the half-life in solution of 55200 seconds, the half-life is much smaller with 3 orders of magnitude.

This result is, of course, very interesting and comparable with thermal back-relaxation times of other different azobenzene functionalized TATA platforms detected by SPR spectroscopy.^[179] The much faster thermal back-relaxation of molecules on surfaces is still not fully understood. The strong electronic coupling with the electron rich surface and the molecules can be a possible reason.

In summary, this publication presents a photoswitchable methoxyazobenzene functionalized TATA platform and a monitoring of the thermal back-relaxation of these molecules with time dependent PM-IRRAS measurements. Only a very limited number of studies are known in literature where the reversible switching of a monolayer was monitored using a vibrational spectroscopy.^[185,186] This publication is the first known in literature which monitors the spectroscopical evidence of a thermal back-relaxation using IRRAS.

4.5 Outlook

As outlook for the platform project in cooperation with Prof. Dr. Rainer Herges, Otto Diels-Institute for Organic Chemistry (Christian-Albrechts-University of Kiel), new azobenzene and diazocine functionalized TATA platforms were synthesized. As presented in our publication in *Physical Chemistry Chemical Physics* the half-life for the methoxy-azo-TATA molecules in solution is 920 minutes and decreases to 42 ± 10 seconds when the molecules are adsorbed on Au(111). The molecules have a smaller relaxation time of 3 orders of magnitudes. The main goal is to increase the half-life of the molecules on the surface in a way that a thermodynamically stable *cis* isomer could be achieved. A *trans* isomer which can be switched to a stable *cis* isomer would lead to two separate states which can be distinguished. So far it is not clear why the thermal back-relaxation of these molecules is drastically decreased on surface. A probable reason could be the electronic coupling of the azo-function with the gold surface. This could lead to a lowering of the rotation-barrier for the isomerization process. To avoid this fast thermal back-relaxation, the electronic coupling between the azobenzene unit and the surface has to be minimized. This idea can be realized by introducing not conjugated, isolating groups.

For example, a trioxabicyclo[2.2.2]octane spacer or a diazocine spacer connected to the TATA platform avoids the direct conjugation to the azobenzene unit and still retains the orthogonality of the switching unit (Fig. 51). STM measurements of the trioxabicyclo[2.2.2]octan-azobenzene-TATA and UV experiments to determine the half-life are in progress in the working group of Prof. Magnussen, Institute for Applied Physics (Christian-Albrechts-University of Kiel). If these molecules form stable ordered monolayers, IRRAS measurement and switching experiments on surfaces will be performed in the hope of longer thermal back-relaxation times through the isolating unit.

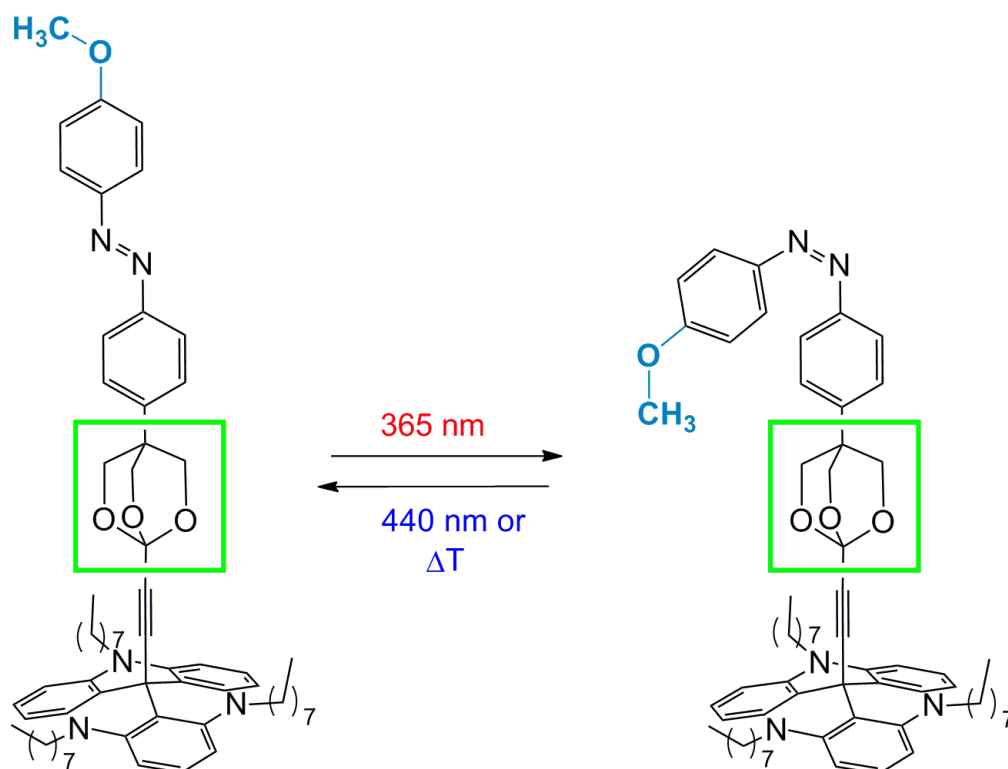


Figure 51: (E)-12c-[(4-4-[(4-Methoxyphenyl)diazenyl]phenyl)-2,6,7-trioxa-bicyclo[2.2.2]octan-1-yl)ethynyl]-4,8,12-tri-n-octyl-4,8,12-triazatriangulen.

5 Characterization of switchable glyco-SAMs on Au(111)

Au(111)

5.1 Glycosides and cell adhesion

Carbohydrates are one of the fundamental class of biomolecules and have a lot of important functions in our body. Carbohydrates are formed of different sugar units and have a concern of metabolic pathways, in the regulation of our water balance and electrolyte balance. In our body, carbohydrates can be found on cell surfaces like the glycocalyx (gr. glykos-sugar; kalyx-coat).

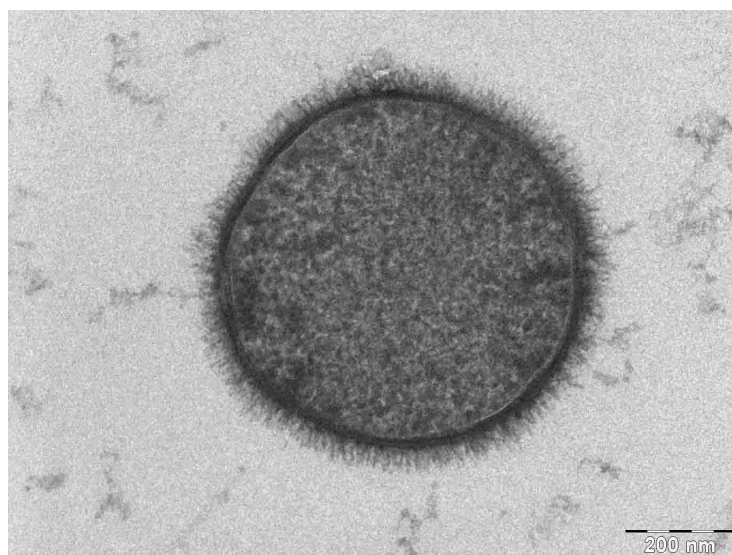


Figure 52: TEM image of a *B. subtilis* bacterium with the visible glycocalyx around the cell.^[187]

The glycocalyx is a thin mucus wallet of a complex glycoconjugate system of over 100 nm around the cell membrane of eucaryotic cells and at the cell wall of procaryotic cells. The outward lipid film contains phospholipids and glycolipids which have oligosaccharides to their outward oriented ends. Plants, in contrast, do not possess a glycocalyx. The oligosaccharides of the glycocalyx are covalently bound to glycoproteins and glycolipids.^[188] The substantial glycosides of the glycocalyx are glucose, galactose, fructose, mannose and glucosamine.

The interaction of these glycoconjugates plays an important role in different biological processes like cell communication, protection against chemical influences, receptor binding and cell adhesion. The processes around the glycocalyx are not fully understood yet. Because of this important role and complex function, the understanding of this biological topic has a high relevance in biological and medical research. The Glycoscience tries to understand the molecular interactions on these surfaces between glycosides and bacteria such as lectins (sugar binding proteins).

5.2 Motivation

This project focusses on the preparation and characterization of carbohydrate containing self assembled monolayers on gold surfaces. These molecules, obtained from the working group of Prof. Dr. Thisbe K. Lindhorst, (Otto Diels-Institute of Organic Chemistry, synthetic work was done by Dr. Vijayanand Chandrasekaran, Christian-Albrechts-University of Kiel), contain azobenzene groups as a light switchable unit. The N=N double bond of the *trans* isomer is isomerizable by irradiation of light of 365 nm to a meta stable *cis* isomer. This *cis* isomer can be irradiated with blue light of 440 nm and the *trans* isomer will be obtained again.

The synthesis of these molecules can be done in a four step synthesis to obtain different alkanethioacetate derivatives of azobenzene α -D mannosides with different chain lengths. These molecules contain acetyl-protected mannoside units. Mannose was employed because of being involved in many important biological recognition processes. The mannose units are connected to an azobenzene group *via* an ether-group, a long alkyl chain as spacer group and a thioacetate group as an anchor group for the gold surface.

The sulfur was protected as a thioacetate group. This thioacetate group can be deprotected *in situ* with the help of an ammoniumhydroxide solution as a base. The isomerization of these molecules in solution works very well with a half-life of 25 hours. Due to the bulky mannose head groups of these molecules, a diluter molecule was added to form mixed SAMs. The diluter molecules, 1-undecane-thioacetate, contain the same number of carbon atoms in the alkyl chain as the azomannose-molecule to obtain optimal *van-der-Waals* interactions between the diluter molecules and the mannose functionalized molecules. The resulting SAMs on the gold surface are stabilized by non covalent *van-der-Waals* interactions and form a densely packed film.

Optimal conditions for SAM formations have been found out and formations of SAMs both with and without adding a base for deprotection have been compared. The main long term goal of this project in the future is to build up model systems to create a switchable glyco-calix model system and to control cell adhesion in different states. The adhesion to the *trans*

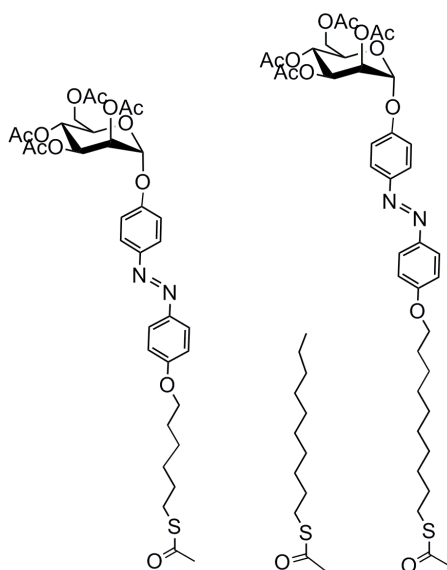


Figure 53: Investigated mannose-containing molecules with different chain length and diluter molecule for mixed SAM preparation.

isomer shall be allowed for bacteria and the adhesion to the *cis* isomer shall be undesirable. For this, the adhesion behavior of the *E. coli* bacteria containing FimH proteins will be tested. The lectin FimH proteins adhere selectively to mannose sugar units. *E. coli* bacteria can lead to sepsis, urinary tract infections and meningitis. The switching of the adhesion behavior of bacteria to the sugar containing groups on the surface was recently published by Weber *et al.* in *Angewandte Chemie*.^[189]

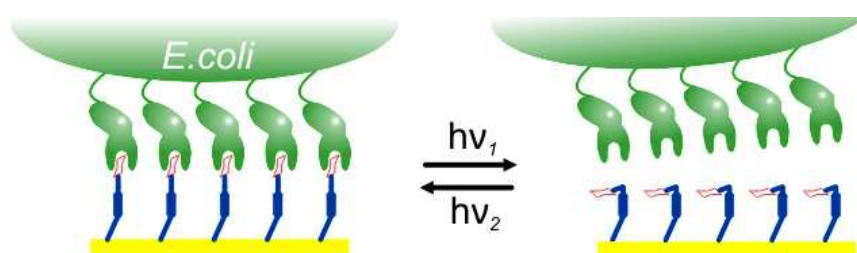


Figure 54: Schematic view of the adhesion of *E. coli* to the mannose containing molecules on the surface.^[189]

Publication in
Chemistry-A European Journal

5.3 Synthesis and surface-spectroscopic characterization of photoisomerizable glyco-SAMs on Au(111)

V. Chandrasekaran, H. Jacob, F. Petersen, K. Kathirvel, F. Tuzek* and T. K. Lindhorst*

Chem. Eur. J. **2014**, *20*, 8744-8752.

DOI: 10.1002/chem.201402075.

Photoswitchable Glycoconjugates

Synthesis and Surface-Spectroscopic Characterization of Photoisomerizable glyco-SAMs on Au(111)

Vijayanand Chandrasekaran,^[a] Hanne Jacob,^[b] Finn Petersen,^[b] Ketheeswari Kathirvel,^[b] Felix Tuczec,^{*,[b]} and Thisbe K. Lindhorst^{*,[a]}

Abstract: Photoisomerizable glyco-SAMs (self-assembled monolayers), utilizing synthetic azobenzene glycoside derivatives were fabricated. The ultimate goal of this project is to assay the influence of the 3D arrangement of sugar ligands on cell adhesion, and eventually make cell adhesion photoswitchable. However, it is a prerequisite for any biological

study on the spatial conditions of carbohydrate recognition, that photoisomerization of the surface molecules can be verified. Here, we employed IRRAS and XPS to spectroscopically characterize glyco-SAMs. In particular and unprecedented to date, we prove reversible $E \rightarrow Z \rightarrow E$ isomerization of azobenzene glycoside-terminated SAMs.

Introduction

The glycocalyx of eukaryotic cells is one of the most important and exciting surfaces in biology. This layer adopts a width of 100 nm and more on the cell surface and is composed of a remarkable variety of complex glycoconjugates.^[1] Molecular interactions of specific proteins such as the lectins^[2] with glyco-calyx components exert multiple biological functions, for example, in cell adhesion, cell signaling and immune response.^[3] Hence, protein-carbohydrate interactions are essential in both health and disease states of an organism. Consequently, it is an important goal of the glycosciences to understand how the plenty of molecular interactions occurring at the glycosylated cell surface are orchestrated in their biological and supra-molecular context. It has been known for long that carbohydrate structure is critical for specific carbohydrate-protein interactions,^[4] however, only recently it has been recognized that also the 3D presentation of saccharides is at least equally important.^[5]

This modern perception of carbohydrate recognition has led to a need for glycomimetic systems, allowing for controlled manipulation of carbohydrate presentation on a surface. Azobenzene glycosides are suited for this purpose as photoisome-

riziation of the azobenzene N=N double bond effects a very explicit change in the 3D orientation of conjugated glycosides or other biomolecules.^[6] In addition, azobenzene glycosides are easily accessible and their photoisomerization in solution works perfectly.^[7]

Here, we extend our work on photoswitchable azobenzene glycosides towards their investigation on surfaces employing self-assembled monolayers, in short SAMs.^[8] SAMs offer a well-defined and reliable system for functional surface studies.^[9] Carbohydrate-terminated SAMs, so-called glyco-SAMs,^[10] have been fabricated before, as well as SAMs in which photoresponsive azobenzene derivatives were employed.^[11] Our project is built on this methodology, involving synthesis of azobenzene glycoside derivatives for fabrication of photoswitchable glyco-SAMs and photoisomerization of such glycosylated monolayers (Figure 1). In a final step, a biological study will be performed to assay carbohydrate-lectin interactions on SAM, dependent on the isomerization state and thus the mode of carbohydrate presentation on the surface. This will eventually provide information about the significance of spatial arrangement in carbohydrate recognition.

However, it is difficult to verify if irradiation of the surface has the desired effect on the immobilized molecular monolayer, while this is of primary importance for any biological study with switchable surfaces. Here, we have investigated photoisomerization of azobenzene glyco-SAMs using infrared reflection absorption spectroscopy (IRRAS).^[12] This technique in principal allows us to observe $E \rightarrow Z$ isomerization as well as $Z \rightarrow E$ back isomerization, and to assess if dilution^[13] of an azobenzene glycoside-terminated SAM is necessary for effective photoisomerization (Figure 1).

[a] Dr. V. Chandrasekaran, Prof. Dr. T. K. Lindhorst
Otto Diels Institute of Organic Chemistry
Christiana Albertina University of Kiel
Otto-Hahn-Platz 3/4, 24118 Kiel (Germany)
Fax: (+49) 431-8807410
E-mail: tkind@oc.uni-kiel.de

[b] H. Jacob, F. Petersen, Dr. K. Kathirvel, Prof. Dr. F. Tuczec
Institute for Inorganic Chemistry
Christiana Albertina University of Kiel
Max-Eyth-Strasse 2, 24118 Kiel (Germany)
Fax: (+49) 431-8801520
E-mail: ftuczec@ac.uni-kiel.de

Supporting information for this article is available on the WWW under <http://dx.doi.org/10.1002/chem.201402075>.

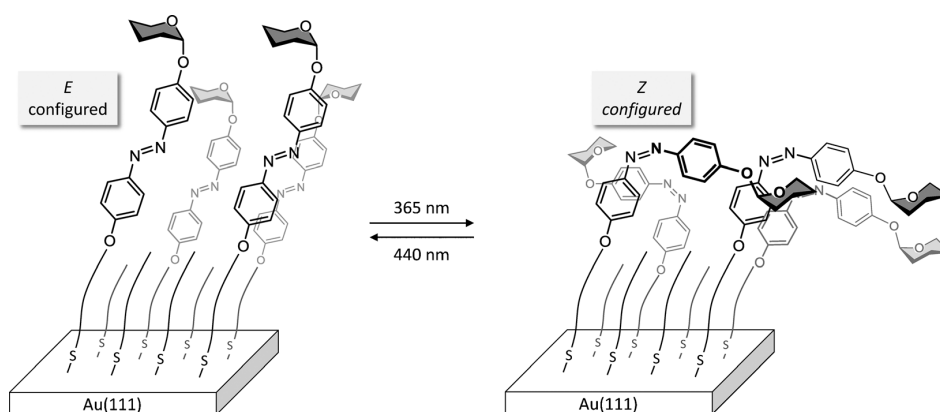


Figure 1. Upon photoisomerization (*E* to *Z* and, vice versa, *Z* to *E*) of azobenzene glycoside-decorated SAMs on Au(111) the spatial situation of carbohydrate exposition on the surface should considerably be changed. “Diluter molecules” could provide enough space for the isomerization process. This cartoon is purposely suggesting some of the 3D complexity on the surface that might occur upon switching.

Results and Discussion

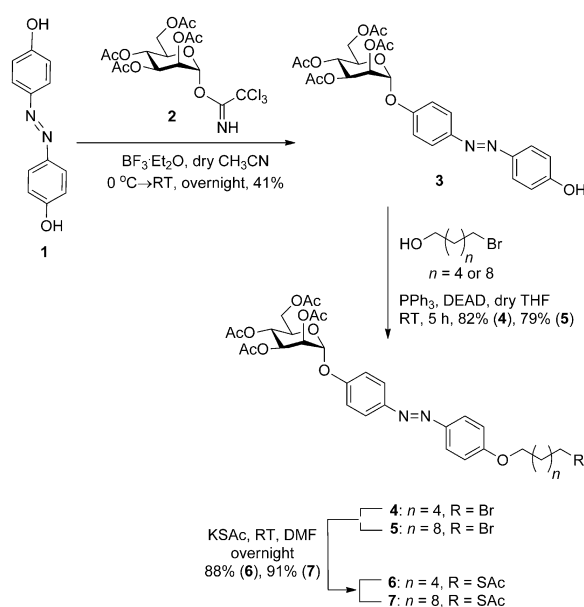
Synthesis of azobenzene glycosides for SAM fabrication

For SAM fabrication, alkanethiol derivatives are required to allow immobilization of the respective molecules on gold wafers through formation of S–Au bonds on the surface. As thiols are rather prone to air oxidation,^[14] thioacetates can be employed alternatively. Thus, we have targeted alkanethioacetate derivatives of azobenzene glycosides. α -Mannose (man) was employed as a typical monosaccharide component of complex glycoconjugates, which is involved in many important biological recognition processes.^[15]

Synthesis of α -azobenzene mannosides started from the literature-known azobenzene diol **1**,^[16] which can be readily mono-functionalized, as shown recently.^[7c] Here, monoglycosylation of **1** with the well-established mannosyl donor **2**^[17] under standard conditions led to the mannosyloxy-azobenzene alcohol **3** in 41% yield (Scheme 1). Next, alcohol **3** can be reacted in a Mitsunobu reaction with ω -bromoalkanol of the desired chain length. Here, 6-bromohexanol and 10-bromodecanol were employed to lead to the respective azobenzene ω -bromoalkyl ethers **4** and **5** in 82 and 79% yield, respectively. Then, the bromo substituent was replaced in a substitution reaction with potassium thioacetate at room temperature leading to the desired thioacetates **6** in 88% and **7** in 91% yield. These were utilized for the formation of SAMs in the next step.

Fabrication of SAMs and characterization by IRRAS

First, optimal conditions for SAM fabrication were evaluated using thioacetate **6**. The compound was dissolved in ethanol and SAM formation was attempted either directly,^[18] or after addition of ammonium hydroxide as a base to effect in situ-deprotection of the thioacetyl group and formation of the free thiol. The latter method has also often been employed in SAM fabrication^[19] and can be controlled so that *O*-acetates remain intact.



Scheme 1. Synthesis of **6** and **7**, two alkanethioacetate derivatives of azobenzene α -D-mannoside with varied chain length.

The resulting SAMs were investigated using IRRAS and compared to the IR bulk spectrum of **6** (Figure 2). Based on the surface selection rule (SSR), only the vibrations with a component of the transition dipole moment (TDM) perpendicular to the surface plane can interact with the incident light and are observed in IRRAS. As a result, a lower number of bands appear in the IRRAS than in the bulk IR spectra. Moreover, vibrational bands with TDMs perpendicular to the gold surface are more intense than those with TDMs nearly parallel to the surface. Of course, most TDMs are neither exactly parallel nor exactly perpendicular and therefore appear in IRRAS with comparable intensity of the bulk material.

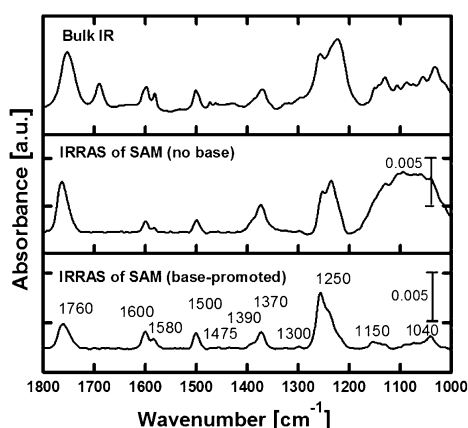


Figure 2. Mid- to low-frequency regions of the bulk IR spectrum of **6** (top) and of IRRAS spectra of SAMs formed from a solution of **6** in ethanol without base (middle) or base-promoted (bottom).

In the bulk spectrum of compound **6** (Figure 2, top) the C=O stretching vibrations of the *O*-acetyl groups of the sugar ring are observed at $\sim 1750\text{ cm}^{-1}$. The carbonyl band of the terminal thioester functionality is found at a lower frequency, namely at 1690 cm^{-1} . In both, direct (middle spectrum) and base-promoted (bottom spectrum) adsorption of **6**, the absence of the thioester C=O stretching band indicates complete conversion of the thioacetate to the respective thiol. We have to note, however, that also some deprotection of the mannose acetyl groups takes place. On the other hand, IRRAS measurements with SAMs formed from a solution of thioacetate **6** without any addition of base showed a rather broad and intense band between 1000 and 1200 cm^{-1} whereas base-promoted SAM formation gave a well-defined IRRAS spectrum in this region. In addition, direct SAM formation from thioacetates is slower^[20] and higher concentrations of **6** were required to achieve reproducible SAMs. From these results it became clear, that base-promoted SAM fabrication from thioacetates such as **6** is superior over direct deposition from a neutral solution and results in SAMs of better quality. Consequently, for the formation of all other monolayers investigated in this study, the base-promoted method was employed.

Then thioacetate **7**, having a longer alkyl chain than **6** was investigated. The base-promoted method was employed for immobilization and the resulting SAM was again investigated by IRRAS (Figure 3). In this Figure, bulk IR and calculated spectra are provided for comparison, and vibrational modes of **7** were assigned in full detail (cf. Table S1, Supporting Information). The most intense band in the IRRAS spectrum of **7**-SAM at $\sim 1250\text{ cm}^{-1}$ contains the $\text{C}_{\text{aryl}}\text{-O}$ stretching vibrations of the azobenzene moiety as well as (at least) one C–O(acetyl) stretch of the *O*-acetyl groups oriented perpendicular to the surface. According to the SSR, this indicates that the molecules are preferentially oriented perpendicular to the gold surface. Importantly, comparison of **6**-SAM and **7**-SAM shows rather similar IRRAS spectra in the mid- to low-frequency regions (Figures 2 and 3, $1800\text{--}1000\text{ cm}^{-1}$) whereas the CH_2 symmetric and

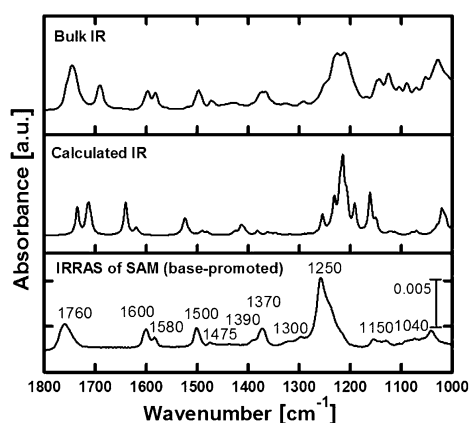


Figure 3. Mid- to low-frequency regions of the bulk IR spectrum of **7** (top) and the IRRAS spectrum of the SAM formed from a slightly basic solution of **7** (bottom), in comparison to the calculated IR spectrum (middle).

asymmetric stretching vibrations at 2850 and 2950 cm^{-1} are much more pronounced in the case of **7**-SAM than in the case of **6**-SAM (cf. Figure S22, Supporting Information). As the intensity increase upon going from **6** to **7** is much larger than 66% (corresponding to a transition from a C_6 to a C_{10} chain length), we conclude that the coverage is increased in case of the long-chain alkanethioacetate **7**. Indeed, it has been reported earlier that thiols and thioacetates, respectively, of longer chain length result in better SAMs than when their analogs with shorter alkyl chains are used.^[21]

Consequently, for the following irradiation experiments, azobenzene mannoside **7** having the long decyl chain was employed. First, photoisomerization of the azobenzene glycoside **7** was tested in solution.

Photoisomerization of compound **7** in solution

Irradiation of a 0.04 mmol solution of *E*-**7** in EtOH was carried out under exclusion of ambient light at room temperature using a 365 nm light-emitting diode (LED). Photostationary states (pss) were reached after 8–10 minutes as monitored by UV/Vis and ^1H NMR spectroscopy. Based on the integration of the anomeric sugar proton H-1 (5.61 ppm for *E* and 5.48 ppm for *Z* isomer), *E/Z* ratios were determined. According to ^1H NMR spectroscopy azobenzene mannoside **7** is *E*-configured by more than 99% in the ground state (gs) and after irradiation, >98% of the *Z* isomer is obtained (cf. Supporting Information, Figure S21). UV/Vis spectra show the typical absorption maximum of 353 nm for the *E* isomer and after irradiation absorption of the *Z* isomer at 312 and 444 nm (Figure 4). *Z*→*E* back isomerization by irradiation at 440 nm led back to $\sim 70\%$ of *E* isomer (Figure S21). Stable switching between *E* and *Z* was shown through five cycles (Figure 4, inset). The half-life $\tau_{1/2}$ of the *Z* isomer was determined by UV/Vis spectroscopy as 25 h (cf. Supporting Information).

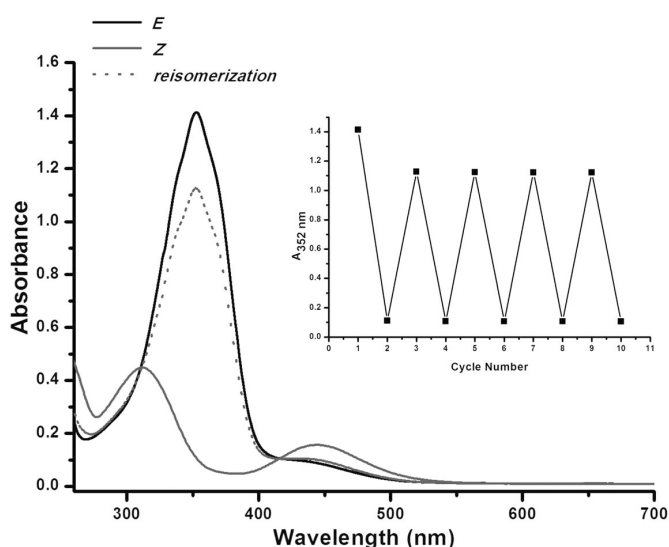


Figure 4. UV/Vis spectra of azobenzene glycoside derivative **7** ($4.0 \times 10^{-5} \text{ mol L}^{-1}$ in EtOH, $18 \pm 1^\circ \text{C}$): *E* and *Z* isomer and after reisolated from *Z* to *E*. Inset: Reversible photo-switching of **7** ($4.0 \times 10^{-5} \text{ mol L}^{-1}$ in EtOH, $18 \pm 1^\circ \text{C}$): alternating irradiation at 365 and 440 nm through 5 cycles.

IRRAS study of *E*→*Z* isomerization of photoswitchable glyco-SAMs

As the azobenzene mannoside derivative **7** shows a reliable switching behavior in solution, photoisomerization on SAM was investigated next. Thus, SAMs were formed from a solution of *E*-**7** and then irradiated with 365 nm LED light for 30–45 minutes to effect isomerization of the azobenzene unit on SAM. IRRAS then indicated a slight decrease in the intensity of the prominent band at 1250 cm^{-1} which contains the $\text{C}_{\text{aryl}}\text{--O}$ stretching vibrations of the azobenzene unit. The mid- to low-frequency regions of the IRRAS spectra of **7**-SAM before (in black) and after irradiation (in gray) are compared in Figure 5. The observed changes are reproducible but weak, though *E*→*Z* isomerization of **7** in solution was almost complete. Therefore, it was reasoned that in contrast to the situation in solution, a SAM formed from azobenzene mannoside **7** might be too densely packed to allow easy *E*→*Z* isomerization on the surface. Additional steric hindrance could arise from the fact that the immobilized molecules might be tilted on the surface,^[8] which can also impair the *E*→*Z* isomerization process. To address this problem and to diminish steric hindrance of *E*→*Z* isomerization on the surface, in the next step so-called mixed SAMs were prepared in which **7** was immobilized together with less bulky alkanethioacetates.

Fabrication of mixed SAMs and characterization by IRRAS

Mixed SAMs (*m*SAMs) were fabricated by immersion of gold wafers in a mixed solution of **7** and an appropriate “diluter molecule”. In our first attempt, 6-phenoxy-hexylthioacetate (**8**) was employed as diluter as it was expected that the terminal phenoxy moiety might effectively separate the more bulky

azobenzene glycoside molecules (**7**). Solutions with **7/8** ratios of 1:1, 3:7, and 1:10 were employed, but according to IRRAS *E*→*Z* isomerization was not improved. Next, 1-undecanethioacetate (**9**) was used as diluter molecule. Different ratios of **7** and **9** were tested and the best result was obtained with **7:9** in a 1:4 ratio. Hence, gold wafers were typically immersed in a 1 mm ethanolic solution of a 1:4 mixture of *E*-**7** and **9** for co-adsorption within 24 h. Comparison of the IRRAS spectra of the *m*SAM with the SAM formed from pure **7**, however, shows that the intensity of azobenzene mannoside **7** only decreases by about 40% (and not by 80%, as anticipated) upon going from the concentrated to the diluted SAM (cf. Figure 6). This indicates that less molecules of the diluter compound **9** have been adsorbed to the surface than expected. However, the band at $\sim 1250 \text{ cm}^{-1}$ gets more symmetric upon dilution, which indicates that the packing of **7** in the *m*SAM has changed, suggesting that indeed a diluted SAM was formed. Nevertheless, statistical distribution of the azobenzene mannoside (**7**) and diluter molecules (**9**) might be compromised by segregation effects evolving with time.^[22]

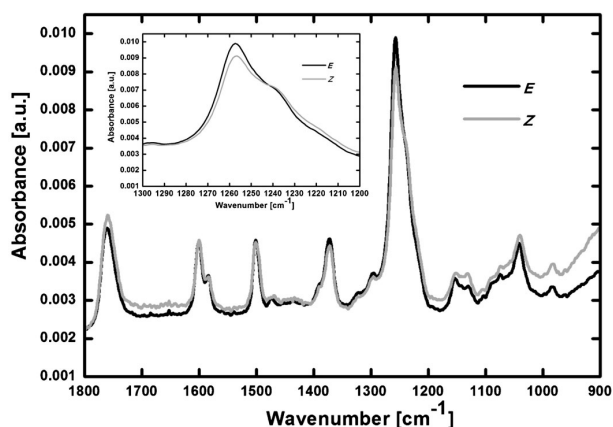


Figure 5. Mid- to low-frequency region of IRRAS spectra of **7**-SAM before (in black) and after irradiation (in gray). The observed change in the intensity of the important peak at $\sim 1250 \text{ cm}^{-1}$ is enlarged in the inset.

To further characterize the obtained *m*SAMs, fabricated from mixtures of *E*-**7** and **9** on Au(111), X-ray photoelectron spectroscopy (XPS) was employed. C 1s, S 2p and N 1s spectra were measured (Figure 7, for XPS characterization of pure SAM cf. Figure S25). The C 1s XP spectrum of the *m*SAM shows three different species. The major peak at 284.6 eV (red, 71% of the total intensity) belongs to aromatic and aliphatic carbon atoms, the minor peak at 285.2 eV (blue, 24% intensity) can be assigned to carbon atoms bound to heteroatoms (C–N, C–O), and a third peak at 286.6 eV (green, 5%) corresponds to the carbon atoms of the carboxyl groups.^[23] The N 1s XP spectrum of *m*SAM shows one species. According to the literature the

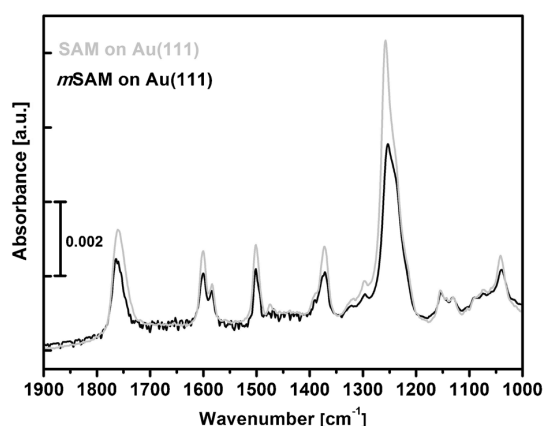


Figure 6. Mid- to low-frequency regions of the IRRRA spectra of SAMs formed from pure *E*-7 (SAM in gray) and from a mixed solution with 7/9 1:4 (*m*SAM in black).

peak at 400.0 eV (magenta) corresponds to the nitrogen atoms of the azobenzene N=N double bond.^[24] The S 2p spectrum of *m*SAM, finally, exhibits three components. The highest contribution (60% of the total intensity) derives from a species with a doublet at 161.9/163.1 eV (red) which corresponds to thiolate bound to Au.^[25] At lower energies, that is, at 161.2/162.4 eV, a second species (23%, blue) is observed which is assigned to sulfur atoms adsorbed to Au.^[8c] This contribution is generally observed in this type of experiments and associated with decomposition of sulfur-containing molecules on the Au surface.^[26] The third species of the spectrum at 163.0/164.2 (17%, green) indicates thiolate units which are not bound to the surface. Based on the literature, we assume that the relatively large fraction of unbound thiolate is due to the employed solvent (EtOH) which is necessary to dissolve mannoside 7, but which is otherwise known as less favorable solvent for long-chain alkanethiols.^[25c]

In summary, XPS supports the formation of mixed SAMs from 7 and 9, as the XP spectra show the expected signals for N 1s, S 2p and C 1s.

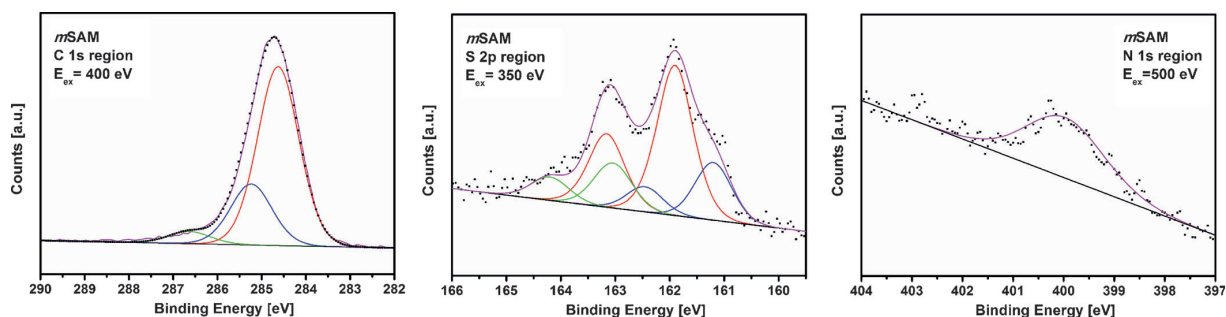


Figure 7. XPS characterization of mixed SAMs, fabricated from a 1:4-mixture of *E*-7 and 9. Carbon 1s, sulfur 2p and nitrogen 1s XP spectra of *m*SAM are shown from left to right.

IRRAS study of *E*→*Z* isomerization of *m*SAMs

Having demonstrated the structural integrity of the mixed SAMs formed from a mixture of 7 and 9 on Au(111), these systems were finally subjected to photoisomerization experiments. Irradiation with light of 365 nm for 10 minutes indeed led to a reduction of the intensity of the 1250 cm⁻¹ band which contains the C_{aryl}-O_{man} stretching vibrations of the azobenzene units (Figure 8). Although this reduction in intensity is not very pronounced, it is larger than observed in the concentrated SAM fabricated from pure 7 (cf. Figure 5). This observation indicates that the dilution concept was principally successful.

Based on the SSR and supporting data from the literature,^[27] we assume that the intensity reduction of the 1250 cm⁻¹ band indicates an *E*→*Z* conversion of the azobenzene moiety of 7 (see above). This hypothesis can be checked by the *Z*→*E* back isomerization experiment using irradiation with 440 nm light (Figure 8). In order to be able to perform these irradiation experiments within the sample chamber of the IRRRA spectrometer, polarization modulation (PM)-IRRAS was employed, using a photo-elastic modulator and a custom-built illumination setup (cf. Experimental Section and Figure S24). In fact, 440 nm

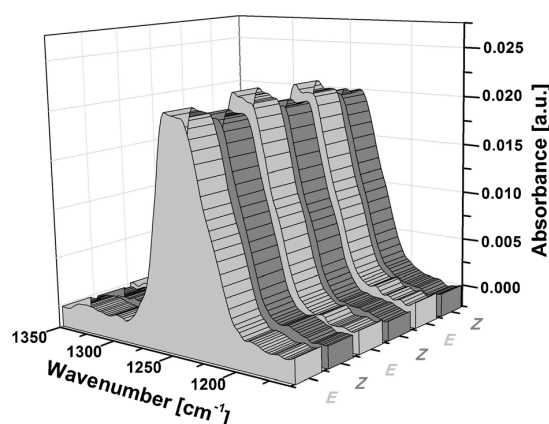


Figure 8. Photoisomerization on SAM: Prominent band ~1250 cm⁻¹ of *E*- and *Z*-isomeric 7-SAM containing the C_{aryl}-O stretching vibrations of the switchable azobenzene moiety (PM-IRRAS spectra).

irradiation of the mixed SAM of **Z-7** and **9** on Au(111) was found to restore the initial intensity of the 1250 cm^{-1} band. Moreover, forward and back isomerization could be effected several times, indicating that these processes are fully reversible within the *m*SAM (Figure 8). Apart from the 1250 cm^{-1} band, we also observe reversible intensity changes in other regions of the PM-IRRAS spectra which can be correlated with a reversible $E \rightarrow Z \rightarrow E$ isomerization of the azobenzene moiety in **7**; for example, within the double peak at $1585/1600\text{ cm}^{-1}$, which corresponds to C–C deformation vibrations of the azobenzene phenyl rings (cf. supporting information, Table S1, Figure S23).

Conclusion

Photoisomerizable glyco-SAMs were fabricated from suitably diluted solutions of synthetic azobenzene mannoside alkane-thioacetates. The characterization of these monolayers was performed using IRRAS and XPS. Then, photoisomerization of azobenzene mannoside **7** was studied in solution and, in particular, $E \rightarrow Z$ isomerization of the azobenzene double bond was shown on SAM. There, photoirradiation at appropriate wavelengths led to a characteristic change in the intensity of the prominent band at $\sim 1250\text{ cm}^{-1}$ containing the $C_{\text{aryl}}\text{--}O_{\text{man}}$ stretching vibrations. This indicates $E \rightarrow Z$ conversion of the azobenzene N=N double bond and thus a spatial change of the orientation of the immobilized glycosides on the surface. Moreover, reversible isomerization of the azobenzene glyco-SAM could be shown employing PM-IRRAS. To date, this study is unprecedented in the literature, paving the way to functional studies with photoisomerizable glyco-SAMs.

In the next step, the switching efficiency of azobenzene glycoside SAMs has to be improved, and in parallel biological assays with photoswitchable glyco-SAMs can be commenced to investigate photosensitive cell adhesion.^[28] This project involves the perspective to turn carbohydrate-specific adhesion on and off by irradiation, both spatially and time-resolved. In addition, photoswitchable glyco-SAMs bear the potential to investigate the importance of three-dimensional presentation of sugar ligands for carbohydrate recognition

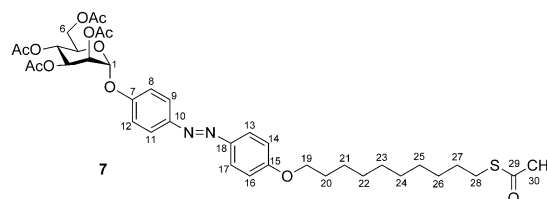
Experimental Section

General procedures

Thin-layer chromatography was performed on silica gel plates (GF 254, Merck). Detection was effected by UV and subsequent charring with 10% sulphuric acid in EtOH followed by heat treatment. Flash chromatography was performed on silica gel 60 (230–400 mesh, particle size 0.040–0.063 mm, Merck) using distilled solvents. Optical rotations were measured with a Perkin-Elmer 241 polarimeter (sodium D-line: 589 nm, length of cell: 1 dm) in the noted solvents. ^1H and ^{13}C NMR spectra were recorded with Bruker DRX-500 and AV-600 spectrometers. Chemical shifts are reported relative to internal tetramethylsilane ($\delta = 0.00\text{ ppm}$) or to D_2O solvent ($\delta = 4.76\text{ ppm}$). IR spectra were measured with a Perkin Elmer FT-IR Paragon 1000 (ATR) spectrometer and for bulk measurements with compounds **6** and **7** (cf. Figures 6 and 7) on a Bruker ATR FT-IR spectrometer in the range of 400 to 4000 cm^{-1} with a resolution of

4 cm^{-1} . ESI-MS measurements were recorded at the mariner ESI-TOF 5280 instrument (Applied Biosystems) and high resolution mass spectral analysis (HRMS) was performed on a JEOL JMS-T100GCV. MALDI-TOF mass spectra were recorded on a Bruker Biflex III instrument with 19 kV acceleration voltage. 2,5-Dihydroxybenzoic acid (DHB) was used as matrix. Air/moisture-sensitive reactions were carried out under nitrogen. UV-Vis absorption spectra were performed on Perkin-Elmer Lambda-14 and Varian Cary-5000 at $18 \pm 1^\circ\text{C}$.

For assignment of NMR spectra of compounds **3–7**, the indicated numbering was used.



Specific material and procedures

Gold surfaces: Glass substrates with a 50 Å titanium base layer and a 1000 Å evaporated gold film were purchased from EMF Corporation (Ithaca, NY) for IRRAS and PM-IRRAS measurements. The polycrystalline gold substrates for XPS were prepared by physical vapor deposition of 5 nm of titanium and subsequently 100 nm of gold onto polished (100) oriented silicon wafers (Wacker) in an evaporation chamber operated at a base pressure of 10^{-7} mbar. These substrates were subsequently used for the surface deposition of SAMs from solution.

Preparation of SAMs: Self-assembled monolayers (SAMs) were prepared on Au(111) by two different methods. First, thioacetates were prepared as 1 mM ethanolic solutions in which the gold wafers were immersed at RT for direct adsorption. According to a superior method, SAMs were formed by immersion of gold wafers in the 1 mM ethanolic thioacetate solutions with added ammonium hydroxide ($\sim 60\text{ mM}$), also at RT. In both cases, the wafer was removed from the solution after 24 h, thoroughly rinsed with ethanol and finally dried in a stream of nitrogen gas. Used glassware was cleaned with Caro's acid before use.

IRRAS: IRRAS was performed using a Bruker VERTEX 70 FT-IR spectrometer equipped with a liquid nitrogen cooled MCT detector and a horizontal reflection unit for grazing incidence (Bruker A518). A p-polarized beam at an incident angle of 80° to the surface normal was used for measurements. The resolution was set to 4 cm^{-1} . The sample chamber was purged with dry nitrogen before and during measurements. A deuterated hexadecanethiol SAM on Au(111) was used as a reference for the background spectrum. Each spectrum contains 2048 averaged spectra. The IRRAS data were processed using the OPUS program (Bruker, Germany). PM-IRRAS data were collected with the PMA 50 accessory using a liquid nitrogen-cooled MCT detector. The PEM maximum efficiency was set for the half-wave retardation at 1600 cm^{-1} for analysis of the $C_{\text{aryl}}\text{--}O_{\text{man}}$ stretching region. All spectra were recorded with 4 cm^{-1} resolution with a sensitivity of 100 mV (gain factor 10). A special illumination unit was constructed and inserted into the PM-IRRAS sample chamber to directly irradiate the samples on the sample holder and immediately start the IRRAS measurement after irradiation.

Irradiation experiments: For the *E*→*Z* isomerization of *m*SAMs, the samples were irradiated with a LED (Nichia NC4U133(T), peak wavelength: 365(±9) nm, monochromator LED with power dissipation 12 W, luminous flux: 10 [lm]). The *Z*→*E* isomerization of *m*SAMs was performed with a LED from Nichia Corporation (NS6C083AT, peak wavelength: 455 nm, monochromator LED with power dissipation 1.5 W, luminous flux: 10 [lm]). During irradiation, the distance between the LED light source and the sample was ~5 cm.

IR data processing: Bulk IR spectra were used without any baseline correction. The processing of IRRAS and PM-IRRAS data was carried out using the OPUS software Version 6.5 (Bruker, Germany). The baseline correction of the resulting IRRAS data was done by the rubber band method in an interactive mode. PM-IRRAS data have been processed by the implicit removal of the Bessel function by manual baseline correction.

Calculation details: The vibrational frequencies were calculated using a commercial program package, Gaussian 09, B3LYP (Becke-3-Parameter-Lee-Yang-Parr) functional together with a 6-31++G(d,p) basis set.^[29] After geometry optimizations, theoretical frequencies were calculated. No negative frequencies were observed. The vibrational modes were assigned by using the GaussView program.

XPS: The XPS data were recorded in the electron storage ring BESSY II, Berlin, at the HE-SGM beamline. XP spectra for C, N and S were measured in normal emission with a Scieta SES 100 analyser at 50 eV pass energy. Carbon 1s spectra were measured with an excitation energy of 400 eV, nitrogen 1s spectra with 500 eV and Sulfur 2p spectra with 350 eV. XP spectra were fitted with the program CASA-XPS.^[30] Sulfur 2p spectra were fitted with two lines of equal width with a fixed splitting of 1.2 eV and a fixed intensity ratio of 1:2 for the doublet.^[27]

Synthesis

E-4-(4'-Hydroxyphenylazo)phenyl 2,3,4,6-tetra-O-acetyl- α -D-mannopyranoside (3): To a solution of the azobenzene derivative **1** (653 mg, 3.05 mmol) and the mannosyl donor **2** (1.00 g, 2.03 mmol) in dry CH₃CN (15 mL), BF₃-etherate (260 μ L, 2.03 mmol) was added at 0 °C under nitrogen atmosphere. It was stirred at this temperature for 15 min and then at room temperature overnight. The reaction was quenched by the addition of satd. aq. NaHCO₃ solution (5 mL) and further diluted with ethyl acetate (100 mL). The phases were separated and the organic layer was washed with water (2×20 mL), dried over Na₂SO₄ and filtered. The filtrate was concentrated under reduced pressure to get the crude product which after purification by column chromatography (cyclohexane/ethyl acetate 6:4) gave the desired mannoside **3** as a yellow crystalline solid (450 mg, 0.827 mmol, 41%). *R*_f=0.26 (cyclohexane/ethyl acetate 1:1); m.p. 109–110 °C; [α]_D²⁰ = +0.75 (*c* = 1.0 in CH₂Cl₂); ¹H NMR (600 MHz, CDCl₃, 300.1 K): δ = 7.85 (d, *J* = 8.9 Hz, 2H; H-14, H-18), 7.83 (d, *J* = 8.9 Hz, 2H; H-9, H-11), 7.19 (d, *J* = 8.9 Hz, 2H; H-15, H-17), 6.94 (d, *J* = 8.8 Hz, 2H; H-8, H-12), 5.61 (d, *J*_{1,2} = 1.6 Hz, 1H; H-1), 5.59 (dd, *J*_{3,2} = 3.4 Hz, *J*_{3,4} = 10.0, 1H; H-3), 5.48 (dd, *J*_{1,2} = 1.8 Hz, *J*_{2,3} = 3.5 Hz, 1H; H-2), 5.39 (t, *J*_{4,3} = *J*_{4,5} = 10.1 Hz, 1H; H-4), 4.30 (dd, *J*_{5,6a} = 12.1, *J*_{6a,6b} = 5.3 Hz, 1H; H-6a), 4.12–4.08 (m, 2H; H-5, H-6b), 2.22, 2.07, 2.06, 2.04 (each s, each 3H; 4 OAc); ¹³C NMR (150 MHz, CD₃OD, 299.9 K): δ = 170.7, 170.3, 170.1, 169.8 (4 COCH₃), 158.3 (C-7), 157.2 (C-16), 148.5 (C-13), 147.1 (C-10), 124.8 (C-14; C-18), 124.3 (C-9, C-11), 116.8 (C-15, C-17), 115.8 (C-8, C-12), 95.7 (C-1), 69.4 (C-5), 69.3 (C-2), 68.9 (C-3), 65.9 (C-4), 62.1 (C-6), 20.9, 20.7, 20.7, 20.7 (4 COCH₃); IR (ATR): $\tilde{\nu}$ = 3407, 1744,

1587, 1498, 1368, 1211 cm⁻¹; MS (ESI): *m/z*: calcd for C₂₆H₂₈N₂O₁₁ + Na⁺: 567.51 [*M*+Na⁺]; found: 567.16.

E-4-(4'-Bromohexylphenylazo)phenyl 2,3,4,6-tetra-O-acetyl- α -D-mannopyranoside (4): To a solution of acetyl-protected mannoside **3** (300 mg, 0.55 mmol), 1-bromohexanol (150 mg, 0.83 mmol), triphenylphosphine (217 mg, 0.83 mmol) in dry THF (6 mL) and DEAD (144 mg, 0.83 mmol) were added at under N₂ atmosphere and the mixture was stirred at 0 °C 15 min. Then, the reaction mixture was allowed to warm to RT and was stirred for another 5 h. The reaction mixture was evaporated to dryness and the crude product purified by column chromatography (cyclohexane/ethyl acetate 3:2) to give the title compound **4** as a yellow solid (320 mg, 0.45 mmol, 82%). *R*_f=0.41 (cyclohexane/ethyl acetate 3:2); m.p. 99–100 °C; [α]_D²⁰ = +0.59 (*c* = 1.0 in CH₂Cl₂); ¹H NMR (500 MHz, CDCl₃, 300.0 K): δ = 7.81 (d, *J* = 8.9 Hz, 2H; H-14, H-18), 7.80 (d, *J* = 8.9 Hz, 2H; H-9, H-11), 7.14 (d, *J* = 8.9 Hz, 2H; H-8, H-12), 6.92 (d, *J* = 8.9 Hz, 2H; H-15, H-17), 5.54 (d, *J*_{1,2} = 1.4 Hz, 1H; H-1), 5.51 (dd, *J*_{3,4} = 3.5 Hz, *J*_{3,4} = 10.0, 1H; H-3), 5.41 (dd, *J*_{1,2} = 1.8 Hz, *J*_{2,3} = 3.4 Hz, 1H; H-2), 5.31 (t, *J*_{3,4} = *J*_{4,5} = 10.2 Hz, 1H; H-4), 4.22 (dd, *J*_{5,6a} = 5.5 Hz, *J*_{6a,6b} = 12.3, 1H; H-6a), 4.03 (m, 2H; H-5, H-6b), 3.98 (t, *J* = 6.4 Hz, 2H; H-19), 3.37 (t, *J* = 6.8 Hz, 2H H-24), 2.14, 1.99, 1.98, 1.96 (each s, each 3H; 4 OAc), 1.87–1.80 (m, 2H; H-23), 1.79–1.73 (m, 2H; H-20), 1.48–1.46 (m, 4H; H-22, H-21); ¹³C NMR (125 MHz, CDCl₃, 300.0 K): δ = 170.5, 169.9, 169.9, 169.7 (4 COCH₃), 161.5 (C-16), 157.1 (C-7), 148.6 (C-10), 146.9 (C-13), 124.6 (C-14, C-18), 124.2 (C-9, C-11), 116.7 (C-8, C-12), 114.7 (C-15, C-17), 95.8 (C-1), 69.4 (C-5), 69.3 (C-2), 68.8 (C-3), 68.1 (C-19), 65.9 (C-4), 62.1 (C-6), 33.8 (C-24), 32.7 (C-23), 29.0 (C-20), 27.9 (C-21), 25.3 (C-22), 20.9, 20.9, 20.7, 20.7 (4 COCH₃); IR (ATR): $\tilde{\nu}$ = 2941, 2860, 1747, 1597, 1494, 1225 cm⁻¹; MS (ESI): *m/z*: calcd for C₃₂H₃₉BrN₂O₁₁: 708.56 [*M*+1⁺]; found: 708.19.

E-4-(4'-Bromodecylphenylazo)phenyl 2,3,4,6-tetra-O-acetyl- α -D-mannopyranoside (5): To a solution of acetyl-protected mannoside **3** (250 mg, 0.46 mmol), 1-bromodecanol (163 mg, 0.69 mmol), triphenylphosphine (181 mg, 0.69 mmol) in dry THF (5 mL) and DEAD (120 mg, 0.69 mmol) were added at 0 °C under N₂ atmosphere and the reaction mixture was stirred for 15 min. Then, the reaction mixture was allowed to warm to RT and stirred for another 5 h. The reaction mixture was evaporated to dryness and the crude product purified by column chromatography (cyclohexane/ethyl acetate 3:2) to give the title compound as yellow solid (277 mg, 0.36 mmol, 79%). *R*_f = 0.19 (cyclohexane/ethyl acetate 3:7); m.p. 107–109 °C; [α]_D²⁰ = +0.56 (*c* = 1.0 in CH₂Cl₂); ¹H NMR (500 MHz, CDCl₃, 300.0 K): δ = 7.87 (d, *J* = 9.0 Hz, 2H; H-14, H-18), 7.86 (d, *J* = 9.0 Hz, 2H; H-9, H-11), 7.20 (d, *J* = 9.0 Hz, 2H; H-8, H-12), 6.99 (d, *J* = 9.0 Hz, 2H; H-15, H-17), 5.61 (d, *J*_{1,2} = 1.8 Hz, 1H; H-1), 5.58 (dd, *J*_{2,3} = 3.6 Hz, *J*_{3,4} = 10.0, 1H; H-3), 5.48 (dd, *J*_{1,2} = 1.8 Hz, *J*_{2,3} = 3.5 Hz, 1H; H-2), 5.38 (t, *J*_{3,4} = *J*_{4,5} = 10.1 Hz, 1H; H-4), 4.29 (dd, *J*_{5,6a} = 5.5 Hz, *J*_{6a,6b} = 12.2, 1H; H-6a), 4.12–4.09 (m, 1H, H-5; H6b), 4.04 (t, *J* = 6.6 Hz, 2H; H-19), 3.41 (t, *J* = 6.9 Hz, 2H; H-28), 2.21, 2.06, 2.05, 2.03 (each s, each 3H; 4 OAc), 1.89–1.79 (m, 4H; H-20, H-27), 1.51–1.45 (m, 2H; H-21), 1.38–1.27 (m, 10H; H-22, H-23, H-24, H-25, H-26); ¹³C NMR (125 MHz, CDCl₃, 300.0 K): δ = 170.5, 169.9, 169.9, 169.7 (4 COCH₃), 161.6 (C-16), 157.1 (C-7), 148.6 (C-10), 146.9 (C-13), 124.6 (C-14, C-18), 124.2 (C-9, C-11), 116.7 (C-8, C-12), 114.7 (C-15, C-17), 95.8 (C-1), 69.4 (C-5), 69.3 (C-2), 68.8 (C-3), 68.3 (C-19), 65.9 (C-4), 62.1 (C-6), 34.0 (C-28), 32.8 (C-20), 29.4 (C-27), 29.4 (C-22), 29.3 (C-23), 29.2 (C-24), 28.7 (C-25), 28.2 (C-26), 20.9, 20.9, 20.7, 20.7 (4 COCH₃); IR (ATR): $\tilde{\nu}$ = 2930, 2854, 1744, 1583, 1497, 1373, 1214 cm⁻¹; MS (ESI): *m/z*: calcd for C₃₆H₄₇BrN₂O₁₁: 764.67 [*M*+1⁺]; found: 764.09.

E-4-(4'-Acetylthiohexylphenylazo)phenyl 2,3,4,6-tetra-O-acetyl- α -D-mannopyranoside (6): A mixture of the alkyl bromide **4** (300 mg, 0.42 mmol) and KSAC (53.0 mg, 0.47 mmol) in DMF (5 mL)

was stirred at RT overnight. Then, the reaction mixture was diluted with diethyl ether (100 mL) and the combined organic phase was washed with water (2×25 mL) and dried over MgSO₄. It was filtered and the filtrate was evaporated to obtain the crude product, which was purified by column chromatography (cyclohexane/ethyl acetate 3:2) to yield the title compound as a yellow solid (262 mg, 0.37 mmol, 88%). *R*_f=0.38 (cyclohexane/ethyl acetate 3:2); m.p. 102–103°C; [α]_D²⁰=+0.39 (*c*=0.81 in CH₂Cl₂); ε = 48842 + 1000 L mol⁻¹ cm⁻¹; ¹H NMR (500 MHz, CDCl₃, 300.1 K): δ = 7.88 (d, *J*=9.0 Hz, 2H, H-14, H-18), 7.87 (d, *J*=9.0 Hz, 2H, H-9, H-11), 7.20 (d, *J*=9.1 Hz, 2H, H-8, H-12), 6.99 (d, *J*=9.1 Hz, 2H, H-15, H-17), 5.61 (d, *J*_{1,2}=1.8 Hz, 1H, H-1), 5.58 (dd, *J*_{2,3}=3.6 Hz, *J*_{3,4}=10.0, 1H, H-3), 5.48 (dd, *J*_{1,2}=1.8 Hz, 1H, *J*_{2,3}=3.5 Hz, H-2), 5.38 (t, *J*_{3,4}=*J*_{4,5}=10.1 Hz, 1H, H-4), 4.03 (t, *J*=6.5 Hz, 2H, H-19), 2.89 (t, *J*=7.0 Hz, 2H, H-24), 2.33 (s, 3H, SCOCH₃), 2.22, 2.06, 2.05, 2.03 (each s, each 3H, 4 COCH₃), 1.85–1.79 (m, 2H, H-23), 1.65–1.59 (m, 2H, H-20), 1.52–1.43 (m, 4H, H-22, H-21); ¹³C NMR (125 MHz, CDCl₃, 300.0 K): δ = 195.9 (C-25, SCOCH₃), 170.5, 169.9, 169.9, 169.7 (4 COCH₃), 161.5 (C-16), 157.1 (C-7), 148.6 (C-10), 146.8 (C-13), 124.6 (C-14, C-18), 124.2 (C-9, C-11), 116.7 (C-8, C-12), 114.7 (C-15, C-17), 95.7 (C-1), 69.4 (C-5), 69.3 (C-2), 68.8 (C-3), 68.1 (C-19), 65.9 (C-4), 62.1 (C-6), 30.7 (C-26), 29.5 (C-20), 29.1 (C-23), 29.0 (C-26, SCOCH₃), 28.5 (C-21), 25.6 (C-22), 20.9, 20.9, 20.7, 20.7 (4 COCH₃); IR (ATR): ν̄ = 2937, 2855, 1746, 1688, 1597, 1253, 1213 cm⁻¹; HRMS (EI): *m/z*: calcd for C₃₄H₄₂N₂O₁₂S: 702.2458 [M⁺]; found: 702.2458; elemental analysis calcd (%) for C₃₄H₄₂N₂O₁₂S: C 58.11, H 6.02, N 3.99, S 4.56; found C 57.77, H 6.20, N 4.03, S 4.29.

E-4-(4'-Acetylthiododecylphenylazo)phenyl 2,3,4,6-tetra-O-acetyl-α-D-mannopyranoside (7): A mixture of the alkyl bromide 5 (250 mg, 0.33 mmol) and KSAC (41 mg, 0.36 mmol) in DMF (5 mL) was stirred at RT overnight. Then, the reaction mixture was diluted with diethyl ether (100 mL) and the combined organic phases were washed with water (2×25 mL) and dried over MgSO₄. It was filtered and the filtrate was evaporated to obtain the crude product, which was purified by column chromatography (cyclohexane/ethyl acetate 3:2) to yield the title compound as a yellow solid (226 mg, 0.29 mmol, 91%). *R*_f=0.17 (cyclohexane/ethyl acetate 7:3); m.p. 113–114°C; [α]_D²⁰=+0.32 (*c*=0.67 in CH₂Cl₂); ε = 18715±498 L mol⁻¹ cm⁻¹; ¹H NMR (500 MHz, CDCl₃, 300.1 K): δ = 7.87 (d, *J*=9.0 Hz, 2H; H-14, H-18), 7.86 (d, *J*=9.0 Hz, 2H; H-9, H-11), 7.20 (d, *J*=9.0 Hz, 2H; H-8, H-12), 6.99 (d, *J*=9.0 Hz, 2H; H-15, H-17), 5.61 (d, *J*_{1,2}=1.7 Hz, 1H; H-1), 5.58 (dd, *J*_{2,3}=3.6 Hz, *J*_{3,4}=10.0, 1H; H-3), 5.48 (dd, *J*_{1,2}=1.8 Hz, *J*_{2,3}=3.5 Hz, 1H; H-2), 5.38 (t, *J*_{3,4}=*J*_{4,5}=10.2 Hz, 1H; H-4), 4.30 (dd, *J*_{5,6a}=5.9 Hz, *J*_{6a,6b}=12.6, 1H; H-6a), 4.13–4.07 (m, 2H, H-5; H-6b), 4.03 (t, *J*=6.4 Hz, 2H; H-19), 2.87 (t, *J*=6.9 Hz, 2H; H-28), 2.32 (s, 3H; SCOCH₃), 2.22, 2.06, 2.05, 2.03 (each s, each 3H; 4 COCH₃), 1.84–1.79 (m, 2H; H-20), 1.59–1.54 (m, 2H; H-27), 1.50–1.44 (m, 2H; H-21), 1.37–1.26 (m, 10H; H-22, H-23, H-24, H-25, H-26); ¹³C NMR (125 MHz, CDCl₃, 300.0 K): δ = 196.1 (C-29, SCOCH₃), 170.5, 169.9, 169.9, 169.7 (4 COCH₃), 161.6 (C-16), 157.1 (C-7), 148.6 (C-10), 146.8 (C-13), 124.6 (C-14, C-18), 124.2 (C-9, C-11), 116.7 (C-8, C-12), 114.7 (C-15, C-17), 95.7 (C-1), 69.4 (C-5), 69.3 (C-2), 68.8 (C-3), 68.4 (C-19), 65.9 (C-4), 62.1 (C-6), 30.6 (C-30, SCOCH₃), 29.5 (C-27), 29.4–26.9 (C-20, C22–C28), 26.0 (C-21), 20.9, 20.9, 20.7, 20.7 (4 COCH₃); IR (ATR): ν̄ = 2925, 2853, 1744, 1691, 1581, 1497, 1365, 1223 cm⁻¹; HRMS (EI): *m/z*: calcd for C₃₈H₅₀N₂O₁₂S: 758.3084 [M⁺]; found: 758.3084; elemental analysis calcd (%) for C₃₈H₅₀N₂O₁₂S: C 60.14, H 6.64, N 3.69, S 4.23; found C 60.20, H 6.78, N 3.74, S 4.05.

Acknowledgements

The authors thank Deutsche Forschungsgemeinschaft (DFG) for funding of this research (SFB 677). We also wish to express our gratitude to Prof. A. Terfort (Frankfurt) for the generous gift of deuterated hexadecanethiol, to Dr. Th. Strunskus (Kiel) for his help with XPS measurements and to Dr. B. Sahlmann (Kiel) for providing the LED illumination unit used in the PM-IRRAS experiments.

Keywords: azobenzene · glycosides · photoswitching · self-assembly · IR spectroscopy

- a) J. C. Paulson, O. Blixt, B. E. Collins, *Nature Chem. Biol.* **2006**, *2*, 238–248; b) M. D. Mager, V. LaPointe, M. M. Stevens, *Nature Chem.* **2011**, *3*, 582–589.
- a) J. M. Rini, *Annu. Rev. Biophys. Biomol. Struct.* **1995**, *24*, 551–577; b) N. Sharon, H. Lis, *Glycobiology* **2004**, *14*, 53R–62R.
- a) L. L. Kiessling, R. A. Splain, *Ann. Rev. Biochem.* **2010**, *79*, 619–653; b) C. D. Rillahan, J. C. Paulson, *Ann. Rev. Biochem.* **2011**, *80*, 797–823; c) J. E. Hudak, S. M. Canham, C. R. Bertozzi, *Nature Chem. Biol.* **2014**, *10*, 69–75.
- a) C. R. Bertozzi, L. L. Kiessling, *Science* **2001**, *291*, 2357–2364; b) M. A. Wolfert, G.-J. Boons, *Nature Chem. Biol.* **2013**, *9*, 776–784.
- H.-J. Gabius, S. André, J. Jiménez-Barbero, A. Romero, D. Solís, *Trends Biochem. Sci.* **2011**, *36*, 298–313.
- a) G. Hayashi, M. Hagihara, K. Nakatani, *Chem. Eur. J.* **2009**, *15*, 424–432; b) R. H. Kramer, D. L. Fortin, D. Trauner, *Curr. Opin. Neurobiol.* **2009**, *19*, 1–9; c) M.-M. Russev, S. Hecht, *Adv. Mater.* **2010**, *22*, 3348–3360.
- a) O. Srinivas, N. Mitra, A. Suroliya, N. Jayaraman, *Glycobiology* **2005**, *15*, 861–873; b) F. Hamon, F. Djedaini-Pilard, F. Barbot, C. Len, *Tetrahedron* **2009**, *65*, 10105–10123; c) V. Chandrasekaran, T. K. Lindhorst, *Chem. Commun.* **2012**, *48*, 7519–7521; d) V. Chandrasekaran, K. Kolbe, F. Beir-oth, T. K. Lindhorst, *Beilstein J. Org. Chem.* **2013**, *9*, 223–233.
- a) K. L. Prime, G. M. Whitesides, *Science* **1991**, *252*, 1164–1167; b) J. C. Love, L. A. Estroff, J. K. Kriebel, R. G. Nuzzo, G. M. Whitesides, *Chem. Rev.* **2005**, *105*, 1103–1169; c) C. Vericat, M. E. Vela, G. Benitez, P. Carro, R. C. Salvarezza, *Chem. Soc. Rev.* **2010**, *39*, 1805–1834.
- a) B. T. Houseman, M. Mrksich, *Chem. Biol.* **2002**, *9*, 443–454; b) Z.-L. Zhi, N. Laurent, A. K. Powell, R. Karamanska, M. Fais, J. Voglmeir, A. Wright, J. M. Blackburn, P. R. Crocker, D. A. Russell, S. Flitsch, R. A. Field, J. E. Turnbull, *ChemBioChem* **2008**, *9*, 1568–1575; c) M. Kind, C. Wöll, *Prog. Surf. Sci.* **2009**, *84*, 230–278; d) J. T. Koepsel, W. L. Murphy, *ChemBioChem* **2012**, *13*, 1717–1724.
- a) Y. Zhang, S. Luo, Y. Tang, L. Yu, K.-Y. Hou, J.-P. Cheng, X. Zeng, P. G. Wang, *Anal. Chem.* **2006**, *78*, 2001–2008; b) M. Kleinert, T. Winkler, A. Terfort, T. K. Lindhorst, *Org. Biomol. Chem.* **2008**, *6*, 2118–2132; c) L. Ban, M. Mrksich, *Angew. Chem.* **2008**, *120*, 3444–3447; *Angew. Chem. Int. Ed.* **2008**, *47*, 3396–3399; d) Y. Liu, A. S. Palma, T. Feizi, *Biol. Chem.* **2009**, *390*, 647–656; e) M. Mrksich, *Acta Biomater.* **2009**, *5*, 832–841; f) P. M. Dietrich, T. Horlacher, P.-L. Girard-Laurault, T. Gross, A. Lippitz, H. Min, T. Wirth, R. Castelli, P. Seeberger, W. E. S. Unger, *J. Carbohydr. Chem.* **2011**, *30*, 361–372; g) P. M. Dietrich, T. Horlacher, P.-L. Girard-Laurault, T. Gross, A. Lippitz, H. Min, T. Wirth, R. Castelli, P. H. Seeberger, W. E. S. Unger, *Langmuir* **2011**, *27*, 4808–4815; h) T. Frymer, H.-H. Lee, A. Mangone, T. Ekblad, M. E. Pettitt, M. E. Callow, J. A. Callow, S. L. Conlan, R. Mutton, A. S. Clare, P. Konradsson, B. Liedberg, T. Ederth, *Langmuir* **2011**, *27*, 15034–15047; i) C. Grabosch, M. Kind, Y. Gies, F. Schweighöfer, A. Terfort, T. K. Lindhorst, *Org. Biomol. Chem.* **2013**, *11*, 4006–4015.
- a) H.-L. Zhang, J. Zhang, H.-Y. Li, Z.-F. Liu, H.-L. Li, *Mater. Sci. Eng. C* **1999**, *8–9*, 179–185; b) S. W. Han, *Bull. Korean Chem. Soc.* **2005**, *26*, 463–466; c) V. Ferri, M. Elbing, G. Pace, M. D. Dickey, M. Zharnikov, P. Samori, M. Mayor, M. A. Rampi, *Angew. Chem.* **2008**, *120*, 3455–3457; *Angew. Chem. Int. Ed.* **2008**, *47*, 3407–3409; d) U. Siemeling, C. Bruhn, F. Bretthauer, M. Borg, F. Träger, F. Vogel, W. Azzam, M. Badin, T. Strunskus, C. Wöll, *Dalton Trans.* **2009**, 8593–8604; e) R. Klajn, *Pure Appl. Chem.* **2010**, *82*, 2247–2279; f) N. Crivillers, S. Osella, C. Van Dyck, G. M. Lazzarini, D.

- Cornil, A. Liscio, F. Di Stasio, S. Mian, O. Fenwick, F. Reinders, M. Neuburger, E. Treossi, M. Mayor, V. Palermo, F. Cacialli, J. Cornil, P. Samori, *Adv. Mater.* **2013**, *25*, 432–436.
- [12] P. Hollis: *Infrared Reflection–Absorption Spectroscopy in Encyclopedia of Analytical Chemistry: Applications, Theory, and Instrumentation* (Ed.: R. A. Meyers), Wiley, **2000**.
- [13] a) Y. B. Zheng, J. L. Payton, C.-H. Chung, R. Liu, S. Cheunkar, B. K. Pathem, Y. Yang, L. Jensen, P. S. Weiss, *Nano Lett.* **2011**, *11*, 3447–3452; b) D. Brete, D. Przyrembel, C. Eickhoff, R. Carley, W. Freyer, K. Reuter, C. Gahl, M. Weinelt, *J. Phys. Condens. Matter* **2012**, *24*, 394015 (10 p).
- [14] a) J. M. Tour, L. Jones, D. L. Pearson, J. J. S. Lamba, T. P. Burgin, G. M. Whitesides, D. L. Allara, A. N. Parikh, S. Atre, *J. Am. Chem. Soc.* **1995**, *117*, 9529–9534; b) R. Klajn, P. J. Wesson, K. J. M. Bishop, B. A. Grzybowski, *Angew. Chem.* **2009**, *121*, 7169–7173; *Angew. Chem. Int. Ed.* **2009**, *48*, 7035–7039.
- [15] T. K. Lindhorst in *Carbohydrate-Modifying Biocatalysts* (Ed.: P. Grunwald), Pan Stanford Publishing, New Jersey, London, Singapore, **2011**, pp 119–182.
- [16] W.-H. Wei, T. Tomohiro, M. Kodaka, H. Okuno, *J. Org. Chem.* **2000**, *65*, 8979–8987.
- [17] K.-H. Jung, M. Hoch, R. R. Schmidt, *Liebigs Ann. Chem.* **1989**, 1099–1106.
- [18] A. Singh, D. H. Dahanayaka, A. Biswas, L. A. Bumm, R. L. Halterman, *Langmuir* **2010**, *26*, 13221–13226.
- [19] a) L. Cai, Y. Yao, J. Yang, D. W. Price, J. M. Tour, *Chem. Mater.* **2002**, *14*, 2905–2909; b) M. G. Badin, A. Bashir, S. Krakert, T. Strunskus, A. Terfort, C. Wöll, *Angew. Chem.* **2007**, *119*, 3837–3829; *Angew. Chem. Int. Ed.* **2007**, *46*, 3762–3764.
- [20] M. I. Béthencourt, L. O. Srisombat, P. Chinwangso, T. R. Lee, *Langmuir* **2009**, *25*, 1265–1271.
- [21] M. Min, G. S. Bang, H. Lee, B.-C. Yu, *Chem. Commun.* **2010**, *46*, 5232–5234.
- [22] F. Tantakitti, J. Burk-Rafel, F. Cheng, R. Egnatchik, T. Owen, M. Hoffman, D. N. Weiss, D. M. Ratner, *Langmuir* **2012**, *28*, 6950–6959.
- [23] H. P. Boehm, *Carbon* **2002**, *40*, 145–149.
- [24] U. Jung, S. Kuhn, U. Cornelissen, F. Tuzcek, T. Strunskus, V. Zaporotchenko, J. Kubitschke, R. Herges, O. Magnussen, *Langmuir* **2011**, *27*, 5899–5908.
- [25] a) H. Wackerbarth, R. Marie, M. Grubb, J. Zhang, A. G. Hansen, I. Chorkendorff, C. B. V. Christensen, A. Boisen, J. Ulstrup, *J. Solid State Electrochem.* **2004**, *8*, 474–481; b) L. Hallmann, A. Bashir, T. Strunskus, R. Adellung, V. Staemmler, C. Wöll, F. Tuzcek, *Langmuir* **2008**, *24*, 5726–5733; c) D. G. Castner, *Langmuir* **1996**, *12*, 5083–5086; d) H. Jacob, K. Kathirvel, F. Petersen, T. Strunskus, A. Bannwarth, S. Meyer, F. Tuzcek, *Langmuir* **2013**, *29*, 8534–8543.
- [26] K. Heister, M. Zharnikov, M. Grunze, *Langmuir* **2001**, *17*, 8–11.
- [27] S.-Y. Wang, D.-C. Huang, Y.-T. Tao, *J. Chin. Chem. Soc.* **2012**, *59*, 9–17.
- [28] J. Robertus, W. R. Browne, B. L. Feringa, *Chem. Soc. Rev.* **2010**, *39*, 354–378.
- [29] Gaussian 09, Revision A.01, M. J. Frisch, G. W. Trucks, H. B. Schlegel, G. E. Scuseria, M. A. Robb, J. R. Cheeseman, G. Scalmani, V. Barone, B. Mennucci, G. A. Petersson, H. Nakatsuji, M. Caricato, X. Li, H. P. Hratchian, A. F. Izmaylov, J. Bloino, G. Zheng, J. L. Sonnenberg, M. Hada, M. Ehara, K. Toyota, R. Fukuda, J. Hasegawa, M. Ishida, T. Nakajima, Y. Honda, O. Kitao, H. Nakai, T. Vreven, J. A. Montgomery, Jr., J. E. Peralta, F. Ogliaro, M. Bearpark, J. J. Heyd, E. Brothers, K. N. Kudin, V. N. Staroverov, R. Kobayashi, J. Normand, K. Raghavachari, A. Rendell, J. C. Burant, S. S. Iyengar, J. Tomasi, M. Cossi, N. Rega, J. M. Millam, M. Klene, J. E. Knox, J. B. Cross, V. Bakken, C. Adamo, J. Jaramillo, R. Gomperts, R. E. Stratmann, O. Yazyev, A. J. Austin, R. Cammi, C. Pomelli, J. W. Ochterski, R. L. Martin, K. Morokuma, V. G. Zakrzewski, G. A. Voth, P. Salvador, J. J. Dannenberg, S. Dapprich, A. D. Daniels, Ö. Farkas, J. B. Foresman, J. V. Ortiz, J. Cioslowski, D. J. Fox, Gaussian, Inc. Wallingford CT, **2009**.
- [30] Casa XPS, casaxps.com, Casa Software Ltd., **2009**.

Received: February 27, 2014

Published online on June 20, 2014

5.4 Conclusion

In this publication we successfully prepared SAMs of azobenzene containing mannose derivatives and also mixed SAMs of these molecules with the diluter molecule undecanethiole (Fig. 55). We characterized these functionalized Au(111) surfaces with the help of IRRAS and XPS. For the first time, pure SAMs of azobenzene mannosides were characterized and optimal conditions for SAM formations were found. Here we tested the formation of SAMs by adding a base for the deprotection of the thioacetate group in comparison to a non-base formation.

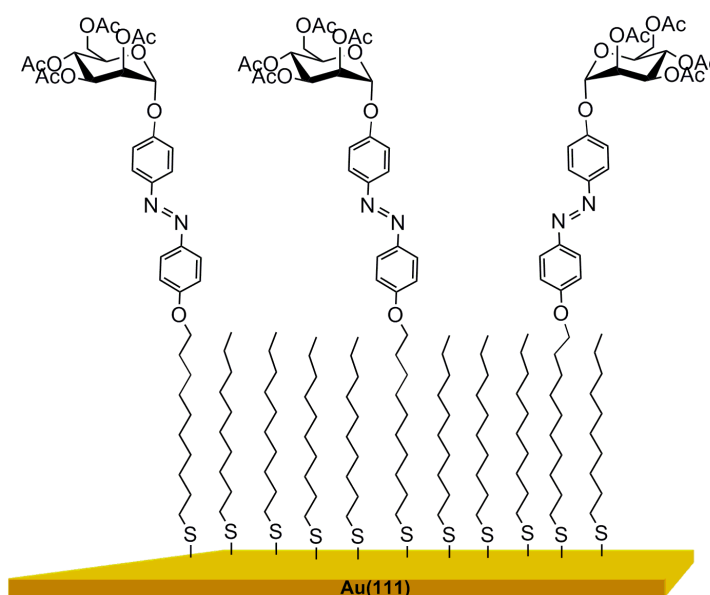


Figure 55: Schematic model of mixed SAM formation of the azomannose-derivatives and the diluter molecule.

Due to the surface selection rule, only vibrations which have a transition dipole moment or a component of the transition dipole moment perpendicular to the surface, the IRRAS data have clearly shown the formation of azobenzene containing mannose SAMs. Because of the small intensities of absorbance units in IRRAS and the XP survey spectrum we can be sure that the molecules form a monolayer on Au(111). From IRRAS data we were able to assign all bands in comparison to a DFT calculation. A full frequency calculation was performed to understand the bulk and IRRA spectra. The XP spectra were performed to define the chemical composition of the resulting SAMs. The carbon 1s spectrum shows

different species which can be assigned to aliphatic carbon atoms of the alkyl chain, aromatic carbon atoms and carbon atoms bound to hetero atoms (C-O carbonyl groups). The S 2p spectrum clearly shows the presence of thiolate bound to the surface. This indicates the formation of covalently bound SAMs and a successful deprotection of the thioacetate groups with the base NH_4OH in solution. Some molecules with a thioacetate group still remain on the surface and can be detected due to the second duplett in the S 2p XP spectrum. The third duplett can be assigned to oxidized sulfur atoms or sulfur atoms bound in an alternative way to Au(111). Irradiation experiments with these mixed SAMs have shown a change in the intensity of the C-O stretching vibration. The *trans* isomer shows higher intensity compared to the *cis* isomer. This process can be reversibly observed by irradiation with 365 nm from the *trans* to the *cis* isomer and with 440 nm from the *cis* to the *trans* isomer.

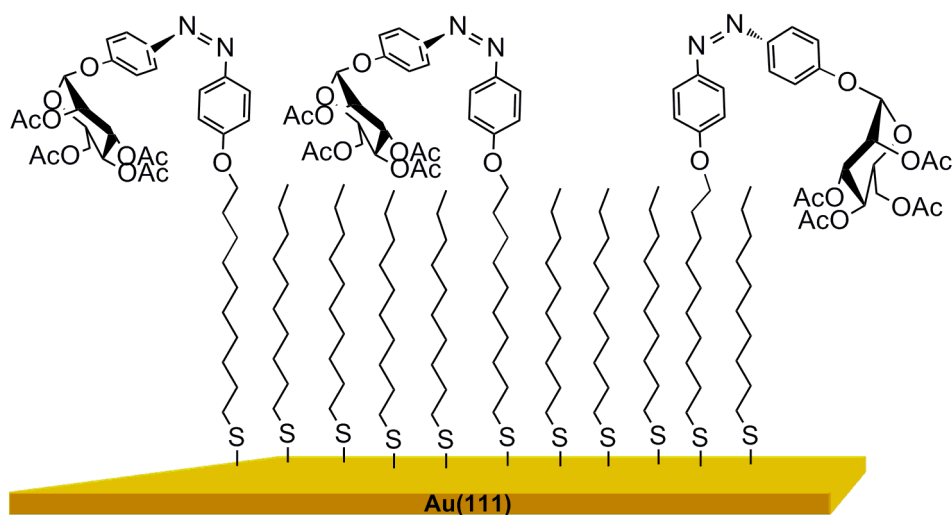


Figure 56: Schematic model of mixed SAM formation of the azomannose-derivatives in *cis* configuration and the diluter molecule.

With this publication we have laid the foundations for the preparation and spectroscopically understanding of a small thin glyco-calix model system on a solid surface and shown the reversible switchability of these molecules with IRRAS for the first time.

5.5 Outlook

As outlook for this project, Thisbe K. Lindhorst in cooperation with Prof. Andreas Terfort (Goethe University of Frankfurt) recently published the switchable adhesion of cells to azobenzene functionalized surfaces.^[189] This model system for the glycocalyx of eucaryotic human cells has a thickness of only 4 nm. Therefore, unprotected azobenzene functionalized mannose derivatives were synthesized and monolayers of these molecules were formed out of solution. The *E. coli* bacteria can adhere to the saccharide molecules of this functionalized gold surface by their contained FimH proteins.

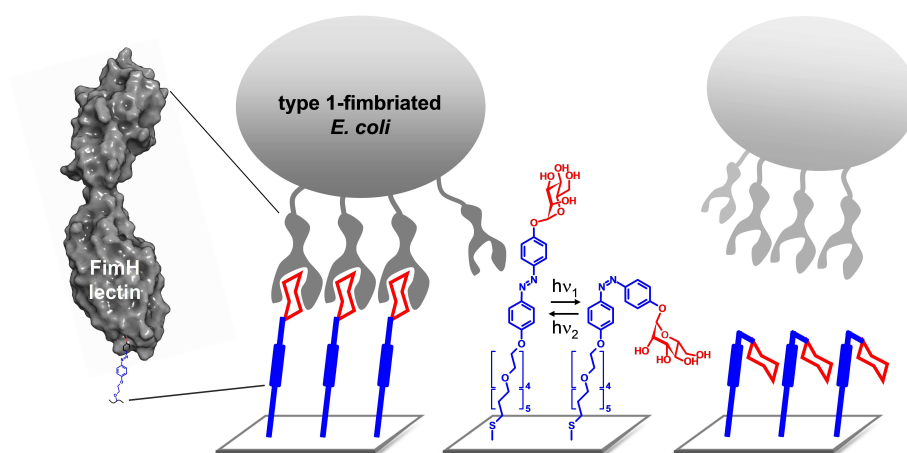


Figure 57: Schematic model of the adhesion of *E. coli* bacteria to an azobenzene mannose functionalized surface.^[189]

By irradiation of this functionalized surface with light of a wavelength of 365 nm, the azobenzene units of these molecules can switch their conformation from *trans* to *cis*. During this switching process, the molecules change their sterical environment and can not adhere to the FimH proteins anymore. After irradiation with 440 nm, the molecules change their conformation back to the *trans* isomer and the bacteria can adhere again. This process resembles a recognition process like a lock and key principle. These findings successfully show that the spatial orientation of the saccharide molecules is crucial for this process and can help to understand the interaction between cells and bacteria in more detail. The opportunity to influence the glycocalyx will lead to new insights in medicine for healing processes.

6 Summary and Outlook

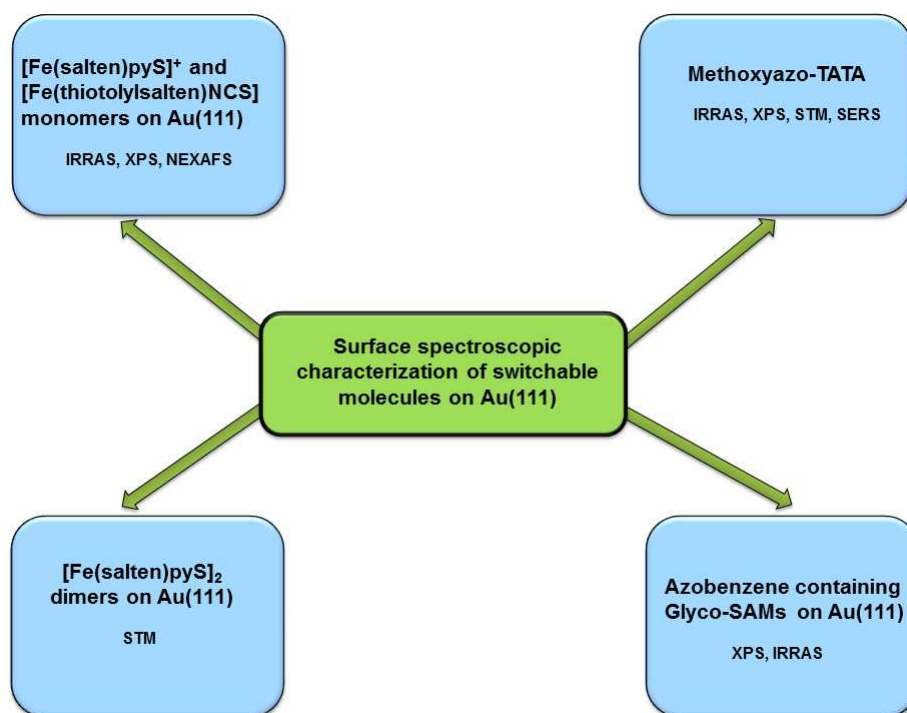


Figure 58: Summary of the presented dissertation.

In summary, this dissertation shows the surface spectroscopic characterization of different types of molecules. Spin crossover complexes were functionalized with disulfide bridging ligands for surface fixation. The resulting monomers on the surface were analyzed in detail with IRRAS, XPS and NEXAFS. The vibrational information of these adsorbed complexes were compared with DFT calculations and geometries of the adsorbed complexes were obtained.

Furthermore, a dimer of a spin crossover system was analyzed with STM regarding the behavior by injecting electrons to a metal centre. This system showed a 'remote' reversible switching process in the ligand conformation.

Moreover, organic self assembled monolayers of an azobenzene functionalized TATA platform were characterized with different techniques like SERS, XPS, STM, IRRAS and PM-

IRRAS. The azobenzene unit has a perpendicular orientation to the surface. The thermal back-relaxation from *cis* to *trans* of the azobenzene unit on top of the platform was detected by time dependent PM-IRRAS measurements.

Self assembled monolayers of mannoside-azobenzene derivatives were characterized with IR-RAS and XPS. By using diluter molecules, mixed SAMs of these molecules were obtained and the light induced reversible isomerization process was followed by IRRAS.

In the future, the ultimate goal of this project is the detection of the spin state switching of spin crossover complexes on the surface to realize bistable systems for data storage materials. Photoisomerizable ligands coordinated to the iron(III) center should realize the LD-LISC effect in monomolecular films on the surface. Alternative techniques to detect the spin state switching such as NEXAFS and XMCD can be useful.

7 General procedures and analytical techniques

Solvents for surface preparation

All used solvents for surface preparation were of pro analysis grade.

Gold substrates

For IRRAS and PM-IRRAS measurements 5.08 cm x 2.29 cm gold (1000 Å) on glass slides with an adlayer of Ti (50 Å) or Cr (50 Å) were used. These slides were purchased from EMF Corporation (Ithaca, NY).

For XPS and NEXAFS measurements sputtered Au/Cr, Au/Ti on polished (100) oriented Si wafers (Wacker) were used (Au 200 nm, Cr or Ti 8 nm).

Reference sample

For all conventional IRRAS measurements, monolayers of perdeuterated hexadecylthiol on gold-coated glass slides were used as background samples. This background sample is used to avoid spurious contamination of the gold substrate. The deuterated background SAM was prepared by immersing the annealed gold substrates into an ethanolic solution of the perdeuterated hexadecylthiol for about 24 hours. The solution was prepared by dissolving a drop of perdeuterated hexadecanethiol ($C_{16}D_{33}SH$) in 80 ml of ethanol. Each spectrum contains 2048 averaged spectra.

Bulk infrared spectroscopy

Bulk IR spectra were recorded with a Bruker ATR FT-IR spectrometer in the range of 400 to 4000 cm^{-1} with a resolution of 4 cm^{-1} .

Infrared reflection absorption spectroscopy

IRRAS measurements were performed using a Bruker VERTEX 70 FT-IR spectrometer equipped with a liquid nitrogen cooled MCT detector and a horizontal reflection unit for grazing incidence (Bruker A518). A p-polarized beam at an angle of 80° to the surface normal was used. The resolution was set to 4 cm^{-1} for all recorded spectra. The sample chamber was purged with dry nitrogen one hour before and during the measurements. PM-IRRAS data were collected with the PMA 50 accessory using a liquid nitrogen-cooled MCT detector. All spectra were recorded with 4 cm^{-1} resolution and a sensitivity of 100 mV (gain factor 10).

IR data processing

Processing of IRRAS and PM-IRRAS data were carried out using the OPUS software Version 6.5 (Bruker, Germany). Baseline corrections of the resulting PM-IRRAS data were performed by the rubber band method in an interactive mode. PM-IRRAS data were processed by the implicit removal of the Bessel function through manual baseline correction.

Irradiation Experiments

For the *trans* to *cis* isomerization of SAMs on surfaces, the samples were irradiated with a LED (Nichia Corporation NC4U133(T)), peak wavelength: 365 nm, 1 LED with power dissipation: 12 W, luminous flux: 10 lm with a distance of 5 cm to the sample. For the *cis* to *trans* isomerization of SAMs on surfaces, a LED (Nichia Corporation (NS6C083AT)), peak wavelength: 455 nm, 1 LED with power dissipation 1.5 W, luminous flux: 10 lm with a distance of 5 cm to the sample was used. This irradiation unit was placed into the spectrometer chamber (Fig. 59).



Figure 59: Irradiation-setup in Bruker Vertex 70 PMA-50 spectrometer.

Raman spectroscopy

The bulk Raman spectra were measured using an ISF66/FRA106 Fourier transform Raman spectrometer (Bruker AXS GmbH, Karlsruhe, Germany) with a resolution of 2 cm^{-1} with a 330 mW Nd-YAG laser at a wavelength of $\lambda_{ex} = 1064\text{ nm}$.

Quantum chemical calculations

Density functional theory (DFT) was used for calculating vibrational frequencies. The structure of the molecules was first optimized before a frequency calculation was performed. Quantum chemical calculations were carried out with the commercial program package Gaussian 09. The calculated results were loaded in GaussView software to animate all vibrational modes. The assignment of all appearing bands was compared to the observed bands in the bulk IR and Raman spectra. The transition dipole moments of all vibrational modes were analyzed to determine the orientation of the molecules on the surface in consideration of the surface selection rule in IRRAS.

8 Appendix

8.1 Supporting information on the Langmuir publication

Supporting Information

Langmuir

H. Jacob, K. Kathirvel, F. Petersen, T. Strunskus, A. Bannwarth, S. Meyer, F. Tucek

”Grafting of functionalized [Fe(III)(salten)] complexes to Au(111) surfaces via thiolate groups: Surface spectroscopic characterization and comparison of different linker designs”

Langmuir **2013**, 29(27), 8534-8543.

DOI: 10.1021/la400663y.

Supporting Informations on the paper

Grafting of functionalized [Fe(III)(salten)] complexes to Au(111) surfaces via thiolate groups: Surface spectroscopic characterization and comparison of different linker designs

*Hanne Jacob^a, Ketheeswari Kathirvel^a, Finn Petersen^a, Thomas Strunskus^b, Alexander
Bannwarth^a, Sven Meyer^a and Felix Tuczek^{a*}*

^aInstitut für Anorganische Chemie, Christian-Albrechts-Universität Kiel, Max-Eyth-Str.2, 24118
Kiel, Germany

^bTechnische Fakultät der Christian-Albrechts-Universität Kiel, Kaiserstraße 2, 24143 Kiel,
Germany

Author Information

corresponding author:

(F.T.) E-Mail: ftuczek@ac.uni-kiel.de, fax: +49 431 880-1523

1. Syntheses and chemical analysis

H₂salten = Bis(3-salicylideneaminopropyl)amine

The salten ligand was synthesized using 13.1 g (100 mmol) of 1,7-diamino-4-azaheptane (bis(3-aminopropylamine)) and 24.4 g (200 mmol) of salicylaldehyde in 100 ml dry methanol. The mixture was refluxed by continuous stirring for 20 min. The ligand is obtained as a yellow oily material after removing the solvent *in vacuo* and was used for the preparation of the [Fe(salten)Cl] complex and the thiotolylsalten ligand without any further purification.³⁰

EA: Calcd for CHN C 70.8, H 7.4, N 12.4, Found C 70.5, H 7.6, N 12.9.

¹H NMR (400 MHz, CDCl₃, 300 K): δ = 13.42 (bs, C-OH, 2 H), 8.32 (s, CH=N, 2 H), 7.28 (m, 2 H, H_{arom}), 7.21 (d, 2 H, H_{arom}), 6.93 (d, 2 H, H_{arom}), 6.85 (t, 2 H, H_{arom}), 3.63 (s, 4 H, N-CH₂), 2.71 (s, 4 H, NH-CH₂), 1.87 (s, 4 H, N-CH₂-CH₂-CH₂) ppm.

¹³C{¹H} NMR (100 MHz, CDCl₃, 300 K): δ = 165.0 (C=N), 161.2 (C-OH), 132.1 (C_{arom}), 131.1 (C_{arom}), 118.7 (C_{arom}), 118.5 (C_{arom}), 116.9 (C_{arom}), 57.3 (C-N), 47.5 (C-NH), 31.0 (NH-CH₂-CH₂-CH₂) ppm.

IR: 1/λ 3056 (C_{arom}/ring), (CH₂), 1632 (N=C), (C_{arom}/ring), 1317 (C-O) cm⁻¹.

[Fe(salten)Cl]

A solution of 1.62 g (10.0 mmol) anhydrous iron(III) chloride in 50 ml dry methanol was added to a solution of 3.70 g (10.0 mmol) of the salten ligand in 40 ml dry methanol. The mixture was stirred for 10 min at 50°C. After that 2.79 ml (20.0 mmol) triethylamine was added and stirred

for 1 h at 50°C. After cooling the mixture, black-violet crystals were obtained. These crystals were washed three times with methanol and diethyl ether and dried *in vacuo*.³¹

EA: Calcd for CHNCl C 56.0, H 5.41, N 9.8, Cl 6.9, Found C 56.6, H 5.5, N 10.1, Cl 7.5.

IR: 1/λ 3237 (NH), 2928,2867 (CH₂), 1627 (N=C), 1596 (C_{arom/ring}), 1310 (C-O).

[Fe(salten)(pyS)]₂(BPh₄)₂ (1-1)

The dinuclear complex was prepared by dissolving 430 mg (1.00 mmol) [Fe(salten)Cl] in 50 ml dry methanol. Then 110 mg (0.50 mmol) 4,4'-di(thiopyridine) was added to the solution and stirred at 60°C for 30 min. Afterwards 860 mg (1.00 mmol) NaBPh₄ were added. The mixture was stirred for 4 h at 60°C and stored in the fridge over night. After filtration violet/black crystals were obtained and were washed with methanol and diethyl ether.³²

EA: Calcd for CHNS C 72.4, H 7.3, N 6.1, S 3.5, Found C 71.7, H 6.6, N 6.2, S 3.9.

4,4'-Dithiobis(benzylbromide)

To a solution of 2.50 g (6.19 mmol) *p*-tolylidysulfide in 30 ml tetrachloromethane 4.30 g (24.2 mmol) of *N*-bromosuccinimide and 60.0 mg 2,2'-azobis(2-methylpropionitrile) were added. The reaction mixture was refluxed for 4 h by irradiation with a portable floodlight. The resulting solution was filtered and washed with saturated Na₂S₂O₃ solution, saturated NaHCO₃ solution, water and brine. The organic layer was dried over MgSO₄ and the solvent was removed *in vacuo*. The light orange precipitate was recrystallized in a mixture of 30 ml cyclohexane:ethylacetate (9:1).³³

EA: Calcd for CHSBr C 41.6, H 2.9, S 15.9, Br 39.5, Found C 41.4, H 2.9, S 15.9, Br 38.5.

$^1\text{H NMR}$ (400 MHz, CD_3OD , 300 K): $\delta = 7.47$ (m_c, 4 H, *H*-2 & *H*-6), 7.38 (m_c, 4 H, *H*-3 & *H*-5), 4.54 (s, 2 H, $\text{CH}_2\text{-Br}$) ppm.

$^{13}\text{C}\{^1\text{H}\}$ NMR (100 MHz, CD_2Cl_2 , 300 K): $\delta = 137.77$ ($C_{\text{arom,q}}$), 137.65 ($C_{\text{arom,q}}$), 130.39 (C_{arom}), 128.13 (C_{arom}), 127.84 (C_{arom}), 127.42 (C_{arom}), 33.47 ($\text{CH}_2\text{-Br}$) ppm.

Thiotolylsalten-ligand and $[\text{Fe}(\text{thiotolylsalten})(\text{NCS})_2$ (2-2)

The ligand and the complex were synthesized according to the literature.²²

EA: Calcd for CHNS C 70.4, H 6.6, N 9.1, S 6.9, Found C 69.1, H 6.4, N 7.5, S 6.4.

$^1\text{H NMR}$ (400 MHz, CDCl_3 , 300 K): $\delta = 13.53$ (bs, 4 H, *OH*), 8.21 (s, 4 H, $\text{CH}=\text{N}$), 7.41 (d, 4 H, $H_{\text{arom-s}}$), 7.22 – 7.30 (m, 8 H, H_{arom}), 7.17 (dd, 4 H, H_{arom}), 6.93 (d, 4 H, $H_{\text{arom-s}}$), 6.85 (t, 4 H, H_{arom}), 3.57 (t, 8 H, $\text{C}=\text{N}-\text{CH}_2$), 3.51 (s, 4 H, $\text{CH}_2\text{-Ph}$), 2.50 (t, 8 H, $\text{CH}_2\text{-N}(\text{CH}_2)_2$), 1.83 (quin, 8 H, $\text{CH}_2\text{-CH}_2\text{-CH}_2$) ppm.

$^{13}\text{C}\{^1\text{H}\}$ NMR (75 MHz, CDCl_3 , 300 K): $\delta = 164.9$ ($\text{C}=\text{N}$), 161.2 ($\text{C}-\text{OH}$), 139.1 ($\text{C}-\text{S}$), 135.4 ($\text{S}-\text{C}=\text{CH}-\text{CH}=\text{C}$), 132.1 ($\text{CH}=\text{CH}-\text{C}-\text{OH}$), 131.1 ($\text{CH}-\text{C}-\text{C}=\text{N}$), 129.5 ($\text{S}-\text{C}=\text{CH}-\text{CH}=\text{C}$), 127.6 ($\text{S}-\text{C}=\text{CH}-\text{CH}=\text{C}$), 118.7 ($\text{CH}=\text{CH}-\text{C}-\text{C}=\text{N}$), 118.4 ($\text{C}-\text{C}=\text{N}$), 116.9 ($\text{CH}=\text{C}-\text{OH}$), 58.1 ($\text{N}-\text{CH}_2\text{-Ph}$), 57.2 ($\text{CH}_2\text{-CH}_2\text{-CH}_2\text{-N}=\text{C}$), 51.2 ($\text{N}-\text{CH}_2\text{-CH}_2\text{-CH}_2$), 28.3 ($\text{CH}_2\text{-CH}_2\text{-CH}_2$) ppm.

NMR

$^{13}\text{C}\{^1\text{H}\}$ NMR spectra were measured with a Bruker Avance 600 instrument with a resonance frequency of 100 or 75 MHz at a temperature of 300 K. The ^1H NMR spectra were recorded with a Bruker Avance 400 Pulse Fourier transform spectrometer operating at proton resonance frequency of 400 MHz at a temperature of 300 K. The sample was measured with deuterated solvents. Deuterated solvents for NMR measurements were purchased from Deutero and used as supplied.

Elemental analyses

Elemental analyses were carried out on a EuroVector EuroEA3000 elemental analyzer configured for CHNS. Halogenide analysis were done by reduce the compound to ashes and made a potentiometric titration against silvernitrate.

2. XPS/ NEXAFS of $[\text{Fe}(\text{salten})\text{pyS}]_2(\text{BPh}_4)_2$ (1-1) and $[\text{Fe}(\text{salten})\text{pyS}]^+$ (1)

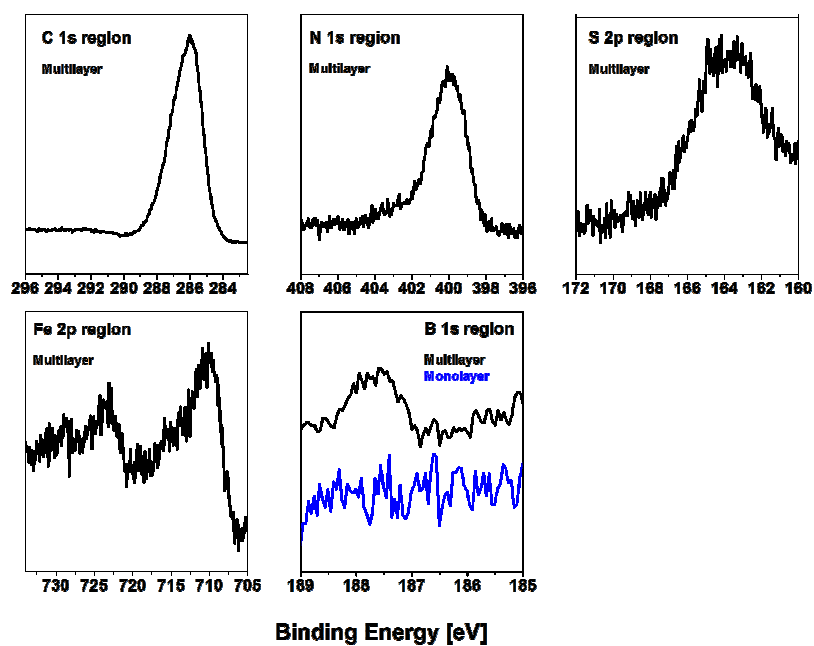


Figure S1. XP spectra of $[\text{Fe}(\text{salten})\text{pyS}]_2(\text{BPh}_4)_2$ (1-1) thick film.

Table S1. Fit parameters for the XP spectra of $[\text{Fe}(\text{salten})\text{pyS}]^+$ (1).

C 1s	Major Component	Minor Component	π to π^* shake-up
Binding Energy (ev)	285.88	287.35	290.46
Area (%)	63	30	7
fwhm	1.5	1.9	2.7

N 1s	Imine	Sec. Amin	Py-N	
Binding Energy (ev)	399.50	400.12	401.26	
Area (%)	50	25	25	
fwhm	1.6	1.6	1.6	
S 2p	Ionic/atomic sulfur	Thiolate	Disulfide	
Binding Energy (eV)	161.2, 162.4	162.0, 163.2	163.7, 164.8	
Area (%)	19, 9	36, 18	12, 6	
fhwmm	0.7	0.7	0.7	
Fe 2p	Fe2p_{3/2}	Sat1	Fe2p_{1/2}	Sat2
Binding Energy (eV)	710.35	715.02	722.47	727.11
Area (%)	37	27	19	17
fhwmm	4.4	6.0	3.5	4.6

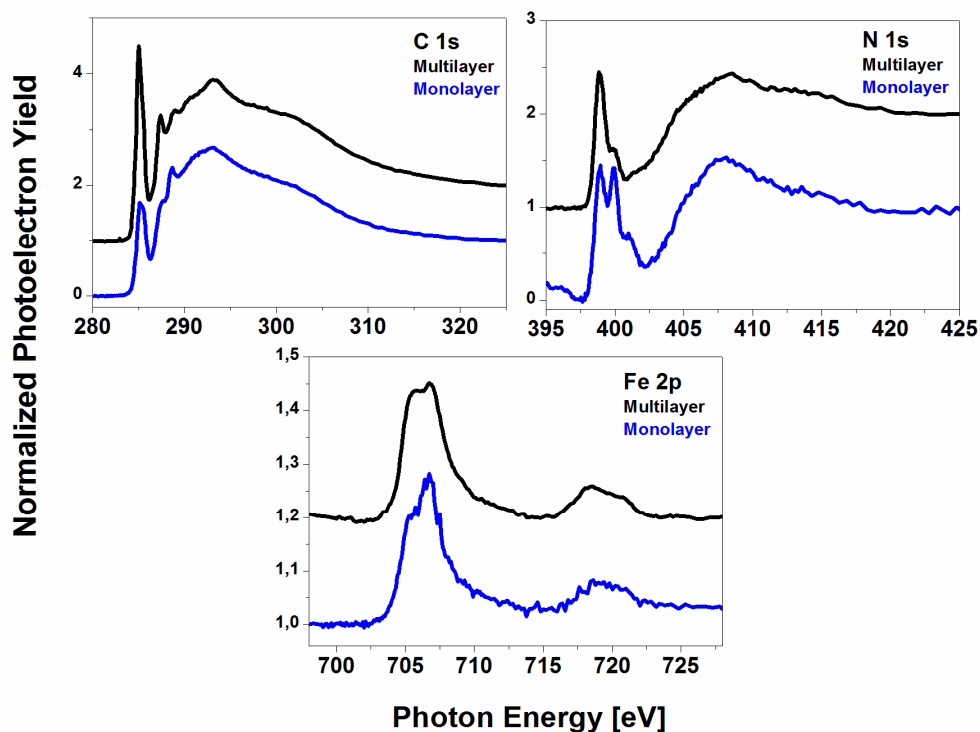


Figure S2. NEXAFS spectra of $[\text{Fe}(\text{salten})\text{pyS}]_2(\text{BPh}_4)_2$ (**1-1**) thick film in comparison with $[\text{Fe}(\text{salten})\text{pyS}]^+$ (**1**) monolayer.

Analysis:

NEXAFS spectra of $[\text{Fe}(\text{salten})(\text{pyS})]_2(\text{BPh}_4)_2$ (**1-1**) and $[\text{Fe}(\text{salten})(\text{pyS})]^+$ (**1**), respectively, obtained at the C K, N K and the Fe $L_{2,3}$ edges are shown in Figure S2. We do not intend to present a complete analysis here, which would require theoretical calculations, but give some tentative assignments or use the spectra as fingerprints of the electronic structure of the investigated molecules. For the thick film of $[\text{Fe}(\text{salten})(\text{pyS})]_2(\text{BPh}_4)_2$ (**1-1**) a pronounced resonance is observed at 285.0 eV at the carbon K edge, accompanied by some smaller

resonances at 287.4 eV, 289.0 eV and 293.1 eV. The strong resonance at 285.0 eV is typical for C 1s- π^* resonances of C-C conjugated systems. That the relative intensity decreases so much upon going from the multilayer to the monolayer can be taken as further indication that the BPh_4^- anion of $[\text{Fe}(\text{salten})(\text{pyS})]_2(\text{BPh}_4)_2$ (**1-1**) is no longer present in the monolayer. The resonances at 287.4 eV and 289.0 eV are present in the multilayer as well as in the monolayer, indicating that they mainly originate from the salten complex. The resonance at 287.4 eV is tentatively assigned to a C 1s- π^* transition of imine groups overlapping with a typical resonance observed for pyridine compounds. The assignment of the resonance at 289.0 eV which is present in the thick film and in the monolayer is less straightforward. The resonance at 293.1 eV, finally, is a σ^* resonance typical for conjugated C-C bonds, indicating that rather similar carbon-carbon bonds are present in the multilayer and the monolayer.

At the N K edge, we mainly observe three resonances for the thick film. The first at 398.9 eV is assigned to an imine-type N 1s- π^* transition, the second at 399.9 eV is tentatively assigned to a second N 1s- π^* transition of the salten ligand overlapping with the pyridine N 1s- π^* transition, and the resonance at 408.0 eV again corresponds to a σ^* resonance. In the monolayer the second resonance increases in intensity and a new feature appears as a shoulder at 401.0 eV. These findings indicate that the electronic structure monitored by the nitrogen atoms must have changed upon going from the multilayer to the monolayer. Note that a structural change of the $[\text{Fe}(\text{salten})(\text{pyS})]^+$ (**1**) complex is also inferred from the analysis of the Fe-NEXAFS and IRRAS data (*vide infra*).

3. XPS/ NEXAFS of $[\text{Fe}(\text{thiotolysalten})\text{NCS}]_2(\text{BPh}_4)_2$ (2-2) and $[\text{Fe}(\text{thiotolysalten})\text{NCS}]$ (2)

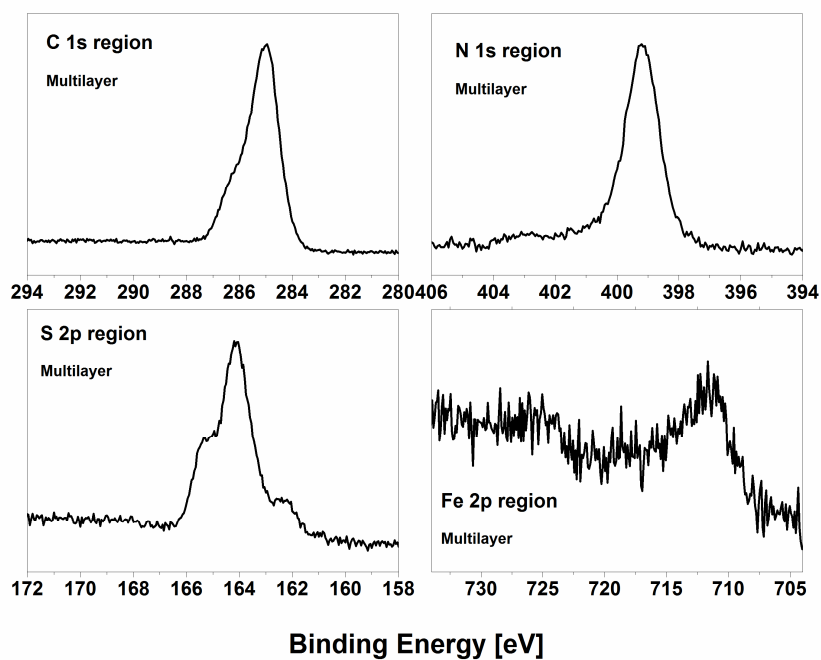


Figure S3. XP spectra of $[\text{Fe}(\text{thiotolysalten})\text{NCS}]_2$ (2-2) thick film.

Table S2. Fit parameters for the XP spectra of $[\text{Fe}(\text{thiotolysalten})(\text{NCS})]$ (2).

C 1s	Major Comp.	Minor Comp.	π to π^* shake-up		
Binding Energy (ev)	285.49	286.57	289.67		
Area (%)	65	30	5		
fwhm	1.3	1.8	3.0		
N 1s	NCS	Imine	Tert. Amin	Comp4	Comp5

Binding Energy (eV)	398.61	399.27	400.31	401.59	402.79
Area (%)	21	41	20	10	8
fhwm	1	1	1	1	1
S 2p	Ionic/atomic sulfur	Thiolate	Disulfide		
Binding Energy (eV)	161.1, 162.3	162.1, 163.3	163.8, 165.0		
Area (%)	18, 8	32,16	17, 9		
fhwm	1	1	1		
Fe 2p	Fe2p_{3/2}	Sat1	Fe2p_{1/2}	Sat2	
Binding Energy (eV)	711.18	715.28	722.89	728.82	
Area (%)	47	28	17	8	
fhwm	4.0	4.6	5	3.7	

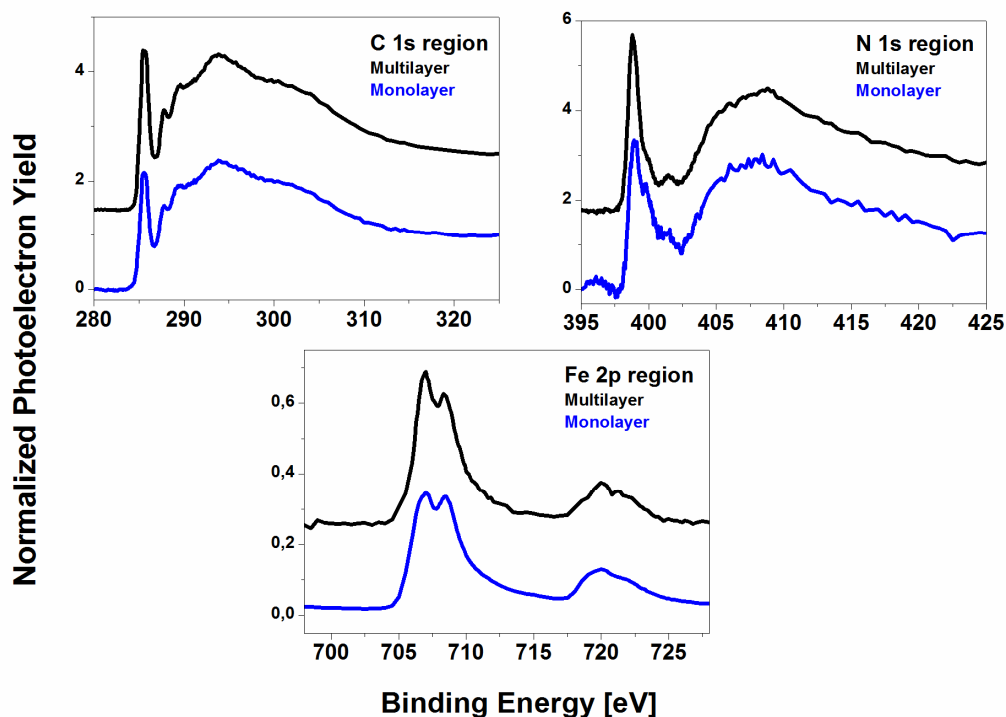


Figure S4. NEXAFS spectra of $[\text{Fe}(\text{thiotolysalten})\text{NCS}]_2$ (**2-2**) thick film in comparison with $[\text{Fe}(\text{thiotolysalten})\text{NCS}]$ (**2**) monolayer

Analysis:

NEXAFS data obtained at the C K, N K and Fe $L_{2,3}$ edges of $[\text{Fe}(\text{thiotolysalten})(\text{NCS})]_2$ (**2-2**) and $[\text{Fe}(\text{thiotolysalten})(\text{NCS})]$ (**2**) are shown in Figure S4. For the thick film a pronounced resonance is observed at 285.6 eV at the carbon K edge, accompanied by some smaller resonances at 287.8 eV, 289.5 eV and 293.8 eV. The assignments are similar to those made for $[\text{Fe}(\text{salten})(\text{pyS})]^+$ (**1**). In general, all resonances are present in the multi- as well as in the

monolayer. Therefore it can be concluded that an intact [Fe(thiotolylsalten)(NCS)] complex **2** is present in the monolayer.

At the N K edge, three resonances appear for the thick film. The first two at 398.9 eV and 399.7 eV are again assigned to N 1s- π^* transition of the salten ligand. The resonance at 401.5 eV is tentatively assigned to a N 1s- π^* transition of the NCS group. Here only small changes in relative intensities are observed between multilayer and monolayer, indicating that for this complex the bonding situations of the nitrogen atoms remain unchanged.

The resonances at the Fe L_{2,3} edge look similar for the multi- and the monolayer. For the monolayer, only the relative intensity of the first resonance at 707.0 eV is slightly decreased relative to the second resonance at 708.3 eV. We attribute this to small changes of the excitation cross sections between multilayer and monolayer due to the proximity of the Fe atoms to the Au metal surface in the monolayer. This would be consistent with a transfer of electron density from the Au to the Fe center.

4. Vibrational Analysis - complementary data

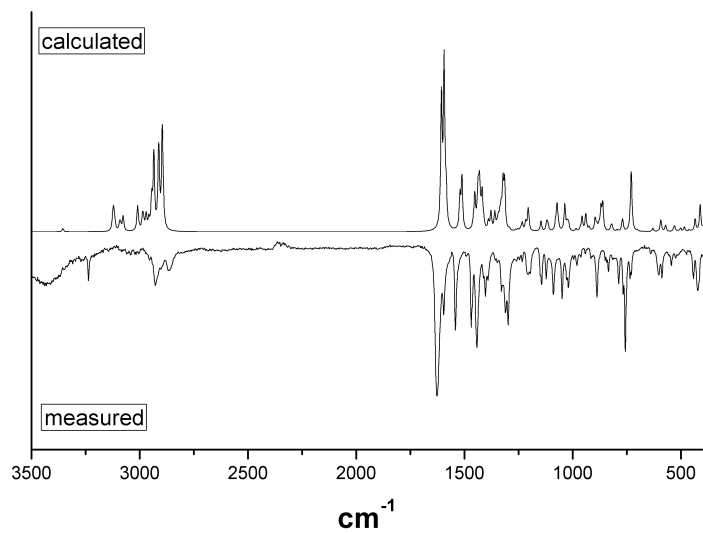


Figure S5. Experimental and calculated IR spectra of [Fe(salten)Cl].

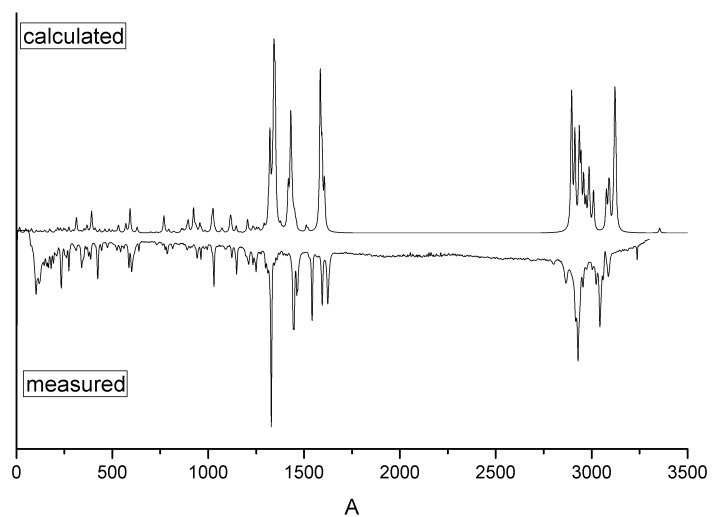


Figure S6. Experimental and calculated Raman spectra of [Fe(salten)Cl].

Table S3. Calculated infrared vibrational frequencies of [Fe(salten)Cl] + assignments of the expt. spectrum.

Calculation method: UBP86; Basis set: TZVP; Charge: zero; Spin: sextet

Mode	Frequency	IR-Int.	Raman-Activity	Assignments	Band Nr.	Freq.
71	1019.3065	13.33	31.38	(CC _{arom}) ring deformation	17	1028
72	1025.6362	11.38	55.95	(CC _{arom}) ring deformation		
73	1036.3983	44.04	6.26	(CH _{arom}) & (CH ₂) bending	16	1049
74	1065.8412	8.05	1.46	(CH ₂) bending		
75	1071.3846	17.31	4.93	(CH ₂) bending		
76	1072.699	25.64	6.79	(CH ₂) bending	14	1089
77	1078.9705	11.57	2.70	(CH ₂) bending	12,13	1144, 1121
78	1113.7722	7.55	19.33	(CH _{arom}) bending		
79	1116.8788	6.65	25.22	(CH _{arom}) bending		
80	1120.5088	11.67	21.52	(CH _{arom}) & (CH ₂) bending		
81	1145.348	7.47	9.50	(CH _{arom}) bending		
82	1146.9734	10.25	9.80	(CH _{arom}) bending		
83	1167.9477	0.77	1.58	(CH ₂) bending		
84	1203.088	11.57	4.94	(CC _{arom}) stretching & (CH) bending		
85	1205.8857	29.44	32.30	(CC _{arom}) stretching & (CH) bending	11	1205
86	1216.6981	14.83	4.36	(CH _{arom}) & (CH ₂) bending		

87	1232.2698	9.81	7.60	(CH _{arom}) & (CH ₂) bending		
88	1233.5256	3.89	7.16	(CH _{arom}) & (CH ₂) bending		
89	1239.6383	4.09	8.14	(CH _{arom}) & (CH ₂) bending		
90	1253.0122	3.06	10.62	(CH ₂) bending		
91	1262.9401	2.19	9.77	(CH ₂) bending		
92	1291.6548	3.37	16.46	(CH ₂) bending		
93	1314.4131	74.48	43.02	(CH _{arom}) & (CH ₂) bending; (C-O) stretch	10	1298
94	1321.8391	71.87	253.00	(CH _{arom}) & (CH ₂) bending; (C-O) stretch	9	1310
95	1328.7095	10.46	20.80	(CH ₂) bending	8	1329
96	1331.3369	21.61	25.09	(CH ₂) bending		
97	1336.0991	15.07	63.21	(CH ₂) bending		
98	1340.8089	4.16	102.63	(CH ₂) bending		
99	1343.2986	12.27	343.07	(CH _{arom}) & (CH ₂) bending		
100	1345.1557	3.22	16.70	(CH ₂) bending		
101	1349.4727	6.02	338.55	(CH _{arom}) & (CH ₂) bending		
102	1359.6117	28.70	2.46	(CH _{arom}) & (CH ₂) bending		
103	1377.5119	29.96	14.89	(CH _{arom}) & (CH ₂) bending	7	1390
104	1389.172	14.44	4.06	(CH ₂) bending		
105	1410.3869	8.31	12.20	(CH ₂) bending		
106	1417.712	56.81	115.63	(CC) _{arom} def. & (CH _{arom}) bending	6	1442
107	1424.2142	15.22	13.60	(CH ₂) bending		
108	1430.3949	65.04	303.53	(CC) arom def. & (CH _{arom}) bending		
109	1434.4386	21.98	46.66	(CH _{arom}) & (CH ₂) bending		
110	1437.452	15.35	21.54	(CH _{arom}) & (CH ₂) bending		

111	1437.8799	34.86	41.02	(CH _{arom}) & (CH ₂) bending		
112	1445.5004	3.26	23.48	(CH ₂) bending		
113	1450.8743	6.01	28.44	(CH _{arom}) & (CH ₂) bending		
114	1452.2933	48.93	7.22	(CH _{arom}) & (CH ₂) bending	5	1469
115	1458.6997	8.88	19.25	(CH ₂) bending		
116	1511.5084	84.43	19.32	(CC) _{arom} deformation	4	1541
117	1520.6642	54.29	9.12	(CC) _{arom} deformation		
118	1584.2968	50.44	406.64	(CC) _{arom} & (C=N) stretch	2	1595
119	1587.3017	1.73	86.62	(CC) _{arom} & (C=N) stretch		
120	1593.8883	271.35	205.88	(CC) _{arom} & (C=N) stretch	1	1626
121	1606.1682	210.29	136.12	(CC) _{arom} & (C=N) stretch		

Table S4. Cartesian coordinates of the optimized structure for [Fe(salten)Cl]

50

XYZ file generated by gabedit : coordinates in Angstrom

```

Fe    0.7049570000    -0.4967800000    -0.6340270000
Cl    1.8878220000    -1.8309490000    -2.1326170000
O     -1.0533350000    -0.5130300000    -1.4379430000
O     0.0283600000    0.6554530000    0.9677330000
N     0.0655880000    -2.2014500000    0.5554310000
N     2.6819460000    -0.2601130000    0.5564850000
N     1.2574630000    1.4130950000    -1.3812030000
C     -2.1908110000    -1.0877330000    -1.1443710000
C     -3.3672000000    -0.7222100000    -1.8534260000
C     -4.5902500000    -1.3121410000    -1.5660540000

```


C	-4.7012270000	-2.3038060000	-0.5709410000
C	-3.5635090000	-2.6875300000	0.1256190000
C	-2.2998400000	-2.1038090000	-0.1321370000
C	-1.1668210000	-2.6034750000	0.6077940000
C	1.0435980000	-2.9402420000	1.3560450000
C	1.9493100000	-2.0333020000	2.2052070000
C	3.0976020000	-1.3782670000	1.4357220000
C	3.8438910000	0.1878210000	-0.2591830000
C	3.6674990000	1.5195350000	-0.9967770000
C	2.5453170000	1.5606380000	-2.0521580000
C	0.4843620000	2.4540810000	-1.2581190000
C	-0.6246040000	2.5731020000	-0.3527220000
C	-2.4828550000	3.9426560000	0.4586810000
C	-2.6100010000	3.0821910000	1.5716770000
C	-1.7648570000	1.9967450000	1.7398970000
C	-0.7588230000	1.6814250000	0.7796890000
C	-1.4878050000	3.6915250000	-0.4718850000
H	4.0378820000	-0.6162480000	-0.9861570000
H	4.7351560000	0.2727080000	0.3950600000
H	3.8702050000	-1.0237560000	2.1474280000
H	3.5805060000	-2.1294340000	0.7889420000
H	2.4005130000	-2.6612390000	2.9913280000
H	1.3387320000	-1.2717150000	2.7176480000
H	0.5171200000	-3.6577580000	2.0139940000
H	1.6696460000	-3.5271610000	0.6603840000
H	-1.8604320000	1.3336420000	2.6018860000
H	-3.3847680000	3.2781930000	2.3177840000

H	-3.1500530000	4.7980530000	0.3419820000
H	0.7285760000	3.3558690000	-1.8511250000
H	2.6707780000	0.7331060000	-2.7675510000
H	2.5915630000	2.5214850000	-2.5999710000
H	-3.2726050000	0.0448960000	-2.6237150000
H	-5.4778580000	-1.0044620000	-2.1247900000
H	-5.6660120000	-2.7644050000	-0.3532910000
H	-3.6294570000	-3.4641560000	0.8938850000
H	2.3323770000	0.5132540000	1.1371200000
H	-1.3559960000	4.3605090000	-1.3280960000
H	4.6245030000	1.7341500000	-1.5017030000
H	3.5059610000	2.3376800000	-0.2723160000
H	-1.4020900000	-3.4466510000	1.2848490000

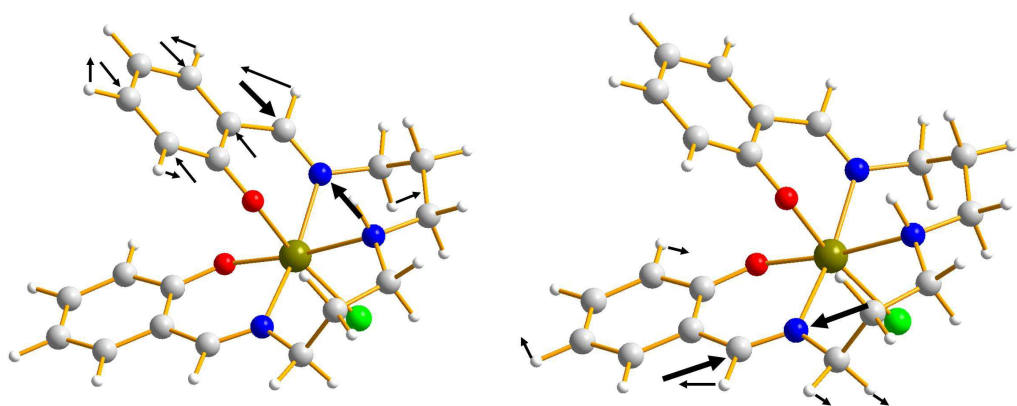


Figure S7. Imine stretching modes (modes 118,121) of [Fe(salten)Cl].

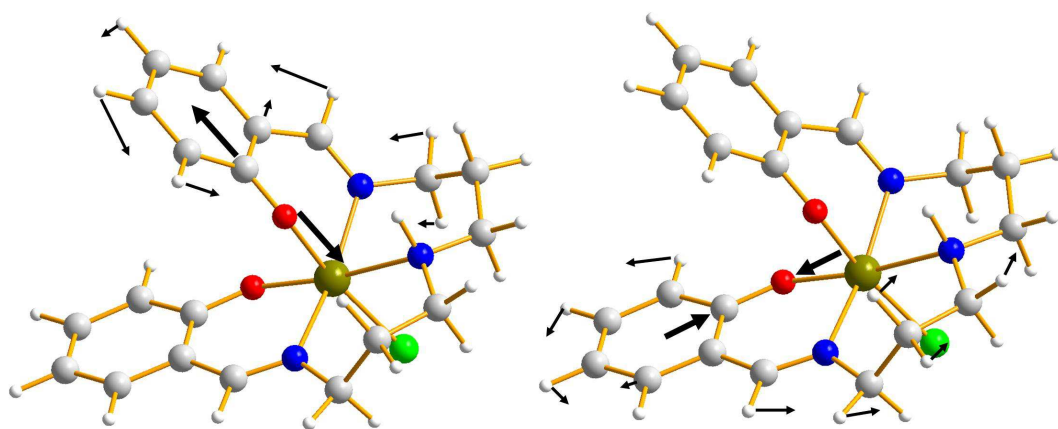


Figure S8. Phenolate C-O stretching modes (modes 93,94) of [Fe(salten)Cl].

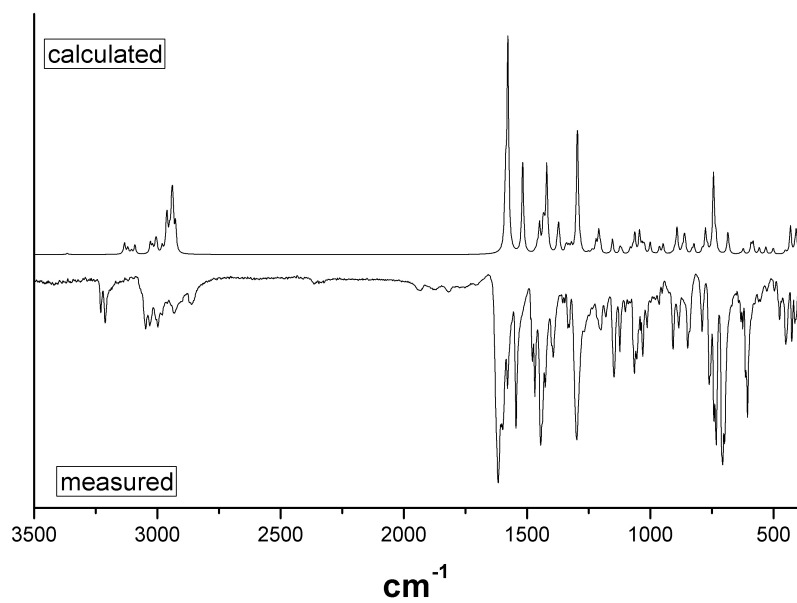


Figure S9. Experimental and calculated IR spectra of *trans* [Fe(salten)py](BPh₄).

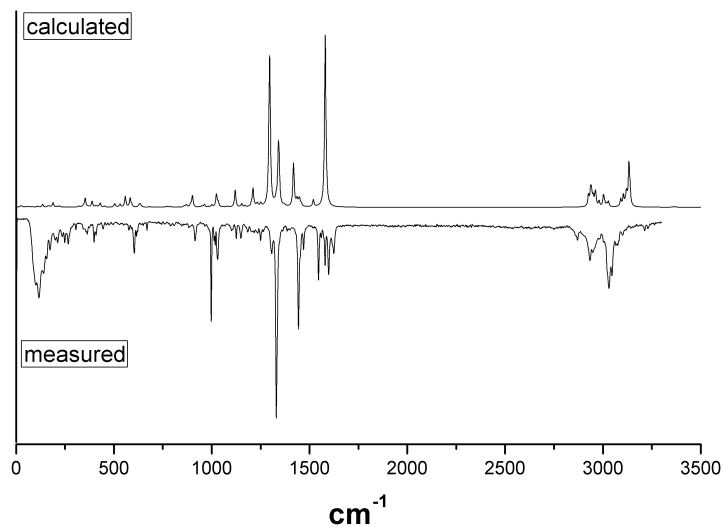


Figure S10. Experimental and calculated Raman spectra of *trans* [Fe(salten)py](BPh₄).

Table S5. Calculated infrared vibrational frequencies of *trans* [Fe(salten)(py)]⁺ + assignment of expt. spectrum.

Calculation method: UBP86; Basis set: TZVP; Charge: one; Spin: sextet

Mode	Frequency	IR-Int.	Raman-Activity	Assignments	Band No.	Freq.
84	1000.2213	17.36	31.61	(CC) _{pyridine} ring deformation	17	1029
85	1022.6205	3.24	55.49	(CC) _{pyridine} ring deformation		
86	1024.0332	4.97	113.56	(CH _{pyridine}), (CH _{arom}) & (CH ₂) bending		
87	1026.6139	7.65	21.55	(CH _{pyridine}), (CH _{arom}) & (CH ₂) bending		

88	1033.282	11.31	62.30	(CH _{pyridine}), (CH _{arom}) & (CH ₂) bending		
89	1043.5912	34.13	2.10	(CH _{pyridine}), (CH _{arom}) & (CH ₂) bending	16	1052
90	1061.7369	9.05	2.55	(CH _{pyridine}), (CH _{arom}) & (CH ₂) bending		
91	1062.8979	15.57	0.53	(CH _{pyridine}) bending	15	1064
92	1063.4014	6.41	0.45	(CH _{pyridine}) bending	12,13,14	1146, 1124, 1101
93	1071.242	8.76	1.69	(CH ₂) bending		
94	1081.5176	8.39	14.22	(CH ₂) bending		
95	1115.7906	6.00	14.57	(CH _{arom}) & (CH ₂) bending		
96	1119.9146	2.90	229.79	(CH _{arom}) & (CH ₂) bending		
97	1123.1806	8.43	9.10	(CH _{arom}) & (CH ₂) bending		
98	1152.8926	8.52	24.25	(CH _{arom}) bending		
99	1153.4882	10.23	18.61	(CH _{arom}) bending		
100	1153.958	3.82	2.62	(CH _{pyridine}) bending		
101	1170.3381	0.43	17.89	(CH _{arom}) & (CH ₂) bending		
102	1202.4374	11.65	30.58	(CH _{pyridine}) bending		
103	1208.7381	28.46	29.38	(CH _{arom}) & (CH ₂) bending	11	1203
104	1211.0298	5.90	246.59	(CH _{arom}) & (CH ₂) bending		
105	1220.3019	18.52	9.94	(CH ₂) bending		
106	1228.4876	0.33	9.82	(CH _{arom}) & (CH ₂) bending		
107	1233.0211	2.87	45.09	(CH _{arom}) & (CH ₂) bending		
108	1237.5721	3.33	3.88	(CH _{arom}) & (CH ₂) bending		
109	1249.9709	2.22	47.48	(CH ₂) bending		
110	1254.0739	0.72	7.23	(CH ₂) bending		
111	1282.6394	4.36	7.40	(CH ₂) bending		

112	1286.332	2.42	0.71	(CC) pyridine ring deformation		
113	1294.3631	113.68	1177.01	(CH _{arom}) & (CH ₂) bending; (C-O) stretch	9,10	1297
114	1297.2226	97.92	1344.97	(CH _{arom}) & (CH ₂) bending; (C-O) stretch		
115	1320.0371	11.05	22.74	(CH ₂) bending		
116	1328.388	4.10	66.49	(CH ₂) bending		
117	1330.6919	5.87	24.88	(CH ₂) bending		
118	1338.4415	8.62	109.25	(CH _{pyridine}) bending		
119	1340.4704	0.67	586.76	(CH _{pyridine}), (CH _{arom}) & (CH ₂) bending	8	1329
120	1340.8863	0.60	32.06	(CH ₂) bending		
121	1344.0698	5.89	294.26	(CH _{pyridine}) & (CH ₂) bending		
122	1344.4569	1.06	173.06	(CH ₂) bending		
123	1367.9457	9.96	14.31	(CH _{arom}) & (CH ₂) bending		
124	1372.0615	38.38	10.48	(CH ₂) bending	7	1393
125	1377.5624	12.77	3.49	(CH ₂) bending		
126	1414.6788	6.69	21.34	(CH ₂) bending		
127	1418.1099	2.53	640.11	(CH _{arom}) & (CH ₂) bending	6	1442
128	1420.1806	125.55	14.84	(CH _{arom}) & (CH ₂) bending		
129	1430.0564	23.02	20.23	(CH ₂) bending		
130	1434.2337	21.05	0.04	(CH _{pyridine}) bending		
131	1435.5059	15.06	56.47	(CH ₂) bending		
132	1436.8604	3.37	47.61	(CH ₂) bending		
133	1444.1254	1.90	41.16	(CH ₂) bending		
134	1448.2988	2.26	85.33	(CH _{arom}) & (CH ₂) bending		

135	1449.373	38.36	17.74	(CH _{arom}) & (CH ₂) bending	5	1469
136	1454.3664	2.35	26.57	(CH _{arom}) & (CH ₂) bending		
137	1458.8276	8.93	28.17	(CH ₂) bending		
138	1467.3787	2.52	2.65	(CH _{pyridine}) bending & (CN _{pyridine}) stretch		
139	1517.2906	122.24	14.88	(CC) arom deformation	4	1545
140	1519.6982	20.04	95.12	(CC) arom deformation		
141	1562.9847	0.24	6.98	(CC) pyridine ring deformation		
142	1577.6484	292.34	107.77	(CC) _{arom} & (C=N) stretch	3	1579
143	1580.4022	27.94	2663.86	(CC) _{arom} & (C=N) stretch	2	1599
144	1586.1007	58.83	16.17	(CC) _{arom} & (C=N) stretch	1	1604
145	1586.9993	15.72	33.22	(CC) _{arom} & (C=N) stretch		1617,
146	1589.1216	31.29	6.67	(CC) _{pyridine} ring stretch		1627

Table S6. Cartesian coordinates of the optimized structure for *trans* [Fe(salten)py]⁺.

60

XYZ file generated by gabedit : coordinates in Angstrom

Fe	-0.0177690000	-0.3703110000	0.0431590000
O	-1.7212440000	-0.2997030000	1.0228390000
O	1.6379620000	-0.2069750000	-1.0120130000
N	-1.1730550000	-0.7684380000	-1.6859640000
N	1.2088920000	-0.5952690000	1.7474640000
N	-0.1011890000	1.8887700000	0.0139580000
C	-2.8940950000	0.1404890000	0.6074230000
C	-3.8563050000	0.5775350000	1.5524750000
C	-5.1044450000	1.0355790000	1.1470680000
C	-5.4584700000	1.0640540000	-0.2159910000
C	-4.5459070000	0.6174530000	-1.1604840000
C	-3.2570630000	0.1600990000	-0.7879840000
C	-2.4083160000	-0.3760260000	-1.8209720000
C	-0.5264990000	-1.4953470000	-2.7833260000
C	-0.3383040000	-2.9781080000	-2.4104730000
C	0.5497660000	-3.2483500000	-1.1908070000
C	0.5941220000	-3.2849400000	1.2879360000
C	0.0237310000	-2.6428030000	2.5574610000
C	0.6544020000	-1.2737090000	2.9268080000
C	2.4395890000	-0.1688050000	1.7997730000
C	3.2198750000	0.3740030000	0.7186370000
C	4.5023550000	0.8938340000	1.0258270000
C	5.3515310000	1.3618890000	0.0339060000
C	4.9400460000	1.2911270000	-1.3116050000

C	3.6985120000	0.7680420000	-1.6527320000
C	2.8005340000	0.3046860000	-0.6576760000
C	0.3064420000	2.5851740000	-1.0691340000
C	0.2686540000	3.9779940000	-1.1245320000
C	-0.1956360000	4.6851400000	-0.0123030000
C	-0.6133960000	3.9692320000	1.1128220000
C	-0.5576300000	2.5763890000	1.0831880000
H	-3.5867750000	0.5412190000	2.6097220000
H	-5.8227820000	1.3698940000	1.8990500000
H	-6.4428230000	1.4191720000	-0.5228790000
H	-4.8152200000	0.6129350000	-2.2204830000
H	-2.8814730000	-0.4882110000	-2.8132560000
H	-1.1319650000	-1.4211320000	-3.7046950000
H	-1.3294820000	-3.4416410000	-2.2590160000
H	1.5495490000	-2.8114720000	-1.3378900000
H	0.6745510000	-4.3419590000	-1.0794580000
H	1.6856490000	-3.1542530000	1.2276290000
H	0.3985840000	-4.3728230000	1.2942660000
H	-1.0646720000	-2.5274860000	2.4361080000
H	0.1711590000	-3.3300630000	3.4037710000
H	-0.1211560000	-0.6299690000	3.3701570000
H	1.4520990000	-1.4101420000	3.6776330000
H	2.9710680000	-0.2517880000	2.7645880000
H	4.8168780000	0.9237610000	2.0728510000
H	6.3310770000	1.7666780000	0.2905400000
H	5.6086090000	1.6433610000	-2.1003830000
H	0.6777820000	1.9905980000	-1.9051690000

H	0.6042130000	4.4939050000	-2.0249980000
H	-0.9846920000	4.4781440000	2.0031810000
H	-0.8927410000	1.9745600000	1.9294130000
N	-0.0038590000	-2.6778080000	0.0681470000
H	-1.0136600000	-2.8665410000	0.0949560000
H	0.4562480000	-1.0344720000	-2.9654360000
H	0.1132290000	-3.4909010000	-3.2747750000
H	3.3852500000	0.6976170000	-2.6961380000
H	-0.2317140000	5.7761100000	-0.0222130000

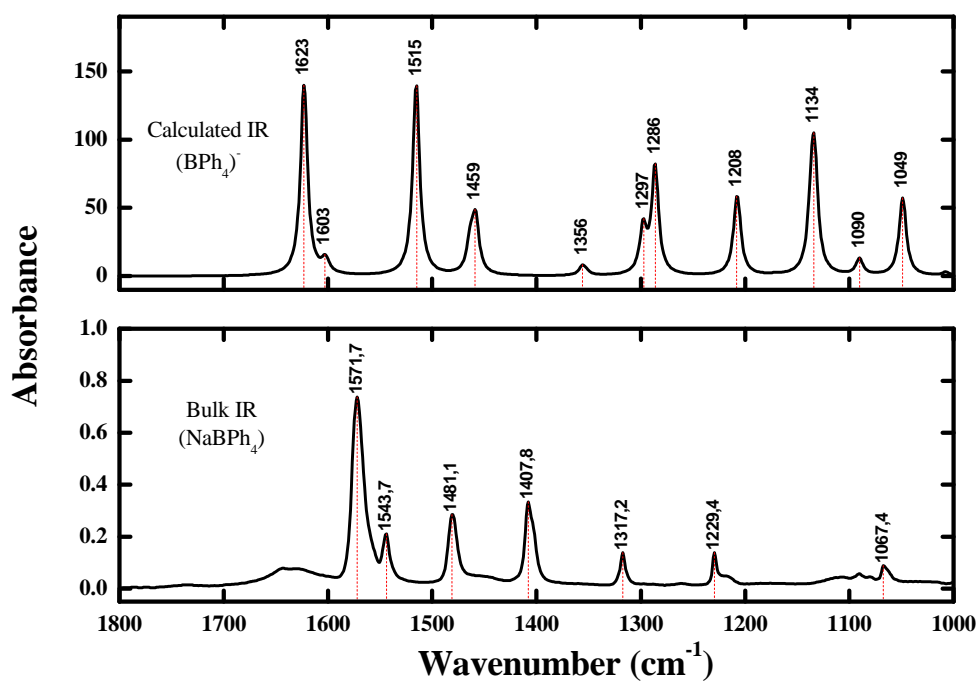


Figure S11. Bulk IR of Sodium tetraphenyl borate and calculated IR of counter ion (BPh₄)⁻ (region: 1800 cm⁻¹ to 1000 cm⁻¹).

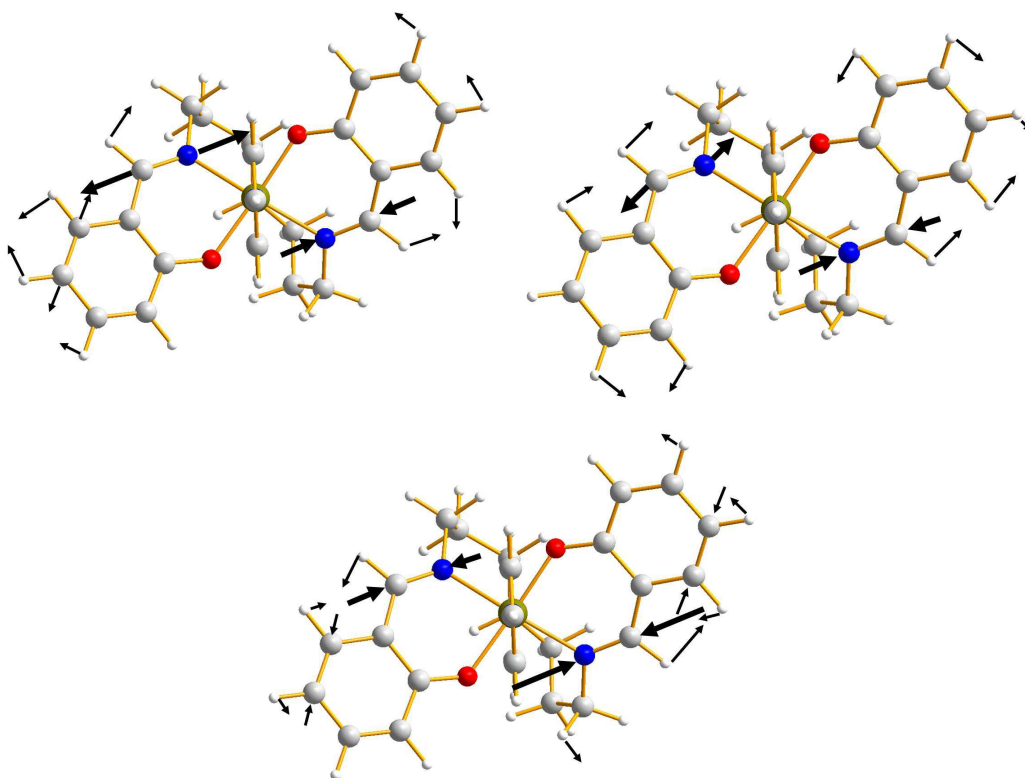


Figure S12. Imine stretching modes (modes 142, 143, 144) of *trans* [Fe(salten)py]⁺.

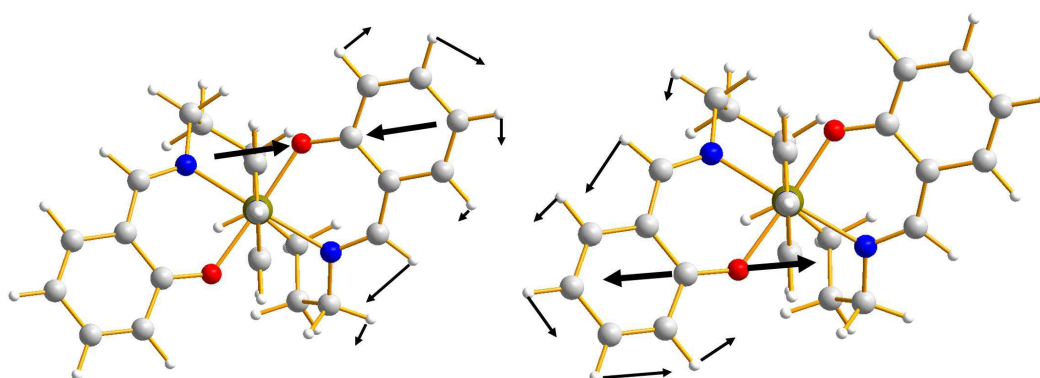


Figure S13. Phenolate stretching modes (modes 113, 114) of *trans* [Fe(salten)py]⁺.

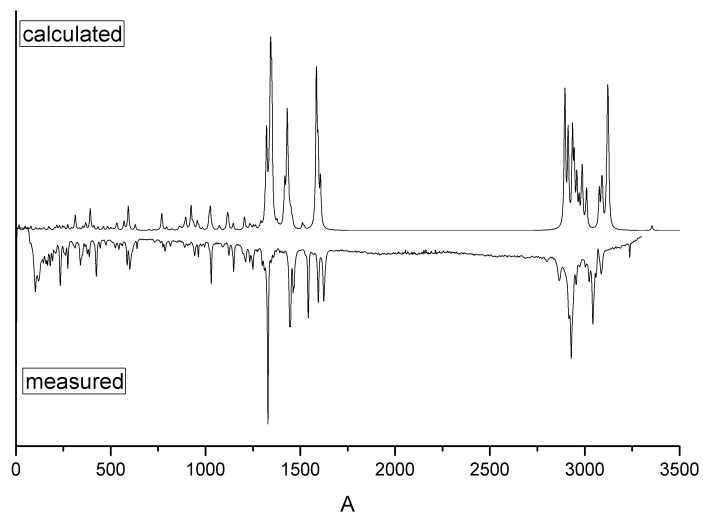


Figure S14. Experimental and calculated Raman spectra of $[\text{Fe}(\text{salten})(\text{pyS})]_2(\text{BPh}_4)_2$ (**1-1**).

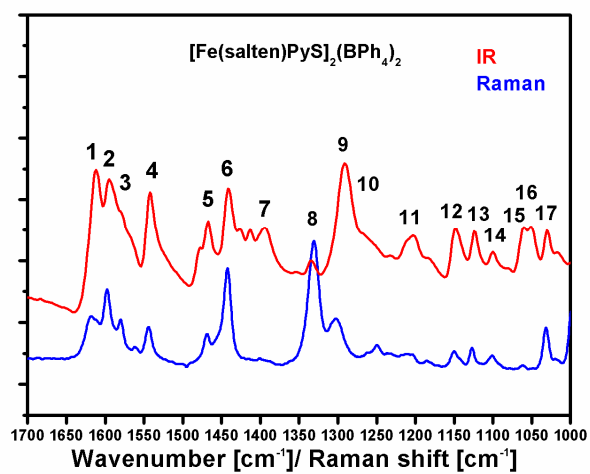


Figure S15. Experimental IR and Raman spectra of $[\text{Fe}(\text{salten})(\text{pyS})]_2(\text{BPh}_4)_2$ (**1-1**).

Table S7. Calculated infrared vibrational frequencies of *cis* [Fe(salten)py]⁺.

Calculation method: UBP86; Basis set: TZVP; Charge: one; Spin: sextet

Mode	Frequency	IR-Intensity	Raman-Activity	Assignment	Peak No.
146	1587.7191	33.75	13.36	(CC) _{pyridine} ring stretch	1
145	1586.0741	72.43	51.41	(CC) _{arom.} & (C=N) stretch	
144	1583.2432	3.14	389.88	(CC) _{arom.} & (C=N) stretch	
143	1576.3572	232.95	834.95	(CC) _{arom.} & (C=N) stretch	2
142	1574.1068	52.34	825.12	(CC) _{arom.} & (C=N) stretch	3
141	1562.8659	1.59	9.95	(CC) _{pyridine} ring deformation	
140	1522.8637	61.07	56.86	(CC) _{arom.} deformation	
139	1514.2012	82.40	82.42	(CC) _{arom.} deformation	4
138	1469.0519	5.18	3.54	(CH _{pyridine}) bending & (CN _{pyridine}) stretch	
137	1467.9496	1.72	12.20	(CH ₂) bending	
136	1452.1737	31.27	25.96	(CH _{arom.}) & (CH ₂) bending	5
135	1451.2683	11.97	17.67	(CH _{arom.}) & (CH ₂) bending	
134	1449.3147	14.36	45.41	(CH _{arom.}) & (CH ₂) bending	
133	1444.7531	1.86	14.73	(CH ₂) bending	
132	1443.6947	18.72	67.88	(CH ₂) bending	
131	1437.0055	13.90	46.94	(CH ₂) bending	
130	1432.9132	21.82	0.92	(CH _{pyridine}) bending	
129	1430.3572	14.19	4.40	(CH ₂) bending	
128	1425.2079	35.41	377.39	(CH _{arom.}) & (CH ₂) bending	6
127	1415.5981	57.31	67.92	(CH _{arom.}) & (CH ₂) bending	

126	1412.3688	13.55	140.07	(CH ₂) bending	7
125	1385.8037	43.47	11.59	(CH ₂) bending	
124	1377.3661	7.23	21.85	(CH ₂) bending	
123	1364.4431	24.32	8.02	(CH _{arom}) & (CH ₂) bending	8
122	1351.8347	4.32	31.71	(CH ₂) bending	
121	1348.7029	0.23	30.67	(CH _{pyridine}) & (CH ₂) bending	
120	1345.8111	2.56	193.97	(CH ₂) bending	
119	1341.0612	1.59	367.79	(CH _{pyridine}), (CH _{arom}) & (CH ₂) bending	
118	1340.4566	2.38	51.46	(CH _{pyridine}) bending	
117	1336.1246	9.40	77.23	(CH ₂) bending	
116	1331.586	12.62	31.95	(CH ₂) bending	
115	1326.4523	11.47	28.59	(CH ₂) bending	
114	1302.8211	58.13	1173.91	(CH _{arom}) & (CH ₂) bending; (C-O) stretch	9
113	1293.9479	67.29	512.86	(CH _{arom}) & (CH ₂) bending; (C-O) stretch	10
112	1289.0604	13.43	99.71	(CC) pyridine ring deformation	
111	1283.0141	0.78	2.39	(CH ₂) bending	
110	1261.3376	5.90	11.03	(CH ₂) bending	
109	1254.4253	0.76	10.35	(CH ₂) bending	
108	1242.7254	6.26	15.43	(CH _{arom}) & (CH ₂) bending	
107	1234.9306	4.77	21.76	(CH _{arom}) & (CH ₂) bending	
106	1232.4911	6.47	8.51	(CH _{arom}) & (CH ₂) bending	
105	1216.8309	25.81	43.65	(CH ₂) bending	
104	1212.4097	30.76	108.01	(CH _{arom}) & (CH ₂) bending	
103	1211.3071	7.06	44.43	(CH _{arom}) & (CH ₂) bending	11

102	1203.6455	19.83	9.40	(CH _{pyridine}) bending	
101	1163.8209	1.26	5.55	(CH _{arom}) & (CH ₂) bending	12-14
100	1154.3777	10.18	23.01	(CH _{pyridine}) bending	
99	1154.0774	1.57	3.70	(CH _{arom}) bending	
98	1151.9555	11.41	20.18	(CH _{arom}) bending	
97	1122.1712	11.59	77.12	(CH _{arom}) & (CH ₂) bending	
96	1119.723	4.47	67.96	(CH _{arom}) & (CH ₂) bending	
95	1117.2373	2.77	40.39	(CH _{arom}) & (CH ₂) bending	
94	1077.1154	1.63	2.83	(CH ₂) bending	
93	1070.8026	16.22	5.74	(CH ₂) bending	
92	1067.2499	11.76	2.60	(CH _{pyridine}) bending	
91	1064.051	18.27	2.12	(CH _{pyridine}) bending	
90	1062.7028	22.51	1.37	(CH _{pyridine}), (CH _{arom}) & (CH ₂) bending	
89	1060.4163	3.97	1.34	(CH _{pyridine}), (CH _{arom}) & (CH ₂) bending	
88	1033.1861	27.00	27.16	(CH _{pyridine}), (CH _{arom}) & (CH ₂) bending	
87	1029.0185	16.33	75.13	(CH _{pyridine}), (CH _{arom}) & (CH ₂) bending	16
86	1023.4921	2.05	51.36	(CH _{pyridine}), (CH _{arom}) & (CH ₂) bending	
85	1020.6502	19.86	46.42	(CC) pyridine ring deformation	17
84	998.4752	44.08	24.40	(CC) pyridine ring deformation	

Table S8. Cartesian coordinates of the optimized structure for *cis* [Fe(salten)py]⁺.

60

XYZ file generated by gabedit : coordinates in Angstrom

Fe	-0.1975610000	-0.2128590000	0.1291650000
O	0.8959940000	1.0107850000	-0.8731180000
O	1.3327030000	-1.1258620000	0.9912920000
N	-0.3259880000	1.2596910000	1.7098510000
N	-1.5184760000	-1.7096780000	1.3023680000
N	-0.1157940000	-1.8110210000	-1.2621790000
C	1.5755440000	2.0914810000	-0.5457300000
C	2.4967580000	2.6458270000	-1.4671800000
C	3.2301580000	3.7829310000	-1.1455390000
C	3.0699080000	4.4173730000	0.1000440000
C	2.1665250000	3.8933280000	1.0156570000
C	1.4039520000	2.7353010000	0.7262180000
C	0.4800950000	2.2831290000	1.7360650000
C	-1.1692260000	1.0656720000	2.9002330000
C	-1.1768490000	-0.3769150000	3.4250960000
C	-2.0677740000	-1.3360530000	2.6364990000
C	-2.5288480000	-2.5007950000	0.5360050000
C	-1.9747830000	-3.2925430000	-0.6515690000
C	-1.3277180000	-2.4560400000	-1.7692650000
C	1.0444370000	-2.2643330000	-1.6552490000
C	2.3132330000	-1.9988430000	-1.0347470000
C	4.7337850000	-2.3358820000	-1.0840670000
C	4.8158950000	-1.8557770000	0.2401110000
C	3.6787810000	-1.4629950000	0.9330110000

C	2.4029610000	-1.4955480000	0.3155050000
C	3.4937570000	-2.4237760000	-1.6957540000
H	-3.3048000000	-1.7991640000	0.1902630000
H	-3.0259320000	-3.2114970000	1.2230080000
H	-2.2522190000	-2.2526050000	3.2271320000
H	-3.0540210000	-0.8700880000	2.4702510000
H	-1.5601850000	-0.3502620000	4.4577600000
H	-0.1455970000	-0.7614450000	3.4843900000
H	-0.8353380000	1.7479530000	3.7021890000
H	-2.2037670000	1.3609890000	2.6447990000
H	3.7388490000	-1.1007840000	1.9605750000
H	5.7888800000	-1.7997140000	0.7335290000
H	5.6346350000	-2.6510110000	-1.6118380000
H	1.0631100000	-2.9659010000	-2.5085340000
H	-2.0339230000	-1.6854690000	-2.1155480000
H	-1.0882830000	-3.1102410000	-2.6272450000
H	2.6217620000	2.1455140000	-2.4288070000
H	3.9389690000	4.1866750000	-1.8718890000
H	3.6482640000	5.3090810000	0.3441500000
H	2.0311680000	4.3793280000	1.9859950000
H	-0.6975300000	-2.3086660000	1.4679200000
H	3.4105390000	-2.8239820000	-2.7101190000
H	-2.8162060000	-3.8575610000	-1.0848370000
H	-1.2468800000	-4.0430780000	-0.2982240000
H	0.4706360000	2.9101730000	2.6454160000
C	-1.8144300000	1.1992930000	-2.1894810000
C	-3.2099100000	0.9679470000	-0.3585650000

C	-2.7887090000	1.9075060000	-2.8937020000
H	-0.8271080000	1.0078920000	-2.6131240000
C	-4.2353230000	1.6724830000	-0.9889750000
H	-3.3416000000	0.5836880000	0.6549880000
C	-4.0232220000	2.1493960000	-2.2852800000
H	-2.5743200000	2.2651910000	-3.9015990000
H	-5.1796230000	1.8410540000	-0.4695000000
H	-4.8037870000	2.7044220000	-2.8088670000
N	-2.0155970000	0.7262750000	-0.9389290000

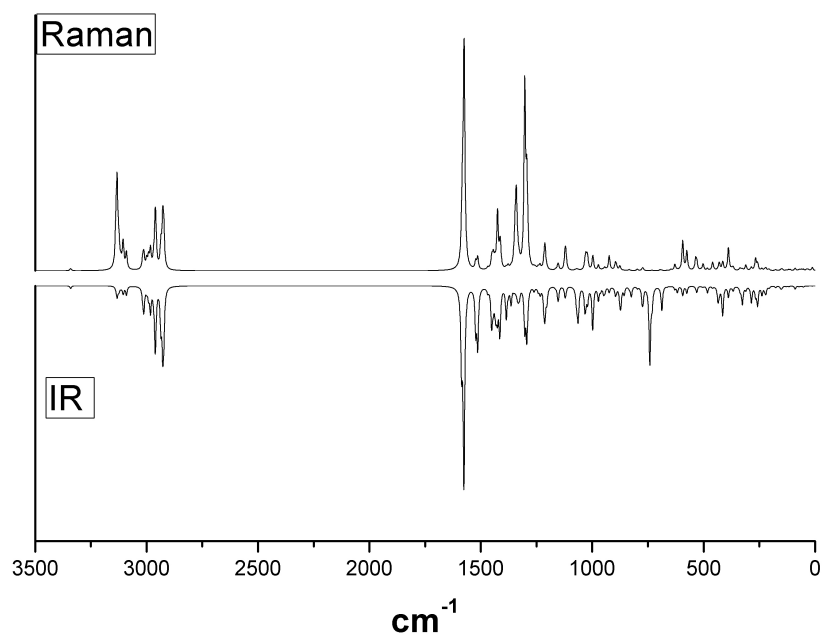


Figure S16. Calculated Raman and IR spectra of *cis* [Fe(salten)py](BPh₄).

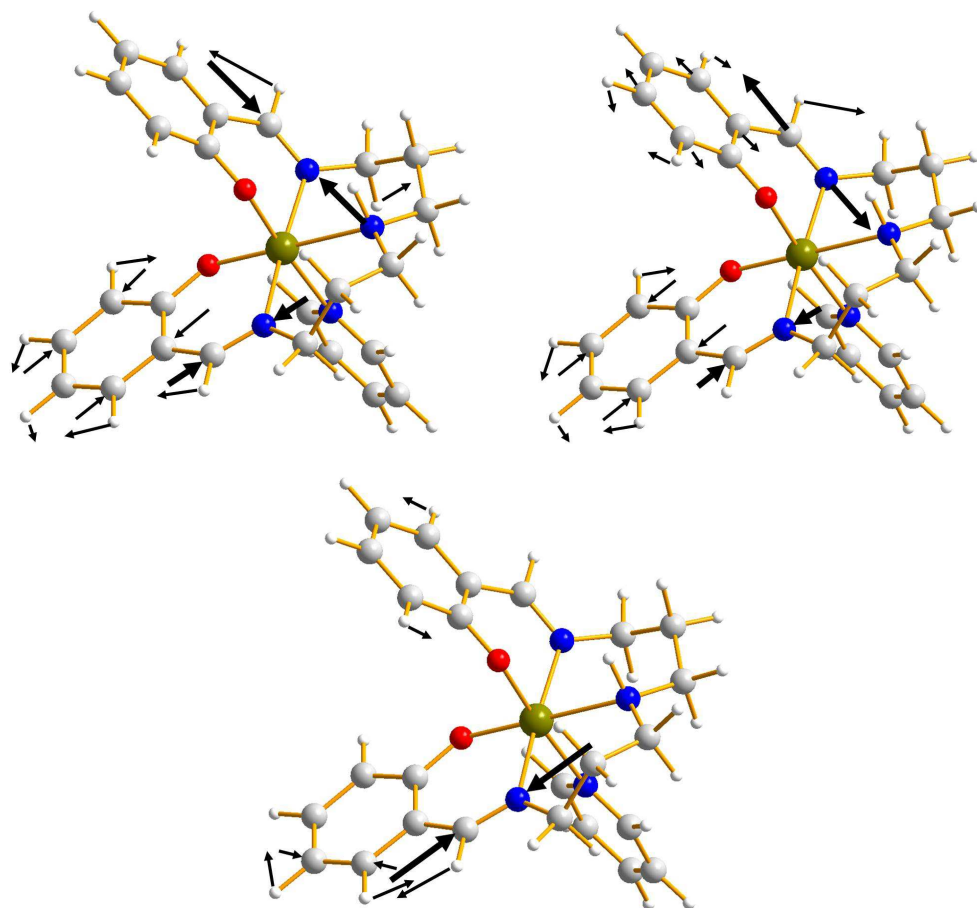


Figure S17. Imine stretching modes (modes 142, 143, 145) of *cis* [Fe(salten)py]⁺.

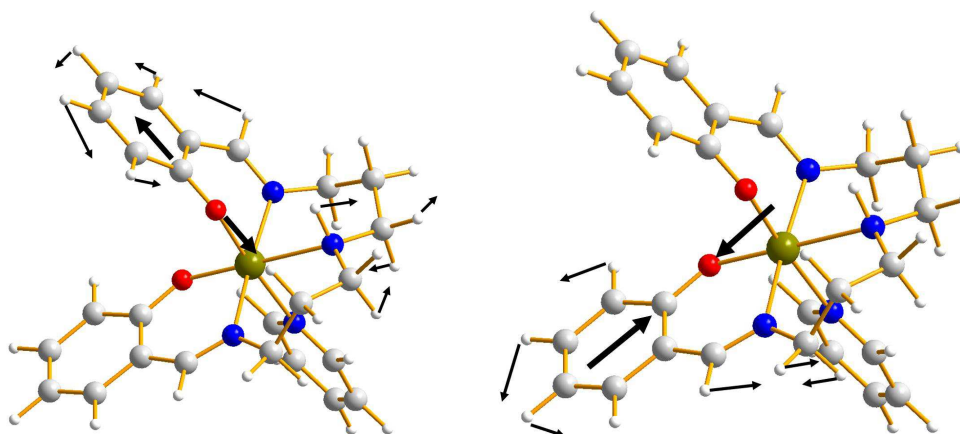


Figure S18. Phenolate stretching modes (modes 113, 114) of *cis* [Fe(salten)py]⁺.

Table S9. Cartesian coordinates of the optimized structure for *cis* [Fe(thiotolysalten)NCS].

66

XYZ file generated by gabedit : coordinates in Angstrom

Fe	-0.1415290000	-0.8489310000	-0.9588150000
N	1.0580040000	-1.7909250000	-2.1606190000
O	-1.6622170000	-1.3159600000	-1.9870070000
O	-1.2694220000	-0.0331030000	0.3229580000
N	-0.3087250000	-2.5014440000	0.1438230000
N	1.7003560000	-0.0350780000	0.0064560000
N	-0.1693660000	0.8076700000	-2.0466640000
C	-2.7027280000	-2.0478620000	-1.5888770000
C	-3.9005790000	-1.9826710000	-2.3428440000
C	-5.0109130000	-2.7197120000	-1.9725600000
C	-4.9765000000	-3.5674090000	-0.8443740000
C	-3.8076530000	-3.6651880000	-0.1138130000

C	-2.6556700000	-2.9146740000	-0.4611490000
C	-1.4402350000	-3.1403270000	0.2604640000
C	0.8512030000	-3.0662260000	0.8595120000
C	1.6313930000	-2.0134590000	1.6442600000
C	2.4661300000	-1.1081740000	0.7437340000
C	2.6660880000	0.4789000000	-1.0507950000
C	2.1610900000	1.5483710000	-2.0207660000
C	0.9883190000	1.1059460000	-2.9045110000
C	-1.1871620000	1.6169550000	-2.0586450000
C	-2.2925600000	1.6110390000	-1.1410570000
C	-4.4021240000	2.6175350000	-0.4400120000
C	-4.3608340000	1.8471980000	0.7391880000
C	-3.3129470000	0.9734650000	0.9815650000
C	-2.2655290000	0.8220880000	0.0446930000
C	-3.3710430000	2.5025290000	-1.3559350000
H	2.9625900000	-0.3928250000	-1.6262720000
H	3.5560360000	0.8535540000	-0.5352310000
H	3.2648990000	-0.6294500000	1.3161510000
H	2.9420200000	-1.7245890000	-0.0171800000
H	2.3228620000	-2.5355750000	2.3122850000
H	0.9479160000	-1.4472170000	2.2794740000
H	0.5048950000	-3.8538130000	1.5355200000
H	1.5074110000	-3.5335910000	0.1208870000
H	-3.2758210000	0.3718180000	1.8781640000
H	-5.1603620000	1.9343260000	1.4635570000
H	-5.2252010000	3.2940360000	-0.6215910000
H	-1.1886520000	2.4173180000	-2.8004380000

H	1.2428940000	0.2100060000	-3.4638560000
H	0.7346480000	1.9031290000	-3.6100870000
H	-3.9131830000	-1.3326650000	-3.2053610000
H	-5.9185430000	-2.6456780000	-2.5578220000
H	-5.8494310000	-4.1403420000	-0.5652990000
H	-3.7554930000	-4.3298330000	0.7408370000
H	-3.3779620000	3.1015180000	-2.2591070000
H	3.0061160000	1.8041820000	-2.6674420000
H	1.8832500000	2.4675960000	-1.4991900000
C	1.2573920000	1.0738740000	0.9572980000
C	1.6226700000	-2.5879370000	-2.8334140000
S	2.4698010000	-3.6782170000	-3.7604830000
C	2.3313430000	1.7150590000	1.8189550000
C	3.0999160000	2.7969290000	1.3587770000
C	2.5459310000	1.2714700000	3.1344990000
C	4.0614850000	3.4016420000	2.1722330000
C	4.2598440000	2.9386360000	3.4734330000
C	3.5049820000	1.8685420000	3.9555420000
S	5.5874190000	3.6999240000	4.5403480000
H	-1.4661720000	-3.9810670000	0.9553480000
H	0.4749140000	0.6465720000	1.5746390000
H	0.7708530000	1.8262030000	0.3435160000
H	2.9411770000	3.1855420000	0.3619210000
H	1.9506510000	0.4573170000	3.5270160000
H	4.6489190000	4.2285620000	1.8002930000
H	3.6626330000	1.5090110000	4.9621020000
H	4.7804820000	4.6554570000	5.1417790000

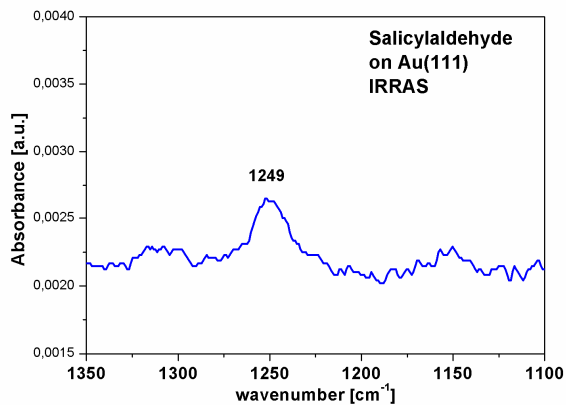


Figure S19. IRRAS spectrum of salicylaldehyde on Au(111).

A 1 mM solution of salicylaldehyde has been prepared in ethanol and the wafer was immersed for 1 day in this solution. Afterwards the sample was rinsed with ethanol p.a. and dried in a stream of nitrogen.

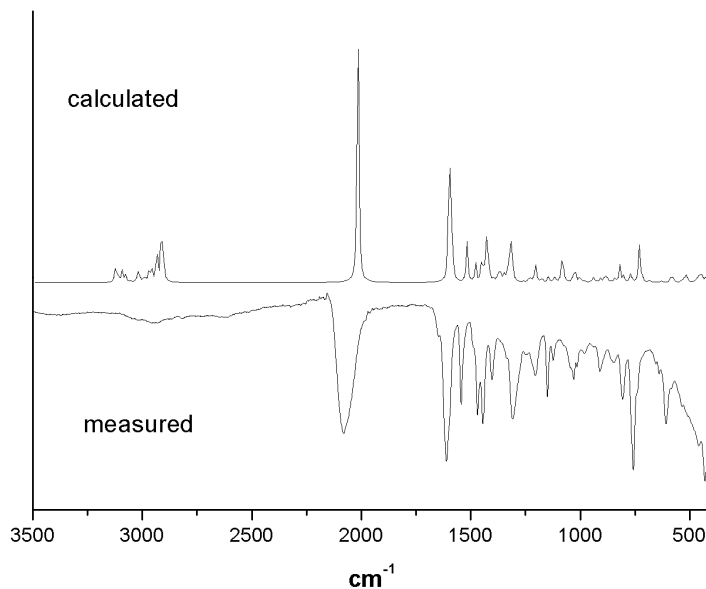


Figure S20. Experimental and calculated IR of $[\text{Fe}(\text{thiolylsalten})\text{NCS}]_2$ (2-2).

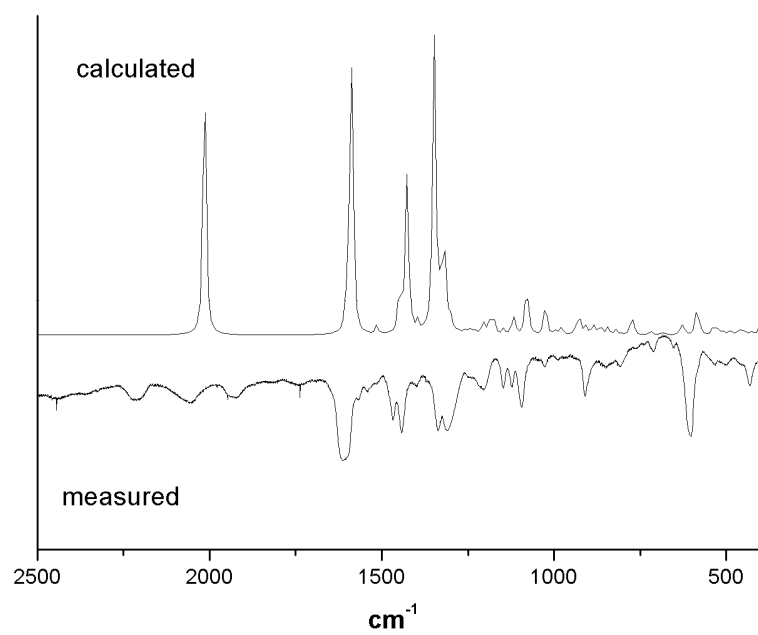


Figure S21. Experimental and calculated Raman of [Fe(thiolylsalten)NCS]₂ (2-2).

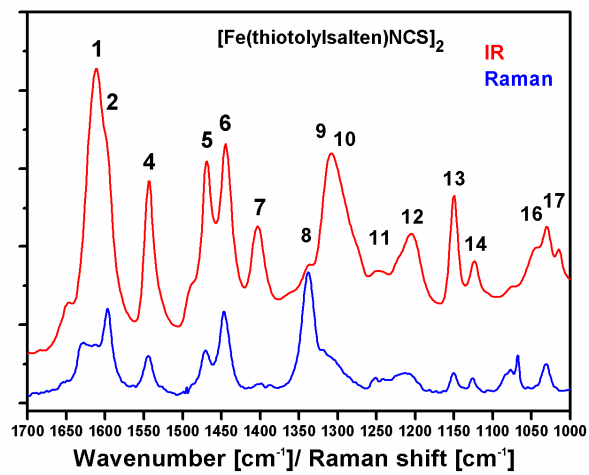


Figure S22. Bulk IR and Raman spectra of [Fe(thiotolylsalten)(NCS)₂]₂ (**2-2**) (Region: 1700 cm⁻¹ to 1000 cm⁻¹).

8.2 Supporting information on the Journal of the American Chemical Society publication

Supporting Information
Journal of the American Chemical Society

S.Karan, T. Gopakumar, H. Jacob, S. Meyer, F. Tucek* and R. Berndt*

”Remotely triggered geometrical isomerization of a binuclear complex” *J. Am. Chem. Soc.*
2014, 136, 6163-6166.
DOI: 10.1021/ja500154g.

Supporting Information for: Remotely triggered geometrical isomerization of a binuclear complex

Sujoy Karan¹, Thiruvancheril G. Gopakumar², Hanne Jacob³, Sven Meyer³, Felix Tuczek³, Richard Berndt¹

¹*Institut für Experimentelle und Angewandte Physik*

Christian-Albrechts-Universität zu Kiel, 24098 Kiel, Germany

²*Department of Chemistry, Indian Institute of Technology Kanpur, Kanpur 208016, India*

³*Institut für Anorganische Chemie, Christian-Albrechts-Universität zu Kiel, Kiel, Germany*

Experimental details

The experiments were carried out with a low-temperature scanning tunneling microscope (STM) in ultrahigh vacuum (UHV). Single crystalline Au(111) substrates were cleaned by Ar⁺ sputtering and annealing at ~ 750 K. Using an electrospray ionization apparatus, freshly synthesized binuclear [Fe(salten)pyS]₂ was sprayed in positive ion mode from a methanolic solution, mass selected, and deposited onto the substrates held at room temperature in UHV. Subsequently the samples were initially cooled to nitrogen temperature and then transferred into the microscope at ≈ 5 K. All STM images shown were acquired at constant currents $I = 10 - 50$ pA and sample voltages $V = 0.20 - 0.25$ V. The image contrasts were essentially unchanged within the range $-1 \text{ V} < V < 1.1 \text{ V}$. Currents exceeding ~ 200 pA usually lead to irreversible damage of the molecules. STM images were processed with WSxM.¹

Computational methods

Density functional theory (DFT) calculations were carried out with the software package Gaussian-09² using Beckes three-parameter hybrid functional with the LYP 196 correlation functional of Lee, Yang, and Parr.³ A 6-311G basis set was used for all atoms.

Calculated total energy differences for [Fe(salten)pyS] and [Fe(salten)pyS]₂

Monomers	$\Delta E(\text{eV})$	Dimers	$\Delta E(\text{eV})$
dc	0	st-st	0
st	0.08	dc-st	0.15
dc'	0.58	dc-dc	0.37
sc	0.98	st-dc'	0.51
		dc-dc'	0.75
		dc-sc	1.06
		sc-sc	1.72

Table S1: Calculated total energy differences with respect to the lowest energy monomer and dimer. Note that the energy difference between st and dc monomers is insignificant compared to the estimated accuracy of the calculations.

Bailar twists not observed in the experiments

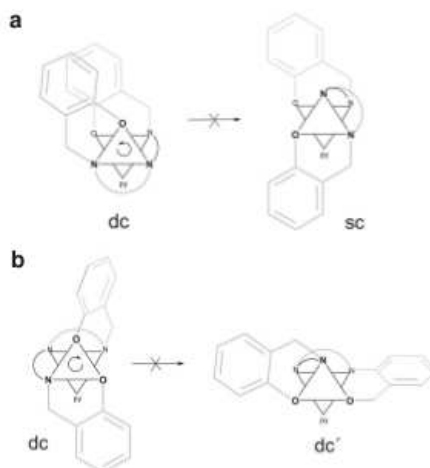


Figure S1: Bailar twists starting from the dc configuration. (a) Twist from dc to sc. Only one flexible C3 linkage is connecting the triangles. However, the final sc configuration is energetically unfavorable. (b) Twist from dc to dc'. The triangular ligand planes are connected by propylene and iminophenol, the latter being rigid owing to its conjugated π electron system.

STM data from dipyridylethane-linked dimers on Au(111)

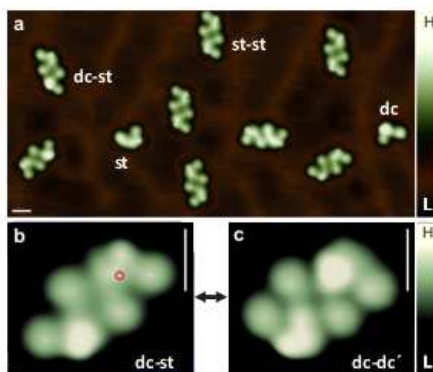


Figure S2: STM images of dipyridylethane-linked dimers on Au(111). Scale bars correspond to 1 nm in all panels, the height scale covers a range of 0.22 nm. (a) The $22 \times 11 \text{ nm}^2$ image shows $[(\text{salten})\text{pyCH}_2]_2$ deposited on Au(111). The majority of molecular features are st-st and dc-st dimers (two examples are labeled). Few dc and st monomers are observed. Small variations of the apparent molecular heights are presumably due to different adsorption sites on the reconstructed substrate. (b) Electron injection into the st subunit at the indicated position (red circle) induces a transition to dc' as shown in (c). By repeating the injection to the st subunit the original state can be restored. In contrast to the disulfide-linked complex, remote switching was never observed.

Calculated orbital energies of $[\text{Fe}(\text{salten})\text{pyS}]_2$ and $[\text{Fe}(\text{salten})\text{pyCH}_2]_2$

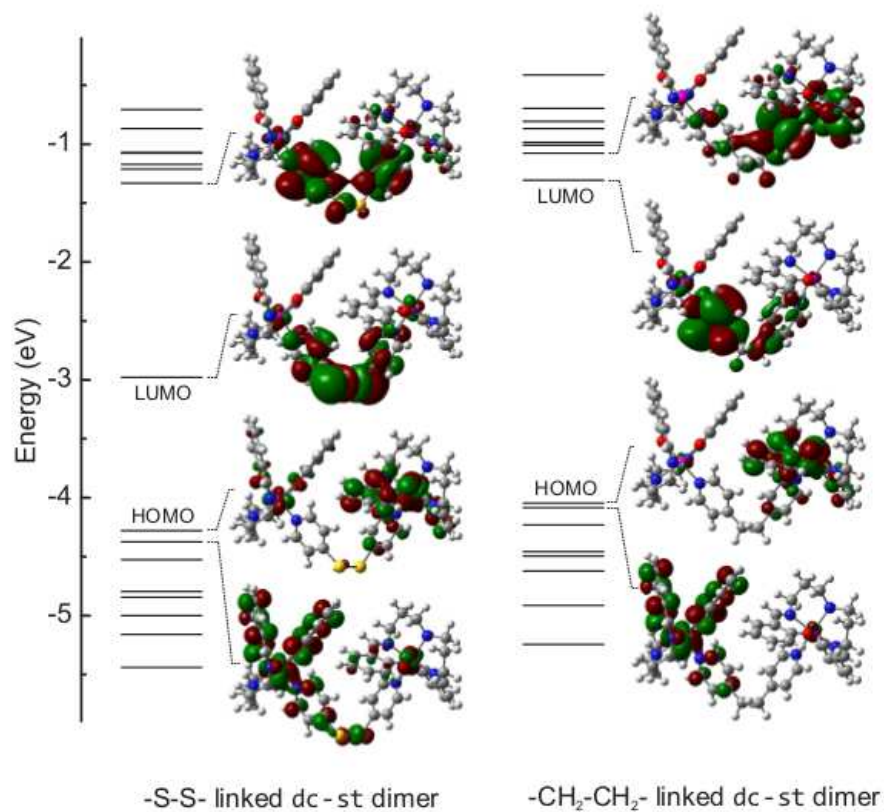


Figure S3: Calculated energy levels and isodensity plots of frontier orbitals. Results for $[\text{Fe}(\text{salten})\text{pyS}]_2$ and $[\text{Fe}(\text{salten})\text{pyCH}_2]_2$ are shown in the left and right columns, respectively. The lowest unoccupied molecular orbital (LUMO) of $[\text{Fe}(\text{salten})\text{pyS}]_2$ exhibits a high density at the disulfide bridge and overlaps with the $\text{Fe}(\text{salten})$ subunits. In contrast, in the dipyriddyethane-linked molecules this orbital is localized at the $\text{Fe}(\text{salten})$ subunits with hardly any overlap via the link. Moreover, the HOMO–LUMO gap is substantially wider.

Oxidation state of Fe centers

The oxidation state of the Fe centers in the synthesized bulk material was III.⁴ However, there are reasons to assume an Fe(II) state on the Au(111) surface. The electron rich gold surface may be expected to reduce deposited compounds.⁵ More importantly, our experimental dI/dV spectra with a wide gap are consistent with a closed-shell Fe(II) molecule and do not match the calculated Fe(III) states. Finally, the DFT calculations predict widely different dihedral angles of the disulfide part. For example, $\approx 85^\circ$ and $\approx 139^\circ$ are obtained for the low-spin Fe(II) and Fe(III) states of the dc-sc dimer (Figure S4). The same trend is observed for the other dimers. The match between the rather flat Fe(III) dimers with the observed STM images is less favorable. Finally, injection of electrons into the antibonding LUMO of the Fe(II) complex weakens the ligand bonds and thus enables a Bailar twist. In contrast, the LUMO of the Fe(III) complex is not involved in the ligand bonds and therefore inactive.

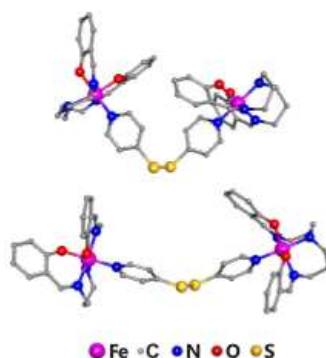


Figure S4: Calculated structures of dc-sc dimers with Fe(II) (top) and Fe(III) (bottom).

-
- ¹ Horcas, I.; Fernandez, R.; Gomez-Rodriguez, J. M.; Colchero, J.; Gomez-Herrero, J.; Baro, A. M. *Rev. Sci. Instrum.* **2007**, *78*, 013705.
- ² Frisch, M. J.; Trucks, G. W.; Schlegel, H. B.; Scuseria, G. E.; Robb, M. A.; Cheeseman, J. R.; Scalmani, G.; Barone, V.; Mennucci, B.; Petersson, G. A.; Nakatsuji, H.; Caricato, M.; Li, X.; Hratchian, H. P.; Izmaylov, A. F.; Bloino, J.; Zheng, G.; Sonnenberg, J. L.; Hada, M.; Ehara, M.; Toyota, K.; Fukuda, R.; Hasegawa, J.; Ishida, M.; Nakajima, T.; Honda, Y.; Kitao, O.; Nakai, H.; Vreven, T.; Montgomery, J. J. A.; Peralta, J. E.; Ogliaro, F.; Bearpark, M.; Heyd, J. J.; Brothers, E.; Kudin, K. N.; Staroverov, V. N.; Kobayashi, R.; Normand, J.; Raghavachari, K.; Rendell, A.; Burant, J. C.; Iyengar, S. S.; Tomasi, J.; Cossi, M.; Rega, N.; Millam, J. M.; Klene, M.; Knox, J. E.; Cross, J. B.; Bakken, V.; Adamo, C.; Jaramillo, J.; Gomperts, R.; Stratmann, R. E.; Yazyev, O.; Austin, A. J.; Cammi, R.; Pomelli, C.; Ochterski, J. W.; Martin, R. L.; Morokuma, K.; Zakrzewski, V. G.; Voth, G. A.; Salvador, P.; Dannenberg, J. J.; Dapprich, S.; Daniels, A. D.; Farkas, Ö.; Foresman, J. B.; Ortiz, J. V.; Cioslowski, J.; Fox, D. J. *Gaussian09, Revision A.02*, Gaussian, Inc.
- ³ Becke, A. D. *J. Chem. Phys.* **1993**, *98*, 5648.
- ⁴ Jacob, H.; Kathirvel, K.; Petersen, F.; Strunskus, T.; Bannwarth, A.; Meyer, S.; Tuzcek, F. *Langmuir* **2013**, *29*, 8534.
- ⁵ Hieringer, W.; Flechtner, K.; Kretschmann, A.; Seufert, K.; Auwärter, W.; Barth, J. V.; Görling, A.; Steinrück, H.-P.; Gottfried, J. M. *J. Am. Chem. Soc.* **2011**, *133*, 6206.

8.3 Supporting information on the Physical Chemistry Chemical Physics publication

Supporting Information *Physical Chemistry Chemical Physics*

H. Jacob, S. Ulrich, U. Jung, S. Lemke, T. Rusch, C. Schütt, F. Petersen, T. Strunskus, O.
Magnussen, R. Herges* and F. Tuczek*

”Monitoring the reversible photoisomerization of an azobenzene-functionalized molecular
triazatriangulene platform on Au(111) by IRRAS”

Phys. Chem. Chem. Phys. **2014**, 16, 22643-22650.

DOI: 10.1039/C4CP03438D

Supporting Information

Monitoring the reversible photoisomerization of an azobenzene- functionalized molecular triazatriangulene platform on Au(111) by IRRAS

*Hanne Jacob^a, Sandra Ulrich^b, Ulrich Jung^c, Sonja Kuhn^c, Talina Rusch^c, Christian Schütt^b,
Finn Petersen^a, Thomas Strunskus^d, Olaf Magnussen^c, Rainer Herges^{*b} and Felix Tuczek^{*a}*

^aInstitut für Anorganische Chemie, Christian-Albrechts-Universität Kiel, Max-Eyth-Str.2,
24118 Kiel, Germany

^bInstitut für Organische Chemie, Christian-Albrechts-Universität Kiel, Otto-Hahn-Platz 4
24098 Kiel, Germany

^cInstitut für Experimentelle und Angewandte Physik der Christian-Albrechts-Universität Kiel,
Leibnizstraße 11-19, 24118 Kiel, Germany

^dTechnische Fakultät der Christian-Albrechts-Universität Kiel, Kaiserstraße 2, 24143 Kiel,
Germany

Corresponding authors:

RH: Email: rherges@ac.uni-kiel.de

FT: E-Mail: ftuczek@ac.uni-kiel.de, fax: +49 431 880-1523

Table S1. Cartesian coordinates of the optimized structure for methoxy-azo-TATA (propyl side chains) *trans*.

XYZ file

90

Energy = -2008.147853891 Basis = RB3LYP 6-31++G(d,p), Charge O, Singlet

C	3.9673356	1.9951678	-1.1887097
N	3.7169768	1.3405710	-2.4086399
C	3.7131519	-0.0668466	-2.4518879
C	3.4349548	-0.7880758	-1.2661601
C	3.0133737	-0.0367514	-0.0061244
C	3.7006529	1.3249226	0.0282536
C	3.9542420	1.9493814	1.2730930
N	3.6801526	1.2418173	2.4595123
C	3.6745915	-0.1646937	2.4406177
C	3.4197272	-0.8422233	1.2252023
C	3.9953742	-0.7846636	-3.6402232
C	3.9617283	-2.1833473	-3.6308746
C	3.6765189	-2.9030012	-2.4655329
C	3.4198689	-2.2026837	-1.2623749
N	3.1501584	-2.8869616	-0.0631139
C	3.4133347	-2.2563100	1.1683781
C	4.4832745	3.3137774	-1.1557025
C	4.7376452	3.9215787	0.0783031
C	4.4926374	3.2598209	1.2864429
C	3.9199662	-0.9168163	3.6151050
C	3.9244731	-2.3140732	3.5478931
C	3.6873274	-2.9920968	2.3470260
H	4.2684892	-0.2632361	-4.5677117
H	4.1851983	-2.7312646	-4.5611776

H	3.6783410	-4.0006821	-2.4917989
H	4.7089262	3.8559465	-2.0834539
H	5.1620113	4.9388512	0.1001290
H	4.7501611	3.7580256	2.2308774
H	4.1398821	-2.8960283	4.4591902
H	3.7457855	-4.0888963	2.3306655
C	1.5395275	0.1368587	-0.0092328
C	0.3142937	0.2581117	-0.0072291
C	-1.1061037	0.3759060	-0.0027081
C	-1.9273026	-0.7891121	-0.0282530
C	-1.7388457	1.6470235	0.0292178
C	-3.3153636	-0.6888109	-0.0212981
C	-3.9392960	0.5843966	0.0117210
C	-3.1313382	1.7446929	0.0362505
N	-5.3314493	0.7955394	0.0225559
N	-6.0377652	-0.2632053	0.0014276
C	-7.4272127	-0.0607840	0.0123860
C	-8.2286471	-1.2221207	-0.0122266
C	-9.6267420	-1.1424768	-0.0046416
C	-10.2486621	0.1253174	0.0286955
C	-9.4498687	1.2991877	0.0540267
C	-8.0638815	1.2095175	0.0460325
H	-1.4396372	-1.7774700	-0.0536940
H	-1.1153166	2.5545635	0.0484612
H	-3.9588734	-1.5813929	-0.0405844
H	-3.6382875	2.7225928	0.0615738
H	-7.7172762	-2.1976837	-0.0380395
H	-10.2215949	-2.0673638	-0.0246384
H	-9.9651727	2.2727876	0.0800961
H	-7.4282772	2.1078192	0.0652199

H	4.1296223	-0.4197847	4.5715869
C	3.4552273	1.9397525	3.7253146
H	4.2326132	1.6585721	4.4745531
H	3.5867375	3.0228196	3.5446912
C	2.6509254	-4.2605835	-0.1200996
H	3.3775654	-4.9245717	-0.6456328
H	2.5860855	-4.6416637	0.9157392
C	3.5206291	2.1376046	-3.6195277
H	4.4212792	2.7610896	-3.8322007
H	3.4253339	1.4415171	-4.4734828
O	-11.5906685	0.3266612	0.0390498
C	-12.4535041	-0.7960901	0.0151910
H	-12.3122175	-1.4050793	-0.9088674
H	-12.3043017	-1.4495288	0.9070105
H	-13.4856422	-0.3915861	0.0295559
C	1.2569513	-4.3769422	-0.7602882
H	1.2813339	-3.9625341	-1.7919614
H	0.5544843	-3.7329256	-0.1832331
C	2.2571087	3.0138521	-3.5753674
H	2.3026013	3.6955753	-2.6974438
H	1.3792593	2.3502264	-3.4077246
C	2.0742162	3.8279616	-4.8592742
H	1.1515239	4.4460408	-4.8136401
H	2.9306810	4.5189419	-5.0313937

Table S2. Raman band positions and assignments for methoxy-azo-TATA (propyl side chains) *trans*. The frequencies are given in wavenumbers (cm^{-1}) obtained from bulk Raman, calculated and SERS spectra. Mode numbers derive from the Gaussian frequency calculation (RB3LYP 6-31++G(d,p)).

Peak #	Mode No.	Calc. freq. uncorrected	Calc. freq. corrected	Calc. Intensity	Bulk freq.	SERS freq.	Assignment
	223	2301.8	2197.1	16040.9	2202	2198	Alkyne stretching
30	219	1647.5	1590.6	4248.4	1598	1598	C=C stretching Ph _{top}
35	212	1547.1	1497.5	8318.3	1495	1493	N=N stretching. C-H bending Ph
43	204	1509.1	1462.2	9126.1	-	1485	C-H bending CH ₃ Methoxy
44	201	1505.9	1459.3	9093.8	1453	1452	C-H bending CH ₃ Methoxy
47	188	1456.8	1413.7	3849.1	1418	1417	C=C ring deformation Ph _{top}
	187	1442.3	1400.4	3711.0	1403	1403	C=C ring deformation Ph _{bot}
52	177	1371.9	1335.1	160.8	1363	-	C=C ring deformation, Ph _{top}
	173	1341.3	1306.7	620.6	1311	1312	C=C ring deformation, Ph _{bot}
	166	1322.9	1289.7	477.8	1302	1304	C-H bending Ph _{top}
	164	1305.2	1273.2	110.5	1287	-	C=C ring deformation Ph _{TATA}
	160	1281.2	1251.0	1797.6	1253	1253	C-Alkyne stretching
55	154	1262.6	1233.7	17.0	1234	-	C-H twisting. Alkyl _{TATA}
56	153	1219.0	1193.3	4146.1	1188	1190	C-H bending Ph _{top} , Ph _{bot}
61	140	1163.4	1141.8	12937.3	1140	1140	C-H bending Ph _{top} , Ph _{bot}
	137	1125.2	1106.4	242.4	1103	1108	C-H bending Ph _{top} , Ph _{bot}
64	123	1011.4	1000.8	270.3	991	998	C _{tertTATA} -Alkyne stretching

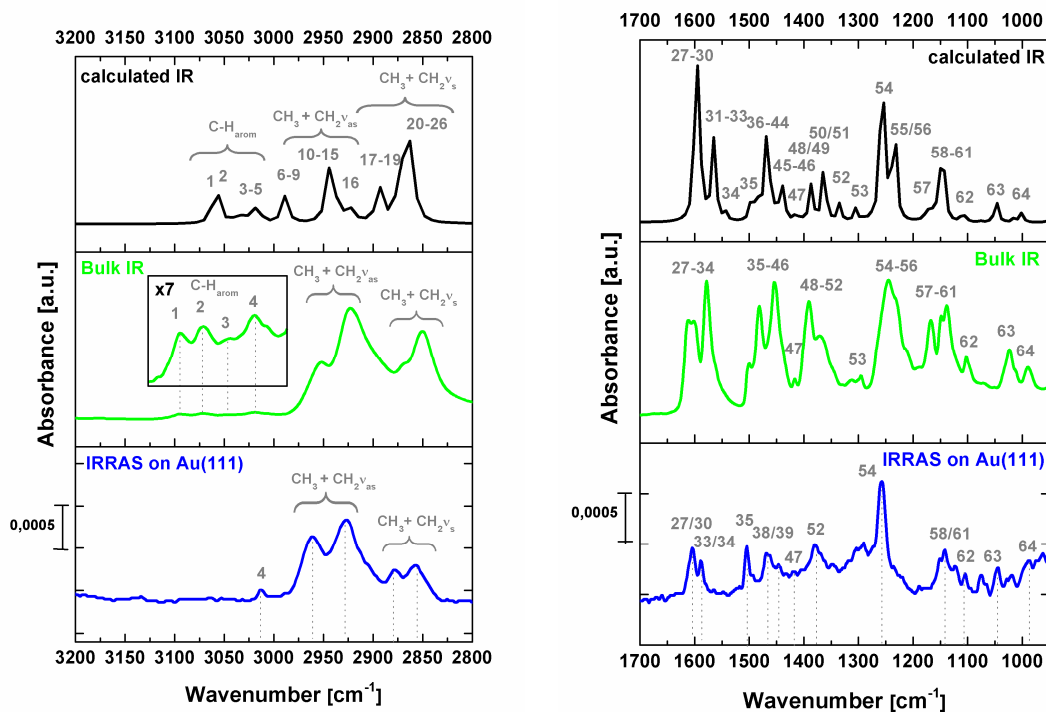


Figure S1. IR data of methoxy-azo-TATA. Left: CH-stretching vibration region, right: fingerprint region. The spectra in the top panels show the calculated, the spectra in the middle the bulk and the blue spectra at the bottom the IRRAS data of the surface-adsorbed monolayer. Band numbers correspond to Table S3.

Table S3. Infrared vibrational band assignments for methoxy-azo-TATA (propyl side chains) *trans*. The vibrational frequencies are given in wavenumbers (cm^{-1}) obtained from ATR, calculated and IRRAS. Mode numbers derive from the Gaussian frequency calculation (RB3LYP 6-31++G(d,p)). The orientation of the transition dipole moment (TDM) is given with respect to the surface plane (perpendicular: \perp , parallel: \parallel and neither totally parallel nor totally perpendicular: \nearrow). *For broad features the experimental frequency regime is indicated instead of exact wavenumbers

Peak #	Mode No.	Calc. freq. uncorrected	Calc. freq. corrected	Calc. Intensity	Bulk freq./ regime*	IRRAS freq.	TDM	Assignment
	264	3234.2	3061.4	8.0			/	C-H stretching Ph _{TATA}
	263	3233.8	3061.0	10.8			\parallel	C-H stretching Ph _{TATA}
	262	3233.5	3060.8	15.5			\parallel	C-H stretching Ph _{TATA}
	261	3229.8	3057.4	19.8			\parallel	C-H stretching Ph _{TATA}
	260	3229.7	3057.2	8.7			\parallel	C-H stretching Ph _{TATA}
	259	3228.9	3056.5	12.1			\perp	C-H stretching Ph _{top}
1	258	3228.1	3055.7	10.2	C-H _{arom}	-	/	C-H stretching Ph _{top}
2	257	3227.8	3055.5	13.0	C-H _{arom}	-	\parallel	C-H stretching Ph _{TATA}
	256	3227.1	3054.8	2.2			/	C-H stretching Ph _{bot}
	255	3213.0	3041.8	7.8			/	C-H stretching Ph _{bot}
	254	3205.0	3034.3	3.0			/	C-H stretching Ph _{top}
	253	3202.6	3032.1	8.5			/	C-H stretching Ph _{top}
	252	3200.2	3029.9	6.6			/	C-H stretching Ph _{bot}
	251	3197.7	3027.6	8.6			\perp	C-H stretching Ph _{bot}
3	250	3186.0	3016.7	13.8	C-H _{arom}	3014	/	C-H stretching Ph _{TATA}
4	249	3185.7	3016.5	16.5	C-H _{arom}		/	C-H stretching Ph _{TATA}
5	248	3185.4	3016.2	17.1	C-H _{arom}	-	/	C-H stretching Ph _{TATA}

6	247	3156.9	2989.7	16.7	CH ₂ v _{as}	-		C-H stretching Alkyl _{TATA}
7	246	3156.4	2989.3	25.8	CH ₃ v _{as}	CH ₃ v _{as}	⊥	C-H stretching CH ₃ -methoxy
8	245	3155.9	2988.8	15.2	CH ₂ v _{as}	CH ₂ v _{as}	/	C-H stretching Alkyl _{TATA}
9	244	3154.4	2987.4	15.1	CH ₂ v _{as}	-		C-H stretching Alkyl _{TATA}
10	243	3108.8	2945.2	29.6	CH ₃ v _{as}	CH ₃ v _{as}	/	C-H stretching CH ₃ -Alkyl _{TATA}
11	242	3108.4	2944.8	29.2			/	C-H stretching CH ₃ -Alkyl _{TATA}
12	241	3108.2	2944.6	29.4			/	C-H stretching CH ₃ -Alkyl _{TATA}
13	240	3104.4	2941.1	32.5	CH ₂ v _{as}	CH ₂ v _{as}	/	C-H stretching Alkyl _{TATA}
14	239	3104.3	2941.0	36.1			/	C-H stretching Alkyl _{TATA}
15	238	3104.1	2940.9	36.8			/	C-H stretching Alkyl _{TATA}
16	237	3087.4	2925.4	34.5	CH ₃ v _{as}	-		C-H stretching CH ₃ -methoxy
	236	3082.1	2920.4	5.0			/	C-H stretching Alkyl _{TATA}
	235	3081.6	2919.9	5.3			/	C-H stretching Alkyl _{TATA}
	234	3081.5	2919.9	6.0			/	C-H stretching Alkyl _{TATA}
17	233	3054.5	2894.8	30.7	CH ₂ v _s	CH ₂ v _s	/	C-H stretching Alkyl _{TATA}
18	232	3053.5	2893.9	30.8			/	C-H stretching Alkyl _{TATA}
19	231	3051.2	2891.8	36.0			/	C-H stretching Alkyl _{TATA}
20	230	3030.6	2872.7	39.2	CH ₃ v _s	-		C-H stretching CH ₃ -Alkyl _{TATA}
21	229	3030.3	2872.4	53.3	CH ₃ v _s	-		C-H stretching CH ₃ -Alkyl _{TATA}
22	228	3030.1	2872.2	68.5	CH ₃ v _s	-		C-H stretching CH ₃ -Alkyl _{TATA}
23	227	3021.6	2864.3	97.0	CH ₃ v _s	CH ₃ v _s	/	C-H stretching CH ₃ -methoxy
24	226	3019.4	2862.3	45.5	CH ₂ v _s	CH ₂ v _s	/	C-H stretching Alkyl _{TATA}
25	225	3017.9	2860.9	46.8			/	C-H stretching Alkyl _{TATA}
26	224	3016.9	2860.0	44.8			/	C-H stretching Alkyl _{TATA}
	223	2301.8	2197.1	28.9			⊥	Alkine stretching

27	222	1655.5	1598.0	190.7	~1600	1606	⊥	C=C stretching Ph _{top}
28	221	1654.4	1596.9	266.0		-		C=C stretching Ph _{TATA}
29	220	1654.3	1596.9	262.3		-		C=C stretching Ph _{TATA}
30	219	1647.5	1590.6	203.2		1606	⊥	C=C stretching Ph _{top}
	218	1638.2	1581.9	17.7			⊥	C=C stretching Ph _{top}
31	217	1621.1	1566.0	139.0	~1590	-		C=C stretching Ph _{TATA}
32	216	1620.7	1565.7	140.1	~1585	-		C=C stretching Ph _{TATA}
33	215	1616.9	1562.2	69.9	~1580	1589	⊥	C=C stretching Ph _{top}
	214	1611.3	1557.0	0.1			/	C=C stretching Ph _{TATA}
34	213	1596.7	1543.4	28.6	~1580	1589	⊥	C=C stretching Ph _{bot}
35	212	1547.1	1497.5	59.4	~1500	1504	⊥	N=N stretching. C-H bending Ph.
36	211	1535.9	1487.1	64.0	~1485	-	⊥	C-H bending Ph _{top,bot}
37	210	1534.7	1485.9	46.9	~1475	-	⊥	C-H bending Ph _{top, Ph_{bot}}
38	209	1520.2	1472.5	24.8	~1470	1468	/	C-H bending Alkyl _{TATA}
39	208	1519.6	1472.0	26.8			/	C-H bending Alkyl _{TATA}
40	207	1517.6	1470.2	46.0	~1460	-		C-H bending Alkyl _{TATA}
41	206	1516.0	1468.6	130.0		-	/	C-H bending Alkyl _{TATA}
42	205	1515.3	1468.0	106.7		-		C-H bending Alkyl _{TATA}
43	204	1509.1	1462.2	41.5		-	⊥	C-H bending CH ₃ Methoxy
	203	1507.3	1460.6	2.8				
	202	1507.3	1460.6	3.6			/	C-H bending Alkyl _{TATA}
44	201	1505.9	1459.3	23.2	~1460	-	⊥	C-H bending CH ₃ Methoxy
	200	1505.9	1459.2	4.8			/	C-H bending Alkyl _{TATA}
	199	1505.0	1458.4	8.3			/	C-H bending Alkyl _{TATA}
	198	1504.8	1458.3	12.2			/	C-H bending Alkyl _{TATA}

	197	1503.2	1456.8	11.0			/	C-H bending Alkyl _{TATA}
	196	1500.0	1453.8	0.4			/	C-H bending Alkyl _{TATA}
	195	1499.9	1453.7	0.7			/	C-H bending Alkyl _{TATA}
	194	1499.1	1452.9	0.3			/	C-H bending Alkyl _{TATA}
	193	1496.9	1451.0	8.5				C-H bending CH ₃ Methoxy
45	192	1486.4	1441.2	79.4	~1450	-		C=C ring deformation, Ph _{TATA}
46	191	1486.1	1440.9	76.8		-		C=C ring deformation, Ph _{TATA}
	190	1482.3	1437.4	1.5				C=C ring deformation, Ph _{TATA}
	189	1478.1	1433.6	19.3			⊥	C-H bending. CH ₃ -Methoxy
47	188	1456.8	1413.7	30.2	~1420	1420	⊥	C=C ring deformation, Ph _{top}
	187	1442.3	1400.4	5.2				C=C ring deformation, Ph _{bot}
48	186	1428.1	1387.1	67.9	~1390	-		C-H bending Alkyl _{TATA}
49	185	1427.7	1386.8	68.1		-		C-H bending Alkyl _{TATA}
	184	1421.3	1380.8	0.7				C-H bending Alkyl _{TATA}
	183	1418.2	1378.0	5.8				CH ₃ bending Alkyl _{TATA}
	182	1417.2	1377.1	2.7				CH ₃ bending Alkyl _{TATA}
	181	1416.4	1376.3	1.1				CH ₃ bending Alkyl _{TATA}
50	180	1402.4	1363.3	115.5	~1375	-		C-H bending Alkyl _{TATA}
51	179	1401.4	1362.4	119.8		-		C-H bending Alkyl _{TATA}
	178	1379.5	1342.1	0.3				C-H bending Alkyl _{TATA}
52	177	1371.9	1335.1	65.0	~1370	1380	⊥	C=C ring deformation, Ph _{top}
	176	1361.3	1325.2	1.1				C=C ring deformation,

								Ph _{TATA}
	175	1361.0	1325.0	1.3				C=C ring deformation, Ph _{TATA}
	174	1345.0	1310.2	0.3				C=C ring deformation, Ph _{TATA}
	173	1341.3	1306.7	4.9			/	C=C ring deformation, Ph _{bot}
53	172	1340.4	1305.8	22.2	~1295	-		C-H bending Alkyl _{TATA}
	171	1339.5	1305.0	4.5				C-H bending Alkyl _{TATA}
	170	1338.7	1304.3	16.6				C-H bending Alkyl _{TATA}
	169	1334.4	1300.3	1.3				C-H bending Alkyl _{TATA}
	168	1332.6	1298.7	0.5				C-H bending Alkyl _{TATA}
	167	1327.0	1293.5	0.3			/	C-H bending Alkyl _{TATA}
	166	1322.9	1289.7	6.5			⊥	C-H bending, Ph _{top}
	165	1317.8	1284.9	0.3				C-H bending, Ph _{bot}
	164	1305.2	1273.2	10.9			⊥	C=C ring deformation, Ph _{TATA}
54	163	1287.9	1257.2	645.3	~1245	1257	⊥	C-O stretching, C=C Ph _{top} , C-H bending CH ₃ Methoxy
	162	1286.7	1256.1	25.4				C-H twisting, Alkyl _{TATA}
	161	1285.8	1255.2	29.6				C-H twisting, Alkyl _{TATA}
	160	1281.2	1251.0	86.1			⊥	C-Alkine stretching
	159	1274.4	1244.7	17.7				C-H bending Ph _{TATA}
	158	1273.9	1244.2	12.9				C-H bending Ph _{TATA}
	157	1269.7	1240.3	2.9			/	C-H twisting, Alkyl _{TATA}
	156	1267.4	1238.2	11.0			⊥	C-N stretching, C-H bending Ph _{top} , Ph _{bot}
	155	1263.0	1234.1	209.2				C-H twisting, Alkyl _{TATA}

55	154	1262.6	1233.8	200.6	~1240	-		C-H twisting, Alkyl _{TATA}	
56	153	1219.0	1193.3	1.2		-	⊥	C-H bending Ph _{top} , Ph _{bot}	
	152	1215.8	1190.4	0.6			/	C-H bending Ph _{TATA}	
	151	1215.4	1190.0	1.0			/	C-H bending Ph _{TATA}	
	150	1211.3	1186.2	1.0			/	C-H bending Ph _{TATA}	
	149	1204.6	1180.0	13.5			/	C-H rocking, CH ₃ Methoxy	
57	148	1192.6	1168.8	23.4	~1165	-		C-H bending Ph _{TATA}	
	147	1192.2	1168.5	9.7					C-H bending Ph _{TATA}
	146	1192.1	1168.4	32.6					C-H bending Ph _{TATA}
58	145	1174.0	1151.6	175.2	~1160	1144	⊥	C-H bending, Ph _{top} , Ph _{bot}	
	144	1169.5	1147.4	0.8					C-H rocking CH ₃ Methoxy
	143	1167.3	1145.4	10.8				C-H rocking Alkyl _{TATA}	
59	142	1166.4	1144.6	70.9	~1150	-		C-H rocking Alkyl _{TATA}	
60	141	1166.0	1144.2	65.8					C-H rocking Alkyl _{TATA}
61	140	1163.4	1141.8	57.1	~1140	1144	/	C-H bending Ph _{top} , Ph _{bot}	
	139	1133.4	1114.0	0.2				/	ring deformation, Ph _{TATA}
62	138	1129.8	1110.7	18.5	~1100	1105	/	C-H bending Ph _{top} , Ph _{bot}	
	137	1125.2	1106.4	4.1				/	C-H bending Ph _{top} , Ph _{bot}
	136	1123.8	1105.1	6.1				ring deformation, Ph _{TATA}	
	135	1123.3	1104.6	6.8				ring deformation, Ph _{TATA}	
	134	1121.6	1103.0	0.2				C-H rocking Alkyl _{TATA}	
	133	1118.8	1100.5	0.0				C-H rocking Alkyl _{TATA}	
	132	1118.5	1100.1	0.1				ring deformation, Ph _{TATA}	
	131	1094.0	1077.4	4.3			⊥	N-C stretching Alkyl _{TATA}	
63	130	1061.8	1047.6	86.8	~1130	1045	/	O-CH ₃ stretching Methoxy, ring	

								deformation Ph _{top}
	129	1043.2	1030.4	1.3			/	C-H bending, Ph _{TATA} , Alkyl _{TATA}
	128	1040.5	1027.9	0.1				C-C stretching Alkyl _{TATA}
	127	1039.2	1026.7	0.1				C-C stretching Alkyl _{TATA}
	126	1036.2	1023.8	0.0				C-C stretching Alkyl _{TATA}
	125	1026.3	1014.7	15.4			⊥	ring deformation, Ph _{bot}
	124	1017.4	1006.4	1.8			/	ring deformation, Ph _{top}
64	123	1011.4	1000.8	33.9	~998	998	⊥	C _{tertTATA} -Alkine stretching
	122	993.2	984.1	0.2				C-H twisting Ph _{bot}
	121	984.0	975.5	0.1				C-H twisting Ph _{top}
	120	979.8	971.6	0.4				C-H twisting Ph _{bot}
	119	965.5	958.3	0.8			/	C-H twisting Ph _{TATA}
	118	964.5	957.4	0.8				C-H twisting Ph _{TATA}
	117	962.8	955.8	0.6			⊥	C-H twisting Ph _{TATA}
	116	916.8	913.2	0.2			/	C-H twisting Ph _{TATA}
	115	960.9	954.1	0.2			/	C-H twisting Ph _{TATA}
	114	955.5	949.0	1.3				C-H twisting Ph _{top}

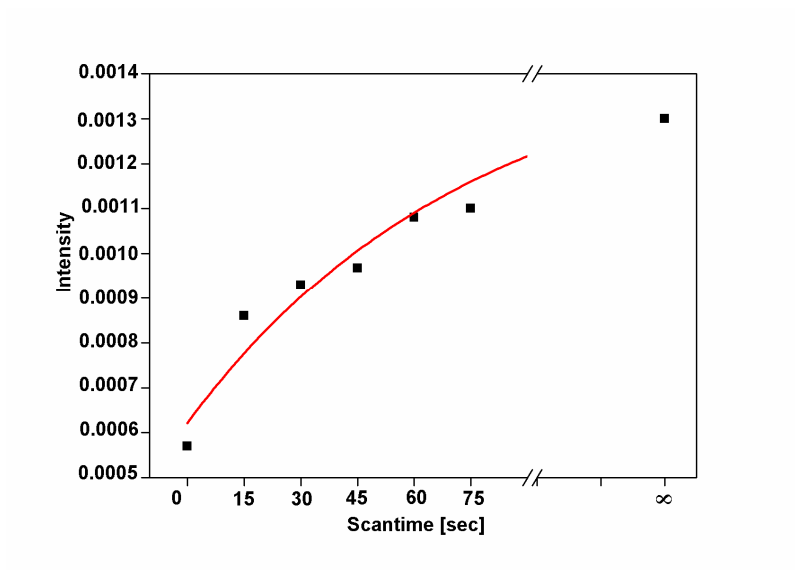


Figure S2. Intensity of the C(phenyl)-O stretch as a function of time and exponential function resulting from the fit of Figure 11 (main paper).

8.4 Supporting information on the Chemistry-A European Journal publication

Supporting Information *Chemistry-A European Journal*

V. Chandrasekaran, H. Jacob, F. Petersen, K. Kathirvel, F. Tucek* and T. K. Lindhorst*

”Synthesis and surface-spectroscopic characterization of photoisomerizable glyco-SAMs on Au(111)”

Chem. Eur. J. **2014**, 20, 8744-8752.

DOI: 10.1002/chem.201402075.

CHEMISTRY

A European Journal

Supporting Information

© Copyright Wiley-VCH Verlag GmbH & Co. KGaA, 69451 Weinheim, 2014

Synthesis and Surface-Spectroscopic Characterization of Photoisomerizable glyco-SAMs on Au(111)

Vijayanand Chandrasekaran,^[a] Hanne Jacob,^[b] Finn Petersen,^[b] Ketheeswari Kathirvel,^[b] Felix Tuzcek,^{*[b]} and Thisbe K. Lindhorst^{*[a]}

chem_201402075_sm_miscellaneous_information.pdf

Supporting Information

Content

1. ^1H and ^{13}C NMR spectra of synthetic compounds	
NMR spectra of compound 4	S2
NMR spectra of compound 5	S3
NMR spectra of compound 6	S4
NMR spectra of compound 7	S5
NMR spectra of compound 8	S6
NMR spectra of compound 9	S7
2. Photoirradiation of synthetic compounds	
General procedures	S8
NMR spectra and their interpretation of Z-6 and Z-7	S9
UV–Vis spectra of thermal $Z \rightarrow E$ isomerization of 6	S12
UV–Vis spectra of thermal $Z \rightarrow E$ isomerization of 7	S13
Efficacy of $Z \rightarrow E$ photoisomerization	S14
3. IRRAS studies	
IRRA spectra of 6 - and 7 -SAMs	S15
PM-IRRA spectra of <i>m</i> SAM	S16
Vibrational frequency calculation and assignment of E-7	S17
Fit parameters for the XP spectra of <i>m</i> SAM	S21
XPS characterization of SAM formed from E-7 .	S22

1. ^1H and ^{13}C NMR spectra of synthetic compounds

NMR spectra of compound 4

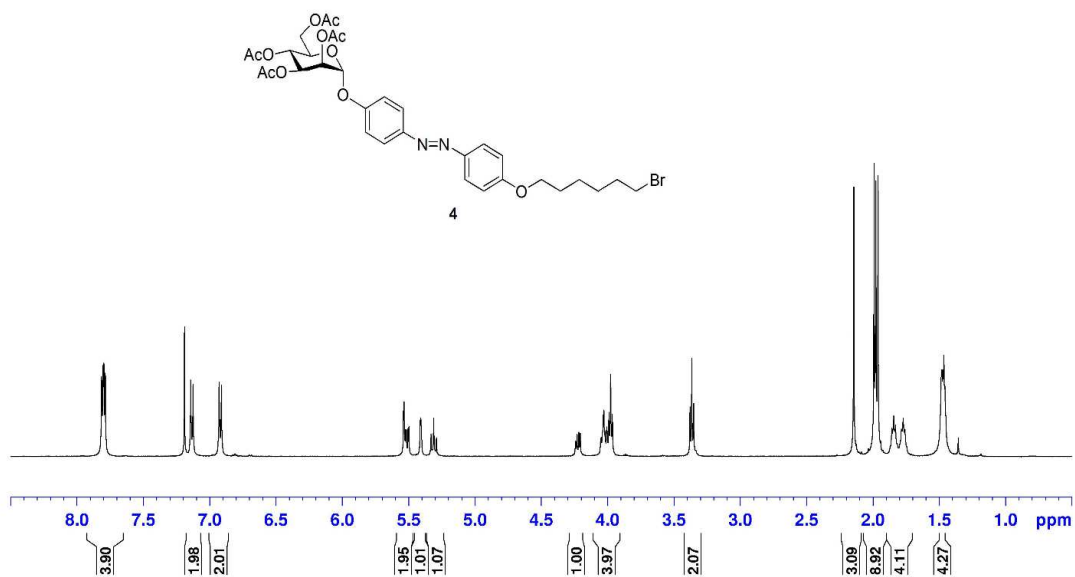


Figure S1. ^1H NMR spectrum (500 MHz, CDCl_3 , 300.0 K).

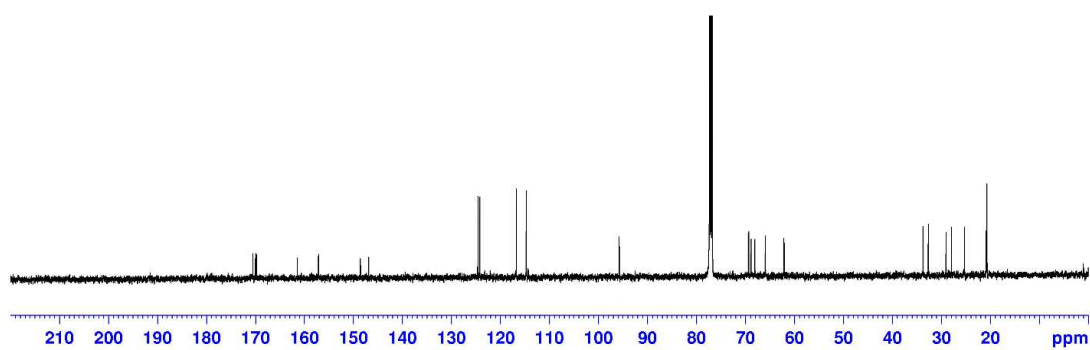


Figure S2. ^{13}C NMR spectrum (125 MHz, CDCl_3 , 300.0 K).

NMR spectra of compound 5

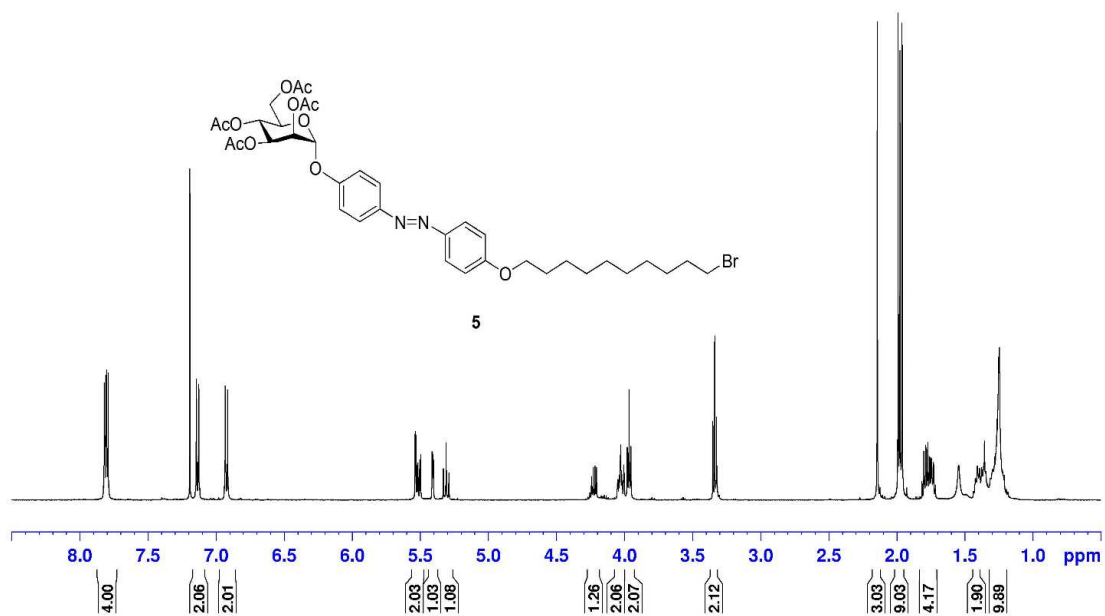


Figure S3. ¹H NMR spectrum (500 MHz, CDCl₃, 300.0 K).

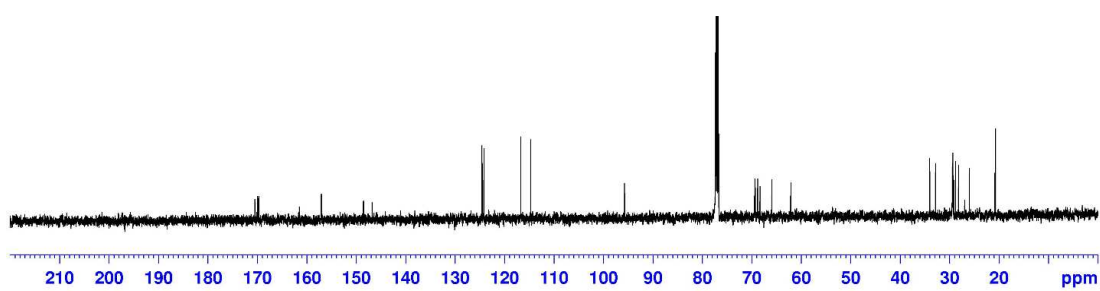


Figure S4. ¹³C NMR spectrum (125 MHz, CDCl₃, 300.0 K).

NMR spectra of compound **6**

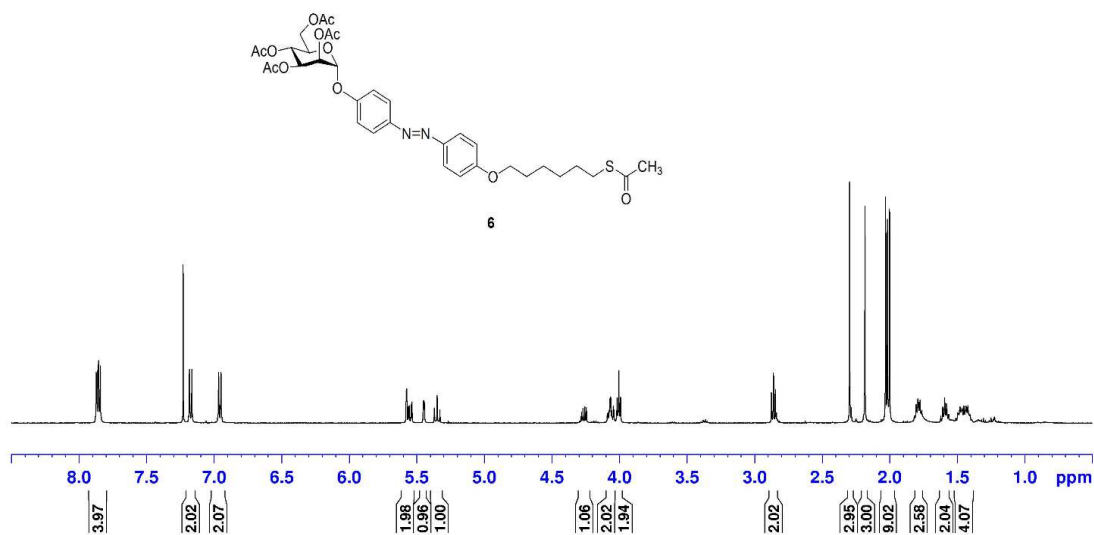


Figure S5. ¹H NMR spectrum (500 MHz, CDCl₃, 300.1 K).

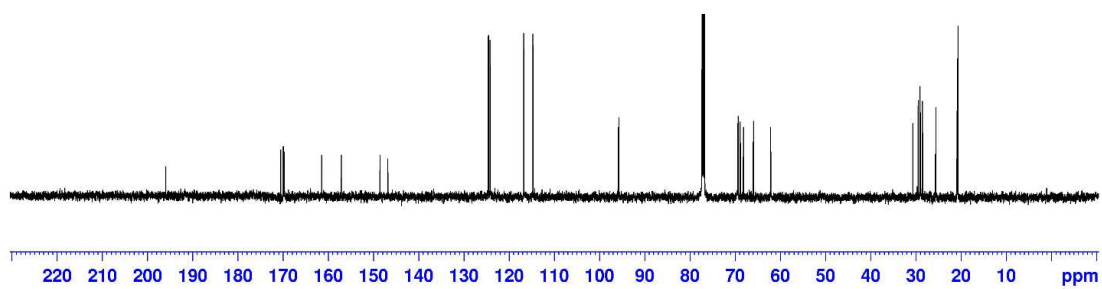


Figure S6. ¹³C NMR spectrum (125 MHz, CDCl₃, 300.0 K).

NMR spectra of compound 7

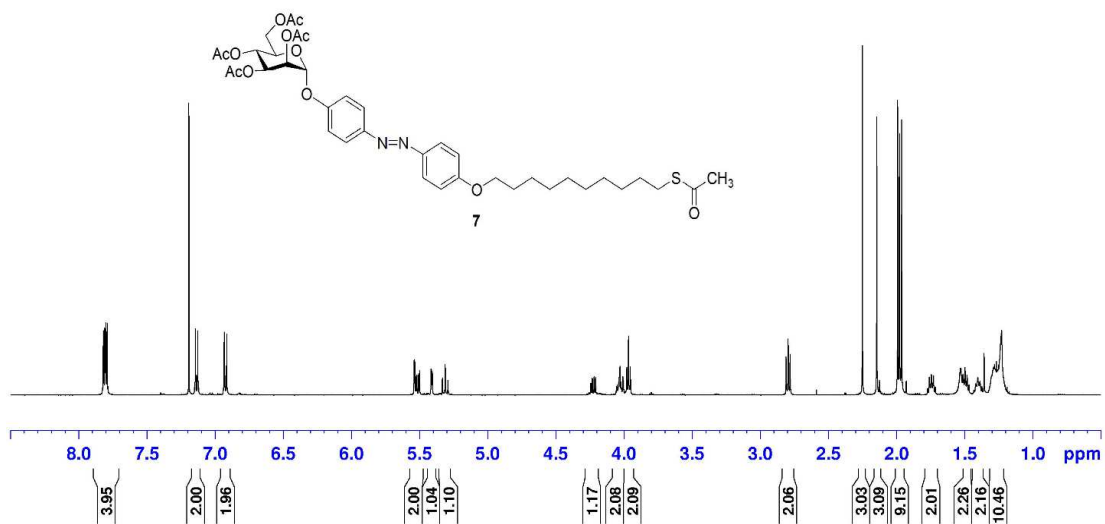


Figure S7. ¹H NMR spectrum (500 MHz, CDCl₃, 300.1 K).

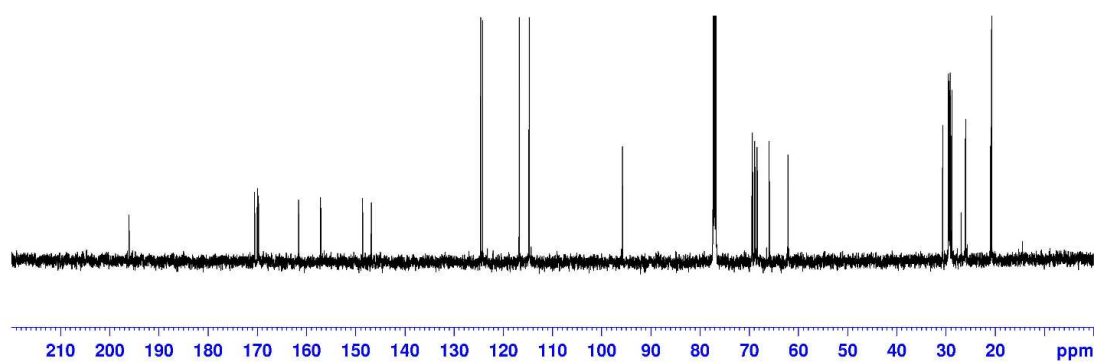


Figure S8. ¹³C NMR spectrum (125 MHz, CDCl₃, 300.0 K).

NMR spectra of compound **8**

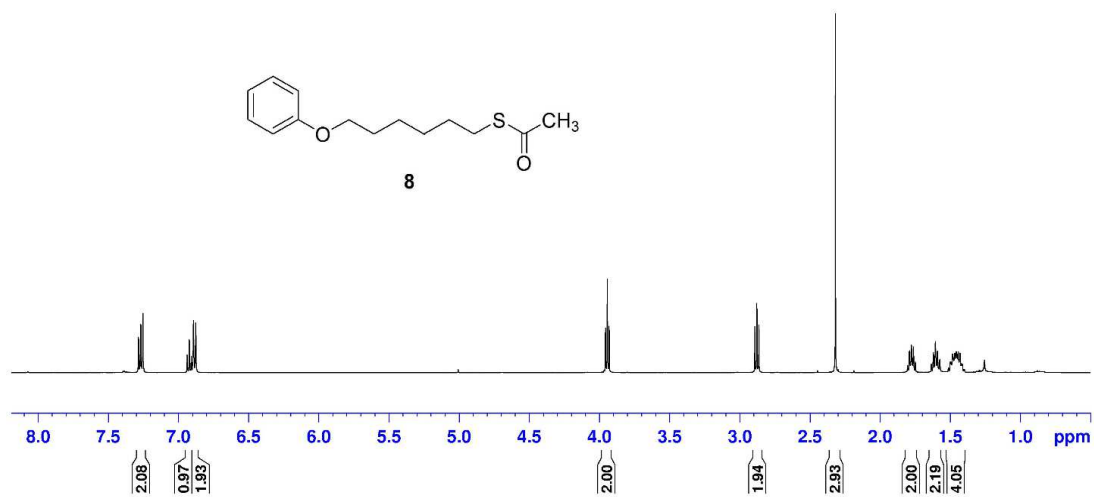


Figure S9. ¹H NMR spectrum (500 MHz, CDCl₃, 300.0 K).

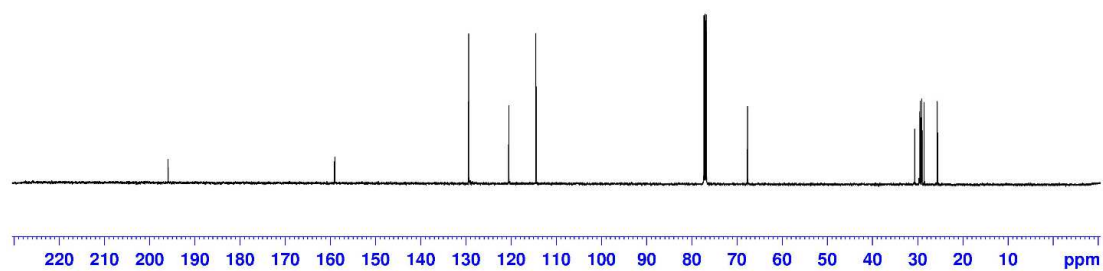


Figure S10. ¹³C NMR spectrum (125 MHz, CDCl₃, 300.0 K).

NMR spectra of compound **9**

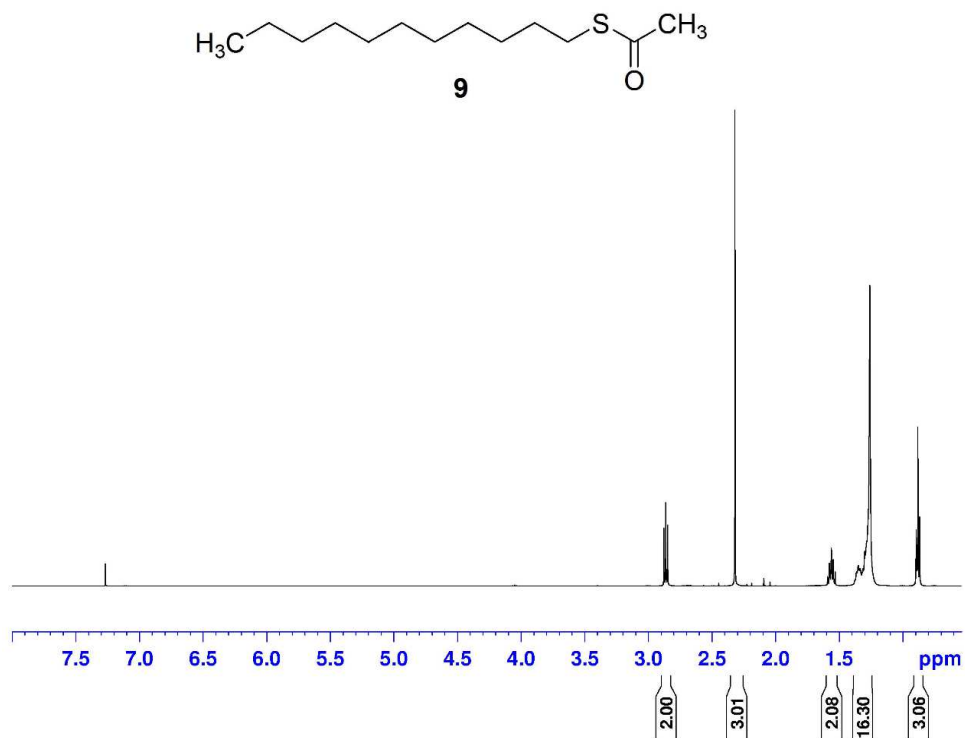


Figure S11. ¹H NMR spectrum (200 MHz, CDCl₃, 299.8 K).

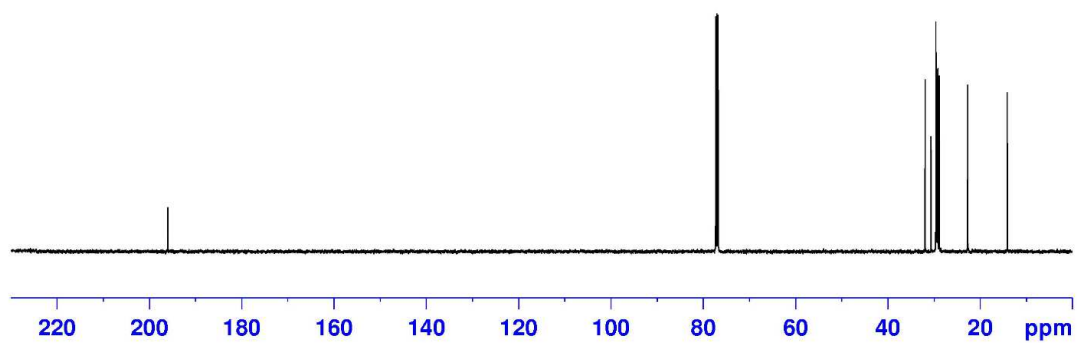


Figure S12. ¹³C NMR spectrum (125 MHz, CDCl₃, 299.8 K).

2. Photoirradiation of synthetic compounds

General procedures

Photoirradiation was performed using LED (emitting 365 nm light). From the Nichia Corporation (NC4U133A) with a FWHM of 9 nm and optical power output (P_o) ~1 W.

By ^1H NMR spectroscopy E/Z ratios were calculated by irradiating the sample in the NMR tube. The distance between the LED and sample in the NMR tube was about ~5 cm. The ground state (gs) as well as in the photostationary state (pss) were determined by the integration of H-1 proton of the sugar.

By UV-Vis spectroscopy, samples were irradiated in the UV cuvette with a distance between LED and cuvette of ~5 cm. Upon irradiation of gs azobenzene glycosides at 365 nm, the absorption spectra showed an increase in the absorbance in the $n-\pi^*$ transition and simultaneous decrease in the $\pi-\pi^*$ transition, indicating the generation of the respective Z isomer.

The kinetics of the $Z \rightarrow E$ relaxation process were determined by UV-Vis spectroscopy in the dark. For determination of the rate constants, a graph of $\ln(A_{infinite} - A_{time})$ was plotted as a function of time; where $A_{infinite}$ is the absorbance of $\pi\pi^*$ transition at infinite time and A_{time} is the absorbance at time t after start of the relaxation process. The negative slope k of the linear plot is the rate constant of the $Z \rightarrow E$ relaxation process. The half life $\tau_{1/2}$ was determined as $\tau_{1/2} = \ln 2/k$.

NMR spectra and their interpretation of Z-6

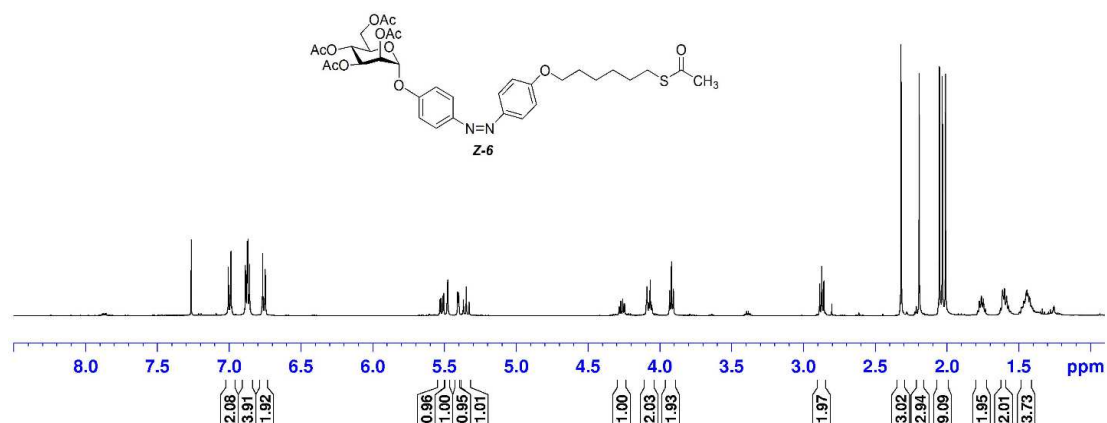


Figure S13. ¹H NMR spectrum (500 MHz, CDCl₃, 300.0 K).

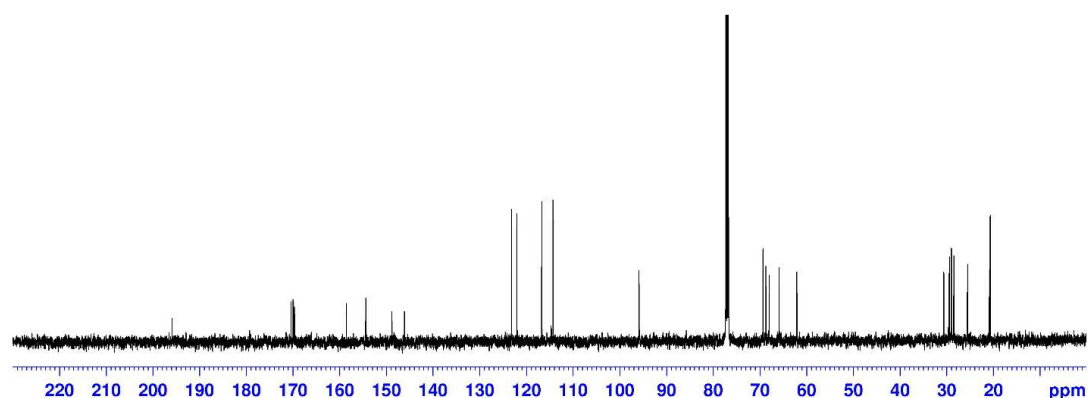


Figure S14. ¹³C NMR spectrum (125 MHz, CDCl₃, 299.9 K).

Z-4-(4'-Acetylthiohexylphenylazo)phenyl 2,3,4,6-tetra-O-acetyl- α -D-mannopyranoside (Z-6):

¹H NMR (500 MHz, CDCl₃, 300.0 K): δ =7.00 (d, J =8.9 Hz, 2H; H-8, H-12), 6.88 (d, J =8.9 Hz, 2H; H-14, H-18), 6.87 (d, J =8.9 Hz, 2H; H-9, H-11), 6.76 (d, J =8.9 Hz, 2H; H-15, H-17), 5.52 (dd, $J_{2,3}$ =3.5 Hz, $J_{3,4}$ = 10.0, 1H; H-3), 5.48 (d, $J_{1,2}$ =1.8 Hz, 1H; H-1), 5.41 (dd, $J_{2,1}$ =1.8 Hz, $J_{2,3}$ =3.5 Hz, 1H; H-2), 5.35 (t, $J_{3,4}$ = $J_{4,5}$ =10.1 Hz, 1H; H-4), 4.27 (dd, $J_{5,6a}$ =5.9 Hz, $J_{6a,6b}$ =12.6, 1H; H-6a), 4.09-4.06 (m, 2H; H-5, H-6b), 3.92 (t, J =6.5 Hz, 2H; H-19),

2.87 (t, $J=7.0$ Hz, 2H; H-24), 2.32 (s, 3H; SCOCH₃), 2.19, 2.05, 2.03, 2.01 (each s, each 3H; 4 COCH₃), 1.79-1.73 (m, 2H; H-23), 1.63-1.57 (m, 2H; H-20), 1.48-1.42 (m, 4H; H-22, H-21); ¹³C NMR (125 MHz, CDCl₃, 299.9 K): δ =195.9 (C-25, SCOCH₃), 170.5, 170.0, 169.9, 169.7 (4 COCH₃), 158.6 (C-16), 154.4 (C-7), 148.9 (C-10), 146.1 (C-13), 123.2 (C-14, C-18), 122.1 (C-9, C-11), 116.7 (C-8, C-12), 114.3 (C-15, C-17), 95.9 (C-1), 69.3 (C-5), 68.7 (C-2), 68.0 (C-3), 68.0 (C-19), 65.9 (C-4), 62.1 (C-6), 30.6 (C-26), 29.4 (C-20), 29.0 (C-23), 28.9 (C-24), 28.5 (C-21), 25.6 (C-22), 20.9, 20.9, 20.7, 20.7 (4 COCH₃).

$\epsilon = 4579 \pm 192$ L x mol⁻¹ x cm⁻¹.

NMR spectra and their interpretation of Z-7

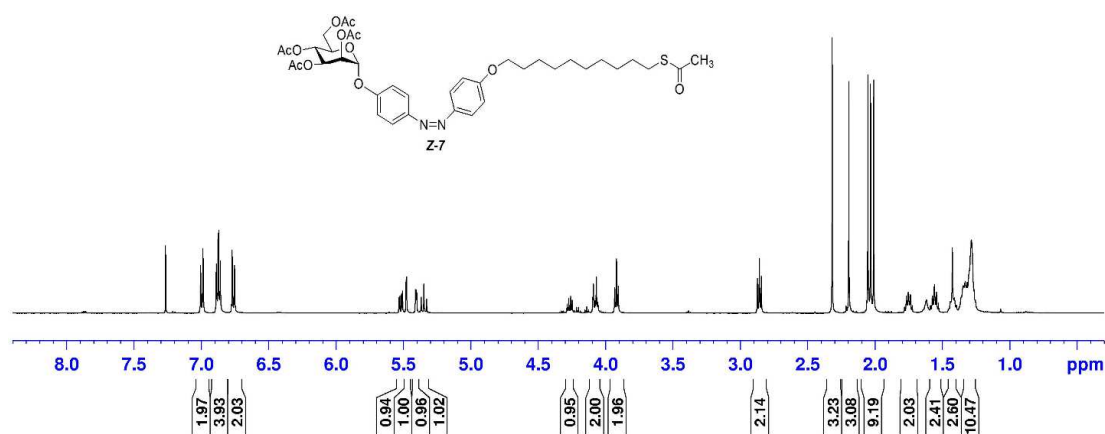


Figure S15. ¹H NMR spectrum (500 MHz, CDCl₃, 300.1 K).

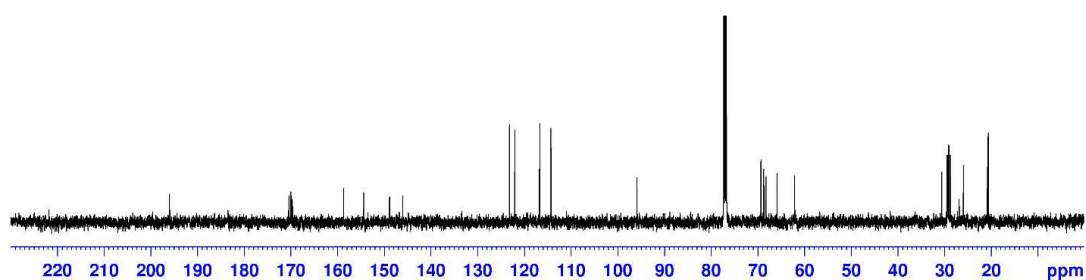


Figure S16. ¹³C NMR spectrum (125 MHz, CDCl₃, 300.0 K).

Z-4-(4'-Acetylthiodecylphenylazo)phenyl 2,3,4,6-tetra-O-acetyl- α -D-mannopyranoside (Z-7):

^1H NMR (500 MHz, CDCl_3 , 300.1 K): δ =7.00 (d, J =8.9 Hz, 2H; H-18, H-12), 6.88 (d, J =8.9 Hz, 2H; H-14, H-18), 6.87 (d, J =8.9 Hz, 2H; H-9, H-11), 6.76 (d, J =8.9 Hz, 2H; H-15, H-17), 5.52 (dd, $J_{2,3}$ =3.5 Hz, $J_{3,4}$ = 10.0, 1H; H-3), 5.48 (d, $J_{1,2}$ =1.7 Hz, 1H; H-1), 5.41 (dd, $J_{1,2}$ =1.8 Hz, $J_{2,3}$ =3.5 Hz, 1H; H-2), 5.35 (t, $J_{3,4}$ = $J_{4,5}$ =9.9 Hz, 1H; H-4), 4.27 (dd, $J_{5,6a}$ =6.0 Hz, $J_{6a,6b}$ =12.6, 1H; H-6a), 4.09-4.06 (m, 2H, H-5; H-6-b), 3.92 (t, J =6.6 Hz, 2H; H-19), 2.86 (t, J =7.4 Hz, 2H; H-28), 2.32 (s, 3H; SCOCH_3), 2.19, 2.05, 2.03, 2.01 (each s, each 3H; 4 COCH_3), 1.78-1.72 (m, 2H; H-20), 1.58-1.53 (m, 2H; H-27), 1.44-1.39 (m, 2H; H-21), 1.34-1.26 (m; 10H); ^{13}C NMR (125 MHz, CDCl_3 , 300.0 K): δ =196.0 (C-30, SCOCH_3), 170.5, 170.0, 169.9, 169.7 (4 COCH_3), 158.7 (C-16), 154.4 (C-7), 148.9 (C-10), 146.1 (C-13), 123.2 (C-14, C-18), 122.1 (C-9, C-11), 116.7 (C-8, C-12), 114.3 (C-15, C-17), 95.9 (C-1), 69.3 (C-5), 69.3 (C-2), 68.7 (C-3), 68.3 (C-19), 65.9 (C-4), 62.1 (C-6), 30.6 (C-30), 29.5 (C-27), 29.4-26.9 (C-20, C-22-C-28), 26.0 (C-21), 20.9, 20.9, 20.7, 20.7 (4 COCH_3).

ϵ = 1780 \pm 69 L x mol $^{-1}$ x cm $^{-1}$.

UV-Vis spectra of thermal Z→E isomerization of **6**

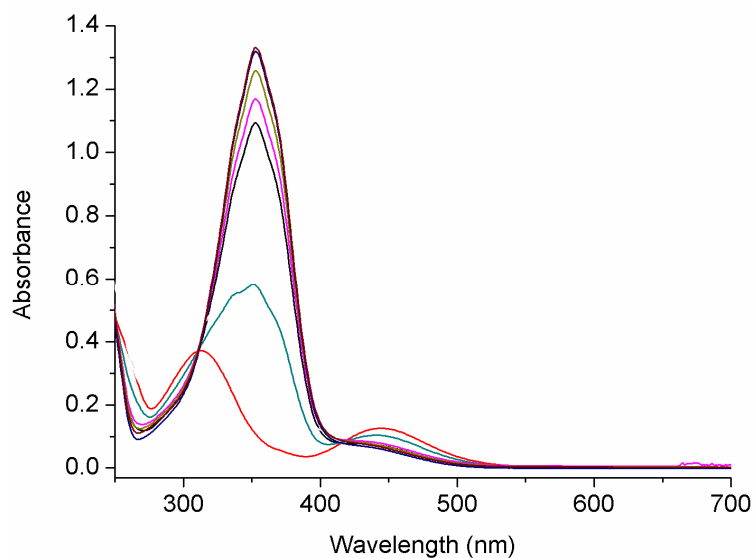


Figure S17. UV-Vis spectra showing thermal Z→E isomerization of **6** in ethanol (35 μM) at 18 ± 1°C in the dark.

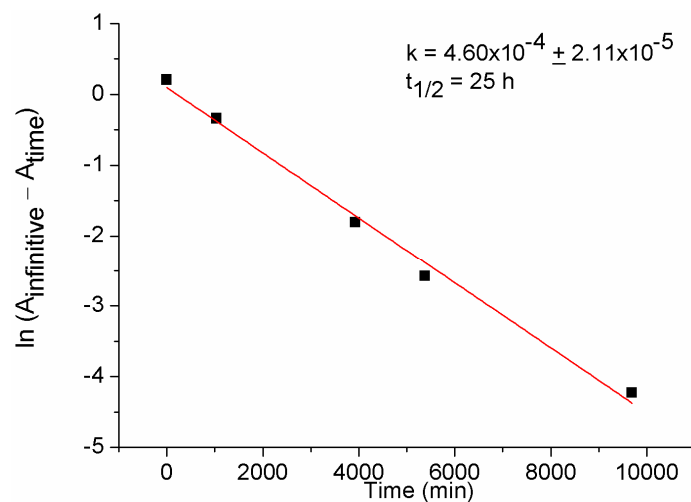


Figure S18. First order kinetics plot for the thermal Z→E isomerization of **6** as a function of time.

UV-Vis spectra of thermal Z→E isomerization of 7

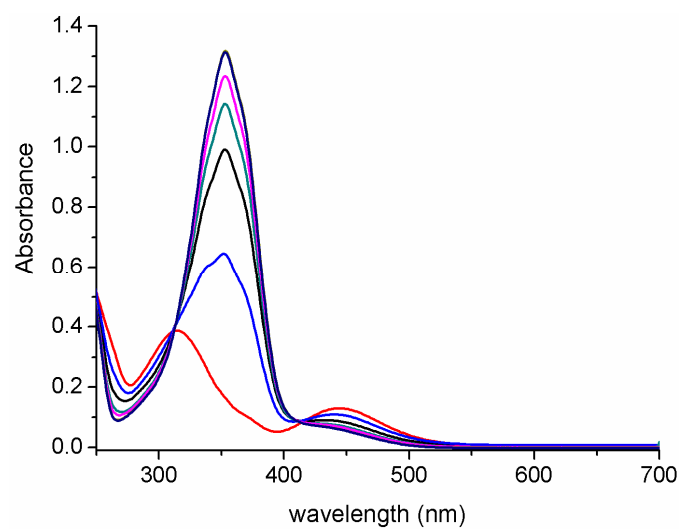


Figure S19. UV-Vis spectra showing thermal Z→E isomerization of **7** in ethanol (35 μ M) at $18 \pm 1^\circ\text{C}$ in the dark.

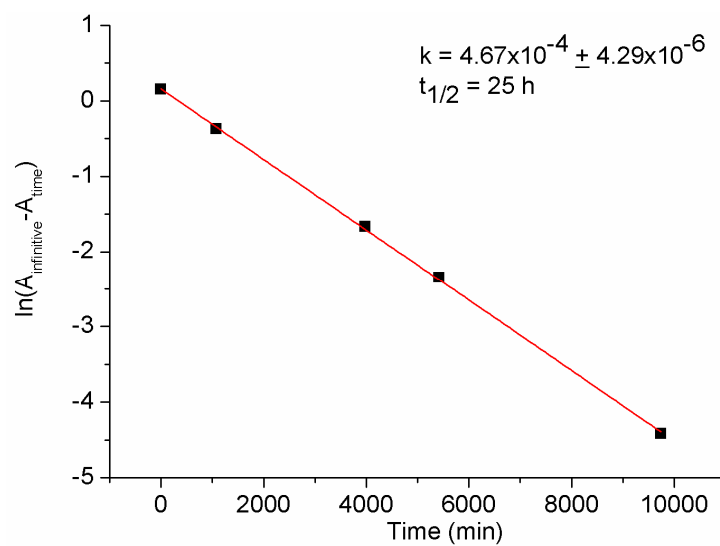


Figure S20. First order kinetics plot for the thermal Z→E isomerization of **7** as a function of time.

Efficacy of $Z \rightarrow E$ photoisomerization of **7**

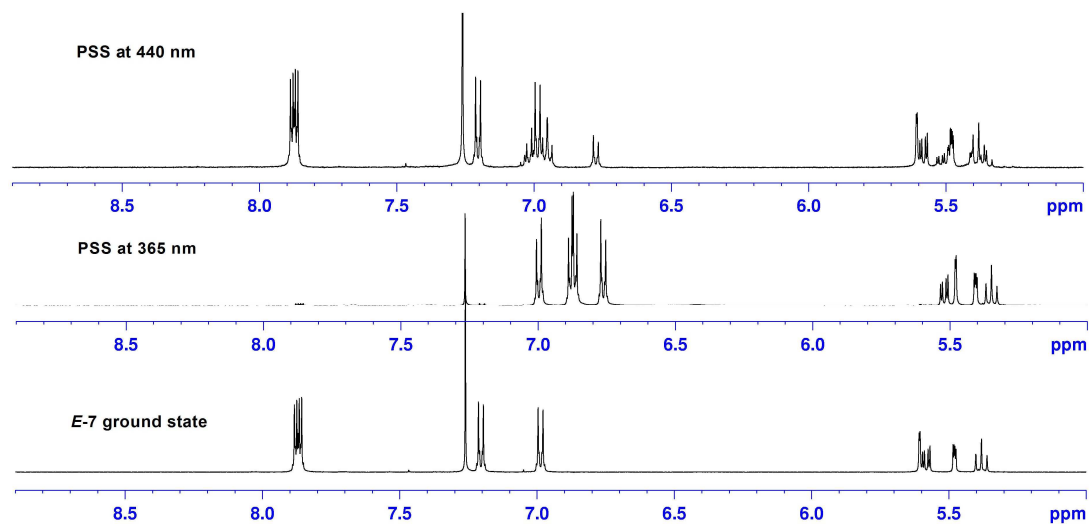


Figure S21. ¹H NMR spectra (500 MHz, CDCl₃, 300.1 K) of **7**. The following states of **7** were recorded:

Bottom: *E*-**7** in its ground state.

Middle: photostationary state (PPS) of *Z*-**7** obtained after 8 min of irradiation at 365 nm (> 98% of *Z*-isomer).

Top: photostationary state (PPS) of *E*-**7** obtained after 8 min of irradiation at 440 nm (~70% *E*-isomer).

E:*Z*-ratios were deduced on the basis of integration of H-3 resonances for each isomer.

3. IRRAS studies

IRRA spectra of 6- and 7-SAMs

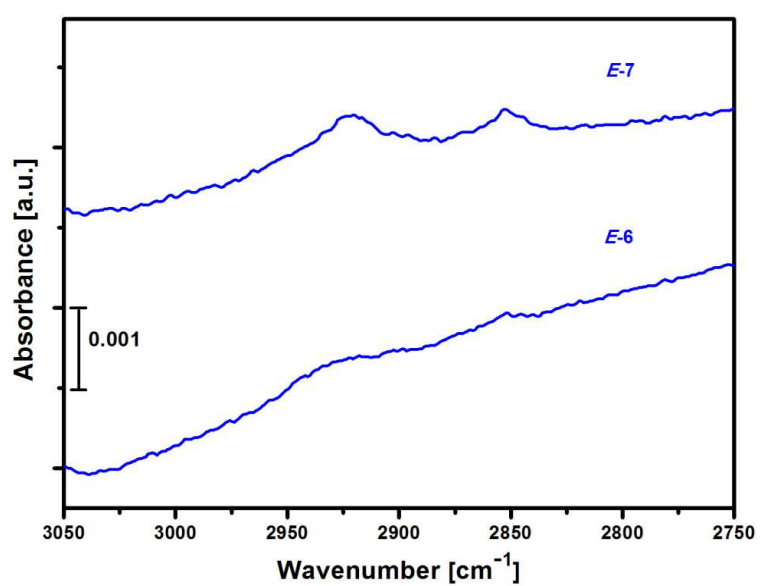


Figure S22. High frequency region of IRRA spectra (CH₂ symmetric and asymmetric stretching vibrations) of SAMs formed from ethanolic solutions of **E-6** and **E-7**, respectively.

PM-IRRA spectra of *m*SAM

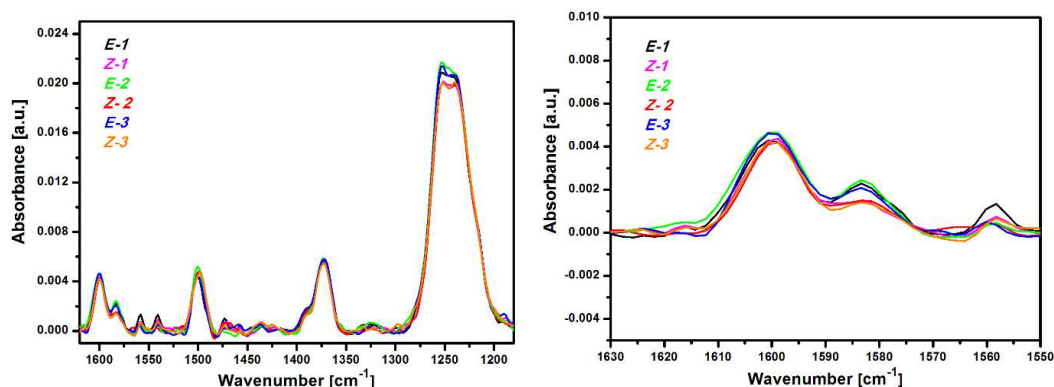


Figure S23. PM-IRRA spectra of *m*SAM prepared from a 1:4 mixture of **7** and **9**. The left spectrum shows the mid- to low frequency region upon $E \rightarrow Z$ isomerization with 365 nm light and $Z \rightarrow E$ back isomerization effected by irradiation at 440 nm through five cycles. In the spectrum on the right, the mid-frequency region is enlarged, showing the changes of the 1580 cm⁻¹ band during isomerization.

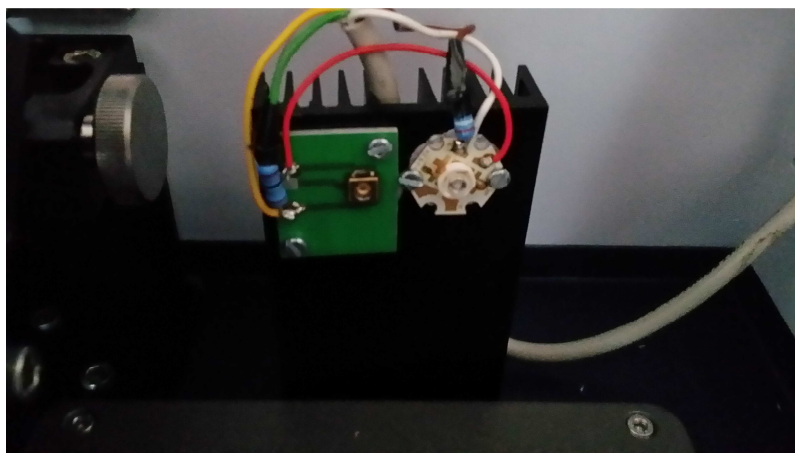


Figure S24. For the $E \rightarrow Z$ isomerization of the molecules on surface the samples were irradiated with a LED (Nichia NC4U133(T), peak wavelength: 365 (\pm 9) nm, 1 LEDs, power dissipation: 12 W, luminous flux: 10 lm, distance \sim 5 cm). $Z \rightarrow E$ conversion was performed with a LED from Nichia Corporation (NS6C083AT, peak wavelength: 440 nm, 1 LEDs, power dissipation: 1.5 W, luminous flux: 10 lm) The distance between the sample and LED is 5 cm for IRRAS measurements. This illumination unit was constructed by Sahlmann Photochemical Solutions (<http://www.sahlmann-ps.de/>).

Vibrational frequency calculation and assignment of E-7

Table S1. The vibrational frequencies (wavenumber, cm^{-1}) for compound **7** obtained from the calculation, transition dipole moment (TDM) with respect to the surface (perpendicular: \perp ; parallel: \parallel ; neither parallel nor perpendicular: $/$) and assignment of the bands are given; man = α -D-mannoside residue.

Calculation method: B3LYP; Basis set: 6-31G(d,p); Charge: zero; Spin: singlet

Mode No.	Calculated	Intensity	IRRAS	TDM	Assignments
288	3241.2	5.1		/	(CH _{azobenzene ring}) stretch
287	3239.9	2.5		/	(CH _{azobenzene ring}) stretch
286	3236.3	9.5		\parallel	(CH _{azobenzene ring}) stretch
285	3232.2	8.8		/	(CH _{azobenzene ring}) stretch
284	3221.9	10.6		\parallel	(CH _{azobenzene ring}) stretch
283	3219.3	3.1		\parallel	(CH _{azobenzene ring}) stretch
282	3217.0	9.4		/	(CH _{azobenzene ring}) stretch
281	3216.0	6.7		\parallel	(CH _{azobenzene ring}) stretch
280	3178.1	4.2		\parallel	(CH) stretch (O-acetyl)
279	3177.2	5.0		\parallel	(CH) stretch (O-acetyl)
278	3175.0	5.3		/	(CH) stretch (O-acetyl)
277	3174.4	5.4		/	(CH) stretch (O-acetyl)
276	3172.2	6.5		/	(CH) stretch (O-acetyl)
275	3148.2	6.7		/	(CH _{man}) stretch
274	3142.8	7.0		\perp	(CH _{man}) stretch
273	3138.1	19.8		\parallel	(CH ₂) asymmetric stretch (alkyl unit)
272	3128.8	3.0		/	(CH) stretch (O-acetyl)
271	3126.9	2.9		\parallel	(CH) stretch (O-acetyl)
270	3125.6	3.3		\parallel	(CH) stretch (O-acetyl)
269	3124.8	2.7		\parallel	(CH) stretch (O-acetyl)
268	3119.3	3.5		/	(CH _{man}) stretch
267	3113.5	4.4		/	(CH _{man}) stretch
266	3108.5	18.0		\perp	(CH ₂) stretch (man unit)
265	3091.1	74.1		\parallel	(CH ₂) stretch (alkyl unit)
264	3068.3	7.1		/	(CH _{man}) stretch
263	3075.2	27.1		\parallel	(CH ₂) stretch (alkyl unit)
262	3074.8	72.1		\parallel	(CH ₂) stretch (alkyl unit)
261	3064.2	71.4		\parallel	(CH ₂) stretch (alkyl unit)
260	3061.0	0.7		\parallel	(CH) stretch (O-acetyl)
259	3060.5	0.6		/	(CH) stretch (O-acetyl)
258	3059.6	1.0		/	(CH) stretch (O-acetyl)

257	3058.8	22.4			(CH ₂) stretch (alkyl unit)
256	3055.2	2.2		/	(CH) stretch (O-acetyl)
255	3053.5	1.0			(CH ₂) stretch (alkyl unit)
254	3041.1	3.0			(CH ₂) stretch (alkyl unit)
253	3040.5	35.5			(CH ₂) stretch (alkyl unit)
252	3031.9	0.1			(CH ₂) stretch (alkyl unit)
251	3029.9	31.1			(CH ₂) stretch (alkyl unit)
250	3026.6	1.0			(CH ₂) stretch (alkyl unit)
249	3022.9	0.0			(CH ₂) stretch (alkyl unit)
248	3015.0	88.0		/	(CH ₂) stretch (alkyl unit)
247	3013.6	68.3		/	(CH ₂) stretch (alkyl unit)
246	3008.5	0.4		/	(CH ₂) stretch (alkyl unit)
245	3002.6	1.5		/	(CH ₂) stretch (alkyl unit)
244	3001.2	0.1		⊥	(CH ₂) stretch (alkyl unit)
243	2999.3	0.4			(CH ₂) stretch (alkyl unit)
242	2997.8	0.2		/	(CH ₂) stretch (alkyl unit)
241	2473.1	22.9		/	S-H stretch
240	1735.2	346.2	} 1760	⊥	C=O stretch (O-acetyl)
239	1716.2	179.5			C=O stretch (O-acetyl)
238	1712.5	273.0			C=O stretch (O-acetyl)
237	1708.4	97.5		/	C=O stretch (O-acetyl)
236	1642.6	18.3		/	(CC _{azobenzene ring}) stretch
235	1640.2	409.5	1600	⊥	(CC _{azobenzene ring}) stretch
234	1620.1	79.2	1580	⊥	(CC _{azobenzene ring}) stretch
233	1615.0	21.5		/	(CC _{azobenzene ring}) stretch
232	1536.0	8.1		⊥	(CH ₂) & (CH _{aryl}) bending
231	1529.3	21.6		/	(CH ₂) & (CH _{aryl}) bending
230	1525.5	94.8		⊥	(CH ₂) & (CH _{aryl}) bending
229	1523.1	113.0	1500	⊥	(CH _{aryl}) bending
228	1520.4	33.5		⊥	(CH ₂) & (CH _{aryl}) bending
227	1515.6	23.9		⊥	(CH ₂) & (CH _{aryl}) bending
226	1509.8	2.3		⊥	(CH ₂) bending (alkyl unit)
225	1504.5	0.2		/	(CH ₂) bending (alkyl unit)
224	1503.4	0.5		/	(CH ₂) bending (alkyl unit)
223	1502.8	9.4			(CH) bending (O-acetyl)
222	1499.88	0.5		⊥	(CH ₂) bending (alkyl unit)
221	1499.2	0.1		/	(CH ₂) bending (alkyl unit)
220	1496.9	0.6		⊥	(CH ₂) bending (alkyl unit)
219	1493.4	16.2	1475	/	(CH) bending (O-acetyl)
218	1490.8	2.1		/	(CH) bending (O-acetyl)
217	1489.9	13.4			(CH) bending (O-acetyl)
216	1489.4	10.5			(CH) bending (O-acetyl)
215	1489.2	12.5			(CH) bending (O-acetyl)
214	1482.8	11.1		/	(CH) bending (O-acetyl)

213	1480.7	13.5			(CH) bending (O-acetyl)
212	1480.1	13.6		/	(CH) bending (O-acetyl)
211	1476.1	3.3		/	(CC _{azobenzene ring}) deformation; N=N stretch
210	1455.6	6.0			(CC _{azobenzene ring}) deformation
209	1429.8	15.7		/	(CH ₂) & (CH _{man}) bending
208	1425.2	38.1	1390	⊥	(CH ₂) bending (alkyl unit)
207	1416.9	12.4		/	(CC _{azobenzene ring}) deformation; N=N stretch
206	1414.4	31.8			(CH) bending (O-acetyl)
205	1414.1	2.1		/	(CH ₂) bending (alkyl unit)
204	1413.9	57.6	1370	/	(CH) bending (O-acetyl)
203	1412.1	2.8			(CH) bending (alkyl unit)
202	1411.4	20.4		⊥	(CH) bending (O-acetyl)
201	1407.9	51.1			(CH) bending (O-acetyl)
200	1404.3	11.2			(CH ₂) bending (alkyl unit)
199	1400.8	8.2			(CH) bending (O-acetyl)
198	1388.9	0.4		/	(CH ₂) bending (man unit)
197	1384.6	2.9		/	(CH ₂) bending (alkyl unit)
196	1381.7	52.9		⊥	(CH _{man}) bending
195	1375.5	1.1		/	(CH ₂) & (CH _{man}) bending
194	1362.8	31.1		/	(CH ₂) & (CH _{man}) bending
193	1356.1	21.3		⊥	(CH ₂) bending (alkyl unit)
192	1350.8	2.0		/	(CH ₂) & (CH _{man}) bending
191	1350.5	0.1		⊥	(CH ₂) bending (alkyl unit)
190	1348.4	0.2		⊥	(CH ₂) bending (alkyl unit)
189	1346.5	25.6			(CH ₂) & (CH _{man}) bending
188	1343.7	0.7			(CH ₂) & (CH _{man}) bending
187	1339.3	0.1		/	(CH ₂) twist (alkyl unit)
186	1337.0	0.1			(CH ₂) twist (alkyl unit)
185	1335.8	6.1			(CH ₂) & (CH _{man}) bending
184	1327.8	0.1		⊥	(CH ₂) twist (alkyl unit)
183	1323.6	0.9		/	(CH _{azobenzene ring}) & (CH _{man}) bending
182	1319.6	2.1			(CH _{azobenzene ring}) bending
181	1318.0	6.0		⊥	(CH _{azobenzene ring}) bending; (CH ₂) twist (alkyl unit)
180	1316.6	1.9		⊥	(CH ₂) twist (alkyl unit)
179	1316.2	1.8			(CH _{azobenzene ring}) bending
178	1291.2	0.2			(CH ₂) twist (alkyl unit)
177	1290.1	8.8			(CH ₂) & (CH _{man}) bending
176	1281.8	6.5		/	(CH ₂) twist (alkyl unit)
175	1266.4	13.2			(CH ₂) twist (man unit)
174	1258.6	0.1		/	(CH ₂) twist (alkyl unit)
173	1254.5	236.8	1300	⊥	(CC _{azobenzene ring}) deformation; (CH _{azobenzene ring}) bending; aryl-N stretch
172	1249.0	14.7		/	(CH ₂) twist (alkyl unit)
171	1240.3	43.6		/	(CH ₂) twist (man unit); (CH _{man}) twist

170	1234.6	50.2		⊥	(CC _{azobenzene ring}) deformation; (CH) bending (O-acetyl)
169	1231.1	363.2	}	⊥	(CC _{azobenzene ring}) deformation, C _{aryl} -O _{alkyl chain} stretch
168	1227.9	0.5		/	(CH ₂) twist (alkyl unit)
167	1224.6	6.5		/	(CH ₂) twist (alkyl unit)
166	1220.0	431.1		/	C-O stretch (O-acetyl)
165	1214.4	783.1		⊥	C-O stretch (O-acetyl)
164	1207.4	138.9		/	(CC _{azobenzene ring}) deformation
163	1206.5	236.9			C-O stretch (O-acetyl)
162	1191.1	345.5		⊥	(CC _{azobenzene ring}) deformation, C _{aryl} -O _{man} stretch
161	1186.3	1.2		/	(CH ₂) twist (alkyl unit)
160	1174.9	16.6		/	(CH ₂) & (CH _{man}) bending
159	1161.0	514.6	1150	⊥	(CC _{azobenzene ring}) deformation
158	1151.7	55.7		⊥	(CC _{azobenzene ring}) deformation
157	1149.0	116.5		⊥	(CH ₂) & (CH _{man}) bending
156	1125.2	12.4			(CH _{azobenzene ring}) bending
155	1122.3	7.2		/	(CH _{azobenzene ring}) bending
154	1120.7	2.4		/	(CH _{azobenzene ring}) bending
153	1119.5	24.5		⊥	(CH _{azobenzene ring}) bending
152	1112.1	18.8		/	(C-C) stretch (man unit)
151	1089.2	0.4		/	(C-C) stretch (alkyl unit)
150	1085.9	0.9			(CH ₂) rocking (alkyl unit)
149	1078.9	29.2			(C-C) stretch (man unit)
148	1070.9	12.1		/	(CH ₃) rocking (O-acetyl)
147	1070.7	4.2		/	(CH ₃) rocking (O-acetyl)
146	1070.4	18.3			(CH ₃) rocking (O-acetyl)
145	1068.8	14.9			(CH ₃) rocking (O-acetyl)
144	1058.9	1.7		⊥	(C-C) stretch (alkyl unit)
143	1057.3	0.1			(C-C) stretch (alkyl unit)
142	1054.6	1.4		⊥	(C-C) stretch (alkyl unit)
141	1043.4	1.1		/	(CH ₂) rocking (alkyl unit)
140	1037.7	26.8		/	(CH ₂) rocking (man unit)
139	1032.6	9.2		⊥	(C-C) stretch (alkyl unit)
138	1030.0	58.1		/	(CH ₃) rocking (O-acetyl)
137	1029.6	5.6		/	(C-C) stretch (alkyl unit)
136	1022.4	7.0		/	(CC _{azobenzene ring}) deformation
135	1020.9	242.2	1040	/	(CH ₃) rocking (O-acetyl)
134	1018.7	7.8		⊥	(CC _{azobenzene ring}) deformation
133	1016.5	97.6		/	(CH ₃) rocking (O-acetyl)
132	1012.3	127.2		/	(CH ₃) rocking (O-acetyl)
131	997.4	161.5			(CH ₃) rocking (O-acetyl)

Fit parameters for the XP spectra of *m*SAM

Table S2. Fit parameters for the XP spectra of *m*SAM; fwhm: full width at half maximum.

C 1s	Major component (aliph+aryl C)	Minor component (hetero atom-C)	Carboxyl
Binding energy (eV)	284.6	285.2	286.6
Area (%)	71	24	5
fwhm	1.1	1.1	1.1
N 1s	Azobenzene N=N		
Binding energy (eV)	400.0		
Area (%)	100		
fwhm	1.8		
S 2p	Ionic/atomic sulfur	Thiolate	Unbound thiolate
Binding energy (eV)	161.2, 162.4	161.9, 163.1	163.0, 164.2
Area (%)	15, 7	40, 20	12, 6
fwhm	0.78	0.78	0.82

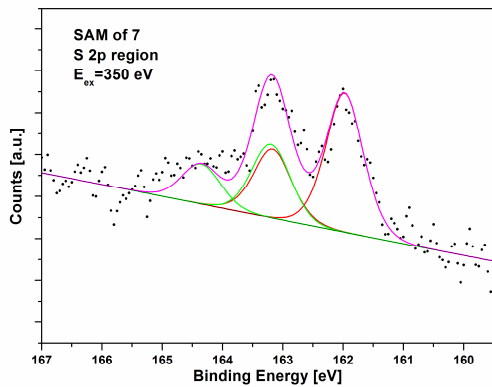


Figure S25. XPS characterization of SAM formed from *E-7*.

9 References

- [1] <http://www.aps.org/publications/apsnews/200402/images/demestral.jpg>,
Online; abgerufen am 29.03.2015.
- [2] http://upload.wikimedia.org/wikipedia/commons/1/12/Burdock_in_Scanning-Electron_Microscope,_magnification_100x.GIF
Online; abgerufen am 29.03.2015.
- [3] <https://blog.h8u.de/uploads/2006/klettverschluss.jpg>,
Online; abgerufen am 29.03.2015.
- [4] <http://www.woman.at/mywoman/static/femme1/layouts/femme1/userbanner0.jpg>,
Online; abgerufen am 29.03.2015.
- [5] http://www.heise.de/tp/artikel/13/13152/13152_1.jpg,
Online; abgerufen am 30.03.2015.
- [6] <http://www.levinegabriella.com/exploringbiomimicry/ciid/wp-content/uploads/2013/07/13.jpg>,
Online; abgerufen am 29.03.2015.
- [7] <http://www.sfb677.de>,
Online; abgerufen am 29.03.2015.
- [8] C. Joachim, J. K. Gimzewski, A. Aviram, *Nature* **2000**, 408, 541.
- [9] M. Ratner, *materials today* **2002**, 20-27.

-
- [10] R. Hagelauer, A. Bode, H. Hellwagner, W. Proebster, D. Schwarzstein, J. Volkert, B. Plattner, P. Schulthess, *Informatik-Handbuch*, 2 Auflage, Pomberger, München **1999**, 298-299.
- [11] G. E. Moore, *Electronics* **1965**, *38*, 114-117.
- [12] <https://norrie.files.wordpress.com/2008/03/moores-law.png>,
Online; abgerufen am 01.04.2015.
- [13] J.E. Green, J. W. Choi, A. Boukai, Y. Bunimovich, E. Johnston-Halperin, E. Delonno, Y. Luo, B. A. Sheriff, K. Xu, Y. S. Shin, H.-R. Tseng, J. F. Stoddart, J. R. Heath, *Nature* **2007**, *445*, 414-417.
- [14] M. A. Reed, C. Zhou, C. J. Muller, T. P. Burgin, J. M. Tour, *Science* **1997**, *278*, 252-254.
- [15] J. Chen, M. A. Reed, A. M. Rawlett, J. M. Tour, *Science* **1999**, *286*, 1550-1552.
- [16] Z. J. Donhauser, B. A. Mantooh, K. F. Kelly, L. A. Bumm, J. D. Monnell, J. J. Stapleton, D. W. Price Jr., A. M. Rawlett, D. L. Allara, J. M. Tour, P. S. Weiss, *Science* **2001**, *292*, 2303-2307.
- [17] M. A. Reed, J. Chen, A. M. Rawlett, D. W. Price, J. M. Tour, *Appl. Phys. Lett.* **2001**, *78*, 3735-3737.
- [18] R. M. Metzger, B. Chen, U. Höpfner, M. V. Lakshmikantham, D. Vuillaume, T. Kawai, X. Wu, H. Tachibana, T. V. Hughes, H. Sakurai, J. W. Baldwin, C. Hosch, M. P. Cava, L. Brehmer, G. J. Ashwell, *J. Am. Chem. Soc.* **1997**, *119*, 10455-10466.

-
- [19] C. Zhou, M. R. Deshpande, M. A. Reed, L. Jones II, J. M. Tour, *Appl. Phys. Lett.* **1997**, *71*, 611-613.
- [20] M.-K. Ng, D.-C. Lee, L. Yu, *J. Am. Chem. Soc.* **2002**, *124*, 11862-11863.
- [21] S. Hauptmann, *Organische Chemie*, 2. Auflage, Deutscher Verlag für Grundstoffindustrie, Leipzig **1988**, 774-775.
- [22] F. Hamelmann, U. Heinzmann, U. Siemeling, F. Bretthauer, J. Vor der Brüggen, *Appl. Surf. Sci.* **2004**, *222*, 1-5.
- [23] Y. Yu, M. Nakano, T. Ikeda *Nature* **2003**, *425*, 145.
- [24] P. P. Birnbaum, D. W. G. Style, *Trans. Faraday Soc.* **1954**, *50*, 1192.
- [25] B. Feringa, *Molecular Switches*, Wiley-VCH, Weinheim **2001**.
- [26] G. Füchsel, T. Klamroth, J. Dokic, P. Saalfrank, *J. Phys. Chem. B* **2006**, *110*, 16337-16345.
- [27] G. S. Hartley, *Nature* **1937**, *140*, 281.
- [28] A. Cembran, F. Bernardi, M. Garavelli, L. Gagliardi, G. Orlandi, *J. Am. Chem. Soc.* **2004**, *126*, 3234.
- [29] S. Monti, G. Orlandi, P. Palmieri, *Chem. Phys.* **1982**, *71*, 87.
- [30] Y.-C. Lu, E. W.-G. Diau, H. Rau, *J. Phys. Chem. A* **2005**, *109*, 2090.

-
- [31] J. Dokić, M. Gothe, J. Wirth, M. V. Peters, J. Schwarz, S. Hecht, P. Saalfrank, *J. Phys. Chem. A* **2009**, *113*, 6763.
- [32] N. Tamai, H. Miyasaka, *Chem. Rev.* **2000**, *100*, 1875.
- [33] G. Füchsel, T. Klamroth, J. Dokić, P. Saalfrank, *J. Phys. Chem. B* **2006**, *110*, 16337.
- [34] S. Kawata, Y. Kawata, *Chem. Rev.* **2000**, *100*, 1777-1788.
- [35] T. Ikeda, O. Tsutsumi, *Science* **1995**, *268*, 1873-1875.
- [36] D. A. Parthenopoulos, P. M. Rentzepis, *Science* **1989**, *245*, 843-845.
- [37] A. A. Ignatin, V. A. Barachevskii, Y. P. Strokach, M. V. Alfimov, R. Guglielmetti, *Zhurnal Nauchnoi I Prikladnoi Fotografii* **2003**, *48*, 27.
- [38] R. B. Morgunov, F. B. Mushenok, S. M. Aldoshin, N. A. Sanina, E. A. Yur'eva, G. V. Shilov, V. V. Tkachev, *New J. Chem.* **2009**, *33*, 1374.
- [39] P. Toman, W. Bartkowiak, S. Nespurek, J. Sworakowski, R. Zalesny, *Chem. Phys.* **2005**, *316*, 267.
- [40] S. Kajimoto, A. Mori, H. Fukumura, *Photochem. Photobiol. Sci.* **2010**, *9*, 208.
- [41] P. Seal, S. Chakrabarti, *J. Phys. Chem. A* **2010**, *114*, 673.
- [42] M. L. Bossi, J. B. Rodriguez, P. F. Aramendia, *J. Photochem. Photobiol. A Chem.* **2006**, *179*, 35.

-
- [43] F. Renth, M. Foca, A. Petter, F. Temps, *Chem. Phys. Lett.* **2006**, *428*, 62.
- [44] R. Siewertsen, F. Renth, F. Temps, F. Sönnichsen, *Phys. Chem. Chem. Phys.* **2009**, *11*, 5952.
- [45] O. Todic, K. Altenhoner, J. Mattay, *Photochem. Photobiol. Sci.* **2010**, *9*, 128.
- [46] V. Guerschais, L. Ordronneau, H. Le Bozec, *Coord. Chem. Rev.* **2010**, *254*, 2533.
- [47] C. J. Xia, C. F. Fang, P. Zhao, H. C. Liu, *Europ. Phys. J. D* **2010**, *59*, 375.
- [48] M. Morimoto, M. Irie, *J. Am. Chem. Soc.* **2010**, *132*, 14172.
- [49] A. Ulman, *Chem. Rev.* **1996**, *96*, 1533-1554.
- [50] J. C. Love, L. A. Estroff, J. K. Kriebel, R. G. Nuzzo, G. M. Whitesides, *Chem. Rev.* **2005**, *105*, 1103-1169.
- [51] S. M. Barlow, R. Raval, *Surf. Sci. Rep.* **2003**, *50*, 201-341.
- [52] S. De Feyter, F. C. De Schreyer, *Chem. Soc. Rev.* **2003**, *32*, 139-150.
- [53] M.A. Chesters, G.A. Somorjai, *Surf. Sci.* **1975**, *52*, 21-28.
- [54] M.J. Ford, C. Masens, M.B. Cortie, *Surf. Rev. Lett.* **2006**, *13*, 297-307.
- [55] F. Schreiber, *Surf. Sci.* **2000**, *65*, 151-257.

- [56] L. S. Alarcon, L. Chen, V. A. Esaulov, J. E. Gayone, E. Sanchez, O. Grizzi, *J. Phys. Chem. C* **2010**, *114*, 19993-19999.
- [57] J. G. Vos, R. J. Forster, T. E. Keyes, *Interfacial Supramolecular Assemblies* **2003**, Wiley, 88-94.
- [58] M. Madou, *Fundamentals of Microfabrication: The Science of Miniaturization*, CRC **2002**, 62-63.
- [59] S. Saliterman, *Self-assembled monolayers (SAMs). Fundamentals of BioMEMS and Medical Microdevices*, SPIE Press **2006**, 94-96.
- [60] A. Shaporenko, J. Muller, T. Weidner, A. Terfort, M. Zharnikov, *J. Am. Chem. Soc.* **2007**, *129*, 2232-2233.
- [61] S. Subramanian, S. Sampath, *J. Colloid Interface Sci.* **2007**, *312*, 413-424.
- [62] J. J. Stapleton, T. A. Daniel, S. Uppili, O. M. Cabarcos, J. Naciri, R. Shashidhar, D. L. Allara, *Langmuir* **2005**, *21*, 11061-11070.
- [63] R. G. Nuzzo, D. L. Allara, *J. Am. Chem. Soc.* **1983**, *105*, 4481-4483.
- [64] D. K. Schwartz, *Annu. Rev. Phys. Chem.* **2001**, *52*, 107-137.
- [65] L. H. Dubois, B.R. Zegarski, R.G. Nuzzo, *J. Chem. Phys.* **1993**, *98*, 678-688.
- [66] J. Libuda, G. Scoles, *J. Phys. Chem. B* **1999**, *103*, 9933-9943.

-
- [67] D. J. Lavrich, S.M. Wetterer, S.L. Bernasek, G. Scoles, *J. Phys. Chem. B* **1998**, *102*, 3456-3465.
- [68] S. M. Wetterer, D.J. Lavrich, T. Cummings, S.L. Bernasek, G. Scoles, *J. Phys. Chem. B* **1998**, *102*, 9266-9275.
- [69] H. Sellers, *Surf. Sci.* **1993**, *294*, 99-107.
- [70] E. Shustorovich, *Surf. Sci. Rep.* **1986**, *6*, 1-63.
- [71] K. Autumn, Y. A. Liang, S. T. Hsieh, W. Zesch, W. P Chan, T. W. Kenny, R. Fearing, R. J. Full, *Nature* **2000**, *405*, 681-685.
- [72] G. Ertl, *Angew. Chem.* **2008**, *120*, 3578-3590.
- [73] R. W. Kessler, *Prozessanalytik: Strategien und Fallbeispiele aus der industriellen Praxis*, Wiley-VCH **2006**, 231.
- [74] P. R. Griffiths, J. A. De Haseth, J. D. Winefordner, *Fourier Transform Infrared Spectrometry*, 2 Auflage, Wiley John & Sons **2007**, 297-300.
- [75] R. Aroca, *Surface-Enhanced Vibrational Spectroscopy*, John Wiley & Sons **2006**, 60.
- [76] P. Hollis, *Infrared Reflection-Absorption Spectroscopy* in R. A. Meyers *Encyclopedia of Analytical Chemistry: Applications, Theory, and Instrumentation*, John Wiley & Sons **2000**.
- [77] P. R. Griffiths, J. A. De Haseth, J. D. Winefordner, *Fourier Transform Infrared Spectrometry*, 2 Auflage, Wiley John & Sons **2007**, 284-285.

- [78] R. G. Greenler, *J. Chem. Phys.* **1966**, *44*, 1963.
- [79] D. C. Harris, M.D. Bertolucci, *Symmetry and Spectroscopy*, Oxford University Press, New York **1978**.
- [80] P. R. Griffith, J. A. d. Haseth, *Fourier Transform Infrared Spectroscopy. Chemical Analysis*, ed. P. J. Elving und J. D. Winefordner, *83*, John Wiley & Sons, Chichester, New York, Brisbane, Toronto, Singapore **1986**.
- [81] P. W. Atkins, *Physikalische Chemie*, VCH, Weinheim, New York, Basel, Cambridge, Tokyo **1996**.
- [82] N. B. Colthup, L. H. Daly, S. E. Wiberly, *Introduction to Infrared and Raman Spectroscopy*, 3rd ed., Academic Press, San Diego, **1990**.
- [83] E. B. Wilson, J. C. Decius, P. C. Cross, *Molecular Vibrations*, McGraw-Hill, New York **1955**.
- [84] J. E. Steward, *Infrared Spectroscopy. Experimental Methods and Techniques*, Marcel Dekker, New York **1970**.
- [85] P. M. Morse, *Phys. Rev.* **1929**, *34*, 57-64.
- [86] R. G. Greenler, *J. Chem. Phys.* **1969**, *50*, 310-315.
- [87] A. Neckel, *Fresenius' Zeitschrift für Analytische Chemie* **1984**, *319*, 682-694.
- [88] M. A. Ramin, G. Le Bourdon, N. Daugey, B. Bennetau, L. Vellutini, T. Buffeteau, *Langmuir* **2011**, *27*, 6076-6084.

-
- [89] A. H. Kycia , K. Koczkur, J. J. Leitch, J. Lipkowski, V. Zamlynny, M. W. P. Petryk, *Anal. Bioanal. Chem.* **2013**, *405*, 1537-1546.
- [90] T. Buffeteau, B. Desbat, D. Blaudez, J. M. Turlet, *Appl. Spectrosc.* **2000**, *54*, 1646-1640.
- [91] L. Cambi, A. Cagnasso, *Atti Accad. Naz. Lincei* **1931**, *13*, 809.
- [92] L. Cambi, L. Szego, *Ber. Dtsch. Chem. Ges. B* **1931**, *64*, 2591-2598.
- [93] K. S. Murray, C. J. Kepert, *Topics Curr. Chem.* **2004**, *233*, 195-228.
- [94] T. Granier, B. Gallois, J. Gaultier, J. A. Real, J. Zarembowitch, *Inorg. Chem.* **1993**, *32*, 5305-5312.
- [95] P. Gütllich, Y. Gracia, T. Woike, *Coord. Chem. Rev.* **2001**, *219*, 839-879.
- [96] P. Gütllich, A. Hauser, H. Spiering, *Angew. Chem.* **1994**, *106*, 2109-2141.
- [97] J. A. Real, A. B. Gaspar, M. C. Muñoz, *Dalton Trans.* **2005**, 2062-2079.
- [98] O. Kahn, *Molecular Magnetism*, Wiley-VCH, New York **1993**.
- [99] P. Gütllich, Y. Garcia, H. A. Goodwin, *Chem. Soc. Rev.* **2000**, *29*, 419-427.
- [100] J. A. Real, A. B. Gaspar, V. Niel, M. C. Muñoz, *Coord. Chem. Rev.* **2003**, *236*, 121-141.

- [101] S. Decurtins, P. Gütlich, C. P. Köhler, H. Spiering, A. Hauser, *Chem. Phys. Lett.* **1984**, *105*, 1-4.
- [102] D. Dolphin, T. Niem, R. H. Felton, I. Fujita, *J. Am. Chem. Soc.* **1975**, *97*, 5288-5290.
- [103] J. Seth, V. Palaniappan, D. F. Bocian, *Inorg. Chem.* **1995**, *34*, 2201-2206.
- [104] C. P. Berlinguette, A. Dragulescu-Andrasi, A. Sieber, J. R. Galán-Mascarós, H.-U. Güdel, C. Achim, K. R. Dunbar, *J. Am. Chem. Soc.* **2004**, *126*, 6222-6223.
- [105] C. P. Berlinguette, A. Dragulescu-Andrasi, A. Sieber, H.-U. Güdel, C. Achim, K. R. Dunbar, *J. Am. Chem. Soc.* **2005**, *127*, 6766-6779.
- [106] P. Gütlich, H. A. Goodwin, *Spin Crossover in Transition Metal Compounds I-III, Topics in Current Chemistry*, Springer-Verlag, Berlin Heidelberg New York **2004**.
- [107] O. Sato, J. Tao, Y.-Z. Zhang, *Angew. Chem.* **2007**, *119*, 2200-2236.
- [108] O. Sato, J. Tao, Y.-Z. Zhang, *Angew. Chem. Int. Ed.* **2007**, *46*, 2152-2187.
- [109] O. Kahn, C. J. Martinez, *Science* **1998**, *279*, 44.
- [110] O. Kahn, J. Kröber, C. Jay, *Adv. Mater.* **1992**, *4*, 718-728.
- [111] A. Tasaki, *J. Appl. Phys.* **1970**, *41*, 1000.
- [112] A. Hauser, *Chem. Phys. Lett.* **1986**, *124*, 543-548.
- [113] A. Hauser, *J. Chem. Phys.* **1991**, *94*, 2741-2748.

-
- [114] A. Sour, M. L. Boillot, E. Riviere, P. Lesot, *Eur. J. Inorg. Chem.* **1999**, 2117.
- [115] M. L. Boillot, S. Chantraine, J. Zarembowitch, J. Y. Lallemand, J. Prunet, *New J. Chem.* **1999**, *23*, 179.
- [116] M. L. Boillot, A. Sour, P. Delhaes, C. Mingotaud, H. Soyer, *Coord. Chem. Rev.* **1999**, *192*, 47.
- [117] Y. Hasegawa, S. Kumea, H. Nishihara, *Dalton Trans.* **2009**, 280-284.
- [118] S. Hirose, S. Hayami, Y. Maeda, *Bull. Chem. Soc. Jpn.* **2000**, *73*, 2059-2066.
- [119] I. Nemeč, R. Boča, M. Gembický, L. Dlhaň, R. Herchel, F. Renz, *Inorg. Chim. Acta* **2009**, *362*, 4754-4759.
- [120] S. Decurtins, P. Gütlich, K. M. Hasselbach, A. Hauser, H. Spiering, *Inorg. Chem.* **1985**, *24*, 2174.
- [121] S. Decurtins, P. Gütlich, C. P. Köhler, H. Spiering, *J. Chem. Soc. Chem. Comm.* **1985**, 430.
- [122] M. S. Alam, M. Stocker, K. Gieb, P. Mueller, M. Haryono, K. Student, A. Grohmann, *Angew. Chem. Int. Ed.* **2010**, *49*, 1159-1163.
- [123] J. P. Collman, N. K. Devaraj, P. A. Todd, *Langmuir* **2006**, *22*, 2457-2464.
- [124] E. Darlatt, C. H.- H. Traulsen, J. Poppenberg, S. Richter, J. Kühn, C. A. Schalley, W. E. S. Unger, *J. Electron. Spectrosc. Relat. Phenom.* **2012**, *185*, 85-89.

-
- [125] T. G. Gopakumar, F. Matino, H. Naggert, A. Bannwarth, F. Tuzcek, R. Berndt, *Angew. Chem. Int. Ed.* **2012**, *51*, 6262.
- [126] T. G. Gopakumar, M. Bernien, H. Naggert, F. Matino, C. F. Hermanns, A. Bannwarth, S. Mühlenberend, A. Krüger, D. Krüger, F. Nickel, W. Walter, R. Berndt, W. Kuch, F. Tuzcek, *Chem. Europ. J.* **2013**, *19*, 15702-15709.
- [127] H. Naggert, A. Bannwarth, S. Chemnitz, T. van Hofe, E. Quandt, F. Tuzcek, *Dalton Trans.* **2011**, *40*, 6364-6366.
- [128] V. Meded, A. Bagrets, K. Fink, R. Chandrasekar, M. Ruben, F. Evers, A. Bernand-Mantel, J. S. Seldenthuis, A. Beukman, H. S. J. van der Zant, *Phys. Rev. B* **2011**, *83*, 245415.
- [129] E. Ludwig, H. Naggert, M. Kalläne, S. Rohlf, E. Kröger, A. Bannwarth, A. Quer, K. Rossnagel, L. Kipp, F. Tuzcek, *Angew. Chem. Int. Ed.* **2014**, *53*, 3019-3023.
- [130] C. R. Mayer, G. Cucchiaro, J. Jullien, F. Dumur, J. Marrot, E. Dumas, F. Séheresse, *Eur. J. Inorg. Chem.* **2008**, 3614-3623.
- [131] H. C. Kolb, M. G. Finn, K. B. Sharpless, *Angew. Chem. Int. Ed.* **2001**, *40*, 2004.
- [132] M. Orchin, R. S. Macomber, A. R. Pinhas, R. M. Wilson, *The Vocabulary and Concepts of Organic Chemistry*, 2. Auflage, John Wiley & Sons, Hoboken **2005**, 583-584.
- [133] W. B. Austin, N. Bilow, W. J. Kelleghan, K. S. Y. Lau, *J. Org. Chem.* **1981**, *46*, 2280-2286.

-
- [134] B. Tang, F. Yu, P. Li, L. Tong, X. Duan, T. Xie, X. Wang, *J. Am. Chem. Soc.* **2009**, *131*, 3016-3023.
- [135] J. Poppenberg, S. Richter, E. Darlatt, Ch. H.- H. Traulsen, H. Min, W. E. S. Unger, Ch. A. Schalley, *Surf. Sci.* **2012**, *606*, 367-377.
- [136] J. Čechal, C.S. Kley, T. Kumagai, F. Schramm, M. Ruben, S. Stepanow, K. Kern, *J. Phys. Chem. C* **2013**, *117*, 8871-8877.
- [137] B. Schwager, *Dissertation*, CAU Kiel, **2014**.
- [138] A. Nitzan, *Annu. Rev. Phys. Chem.* **2001**, *52*, 681.
- [139] A. Nitzan, M. A. Ratner, *Science* **2003**, *300*, 1384.
- [140] N. J. Tao, *Nat. Nanotechnol.* **2006**, *1*, 173.
- [141] L. Lafferentz, F. Ample, H. Yu, S. Hecht, C. Joachim, L. Grill, *Science* **2009**, *323*, 193-197.
- [142] M. J. Frampton, H. L. Anderson, *Angew. Chem.* **2007**, *119*, 1046-1083.
- [143] J. H. Burroughes, D. D. C. Bradley, A. R. Brown, R. N. Marks, K. Mackay, R. H. Friend, P. L. Burn, A. B. Holmes, *Nature* **1990**, *347*, 539-541.
- [144] S. R. Forrest, *Nature* **2004**, *428*, 911-918.

-
- [145] R. H. Friend, R. W. Gymer, A. B. Holmes, J. H. Burroughes, R. N. Marks, C. Taliani, D. D. C. Bradley, D. A. Dos Santos, J. L. Brédas, M. Lögdlund, W. R. Salaneck, *Nature* **1999**, *397*, 121-128.
- [146] A. Kraft, A. C. Grimsdale, A. B. Holmes, *Angew. Chem.* **1998**, *110*, 416-443.
- [147] H. Sirringhaus, N. Tessler, R. H. Friend, *Science* **1998**, *280*, 1741-1744.
- [148] M. Granström, K. Petritsch, A. C. Arias, A. Lux, M. R. Andersson, R. H. Friend, *Nature* **1998**, *395*, 257-260.
- [149] A. Rose, Z. G. Zhu, C. F. Madigan, T. M. Swager, V. Bulovic, *Nature* **2005**, *434*, 876-879.
- [150] M. Ikegame, K. Tajima, T. Aida, *Angew. Chem.* **2003**, *115*, 2204-2207.
- [151] G. Li, S. Bhosale, T. Wang, Y. Zhang, H. Zhu, J.-H. Fuhrhop, *Angew. Chem.* **2003**, *115*, 3948-3951.
- [152] D. Chapman, R. J. Warn, A. G. Fitzgerald, A. D. Yoffe, *Trans. Faraday Soc.* **1964**, *60*, 294-300.
- [153] J. C. Bailar, *J. Inorg. Nucl. Chem.* **1958**, *8*, 165.
- [154] H. S. Rzepa, M. E. Cass, *Inorg. Chem.* **2007**, *46*, 8024-8032.
- [155] S. D. Evans, S. R. Johnson, H. Ringsdorf, L. M. Williams, H. Wolf, *Langmuir* **1998**, *14*, 6436-6440.

-
- [156] T. Weidner, F. Bretthauer, N. Ballav, H. Motschmann, H. Orendi, C. Bruhn, U. Siemeling, M. Zharnikov, *Langmuir* **2008**, *24*, 11691-11700.
- [157] R. Wang, T. Iyoda, L. Jiang, D. A. Tryk, K. Hashimoto, A. Fujishima, *Langmuir* **1996**, *12*, 2052.
- [158] D. Takamatsu, Y. Yamakoshi, K.-I. Fukui, *J. Phys. Chem. B* **2006**, *110*, 1968-1970.
- [159] S. Wagner, F. Leyssner, C. Kordel, S. Zarwell, R. Schmidt, M. Weinelt, K. Rück-Braun, M. Wolf, P. Tegeder, *Phys. Chem. Chem. Phys.* **2009**, *11*, 6242-6248.
- [160] V. Balzani, A. Credi, F. M. Raymo, J. F. Stoddart, *Angew. Chem.* **2000**, *112*, 3484-3530.
- [161] E. R. Kay, D. A. Leigh, F. Zerbetto, *Angew. Chem.* **2007**, *119*, 72-196.
- [162] H. Noji, R. Yasuda, M. Yoshida, K. Kinosita, *Nature* **1997**, *386*, 299-302.
- [163] K. Kinbara, T. Aida, *Chem. Rev.* **2005**, *105*, 1377-1400.
- [164] M. V. V. Balzani, A. Credi, *Molecular Devices and Machines: Concepts and Perspectives for the Nanoworld*, Wiley-VCH, Weinheim, **2008**.
- [165] G. S. Kottas, L. I. Clarke, D. Horinek, J. Michl, *Chem. Rev.* **2005**, *105*, 1281-1376.
- [166] G. Bottari, D. A. Leigh, E. M. Pérez, *J. Am. Chem. Soc.* **2003**, *125*, 13360-13361.

- [167] A. M. Brouwer, C. Frochot, F. G. Gatti, D. A. Leigh, L. Mottier, F. Paolucci, S. Roffia, G. W. H. Wurpel, *Science* **2001**, *291*, 2124-2128.
- [168] V. Balzani, M. Clemente-Leon, A. Credi, B. Ferrer, M. Venturi, A. H. Flood, J. F. Stoddart, *Proc. Natl. Acad. Sci. U. S. A.* **2006**, *103*, 1178-1183.
- [169] T. R. Kelly, H. De Silva, R. A. Silva, *Nature* **1999**, *401*, 150-152.
- [170] N. Koumura, R. W. J. Zijlstra, R. A. van Delden, N. Harada, B. L. Feringa, *Nature* **1999**, *401*, 152-155.
- [171] N. Koumura, E. M. Geertsema, A. Meetsma, B. L. Feringa, *J. Am. Chem. Soc.* **2000**, *122*, 12005-12006.
- [172] D. A. Leigh, J. K. Y. Wong, F. Dehez, F. Zerbetto, *Nature* **2003**, *424*, 174-179.
- [173] <http://remf.dartmouth.edu/images/mammalianLungSEM/source/13.html>,
Online; abgerufen am 29.03.2015.
- [174] J. Kubitschke, *Dissertation*, CAU Kiel, **2010**.
- [175] B. W. Laursen, F. C. Krebs, *Angew. Chem.* **2000**, *112*, 3574-3576.
- [176] B. Baisch, D. Raffa, U. Jung, O. M. Magnussen, C. Nicolas, J. Lacour, J. Kubitschke, R. Herges, *J. Am. Chem. Soc.* **2009**, *131*, 442-443.
- [177] S. Lemke, S. Ulrich, F. Claußen, A. Bloedorn, U. Jung, R. Herges, O. Magnussen, *Surf. Sci.* **2015**, *632*, 71-76.

-
- [178] S. Kuhn, B. Baisch, U. Jung, T. Johannsen, J. Kubitschke, R. Herges, O. Magnussen, *Phys. Chem. Chem. Phys.* **2010**, *12*, 4481-4487.
- [179] U. Jung, C. Schütt, O. Filinova, J. Kubitschke, R. Herges, O. Magnussen, *J. Phys. Chem. C* **2012**, *116*, 25943-25948.
- [180] U. Jung, J. Kubitschke, R. Herges, O. Magnussen, *Electrochim. Acta* **2013**, *112*, 869-880.
- [181] J. Kubitschke, C. Näther, R. Herges, *Eur. J. Org. Chem.* **2010**, *26*, 5041-5055.
- [182] U. Jung, M. Müller, N. Fujimoto, K. Ikeda, K. Uosaki, U. Cornelissen, F. Tucek, C. Bornholdt, D. Zargarani, R. Herges, O. Magnussen, *J. Colloid Interface Sci.* **2010**, *341*, 366-375.
- [183] U. Jung, S. Kuhn, U. Cornelissen, F. Tucek, T. Strunskus, V. Zaporojtchenko, J. Kubitschke, R. Herges, O. Magnussen, *Langmuir* **2011**, *7*, 5899-5908.
- [184] U. Jung, O. Filinova, S. Kuhn, D. Zargarani, C. Bornholdt, R. Herges, O. Magnussen, *Langmuir* **2010**, *26*, 13913-13923.
- [185] S. Y. Wang, D. C. Huang, Y. T. Tao, *Chin. Chem. Soc.* **2012**, *59*, 9-17.
- [186] T. A. Darwish, Y. Tong, M. James, T. L. Hanley, Q. Peng, S. Ye, *Langmuir* **2012**, *28*, 13852-13860.
- [187] http://en.wikipedia.org/wiki/Glycocalyx#/media/File:Baillus_subtilis.jpg
Online; abgerufen am 01.04.2015.

- [188] R. Lüllmann-Rauch, *Histologie*, 4. Auflage, Thieme, Stuttgart, New York, **2003**.
- [189] T. Weber, V. Chandrasekaran, I. Stamer, M. B. Thygesen, A. Terfort, T. K. Lindhorst, *Angew. Chem. Int. Ed.* **2014**, *53*, 14583-14586.

10 Eidesstattliche Erklärung

Hiermit erkläre ich, Hanne Jacob, an Eides statt, dass ich die vorliegende Arbeit selbstständig und nur mit den angegebenen Hilfsmitteln angefertigt habe. Diese Arbeit ist nach Inhalt und Form - abgesehen von der Beratung durch meinen Betreuer Herrn Prof. Dr. F. Tuzek - durch mich eigenständig verfasst worden. Sie ist nach den Regeln guter wissenschaftlicher Praxis der Deutschen Forschungsgemeinschaft verfasst worden und hat, außer in Auszügen der eigenen Diplomarbeit, nicht an einer anderen Stelle im Rahmen eines Prüfungsverfahrens vorgelegen. Dies ist mein erster Promotionsversuch.

Kiel, 01.04.2015

Hanne Jacob

11 Curriculum vitae

Persönliche Daten

Dipl. Chem. Hanne Jacob

Goethestr. 29

24116 Kiel

geb. am 17. Januar 1986

in Brunsbüttel

Staatsangehörigkeit: deutsch

Schulbildung

1992-1996: Grund-und Hauptschule Marne

1996-2005: Gymnasium Marne, Abitur

2005-2006: Studium der Lebensmitteltechnologie an der "University of Science" in Bremerhaven

Mai-September 2006: Praktikum Sasol Germany GmbH im Bereich Forschung und Entwicklung, Brunsbüttel

ab Oktober 2006: Studium der Chemie an der Christian-Albrechts-Universität zu Kiel

Oktober 2008: Diplomchemiker Vorprüfung, Vordiplom

ab August 2010-Januar 2011: Diplomarbeit bei Prof. Dr. F. Tucek

ab April 2011: Dissertation bei Prof. Dr. F. Tucek